Process-based modelling of waves interacting with porous bonded revetments and their sand foundation

Von der
Fakultät Architektur, Bauingenieurwesen und Umweltwissenschaften
der Technischen Universität Carolo-Wilhelmina
zu Braunschweig

zur Erlangung des Grades eines
Doktoringenieurs (Dr.-Ing.)
genehmigte

Dissertation

von
Juan Carlos Alcérreca-Huerta
geboren am 30.08.1986
aus Mexiko Stadt, Mexiko

Eingereicht am: 04. Juni 2014
Disputation am: 26. September 2014

Berichterstatter: Prof. Hocine Oumeraci
Prof. Rodolfo Silva

2014

Preface

The present PhD research has been conducted thanks to a scholarship for postgraduate studies given by the Consejo Nacional de Ciencia y Tecnología (CONACyT) in collaboration with the Deutsche Academischer Austauschdienst (DAAD), which is greatly acknowledged (scholarship CONACyT-DAAD 310076).

I would also like to express my special gratitude and thanks to Prof. Dr.-Ing Hocine Oumeraci for allowing me to conduct the PhD study under his supervision in the Leichtweiß-Institut für Wasserbau (LWI), Braunschweig, Germany and for encouraging my research with his valuable guidance and experience. Support from Prof. Dr.-Ing. Andreas Kortenhaus during the PhD research is highly appreciated. A special thanks to Prof. Dr. Rodolfo Silva Casarín for motivating me to study the PhD abroad and for his help and that of M.Eng. Jair del Valle Morales for help with the laboratory tests in the wave flume at the Engineering Institute, UNAM.

I would also like to thank my colleagues at the LWI for their friendship, guidance, assistance and especially for all those meaningful and rewarding opportunities for personal and professional growth inside and outside the Institute. This acknowledgment also extends to the colleagues in the Large Wave Flume (GWK) at the Forschungszentrum Küste (FZK), Hannover, Germany.

Finally, I would like to thank my parents Jorge Alejandro Alcérreca Félix and María Luisa Huerta Bravo, my brother Jorge Alejandro Alcérreca Huerta, my loved ones and friends, who have supported me throughout the entire process and, together with me, have overcome so many challenges. I really appreciate all your help, presents and kind feelings which help me to make me smile and to stay always with you. I feel proud of being part of your heart and of your lives. Moreover, thanks to God for listening to my prayers, for allowing me to stay with Him every day and for filling up my life with happiness and love.

Braunschweig, June 2014

Juan Carlos Alcérreca Huerta

Kurzfassung

Um dem möglichen Anstieg der Sturmhäufigkeit und dem steigenden klimabedingten Meeresspiegel bei der dramatisch zunehmenden Nutzung des Küstenraumes zukünftig gewachsen zu sein, werden neue Küstenschutzsysteme benötigt. Die hochporösen polyurethangebundenen (PBA) Deckwerke sind ein Beispiel für solche neuen umweltverträglichen Alternativen für den Küsten- und Uferschutz, die bereits in Europa und anderen Ländern Verwendung finden. Weitere erwähnenswerte Vorteile von PBA-Deckwerken gegenüber herkömmlichen undurchlässigen Deckwerken bestehen in der Reduzierung der Wellenreflexion, des Wellenauf- und -ablaufs sowie der welleninduzierten Druckbelastung. Dennoch besteht noch kein ausreichendes Verständnis der ablaufenden hydrogeotechnischen Prozesse beim Wellenangriff auf PBA-Deckwerke und deren Unterbau, um eine sichere Bemessung gewährleisten zu können.

Vor diesem Hintergrund besteht das Hauptziel dieser Arbeit in der Modellierung dieser hydrogeotechnischen Prozesse durch ein neu zu entwickelnden CFD-CSD-System, das mit den Daten aus den weltweit einzigartigen großmaßstäblichen Modellversuchen mit einem PBA-Deckwerk im Großen Wellenkanal (GWK) des Forschungszentrums Küste (FZK) in Hannover, Deutschland (Oumeraci et al. (2010)), validiert wird. Zu diesem Zweck wurde zunächst eine umfassende Wissenstandsanalyse durchgeführt. Als zweiter Schritt erfolgte die Implementierung der *„Volume-Averaged RANS-VOF“* basierten Gleichungen in das CFD-Modell und der schwachen Kopplung mit dem CSD-Modell, um die Interaktion der Wellen mit dem PBA-Deckwerk und seinem sandigen Unterbau beschreiben zu können. Der dritte Schritt umfasste die Kalibrierung und Validierung des CFD-CSD-Modellsystems "`wavePoreGeoFoam`" unter Verwendung der großmaßstäblichen Versuche im GWK und kleinmaßstäblicher Versuche, die am Leichtweiß-Institut für Wasserbau (LWI) (Liebisch & Oumeraci (2014)) durchgeführt wurden. Das validierte Modell wurde anschließend für eine systematische Parameterstudie verwendet, um die Versuchsbedindungen (z.B. Wellenhöhe und -periode) und die Deckwerkseigenschaften (z.B. Böschungsneigung und Dicke der Filterschicht) zu erweitern.

Abschließend wurde eine Analyse der hydrogeotechnischen Prozesse basierend auf den Ergebnissen der Parameterstudie durchgeführt. Hierbei konnten neue Bemessungsformeln für die hydrodynamischen Prozesse auf und vor dem PBA-Deckwerke sowie für die welleninduzierten Drücke auf und unter dem Deckwerk, einschließlich der Porenwasserdrücke im Sandkern, entwickelt werden. Weiterhin wird eine systematische Methode für die Stabilitätsanalyse des Sandkerns unterhalb von PBA-Deckwerken vorgeschlagen, um der welleninduzierten Bodenverflüssigung vorzubeugen.

Die Ergebnisse zeigen insbesondere die Wichtigkeit des Einflusses der Böschungsneigung auf den Brandungsstau sowie auf die Wellenreflexion und den Brechvorgang. Wellenauf- und -ablauf werden außerdem von der Filterschichtdicke beeinflusst, die auch eine entscheidende Größe für die maximalen Drücke auf und unter dem Deckwerk sowie für die Stabilität des Unterbaus gegen Bodenverflüssigung darstellt. Die in der numerischen Parameterstudie gewonnenen Porenwasserdruckverteilungen im Sandkern senkrecht zur Deckwerksoberfläche ergaben eine gute Übereinstimmung im Vergleich mit den Ergebnissen einer Analyse des durchlässigen Seebodens ohne Deckwerk, in welcher die Durchlässigkeit, die Porosität und der Luftgehalt in den Poren die Schlüsselparameter darstellen. Insgesamt konnten mit den Ergebnissen und Methoden dieser Arbeit die in den vorigen Studien (z.B. Oumeraci et al. (2010) und Foyer (2013)) aufgetretenen Einschränkungen überwunden, so dass substanziell verbesserte und neue wissenschaftlich-technische Grundlage für die Praxis und weitere Forschung erarbeitet wurden.

Abstract

New coastal protection systems against erosion are required to cope with the possible increasing storminess and sea level rise induced by climate change and the increased use of coastal zones. Highly porous Polyurethane Bonded Aggregates (PBA) revetments are an example of ecologically friendly alternatives for the protection of the shoreline and embankments which have been implemented in Europe and further countries. Advantages of PBA-revetments over common impermeable revetments are: reduction of wave reflection, wave run-up/run-down and wave-induced pressures. However, for a safe design, the hydro-geotechnical processes involved in the interaction of waves with such PBA-revetments and their foundation are still not sufficiently understood.

The main objective of this PhD study is therefore to enhance the knowledge of these hydro-geotechnical processes through the use of a new CFD-CSD model system "`wavePoreGeoFoam`", which is validated with data from unique, large-scale model tests with PBA-revetments conducted in the Large Wave Flume (GWK) at the Coastal Research Centre (FZK) in Hanover, Germany (Oumeraci et al. (2010)). For this purpose, a comprehensive analysis of current knowledge is firstly presented. Secondly, the implementation of the Volume-Averaged RANS-VOF governing equations in the CFD model and its weakly coupling with the CSD model are performed to describe the interaction of the waves with PBA-revetments and their foundation. Thirdly, the calibration and validation of the CFD-CSD model system "`wavePoreGeoFoam`" are carried out by using the large-scale tests in GWK and small-scale tests performed at Leichtweiß-Institute für Wasserbau (LWI) (Liebisch & Oumeraci (2014)). The validated model is then applied for a very systematic parameter study in order to extend the range of wave conditions (e.g., height and period) and revetment configurations (e.g., slope steepness and revetment-filter thickness) tested in the laboratory.

Finally, the analysis of the hydro-geotechnical processes is conducted based on the results of the parameter study using the validated CFD-CSD model. Based on these results, new prediction formulae are developed for the hydrodynamic processes on and in front of PBA-revetments as well as for the wave-induced pressures on and beneath the revetment, including the development of pore pressure in the sand core. Also, the development of a systematic methodology for the stability analysis of the soil beneath PBA-revetments against wave-induced soil liquefaction risk is proposed.

The results show the importance of the effect of the revetment slope steepness on the wave set-up, wave reflection and wave breaking and also that wave run-up and run-down are affected by the revetment-filter thickness. Moreover, the revetment-filter thickness constitutes a key parameter for the peak pressure on and beneath PBA-revetments as well as for the stability of the soil beneath the revetment against liquefaction. The pore pressure distribution in the sand core normal to the revetment slope obtained from the numerical parameter study are also in good agreement with the results obtained from porous seabed analysis without any revetment and where the permeability, porosity and air content are the key parameters. Overall, the results of this study, related to the process analyses as well as to the new formulae and the proposed methodology for the stability analysis of PBA-revetments, enabled the limitations identified in previous studies (e.g., Oumeraci et al. (2010) and Foyer (2013)) to be overcome, thus providing a substantially improved basis for both engineering practice and further research.

Contents

List of Notations

Parameter	Dimension	Description
A, B, C ...	-	Random parameter for curve fitting
a, b, c		Darcy-Forchheimer and Polubarinova-Kochina coefficients
C_r	-	Reflection coefficient $= H_r/H_i$
CoV	-	Coefficient of variation (ratio of the standard deviation to the mean)
c_{ve}	m^2/s	Elastic component of consolidation coefficient $c_{ve}=K/[\gamma_w(\beta_S+n\beta_w)]$
D	m	Grain diameter
D_{15}, D_{50}, D_{85}...	m	Grain diameter which is not exceeded by 15, 50, 85%, ...
D_{eq}	m	Equivalent grain diameter
d_{rev}	m	Revetment-filter thickness
E	Pa	Young's (elasticity) modulus
E_i	J	Incident energy
E_r	J	Reflected energy
g	m/s^2	Gravitational acceleration
H	m	Wave height
h	m	Water depth
H_0	m	Mean deep water wave height
h_0	m	Initial water depth
H_b	m	Wave height at breaking point
h_b	m	Water depth at breaking point
H_i	m	Incident wave height
H_{m0}	m	Zero moment wave height in deep water
H_r	m	Reflected wave height
H_s	m	Significant wave height
h_{toe}	m	Water depth at the toe of the revetment
i	-	Hydraulic gradient
K	m/s	Hydraulic conductivity
k	m^{-1}	Wave number
K_{app}	m/s	Apparent permeability
K_f	Pa	Bulk modulus of the pore fluid
K_w	Pa	Bulk modulus of the pure water
K_N	m/s	Permeability due to flow normal to the soil layers
K_P	m/s	Permeability due to flow parallel to the soil layers
$k_{r,\alpha}$	-	Relative permeability for a fluid phase α.
L	m	Wave length
L_0	m	Deep water wave length
L_{op}	m	Deep water wave length related to peak period T_p
ℓ	m	Displacement vector
m	-	Tangent of the revetment slope angle, m=tan α
M_F	N/m	Momentum flux parameter
n	-	Porosity
N_L	-	Number of cycles to liquefaction in undrained cyclic tests.
P_{diff}	Pa	Pressure difference between P_{max} and P_{stat}
P_{max}	Pa	Peak pressure
P_{max1}	Pa	Peak pressure on the revetment
P_{max2}	Pa	Peak pore-pressure at the revetment-filter interface
P_{max3}	Pa	Peak pore-pressure at the filter-sand core interface
P_{stat}	Pa	Quasi-static peak pressure
P_{topSC}	Pa	Pore-pressure on top of the sand core

p_0	Pa	Absolute zero pressure
Q	m^3/s	Rate of flow.
R	-	Reflection number
r^2	-	Coefficient of determination
Rd	m	Wave run-down
$Rd_{2\%}$	m	Wave run-down height exceeded by 2%
Rd_{Lay2}	m	Wave run-down at the revetment-filter interface
Rd_{Lay3}	m	Wave run-down at the revetment-sand core interface
Re	-	Reynolds number
Ru	m	Wave run-up height
$Ru_{2\%}$	m	Wave run-up height exceeded by 2%
Ru_{Lay2}	m	Wave run-up at the revetment-filter interface
Ru_{Lay3}	m	Wave run-up at the revetment-sand core interface
S_w	-	Saturation rate
T	s	Wave period
t	s	Time
t_a	s	Rise time to reach the peak pressure P_{max1}
t_d	s	Duration time of the peak pressure
T_p	s	Peak period
t_{stat}	s	Rise time to reach the quasi-static peak pressure.
U	m/s	Velocity
u	Pa	Pore pressure
u_{0*}	Pa	Negative pore pressure on top of the sand core
u_{t*}	Pa	Transient negative pore pressure at a depth z' in the sand core
u_r	Pa	Residual pore pressure at a depth z' in the sand core
$u_{r,0}$	Pa	Residual pore pressure on top of the sand core
V	m^3	Volume
V_f	m^3	Volume occupied by the fluid
V_v	m^3	Volume of voids
V_w	m^3	Volume occupied by water
x'	m	Distance parallel to the revetment slope and positive above the SWL
x'_{max}	m	Distance parallel to the revetment slope and positive above the SWL where P_{max} occurs
x'_{Rd}	m	Distance parallel to the revetment slope and positive above the SWL where Rd takes place
x'_{rel}	-	Relative distance parallel to the revetment slope $x'_{rel}=x'/\lvert x'_{max}\rvert$
x'_{Ru}	m	Distance parallel to the revetment slope and positive above the SWL where Ru takes place
z'	m	Distance normal to the revetment slope and positive above the sand core
z_{max1}	m	Vertical location of the peak pressure P_{max1}, referred to the SWL
z_{max3}	m	Vertical location of the peak pressure P_{max3}, referred to the SWL
α	°	Slope angle
α_f, β_f	-	Dimensionless parameters for definition of Forchheimer coefficients
β_S, β_w	m^2/N	Elastic compressibility of the soil and pore-water, respectively
ε	-	Strain
γ'	N/m^3	Submerged specific weight of the soil
γ_b	-	Wave breaking index ($\gamma_b=H_b/h_b$).
γ_f, γ_β, γ_h and γ_B	-	Correction factors to account for shallow water, slope roughness, oblique wave attack and berm effects, respectively
γ_{RF}	-	Factor that account for the effect of the wave-load dissipation by the revetment and filter layers

γ_w	N/m^3	Specific weight of water
Δu	m	Excess of pore pressure $\Delta u = u_{0*} - (u_{t*} + u_r))$ Specific weight of water
Δu_{rel}	m	Relative excess of pore pressure $\Delta u_{rel} = \lvert\Delta u\rvert/\rho g H_0$
$\bar{\eta}$	m	Wave set-up (distance from SWL to MWL)
$\bar{\eta}_b$	m	Maximum wave set -down
$\bar{\eta}_{S1,RuG}$	m	Wave set-up on the revetment
$\bar{\eta}_{S2,RuG}$	m	Wave set-up at the revetment-filter interface
$\bar{\eta}_{S3,RuG}$	m	Wave set-up at the filter-sand core interface
Λ	-	Leakage length.
μ	Ns/m^2	Dynamic viscosity
ν	m^2/s	Kinematic viscosity
ν	-	Poisson's ratio
ξ	-	Surf similarity parameter/Iribarren number = $\tan\alpha/\sqrt{(H/L)}$
ξ_0	-	Surf similarity parameter based on H_0 and L_0
ξ_{ad}	-	Modified surf similarity parameter $= \frac{\tan\alpha}{\sqrt{H/L\cdot\left(1+\frac{drev}{H}\right)}}$
ξ_{eq}	-	Equivalent surf similarity parameter $\xi_{eq} = \xi_{op}\,\gamma_B$
ξ_m	-	Surf similarity parameter based on mean values in deep water
$\xi_{m-1,0}$	-	Surf similarity parameter based on H_{m0} and L_0 ($T_{m-1,0}$)
ξ_{S0}	-	Surf similarity parameter based on H_S and L_0
ρ, ρ'	kg/m^3	Density and submerged density of water
ρ_s, ρ'_s	kg/m^3	Density and submerged density of the soil
σ	Pa	Normal stress
σ'	Pa	Effective stress
σ'_{vo}	Pa	Vertical effective stress before excess pore pressure starts.
Φ_b	m	Potential pressure head of H_b.
Φ_w	m	Potential pressure head at any point.

CFD	Computational Fluid Dynamics
CPB	Concrete Placed Blocks.
CSD	Computational Soil Dynamics
DES	Detached Eddy Simulation
DNS	Direct Numerical Simulation
eMWL	External mean water level
FZK	Forschungszentrum Küste (Coastal research centre)
GWK	Großer Wellenkanal (Large wave flume)
iMWL	Internal mean water level
LWI	Leichtweiß-Institute for hydraulic engineering and water resources
LES	Large Eddy Simulation
MWL	Mean water level
NS	Navier Stokes
PBA	Polyurethane bonded aggregate
PT	Pressure transducer
RANS	Reynolds Averaged Navier Stokes
RAS	Reynolds Average Simulation
RE	Relative Error
REV	Representative Elementary Volume
RuG	Run-up Gauge
SWL	Still water level
VARANS	Volume Averaged RANS
VOF	Volume Of Fluid
WG	Wave Gauge

List of Figures

List of Tables

1 Introduction

1.1 Motivation

Shorelines, harbours and vulnerable coastal areas are subject to storms and prevailing wave action combined with the sea level fluctuation associated to storm surges and tides which may induce erosion and scour problems. For this purpose, coastal structures such as revetments are widely used as a solution to protect an embankment from wave attack and to avoid erosion of the shoreline. Polyurethane bonded aggregates (PBA) revetments are open-pored structures that have emerged as an alternative to enhance coastal safety and that provide advantages over impermeable revetments such as: reduction of the wave run-up and wave-induced pressures on and beneath the revetment (Oumeraci et al. (2010); Liebisch et al. (2012); Foyer (2013)). Moreover, PBA-revetments are less aggressive and environmental friendly solutions for coastal protection that may be better integrated to coastal ecosystems (Fig. 1-1a). However, the performance of these kind of revetments and their interaction with waves is poorly understood and therefore, a better description of the wave-structure-interaction for these permeable structures must be required.

Fig. 1-1: Porous bounded revetment: PBA-revetment applications in the field (BASF (2008)) and b) large-scale wave flume tests (Oumeraci et al. (2010)).

Comprehensive studies considering open pored PBA-revetments have been conducted in large-scale facilities such as the Large Wave Flume (GWK) at the Coastal Research Centre (FZK) in Hannover, Germany (Oumeraci, *et al.*, 2010) together with numerical modelling (Foyer (2013)) with the aim to provide a better understanding of the hydro-geotechnical processes and the wave-structure subsoil interaction. Nevertheless, shortcomings and limitations of these studies are found: i) One slope steepness (1:3) was analysed and limited parameter range of GWK tests was considered due to the time and costs that large-scale tests imply, ii) limitation in the number of measurement devices in GWK tests especially for the analysis of pore pressure development in the embankment subsoil beneath the revetment and iii) shortcomings for the analysis of wave-induced pressures on and beneath revetment were detected in numerical simulations of PBA-revetments with COBRAS-UC (Foyer (2013)).

Thus, a reliable new CFD-CSD model system should be developed and systematically validated with GWK tests in order to enhance the knowledge of hydro-geotechnical processes involved in the wave-structure-subsoil interaction with PBA-revetments. Moreover, no reliable prediction formulae based on experimental or numerical investigations is yet available for the assessment of the stability of PBA-revetments. For this reason, a systematic analysis of the hydro-geotechnical processes should be conducted which allows a consistent stability analysis of PBA-revetments and their sand foundation.

1.2 Objectives

The performance of a bonded porous revetment due to wave-structure-subsoil interactions should be numerically modelled in order to provide a better understanding of the hydro-geotechnical processes and to provide the assessment of the safety of PBA-revetments and their foundation. Furthermore, a systematic validation of the new CFD-CSD model system must be performed by making use of GWK tests which is then used as basis for the conduction of a comprehensive parameter study.

For this purpose, the main objectives of the current research are: i) development of a numerical model to simulate the aforementioned processes and mechanisms and their interactions by improving, modifying or extending the best available numerical codes; ii) validation of the model by the data available from large scale experiments (GWK tests), including adjustments and further improvements; iii) application of the validated model to perform a comprehensive parameter study to extend the range of tested conditions in GWK tests and to overcome the shortcoming from previous studies based on numerical simulations; iv) development of simple semi-analytical formulae for the hydro-geotechnical processes and the assessment of the stability of PBA-revetments and their foundation.

1.3 Methodology

As shown in Fig. 1-2, the methodology proposed to achieve the aforementioned objectives includes the following four work phases:

- In Phase I, a comprehensive review and analysis of the current knowledge is performed, together with the analysis of the datasets of the large-scale experiments carried out in the GWK.
- In Phase II, the development and validation of the new CFD-CSD numerical model with small- and large- scale experiments in wave flumes is performed. Furthermore, a more comprehensive parameter study based on numerical simulations of porous

bonded revetments is conducted using the validated CFD-CSD model in order to extend the results provided by the large-scale tests from GWK and by Foyer (2013).

- In Phase III, detailed analysis of the processes on and in front of PBA-revetments as well as the wave-induce pressures is conducted considering the results from the numerical simulations (Phase II). Furthermore, an approach for the stability analysis of this type of revetments is implemented.
- In Phase IV, the key results are summarized and concluding remarks are drawn.

The tentative methodology as well as the objectives are specified in more detail in Chapter 2 as a result of the review and analysis of the state of the art.

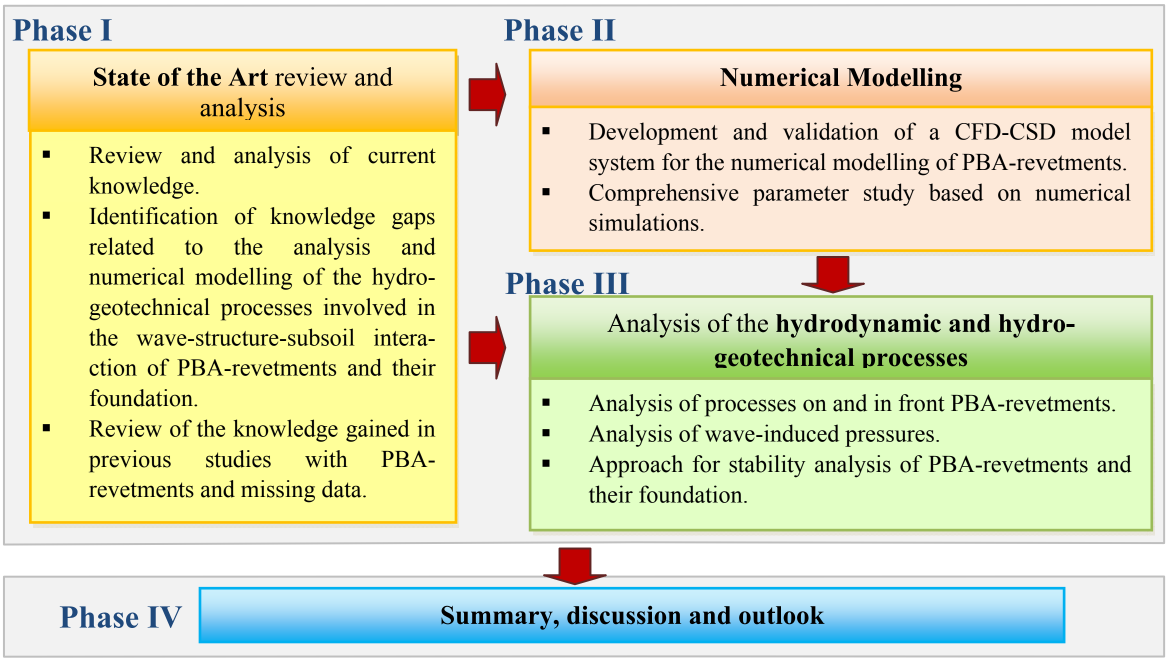

Fig. 1-2: Tentative methodology of the research.

2 Current knowledge and modelling

The current knowledge on the hydrodynamic processes related to the wave-structure interaction as well as its numerical modelling are reviewed and analysed in the present chapter. The structure of the chapter is summarized in Fig. 2-1 where the relation between the different wave-structure interaction processes is also schematized.

Prediction formulae and existing theories describing the hydrodynamic processes on and in front of the revetments are firstly presented (Section 2.1): wave breaking, wave run-up and run-down, wave set-up and set-down as well as wave reflection. These processes are in very close relation with the energy balance in the wave-structure interaction and thus with the wave-induced loading on the structure.

Classification of the wave-induced loads, theory and prediction formulae for uplift pressures as well as impact and non-impact loads induced by wave breaking are presented in Section 2.2. For this purpose, the presented studies are focused on results from semi-empirical approaches based on laboratory tests with revetments (e.g., Davidse (2009); Oumeraci et al. (2010); Alcérreca-Huerta & Oumeraci (2012)).

Flow in porous media is one of the most important processes to be considered on the understanding of wave-structure-subsoil interaction in porous coastal structures. Several approaches based on Darcy's Law have been implemented (e.g., Bennethum & Giorgi (1997); Barree & Conway (2004)) in order to extend its application for further flow motion conditions (e.g. moderate Reynolds numbers, flow in deformable solids, multiphase flow). Therefore, the theory of flow motion in porous media is reviewed in Section 2.3. Moreover, a brief description of the development of stresses and pore pressures in the porous media due to loading is also presented since they represent the most relevant parameters for the description of the response and performance of the embankment subsoil beneath a revetment.

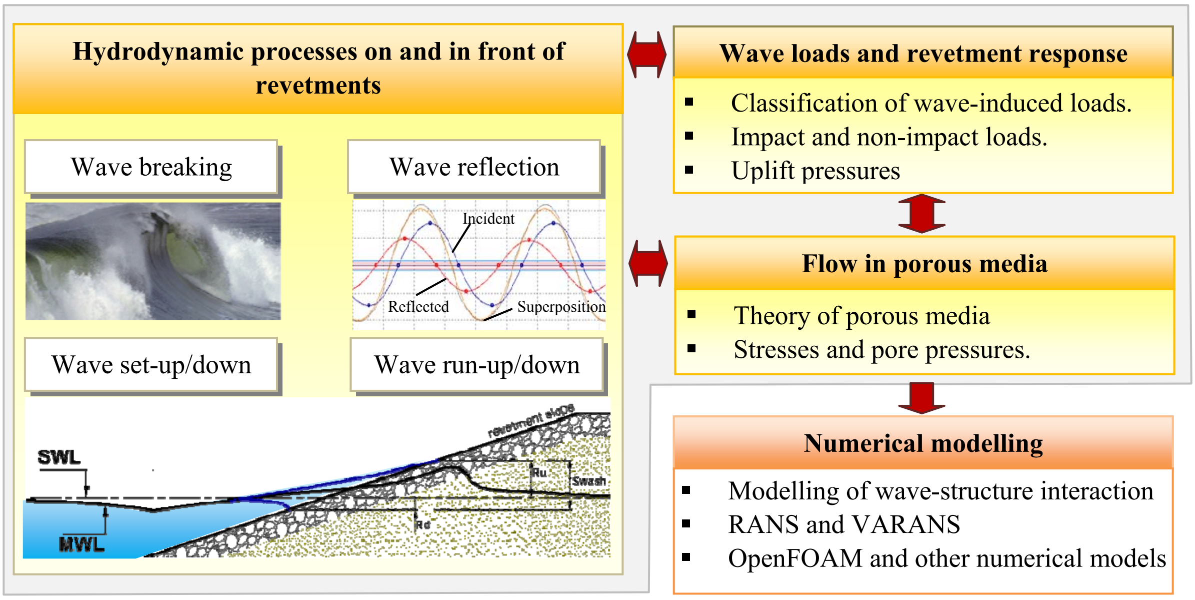

Fig. 2-1: Processes involved in the wave-structure interaction and their inclusion in numerical modelling.

An overview of the current theories for numerical modelling of wave-structure interaction is provided in Section 2.4 with special focus on those which include the modelling of porous media. The solutions based on the Navier Stokes equations are reviewed in detail since they represent, in principle, the basic mathematical expressions that can model water wave motions (Liu & Losada (2002)). For this purpose, the basics of numerical modelling Reynolds-Averaged-Navier-Stokes (RANS) and Volume Averaged RANS (VARANS) equations are introduced in Section 2.4 together with those implemented in CSD simulations. Furthermore, a brief introduction to the CFD (Computational Fluid Dynamics) numerical model OpenFOAM used for the thesis is also made in this section including a comparison with other available models. Further details of the numerical model used in the thesis are described in Chapter 3 and in Alcérreca-Huerta & Oumeraci (2013).

2.1 Hydrodynamic processes on and in front of revetments

The hydrodynamic processes on and in front of a revetment are described in the present section. The wave breaking and the wave reflection are related to the energy balance within the wave-structure interaction as dissipation and reflection of waves occur at the revetment. The wave run-up and run-down in interaction with the wave set-up and set-down are processes in close relation with the revetment features (e.g., revetment slope, porosity, permeability, roughness) and represent therefore key processes for the understanding of the wave structure interaction.

For this purpose, in the present section the current knowledge of wave breaking and wave reflection is firstly reviewed. Second, the theoretical background and the available prediction formulae for the description of the wave run-up and the run-down are presented. Third, the wave set-up and set-down are considered.

2.1.1 Wave breaking and wave reflection

Wave breaking constitutes the most important mechanism for wave dissipation. It depends on the water depth, wave conditions (i.e., wave period T, wave height H) and the revetment characteristics (i.e., slope, roughness, permeability). Moreover, the wave breaking in front of the revetment may be induced when the crest particle velocity (proportional to the wave height for a given wave period) becomes equal or larger than the wave celerity and thus the water particles at the wave crest move faster than the wave profile and the wave starts to break (kinematic wave breaking criterion).

The surf similarity parameter or Iribarren number (ξ) has long been accepted as a key parameter for the definition of the breaker type classification on a sloping bottom/structure (Okazaki & Sunamura (1991)). The combination of structure slope and wave steepness was first pointed out by Iribarren (1965), who defined the surf similarity ξ_0 as shown in eq. (2.1), where α is the slope angle, and H_0 the incident wave height and L_0 the wavelength in deep water.

$$\xi_0 = \frac{\tan\alpha}{\sqrt{H_0 / L_0}} \tag{2.1}$$

The surf similarity parameter was later physically interpreted by Battjes (1974) and confirmed by Bruun (1974). The application of ξ_0 has been extended to formulae describing processes associated with wave breaking such as wave reflection, wave run-up/run-down and energy dissipation.

Indeed wave energy dissipation by a structure is directly and closely related to the wave breaker type. A first breaker type classification in this respect was developed by Iversen (1952):

- ***Spilling breakers*** (ξ_0<0.47), mostly develop over mild slopes. The dissipation of energy occurs when the crest becomes unstable and develops over a large distance, resulting in foam spilling down the face of the wave. The reflection is significantly less than other breaker types.
- ***Plunging breakers*** (0.47<ξ_0<3.30) occur when the crest of the wave curls forward, and breaks onto the wave trough. Most of the wave energy is released at once in a relatively violent impact. Most of the energy is therefore dissipated within a very short distance.
- **Surging breakers** (ξ_0 < 3.30) occur on very steep slopes and are commonly reflected. They are also characterized by a narrow or non-existing surf zone.

Another breaker type called collapsing was introduced as a transition between plunging and surging breakers by Galvin (1968) (2.5<ξ_0<3.3). However, for Dean & Dalrymple (1991), and other authors (i.e., Horikawa (1988); Svendsen (2006)) the collapsing breaker type should not be considered since it results from the combination between other breaker types (plunging and surging breakers). Guidelines such as USACE (2002), and EurOtop (2007), consider the collapsing breaker since it constitutes the transition between plunging and surging breakers and therefore it is important to describe the ξ_0-limits where this transition occurs.

The processes involved into the wave breaking, the breaker type and also the initiation of breaking should be determined in order to analyse and simulate the hydrodynamics near a structure or to compute wave transformation (Camenen & Larson (2007)). For this reason, several studies have been made in order to determine the initiation of breaking waves and its description through a breaker depth index. The latter is described as function of the depth where the wave breaking initiates (h_b) and the wave breaker height (H_b). Therefore, the breaker index formulae can be categorized into four functional forms (Goda (2010a)):

$$H_b / h_b = f_1(0) = constant \tag{2.2}$$

$$H_b / h_b = f_2(h_b/L_0 \ or \ h_b/L_b) \tag{2.3}$$

$$H_b / h_b = f_3(m) \tag{2.4}$$

$$H_b / h_b = f_4(m\, , h_b/L_0 \ or \ h_b/L_b) \tag{2.5}$$

where m denotes the bed slope ($m = \tan\alpha$), L_0, the deep water wavelength, and the subscript b denotes the breaking point.

A typical formula of the first type is the one developed by McCowan (1894) for solitary waves, where the constant takes a value of 0.78; further investigations provide a value of 0.826 (Yamada et al. (1968)). Miche (1944) and Battjes (1978), considered the wave length and the water depth as the key parameters for the breaker index but did not take into account the effect of the slope steepness tanα on the breaking process (second functional form - eq. (2.3)). The third functional form with inclusion of the slope steepness into the breaker index (eq. (2.4)) was implemented in the studies by Kishi & Saeki (1966); Galvin (1969) and Collins (1969). A comparison between different breaker index formulae made by Rattanapitikon & Shibayama (2002) shows that the four functional form of the breaking index (eq. (2.5)) has the best prediction performance. Some approaches based on this functional form are Ostendorf & Madsen (1979), Larson (1989); Gourlay (1978); Goda (1970) modified by Rattanapitikon & Shibayama (2000), and Kamphuis (1991) for irregular waves. A summary of the wave breaking indices available for the determination of the initiation of the wave breaking is given in Table 2-1.

Table 2-1: Available breaking indices.

Author	***Formula***	***Description***	***Form***
McCowan (1894)	$H_b/h_b = 0.78$	Criterion based on solitary wave theory (horiz. bottom)	eq. (2.2)
Miche (1944)	$H_b/L_b = (1/7)\tanh(2\pi h_b / L_b)$	Empirical approach for regular waves in finite water depth (horiz. bottom)	eq. (2.3)
Kishi & Saeki (1966)	$H_b/h_b = 5.68m^{0.40}$	Empirical formula based on experiments with solitary waves on sloping bottom.	eq. (2.4)
Galvin (1969)	$\frac{H_b}{h_b} = \beta_b \quad \begin{cases} 1.09 & \mathit{for}\ m \geq 0.07 \\ (1.40 - 6.85m)^{-1} & \mathit{for}\ m \geq 0.07 \end{cases}$	Laboratory experiments with regular waves on plane-sloped beaches.	eq. (2.4)
Collins (1969)	$\frac{H_b}{h_b} = \beta_b \quad \begin{cases} 1.28 & \mathit{for}\ m \geq 0.07 \\ 0.72 + 5.6m & \mathit{for}\ m \geq 0.07 \end{cases}$	Formula derived from linear wave theory and empirical inclusion of the slope effect.	eq. (2.4)
Battjes (1978)	$H_b/L_b = (1/7)\tanh\left(\gamma_b 2\pi h_b / (0.88L_b)\right)$	Recalibration of Miche's approach by a coefficient $\gamma_b \approx 0.8$.	eq. (2.3)
Ostendorf & Madsen (1979)	$\frac{H_b}{h_b} = 0.14\frac{L_b}{h_b}\tanh\left\{\left[0.8 + 5\min(m, 0.1)\right]\frac{2\pi h_b}{L_b}\right\}$	Based on Miche´s approach, introduces the slope angle.	eq. (2.5)
Larson (1989)	$\frac{H_b}{h_b} = 1.14\left(\frac{m}{\sqrt{H_0/L_0}}\right)^{0.21} = 1.14 \cdot \xi_0^{\,0.21}$	Based on large-scale wave flume dataset by Kajima et al. (1983)	eq. (2.5)
Kamphuis (1991)	$H_{sb} = 0.095\exp(4m) L_p \tanh\left(\frac{2\pi h_b}{L_p}\right)$	Developed for irregular waves, also introduces the exponential form of the slope.	eq. (2.5)
Gourlay (1992)	$H_b = 0.478H_0\left(\frac{H_0}{L_0}\right)^{-0.28}$	Empirical formula based on different sources of laboratory data.	eq. (2.3)
Rattanapitikon & Shibayama (2002)	$\frac{H_b}{h_b} = 0.17\frac{L_0}{h_b}\left\{1 - \exp\left[\frac{\pi h_b}{L_0}\left(16.21m^2 - 7.07m - 1.55\right)\right]\right\}$	Empirical formula based on a re-analysis of existing breaker height formulae.	eq. (2.5)
Goda (2010b)	$\frac{H_b}{h_b} = A\frac{L_0}{h_b}\left\{1 - \exp\left[-1.5\frac{\pi h_b}{L_0}\left(1 + 11m^{4/3}\right)\right]\right\}$ with A=0.17 & A=0.12 for regular and irregular waves, respectively	Reanalysis of regular and irregular wave breaking based on various sets of field and laboratory data	eq. (2.5)

While part of the wave energy is dissipated by the wave breaking process, another portion is reflected by the structure. Therefore, wave reflection affects the wave-wave interaction and it is thus relevant for the description of the hydrodynamic performance of revetments. For this purpose, the reflection is quantified through a reflection coefficient (C_r) defined in terms of the ratio of the reflected (H_r) to the incident wave height (H_i), or through the square root of the ratio of the reflected (E_r) to the incident energy (E_i):

$$C_r = \frac{H_r}{H_i} = \sqrt{\frac{E_r}{E_i}} \tag{2.6}$$

Laboratory studies to determine the value of C_r have been conducted and are normally described as function of the surf similarity parameter ξ_0. Miche (1951) provided a first attempt to develop an expression for the reflection coefficient C_r in terms of the wave steepness. Battjes (1974), provided a re-definition of Miche's approach by introducing the surf similarity parameter as a key parameter for the wave reflection (eq. (2.7)).

$$C_r = 0.1\xi_0^{\,2} \tag{2.7}$$

Seelig & Ahrens (1981) proposed an approach based on laboratory tests for regular and irregular waves which also considers different coastal structures: smooth impermeable slopes, permeable sea dikes, sand beaches and rubble mound breakwaters with multiple layers. As a result, eq. (2.8) was developed where coefficient A accounts for the location of the wave breaking onset and variations of the slope surface (through d_{eq}= equivalent grain diameter) while coefficient B is purely empirical.

$$C_r = \min\left[\frac{A\xi^2}{\xi^2 + B}, A\tanh\left(0.1\xi^2\right)\right] \text{ with } A = \exp\left[-1.7\sqrt{\frac{d_{eq}}{L_0}}\cot\alpha - 0.5\left(\frac{H_i}{H_b}\right)^{1.2}\right] \tag{2.8}$$

Losada & Giménez-Curto (1981), presented an exponential model (eq.(2.9)) in terms of the surf similarity parameter which is applicable for rough permeable slopes. For this purpose, coefficients A_U and B_U have been defined for quadripods, dolos, rubble mound breakwaters, and rip-rap revetments (s. Table 2-2).

$$C_r = A_U\left[1 - \exp\left(B_U\xi\right)\right] \tag{2.9}$$

Table 2-2: Values for the coefficients A_U and B_U to estimate C_f with eq. (2.9), (Losada & Giménez-Curto (1981)).

TYPE OF ARMOUR UNITS	A_U	B_U
Rip-rap	1.451-1.7887	-0.4552
Rubble	1.3698	-0.5964
Dolos	1.2158	-0.5675
Quadripods	1.5382	-0.2483

Further studies carried out by Postma (1989) with irregular waves over rubble mound breakwaters showed the effect of the permeability (eq. (2.10)) by considering it through the notional permeability P (van der Meer (1988)). Furthermore, the wave period was recognized to provide larger influence into the reflection behaviour than the wave height.

$$C_r = 0.071 P^{-0.082} \cot^{-0.62} \alpha \left(\frac{H_S}{L_{op}} \right)^{-0.46} \tag{2.10}$$

with $L_{op}=gT_p^2/(2\pi)$ as the deep water wave length related to peak period T_p.

Measurements of wave reflection over a rock island breakwater were carried out by Davidson et al. (1996). Comparisons of the results of these measurements with previous approaches provided eq. (2.11) that is described in terms of a reflection number R which considers the local water depth at the toe of the structure (h_{toe}), the slope angle, the wave length in deep water and the diameter of the rock armour units.

$$C_r = 0.151 R^{0.11} \text{ with } R = \frac{h_{toe} L_0^2 \tan\alpha}{H_i d_{eq}} \tag{2.11}$$

Davidson et al. (1996) pointed out the key parameters affecting the reflection process and concluded that: i) the wave length L_0 is one of the most important variables since an increase of L_0 increases the reflection coefficient until a ξ_0-value at which C_r becomes constant, ii) the wave height and the local water depth at the toe of the structure h_{toe} slightly affects C_r and iii) the slope angle significantly contributes to a large variation of the reflection coefficient.

Zanuttigh & van der Meer (2006) analysed the reflection behaviour of various types of structures (e.g., permeable rock slopes with impermeable slopes, slopes with artificial armour units, berm breakwaters, vertical structures). Moreover, existing formulae were analysed (e.g., Battjes (1974), Seelig & Ahrens (1981), Losada & Giménez-Curto (1981)) and an extensive and homogeneous database was obtained. From the analysis of the database, it was concluded that Seelig & Ahrens (1981) provides a proper fitting to the data for smooth slopes, however, limitations were found for the prediction of the reflection behaviour of impermeable slopes and slopes covered by rock material (permeable and porous slopes) and other armour units. Therefore eq. (2.12) was developed to provide a unique expression for all types of structures. For this purpose, eq. (2.12) describes the reflection coefficient in terms of the surf similarity parameter ξ_0 and coefficients A and B that may be expressed as function of the slope roughness.

$$C_r = \tanh\left(A \xi_0^B \right) \tag{2.12}$$

In addition to the application of Zanuttigh's formula for several structure types, it also represents the physical bounds (for $\xi 0 \rightarrow 0$, Cr=0 and for $\xi 0 \rightarrow \infty$, Cr=1), and the coefficients are related to the slope roughness which makes the approach extensible for other structure types such as porous bonded revetments.

2.1.2 Wave set-up and set-down

The wave set-up is commonly defined as the elevation of the mean water level (MWL) over the still water level (SWL) associated with the conversion of kinetic energy of wave motion to a quasi-steady potential energy as a result of the breaking process. Wave set-down is also induced during the shoaling process and thus the MWL is depressed up to the wave breaking onset. The maximum wave set-down is developed at the breaker point and afterwards the MWL then increases to a maximum level over the SWL on the slope. The importance of this phenomenon is associated with the determination of water levels in front a structure and therefore strongly affects all other processes such as wave reflection, wave run-up and run-down.

The initial assessment of the phenomena was theoretically developed independently by Longuet-Higguins & Stewart (1963); Dorrestein (1962) and Lundgren (1963). The theory is based on the conservation of momentum flux in regular waves and the concept of radiation stress, which is the momentum flux due to the presence of waves. Wave breaking and wave shoaling induce a change in momentum flux which is balanced by a decrease or an increase of the MWL (wave set-down and wave set-up, respectively) (Hsu et al. (2006)). From the analytical approaches, the wave set-up was found to be dependent on the wave breaking index as shown in eq. (2.13) for the maximum set-down ($\bar{\eta}_b$) and eq. (2.14) for the wave set-up, with $\gamma_b = H_b/h_b$ as the wave breaking index (see Section 2.1.1 and Table 2-1):

$$\bar{\eta}_b = -\frac{\gamma_b^2 h_b}{16} \tag{2.13}$$

$$\bar{\eta}(x) = \bar{\eta}_b + \left(\frac{3\gamma_b{}^2/8}{1+3\gamma_b{}^2/8} \right) \left[h_b - h(x) \right] \tag{2.14}$$

Laboratory experiments and field measurements of wave set-up have been conducted since the first analytical approaches were developed in the 1960's. Improvements of the analytical expression were performed to consider irregular waves, roughness and bottom friction.

One of the first laboratory measurements was performed by Bowen et al. (1968) with regular waves on a beach slope. The wave set-down and set-up from analytical approaches overestimated the results from the laboratory measurements especially close to the breaker point. However, the changes of the MWL were recognized. Battjes (1972) discussed the fact that for irregular waves the breaking point could not be defined, and thus, results given by theory are not applicable for this type of waves.

An analytical study of the wave set-up for a given wave spectrum was conducted by Lo (1988). Lo included the low frequency terms into the radiation stress and referred to the resulting wave set-up as the "dynamic wave set-up" which is caused by infragravity waves (from 30sec to several minutes also named surf beat). Hedges & Mase (2004), confirmed the presence of the "dynamic wave set-up" by a reanalysis of laboratory measurements performed by Mase (1989). Thus, these analysis concluded that the wave set-up is composed of: i) a steady component (directly caused by the waves as described by the theory of radiation stress) and ii) a dynamic component (caused by infragravity waves as described by the theory of surf beat Lo (1988)).

Field studies have also been performed over beach slopes in addition to laboratory and analytical approaches of the wave set-up. However, considerable scatter was obtained since field measurements cannot be controlled as in the laboratory. Dean & Walton (2008), provide a comprehensive review of field measurements on wave set-up. Within this review, a wide number of methodologies were employed to measure the wave set-up: cameras, pressure sensors, manometers, etc. Moreover, empirical formulae from field measurements before 1990's considered the ratio of wave set-up to a characteristic wave height ($\bar{\eta}$/H) as a key parameter for the description of the wave set-up. However, further field studies also considered the effect of wave length and the beach slope across the surf zone. The permeability and porosity of the beach slope is not taken into account in the formulae resulting from field measurements, through its effect has been recognized (Dean & Walton (2008)). Furthermore, the steady and the dynamic components of the wave set-up could not be estimated separately with the empirical expressions.

General guidance to calculate wave set-up for regular and irregular waves can be found on the CEM (USACE (2002)). For regular waves, the general procedure is given by the theoretical derivation given through eq. (2.15), which is also suggested to be applicable for non-planar beach profiles:

$$\bar{\eta} = -\frac{1}{8}\frac{H^2 k}{\sinh(2kh)} \quad \text{with } k=2\pi/L \text{ (wave number)} \tag{2.15}$$

2.1.3 Wave run-up and run-down

The wave run-up and run-down are processes that are strongly affected by the porosity and permeability of revetments. Numerous studies with an emphasis on experimental and numerical investigations have been performed in the last decades for the analysis of the maximum wave run-up and run-down (Na et al. (2011)). Research related to wave run-down has normally not been considered as important if compared with wave run-up. However, both provide of the total water excursion over the slope of a breakwater (Goda (2010a)) and lead to boundary points related with the development of pressures changes on and beneath the revetment of porous bonded structures (Pilarczyk (1998)).

The maximum wave run-up and run-down are defined as the maximum vertical distance between still water level (SWL) and the highest/ lowest point (respectively) reached by the water surface on the seaward face of the revetment. For regular waves the run-up (Ru) and the run-down (Rd) have a unique value, however, for irregular waves, the wave run-up $Ru_{2\%}$ and the run-down $Rd_{2\%}$ which are exceeded by 2% of the incident waves are commonly used as characteristic values for design purposes (EurOtop (2007)).

a) Wave run-up

The surf similarity parameter, the incident wave angle and features of the slope such as berms, roughness, porosity and permeability are variables that take part in the determination of the wave run-up and thus are considered in several formulae and studies.

Hunt (1959), developed a formula derived for regular waves on uniform smooth impermeable slope where the relative wave run-up (Ru/H_0) is directly proportional to the surf similarity parameter ξ_0. This assumption is not valid for all range of ξ_0-values; however, further studies were developed on this basis. Battjes (1974) extended Hunt's formula for irregular waves and Ahrens (1981) and van der Meer & Stam (1992) carried out laboratory measurements over impermeable plane smooth slopes.

Losada & Giménez-Curto (1981), listed and categorized the parameters that take place in the wave run-up into three groups: i) parameters of the medium, such as depth, bottom slope, gravity, viscosity, specific weight of the water; ii) parameters of incident waves such as wave height, wave period, wave approach angle; and iii) parameters of the structure such as geometry, roughness and/or permeability. Also, an empirical formula based on a dimensionless analysis and experimental databases for the wave run-up on rough permeable slopes was developed.

Ahrens & Heisnbaugh (1988), developed a formula for the maximum wave run-up for irregular waves on rip rap revetments. The zero moment wave height (H_{m0}), defined as the wave height that has four times the standard deviation of the surface elevation, is included in this formula. Furthermore, Silva et al. (1998) related this formula to the porosity of: a) homogeneous breakwaters and b) for impermeable core slopes.

Schüttrumpf (2001), developed a steady function based on a hyperbolic tangent approach and considering model scale tests with sea dikes. The surf similarity parameter ξ_{S0} is used and it is described through the significant wave height H_S and the deepwater wavelength L_0. The advantage of this formula is the smooth transition over the entire range of the surf similarity parameter values.

The effects of the shallow water, slope roughness and oblique wave attack were considered by van der Meer & Janssen (1995) through corrections factors γ_f, γ_β and γ_h, respectively. The formula developed is also based in Hunt's formula but it also includes the effect of a berm over the slope by considering an equivalent surf similarity parameter: $\xi_{eq} = \xi_{op}\,\gamma_B$ where γ_B is a reduction factor. The values of γ_f, γ_β and γ_h can be calculated according to expressions provided by de Waal & van der Meer (1992). Further modifications to van der Meer's approach were implemented by Schüttrumpf et al. (2010) for irregular waves and considering a different definition of the surf similarity parameter: $\xi_{m-1,0}$ as function of the wave height H_{m0} and the wave length $L_{m-1,0}$ associated with the spectral moments m_{-1} and m_0 at the toe of the structure. Schüttrumpf's approach is recommend by EurOtop (2007) for design purposes. Other guidelines such as the CEM- Coastal Engineering Manual (USACE (2002)) recommend a different approach for smooth impermeable slopes which is based on Hunt's formula.

Hughes (2004), suggested the wave momentum flux parameter as a physical descriptor to derive a wave run-up equation. The relationship between wave momentum flux and the wave run-up was estimated empirically using the laboratory databases for wave run-up on smooth, impermeable plane slopes from Ahrens (1981) and Mase (1989) and thus, two formulae were developed for considering impact and non-impact waves.

Analytical approaches to calculate wave run-up have been carried out by different authors, however, this kind of expressions are based on linear and nonlinear shallow water equations for periodic long waves. Madsen & Fuhrman (2008), proposed an analytical solution that is generalized to be applied to irregular waves assuming a Rayleigh distribution. A comparison with the dataset from Ahrens (1981) was made with a good prediction of the wave run-up for collapsing and surging breakers but not for plunging breakers, and therefore not providing improvements compared to empirical formulae.

Recently, the assessment of the wave run-up on PBA-revetments was developed by Oumeraci et al. (2010) based on the analysis of large-scale tests and introducing a reduction factor in Schüttrumpf's approach which is described as function of the revetment-filter thickness (d_{rev}). Further studies with PBA-revetments from Foyer (2013) considered the wave run-up on the mean water level (MWL) instead of the wave run-up referred to the SWL. Within this approach, the wave set-up effect on the wave run-up is removed and as a result the maximum wave run-up and run-down were found to be almost symmetrical around the MWL. The permeability of the PBA-revetments reduces the wave run-up, however, a slight effect of the revetment-filter thickness $d_{rev} > 0.25$m was noticed.

An overview and comparison of the different formulae is summarized in Table 2-3 and those particularly described in terms of $Ru_{2\%}/H_s$ as function of ξ_0 are shown in Fig. 2-2.

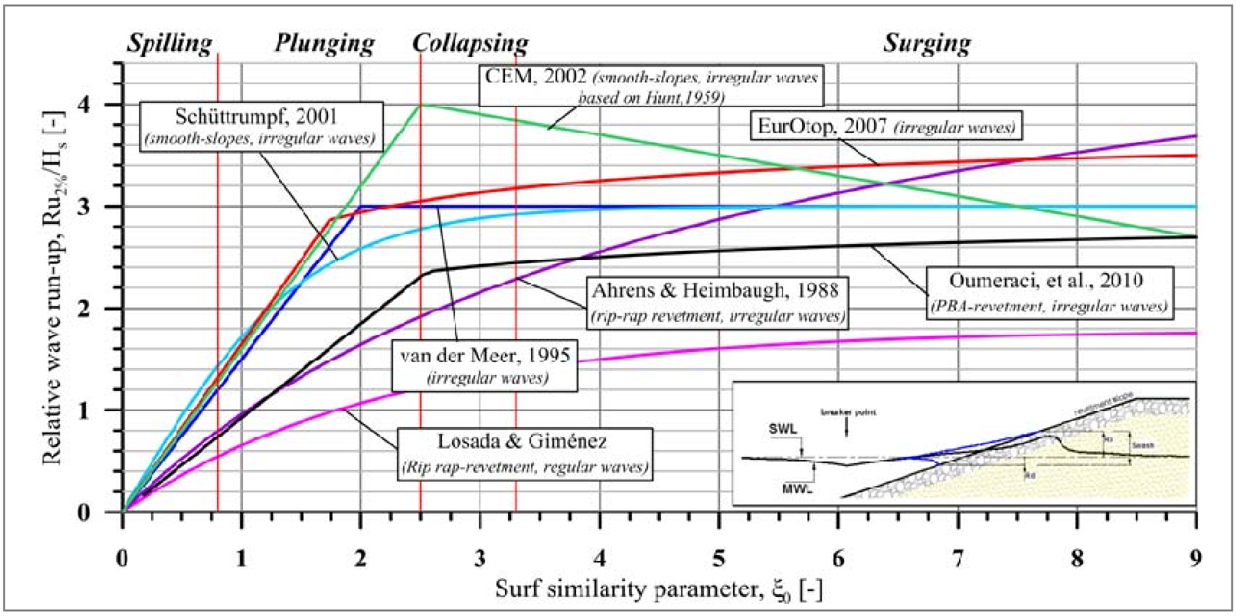

Fig. 2-2: Comparison of wave run-up formulae related to the SWL.

Table 2-3: Wave run-up formulae from previous studies.

Author	*Formula*	*Description*
Hunt (1959)	$Ru / H_0 = C\xi_0$ with 1.49<C<1.87	Empirical approach for regular waves and uniform gentle slope. Extend by Battjes & Roos (1974) for irregular waves and C=1.6.
Losada & Giménez-Curto (1981)	$Ru / H_0 = A_U \left(1 - \exp\left(B_U \xi\right)\right)$	Based on a dimensionless analysis and experimental databases for rough permeable slopes under regular waves.
Ahrens & Heisnbaugh (1988)	$Ru / H_{m0} = \frac{A\xi}{1+B\xi}$	Developed for irregular waves on rip-rap revetments.
van der Meer & Janssen (1995)	$Ru_{2\%} / H_S = 1.5\gamma_h \gamma_f \gamma_\beta \xi_{eq}$	Inclusion of correction factors due to: shallow waters, slope roughness and oblique wave attack.
Schüttrumpf (2001)	$Ru_{2\%} / H_S = 3.0 \tanh\left(0.65 \cdot \xi_{S0}\right)$	Based on scale model tests with sea dikes. It provides a smooth transition along the entire range of ξ_0-values.
Hughes (2004)	$\frac{Ru_{2\%}}{h} = 1.75\left(1 - \exp\left[-1.3\cot\alpha\right]\right)\left(\frac{M_F}{\rho g h^2}\right)$ $\frac{Ru_{2\%}}{h} = 4.4\left(\tan\alpha\right)^{0.7}\left(\frac{M_F}{\rho g h^2}\right)^{1/2}$	Based on the momentum flux parameter (M_F) as a physical descriptor instead of surf similarity parameter ξ_0.
Madsen & Fuhrman (2008)	$\frac{Ru_{2\%}}{H_{m0}} = \left(\frac{1.6}{2}\right) 2\pi^{3/4} \left(\frac{H_{m0}}{2h_0}\right)^{-1/4} \xi^{-1/2}$	Analytical approach based on linear and nonlinear shallow water equations for periodic long waves
Oumeraci et al. (2010)	$\frac{Ru_{2\%}}{H_{m0}} = \min\left[0.54 \cdot \left(1.65 \cdot \xi_{m-1,0}\right), 0.77\left(4 - \frac{1.5}{\sqrt{\xi_{m-1,0}}}\right)\right]$	Based on large-scale tests with PBA-revetments and on Schüttrumpf et al. (2010) approach.
Foyer (2013)	$Ru / H_m = \frac{\xi_m^{\;2} + 14.6\xi_m}{\xi_m^{\;2} + 6.23^2} + \bar{\eta}$	Wave run-up on MWL, the effect of the wave set-up is removed. Based on numerical modelling of PBA-revetments.

b) Wave run-down

Compared to wave run-up,, less experimental data and studies have been conducted for wave run-down. For regular waves and rough permeable slopes, Battjes & Roos (1974) proposed eq. (2.16) allowing positive values for the run-down for spilling and plunging waves with ξ_0<2.3 which means that the run-down occurs above the SWL.

$$Rd = Ru\left(1 - 0.4\xi_0\right) \tag{2.16}$$

When this condition occurs, the wave run-down is not completed and the next run-up meets the water layer of the preceding wave (Kemp & Plinston (1974)). Experimental data from Burcharth (1978) for smooth slopes concluded that the interaction between run-up and run-down exist mostly for spilling, plunging and collapsing breakers.

Losada & Giménez-Curto (1981), provided a run-down expression for rubble mound slopes, based on different experimental datasets. The empirical formula (eq. (2.17)) is expressed in a similar way as the wave run-up (see Table 2-3) and is applicable for regular waves considering that the maximum wave run-down cannot occur above the SWL.

$$\frac{R_d}{H} = A_U\left(1 - \exp\left(B_U \xi\right)\right) \tag{2.17}$$

with A_U=-6.22, -0.855, -1.06, -0.795 and B_U=-0.040, -0.426, 0.266, -0.448 for rip-rap slopes, rubble mound breakwaters, dolos and quadripods armour units, respectively.

Studies performed by van der Meer (1988) with irregular waves over rock slopes derived in a formulae that includes the notional permeability P, which is dependent on the armour, filter and core characteristics.

$$\frac{R_{d2\%}}{H_S} = -2.1\sqrt{\tan\alpha} + 12P^{0.15} - 1.5\exp\left(-60 s_{om}\right) \text{ with } s_{om} = 2\pi H_S/(gT_m^2) \tag{2.18}$$

An expression available for the assessment of the wave run-down for irregular waves on impermeable and rip-rap smooth slopes is described by Pilarczyk (1987). A limit for the maximum wave run-down is roughly evaluated by eq. (2.19) and no explicit account is made for the effect of the roughness, permeability or porosity of the slope.

Maximum Rd-value:

$$\frac{Rd_{2\%}}{H_S} = \begin{cases} -0.8\xi_0 - 0.5 & \mathit{for}\ 0 < \xi_0 < 2.5 \\ -2.5 & \mathit{for}\ \xi_0 > 2.5 \end{cases} \tag{2.19}$$

Schüttrumpf (2001), based on scale model tests of sea dikes developed eq. (2.20) which considers an hyperbolic tangent approach valid for any ξ_0-value but considering that the Rd only occurs below the SWL.

$$\frac{R_{d2\%}}{H_S} = -0.7\left[1 + \tanh\left(\xi_{s0} - 2.1\right)\right] \tag{2.20}$$

Neelamani & Sandhya (2005) performed experiments over plane, dentate and serrated sloped seawalls with irregular waves. The formula suggested (eq. (2.21)) was not described in terms of ξ_0, but in terms of the ratio water depth to wavelength (h/L_0).

$$\frac{Rd_{2\%}}{H_S} = -0.39\left(\frac{h}{L_0}\right)^{-0.50} \tag{2.21}$$

For PBA-revetments, Oumeraci et al. (2010) defined a prediction formulae (eq. (2.22)) for the run-down which is based on the guidelines by the CEM (USACE (2002)) and of similar form of that proposed by Pilarczyk (1987) in eq. (2.19).

$$Rd_{2\%}/H_S = \max\left(-0.42\xi_0 + 0.17, -2.25\right) \tag{2.22}$$

Foyer (2013) also provided a prediction formulae for the wave run-down on MWL for PBA-revetments (eq.(2.23)) which is similar to that of the wave run-up on MWL which has the advantage (as already mentioned) to separate the effect of the wave set-up on the wave run-down.

$$Rd/H_m = -\frac{\xi_m^{\ 2} + 14.6\xi_m}{\xi_m^{\ 2} + 6.23^2} + \bar{\eta} \tag{2.23}$$

A summary of the formulae aforementioned is described in Table 2-4 and comparison of selected formulae for the maximum wave run-down as function of the surf similarity parameter is shown in Fig. 2-3.

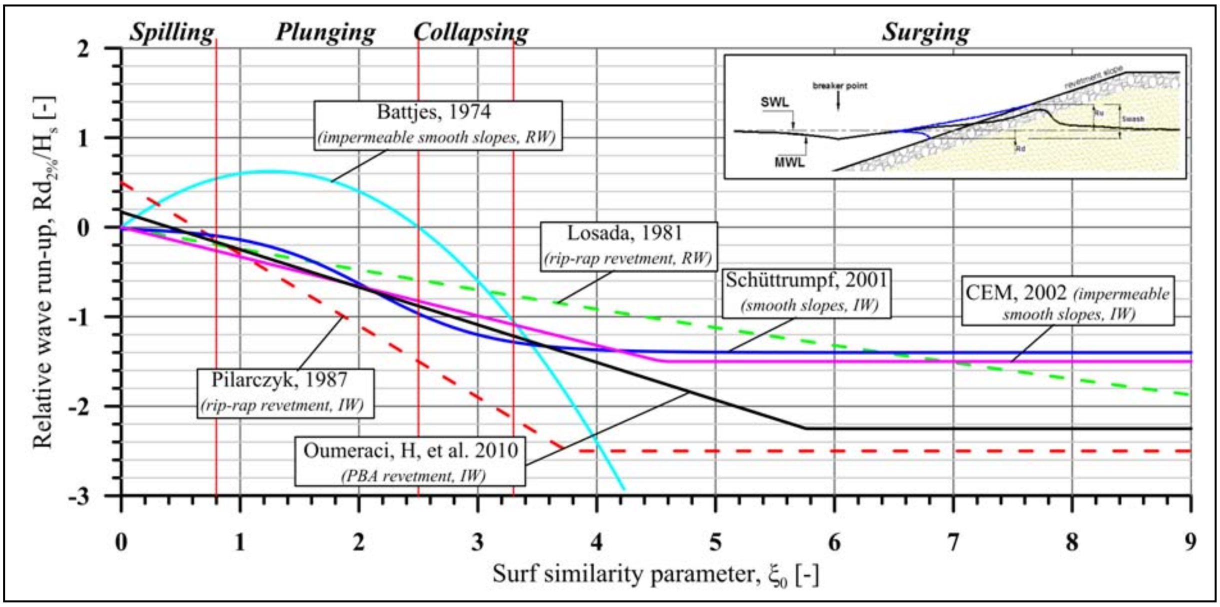

Fig. 2-3: Comparison of wave run-down formulae.

Table 2-4: Wave run-down formulae from previous studies

Author	*Formula*	*Description*
Battjes & Roos (1974)	$Rd = Ru\left(1-0.4\xi_0\right)$	Empirical approach for regular waves and uniform smooth impermeable slope.
Losada & Giménez-Curto (1981)	$Ru / H_0 = A_U\left(1-\exp\left(B_U\xi\right)\right)$	Based on a dimensionless analysis and experimental databases for rough permeable slopes under regular waves.
van der Meer (1988)	$\frac{R_{d2\%}}{H_S} = -2.1\sqrt{\tan\alpha} + 12P^{0.15} - 1.5\exp\left(-60s_{om}\right)$ with $s_{om} = 2\pi H_S/(gT_m^2)$	Developed for irregular waves over rock slopes with inclusion of the notional permeability P.
Pilarczyk (1987)	$\frac{Rd_{2\%}}{H_S} = \begin{cases} -0.8\xi_0 - 0.5 & \mathit{for}\ 0 < \xi_0 < 2.5 \\ -2.5 & \mathit{for}\ \xi_0 > 2.5 \end{cases}$	Maximum wave run-down for irregular waves on impermeable and rip-rap slopes
Schüttrumpf (2001)	$\frac{R_{d2\%}}{H_S} = -0.7\left[1+\tanh\left(\xi_{s0}-2.1\right)\right]$	Based on scale model tests with sea dikes. It provides a smooth transition along the entire range of ξ_0-values.
Neelamani (2005)	$\frac{Rd_{2\%}}{H_S} = -0.39\left(\frac{h}{L_0}\right)^{-0.50}$	Empirical approach considering irregular waves over plane, dentate and serrated sloped seawalls.
Oumeraci et al. (2010)	$\frac{Ru_{2\%}}{H_{m0}} = \min\left[0.54\cdot\left(1.65\cdot\xi_{m-1,0}\right), 0.77\left(4-\frac{1.5}{\sqrt{\xi_{m-1,0}}}\right)\right]$	Based on large-scale tests with PBA-revetments and on Schüttrumpf et al. (2010) approach.
Foyer (2013)	$Rd / H_m = -\frac{\xi_m{}^2 + 14.6\xi_m}{\xi_m{}^2 + 6.23^2} + \bar{\eta}$	Wave run-down on MWL, the effect of the wave set-up is removed. Based on numerical modelling of PBA-revetments.

The wave breaking and the breaker type are closely related to several processes: wave reflection, wave set-up/set-down, wave run-up/run-down. While part of the wave energy is dissipated during the wave breaking process another portion is reflected by the structure. According to Zanuttigh & van der Meer (2006), the approach suggested by Seelig & Ahrens (1981) provides a proper fitting for smooth impermeable revetments but not for porous and permeable slopes in addition to not fulfilling the physical bound $\xi 0 \rightarrow \infty$, Cr=1 and therefore, based on an extensive and homogeneous database considering various types of structures, a wave reflection approach was developed but not considering PBA-revetments.

The wave run-up was found to be similar for impermeable smooth and porous rough slopes within the range $\xi_0<1.5$ (spilling and plunging breakers). A large variation of the wave run-up is noticed for different permeable and porous structures but in any case the wave run-up is smaller than that of smooth impermeable slopes. The large variation is also observed in both permeable and impermeable slopes for $\xi_0>1.5$ (plunging, collapsing and surging breakers) and especially for $2<\xi_0<5$ (mainly collapsing breakers). Therefore, roughness and permeability of the revetment decreases the wave run-up (s. Fig. 2-2). On the other hand, the wave run-down is generally lower for permeable slopes than for impermeable ones probably as consequence of the infiltration and accumulation of the water in the porous structure of the slope. Furthermore, a small number of approaches show as a result a wave run-down developed above the SWL. The prediction of the wave run-up/run-down even for similar conditions can have a large variation (e.g. for rip-rap revetments or smooth impermeable slope). For this purpose, Foyer (2013) has considered explicitly the effect of the wave set-up in the run-up and run-down which allows a better understanding of the processes.

2.2 Wave loads and revetment response

The response of a revetment due to wave-induced loads, pressures and forces is in close relation with the hydrodynamic processes described in Section 2.1. For this purpose, a classification of the wave-induced loads was presented by Witte (1988). In this classification, two groups of wave-induced loads were distinguished: i) quasi-static loads and ii) dynamic loads. Furthermore, in van Vledder (1990) a classification of the dynamic loads into three different groups (Fig. 2-4) is presented: i) quasi-static and impact loads, ii) uplift loads, iii) cyclic loads and vibrations.

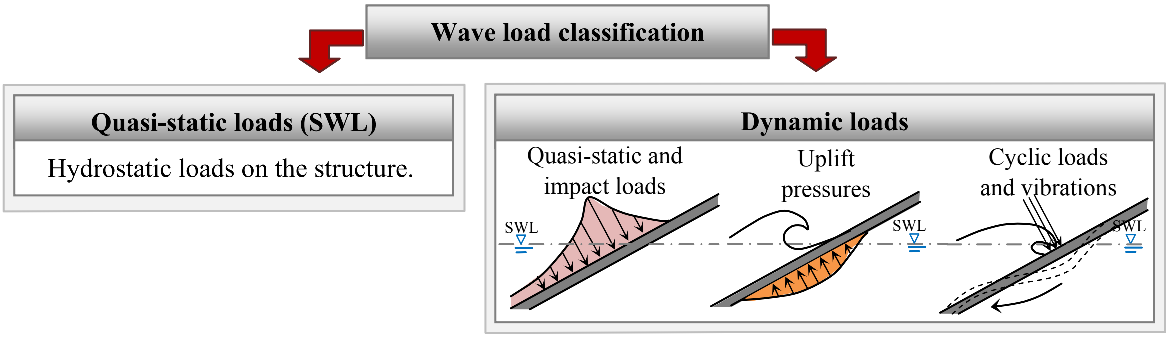

Fig. 2-4: Wave-induced loads classification on revetments (modified from van Vledder (1990).

2.2.1 Quasi-static and impact loads

Within the dynamic loads, the quasi-static and impact loads are produced normally because of the wave breaking on the revetment. Several studies (e.g., Oumeraci & Kudella (2004); Muttray et al. (2006); Davidse (2009); Oumeraci et al. (2010)) have been conducted which provide a parameterization of the pressure signals observed. Therefore, the wave-induced load was noticed to be composed by two components: i) the quasi static component and ii) the impact component.

The impact component of the wave-induced load generates a force that acts on a small area and for a very short time on the revetment slope and the pressures generated are transmitted almost instantaneously to the layers underneath. For this reason, the impact load (component of the wave-induced load) is mainly characterized by: i) peak pressure (P_{max}), ii) rise time t_a to reach P_{max} and iii) impact duration t_d. Moreover, once the impact load is produced, the quasi-static load is observed and could be described mainly by: i) quasi-static peak pressure (P_{stat}) and ii) the time t_{stat} where P_{stat} is found (the load duration t_d of this component is equal to the wave period T). The quasi-static loads can interact with the impact load in such a way that the impact load is superposed to the quasi-static load. Generally, the impact load and the quasi-static load start simultaneously at the point where the maximum peak pressure on the revetment occurs.

Those waves that produce a pressure signal similar to that in Fig. 2-5a composed by the two load components (impact and quasi-static) are commonly referred as "impact loads", while those without the impact component (Fig. 2-5b) are named "non-impact loads" and are fully described by the quasi-static load component.

For the description of the pressure distribution parallel and normal to a revetment, the definition of the magnitude of the maximum pressure on the revetment is of great relevance due to the response of the structure at the location where the peak pressure is reached and also because it is commonly used for the normalization of the pressure distributions (Oumeraci et al. (2010); Alcérreca-Huerta & Oumeraci (2012); Foyer (2013)).

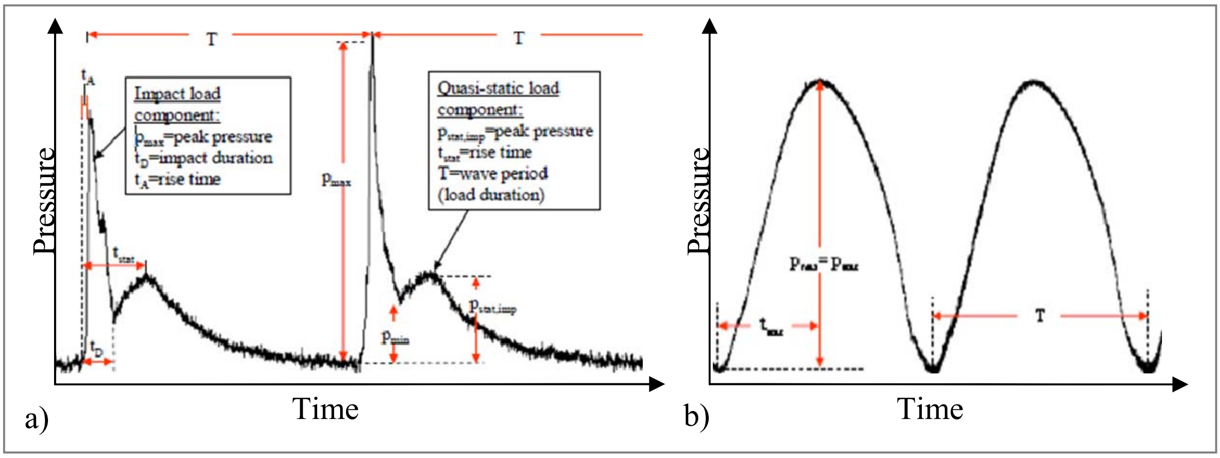

Fig. 2-5: Parameterization of the pressure time series for a) impact loads and b) non-impact loads.

Some approaches have been made in order to define the value of this maximum pressure reached by impact loads. Führböter et al. (1976), provided a prediction formulae (eq. (2.24)) which considers air entrainment and the effect of the slope into the wave impact development.

$$P_{\max,i} = \frac{const_i}{m} \rho_w g H \tag{2.24}$$

This prediction formulae is described by a probabilistic approach considering: i) a constant that is dependent on the dike slope and on the probability of no exceedance of a certain maximum pressure (4.8 ± 0.7 for regular waves and 30 for wave spectra for a probability of 99.9%), ii) the wave height H, iii) the water density ρ_w and iv) the slope steepness (m=cotα) of the revetment.

Oumeraci et al. (2010) presented a prediction formulae to describe the peak pressure on PBA revetments as a function of the surf similarity parameter for regular (eq. (2.25)) and irregular waves ((2.26)). Furthermore, the peak pressure beneath the revetment on the sand core (P_{max3}) was investigated leading to eq. (2.27) for regular waves and eq. (2.28) for irregular waves.

For regular waves, on revetment
$$\frac{P_{\max}}{\rho g H_{m0}} = -0.69\xi_{m-1,0} + 3.1 \text{ for } 1.6 < \xi_{m-1,0} < 2.6 \tag{2.25}$$

For wave spectra, on revetment
$$\frac{P_{\max}}{\rho g H_{m0}} = -4\xi_{m-1,0} + 12.5 \text{ for } 1.6 < \xi_{m-1,0} < 2.5 \tag{2.26}$$

For regular waves, beneath revetment
$$\frac{P_{\max 3}}{\rho g H_{m0}} = -0.11\xi_{m-1,0} + 1.0 \text{ for } 1.6 < \xi_{m-1,0} < 2.6 \tag{2.27}$$

For wave spectra, beneath revetment
$$\frac{P_{\max 3}}{\rho g H_{m0}} = 0.6\left[-4\xi_{m-1,0} + 12.5\right] \text{ for } 1.6 < \xi_{m-1,0} < 2.5 \tag{2.28}$$

Experimental data (Oumeraci et al. (2010), Gier & Schüttrumpf (2011) and Alcérreca-Huerta & Oumeraci (2012)) described the peak pressure on the revetment as function of the surf similarity parameter and specifically, for the case of PBA revetments the relationship is given by eq. (2.29).

$$\frac{P_{\max}}{\rho g H_{m0}} = 0.68 \cdot \xi_{m-1,0} \tag{2.29}$$

In addition to the determination of the peak pressure, prediction formulae for its location on the revetment are available in the literature. These formulae have been empirically derived from laboratory tests. Klein Breteler (2007) considered the wave height as the key parameter to describe the location of the peak pressure ($z_{\max 1}$).

$$\frac{z_{\max 1}}{H_{m0}} = \min\begin{pmatrix} 0.45\xi_0 - 0.3 \\ 1.7 \end{pmatrix} \tag{2.30}$$

Schüttrumpf (2001), proposed a hyperbolic tangent approach for smooth impermeable revetments which is also described in terms of the surf similarity parameter and the wave height (eq. (2.31).

$$\frac{z_{\max 1}}{H_{m0}} = 0.8 + 0.6\tan\left(\xi_0 - 2.1\right) \tag{2.31}$$

Oumeraci et al. (2010) suggested empirical equations for determining the location of $z_{\max1}$ on PBA-revetments based on both Schüttrumpf's and Breteler's approaches. The first equation (eq.(2.32)) is based on the Schüttrumpf's approach by introducing an amplification factor equal to 1.3. Therefore, this implies that the distance between the SWL and the peak pressure is approximately 30% higher for a PBA revetment than for smooth impermeable revetment. On the other hand, the second proposed equation (eq. (2.33)) based on Breteler's approach is restricted to $1.6 < \xi < 6.6$.

$$\frac{z_{p\max}}{H_{m0}} = 1.3\left[0.8 + 0.6\tan\left(\xi - 2.1\right)\right] \tag{2.32}$$

$$\frac{z_{p\max}}{H_{m0}} = \min\begin{pmatrix} 0.7\xi - 0.6 \\ 0.2\xi + 1.0 \end{pmatrix} \tag{2.33}$$

Recent experimental studies from large-scale tests have provided the first attempts to characterize the peak pressure induced by waves on a revetment and to obtain the pressure distribution parallel to the revetment slope. The results of this tests were provided by Oumeraci et al. (2010) and Alcérreca-Huerta & Oumeraci (2012) for PBA- and concrete placed blocks revetments, respectively.

Oumeraci et al. (2010) proposed the pressure distribution on the revetment to be described by the linear interpolation of five characteristic points for impact loads and 3 points for non-impact points (see Table 2-5). The location of this points is referred to the x'-axis parallel to the revetment slope and positive above the SWL and thus $P_{\max}$ is located at $x'_{\max}$ and the maximum run-up at x'_{Ru}, (where x' is the distance measured parallel to the revetment slope and positive above the SWL).

Table 2-5: Points to describe the pressure distribution parallel to a PBA revetment slope.

	Impact waves					*Non-impact waves*		
Point	**1**	**2**	**3**	**4**	**5**	**1**	**2**	**3**
$P/P_{\max}$	0.4	0.5	1.0	0.4	0.0	0.4	1.0	0.0
x'/x'max	-3.0	-1.5	-1.0	-0.6	$x'_{Ru}/x'_{\max}$	-2.6	-1.0	$x'_{Ru}/x'_{\max}$

Alcérreca-Huerta & Oumeraci (2012), proposed the pressure distribution on concrete placed blocks (CPB) revetments to be described by a continuous equation (eq. (2.34)). This approach was only developed for impact waves and the pressure distribution may be similar to that of impermeable smooth revetments.

$$\frac{P}{P_{\max}} = \frac{0.41 - 0.29\left(x'/x'_{\max}\right)}{1 + 0.9\left(x'/x'_{\max}\right) + 0.59\left(x'/x'_{\max}\right)^2} \tag{2.34}$$

The approaches proposed by Oumeraci et al. (2010) and Alcérreca-Huerta & Oumeraci (2012) for both PBA-revetment (impact and non-impact loads) and CPB-revetments, respectively, are depicted in Fig. 2-6.

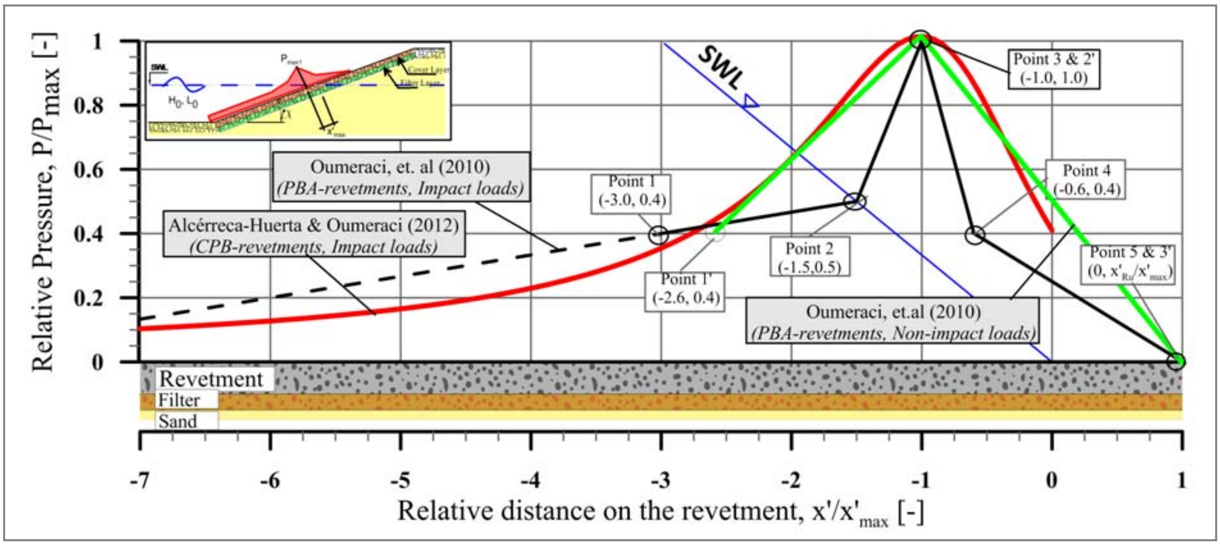

Fig. 2-6: Pressure distribution on PBA-revetments (Oumeraci et al. (2010)) for impact and non-impact loads, and on CPB revetments (Alcérreca-Huerta & Oumeraci (2012)) for impact loads.

The revetment response due to impact loads is also dependent on aeration effects. Even for regular waves, the wave-wave and the wave-structure interactions can produce aeration. The classification of Lundgren (see Griffiths (1993)), for the trapped air contained in the impact wave, leads to three air aeration conditions that may induce different physical processes: i) ventilated shocks, where the air escapes prior the collision of the wave breaking with the structure, ii) compression shocks, that may induce a dissipation of the energy (up to 15% for some cases) through the motion of air pockets trapped during the breaking and iii) hammer shocks that are relevant especially for vertical walls where a strong compression of the air trapped is induced due to the water mass striking the wall with high intensity and with a short duration pulse. Bullock et al. (2007) defined two basic conditions related to the effects of air trapped by a wave breaking on the pressure at the structure, (Fig. 2-7): i) low-aeration when the water adjacent to the revetment slope contain relatively small amount of air (considering a void ratio <5%); and ii) high-aeration when water contains a bigger amount of air.

Investigations on the development of impact loads over revetments (Führböter et al. (1976); Piontkowitz et al. (2009)) have shown that the wave impact load can also be affected by the presence of a water layer at the impact point on the revetment caused by the preceding wave run-down. Führböter et al. (1976) conclude that for a water sheet with a thickness of 0.1 m no impact loads were registered, which means, that almost all the impact forces were damped by this water layer thickness. The damping effect of the water layer increases with flatter slope so that the peak pressure decreases proportionally. Moreover, the limit slope steepness for which plunging breakers impacts a water free slope is found between 1:4 and 1:6 (Stanczak (2008)). The damping effect of the water layer on the revetment at the impact point is described in Fig. 2-8.

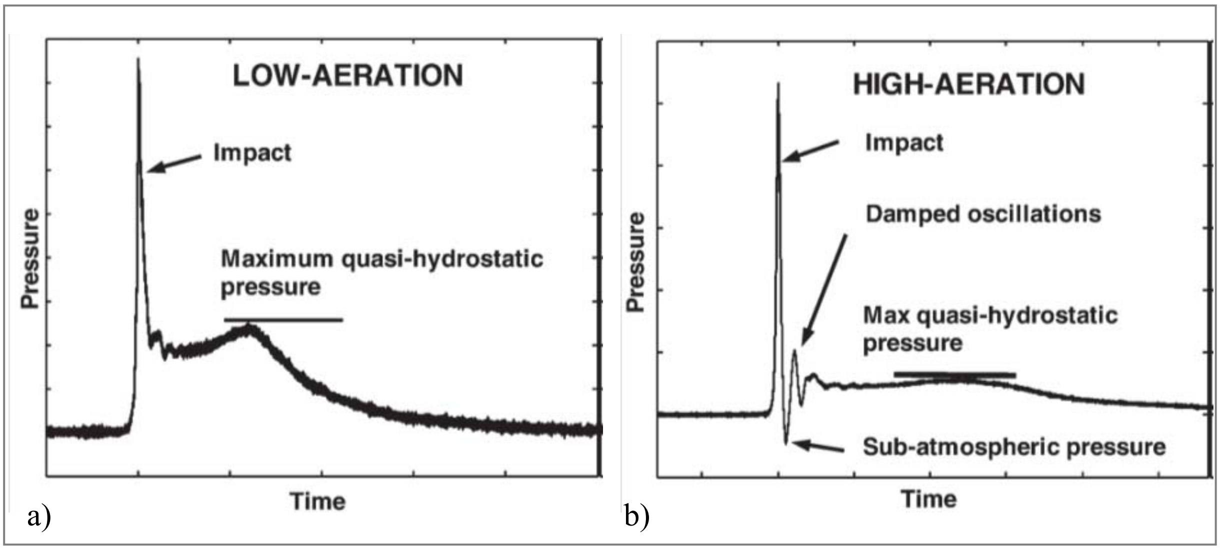

a) b)

Fig. 2-7: Effect of aeration in impact loads: a) waves with low aeration, b) waves with high aeration (Bullock et al. (2007)).

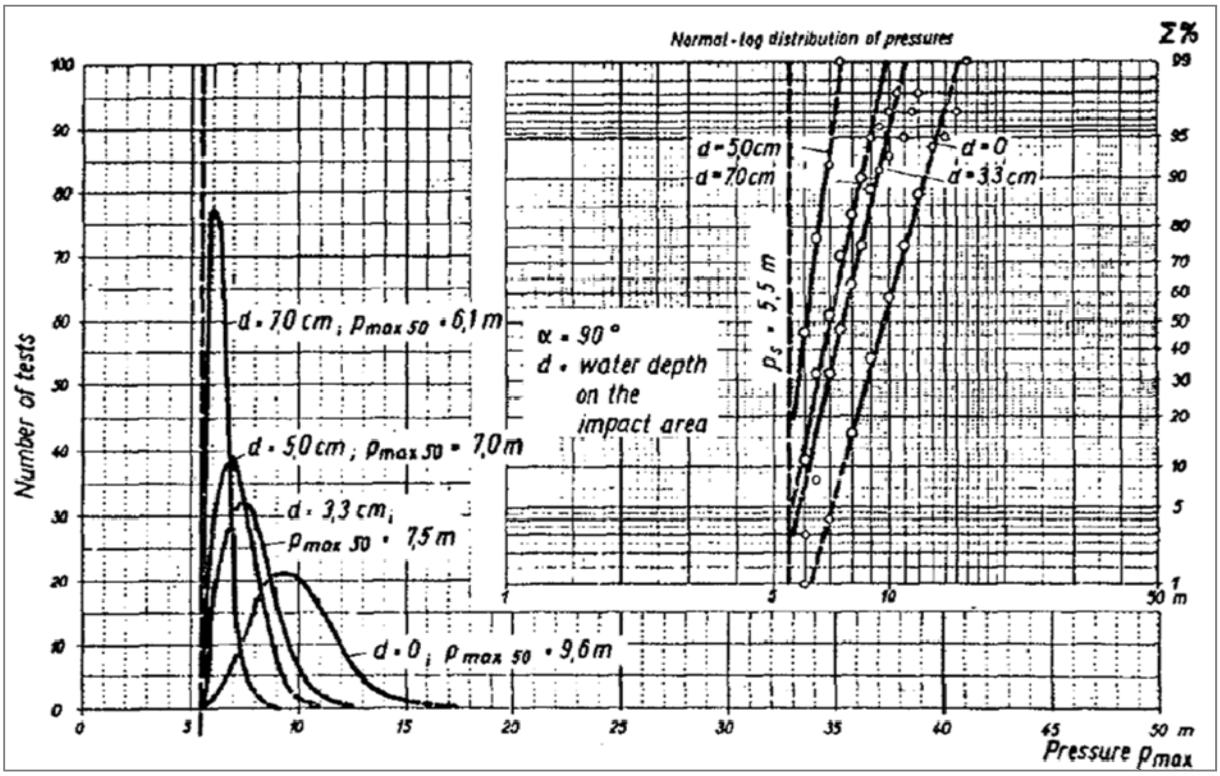

Fig. 2-8: Damping effect on impact loads caused by water layer on the revetment (Führböter et al. (1976)).

2.2.2 Uplift pressures

The main effects of uplift pressures on revetments are related to the decrease of the effective weight of the filter and the cover layer and consequently to: i) a decrease of the friction between the filter and the cover layer allowing sliding between the layers, ii) washing out of subsoil and /or iii) the presence of displacements of particles, which can cause a S-shaped deformation of the embankment and in case of block revetments, the possibility of uplifting of individual pieces out of the revetment (Pilarczyk, 1988).

Several factors can affect the development of uplift pressures (Führböter et al. (1976)): i) permeability and thickness revetment and filter layers; ii) water storage capacity of the embankment subsoil; iii) the presence of drainage systems and iv) the location of the maximum wave run-down.

Guidelines for the estimation of the uplift pressures on caisson breakwaters and vertical walls are provided by USACE (2002) considering the approach by Goda (1974). A rough solution proposed by the Delft Soil Mechanics Laboratory was developed for revetments and it considers that the uplift pressure on the revetments can be estimated through the calculation of the excess of pore pressure (Fig. 2-9) multiplied by the specific weight of water (van Gent (1994)).

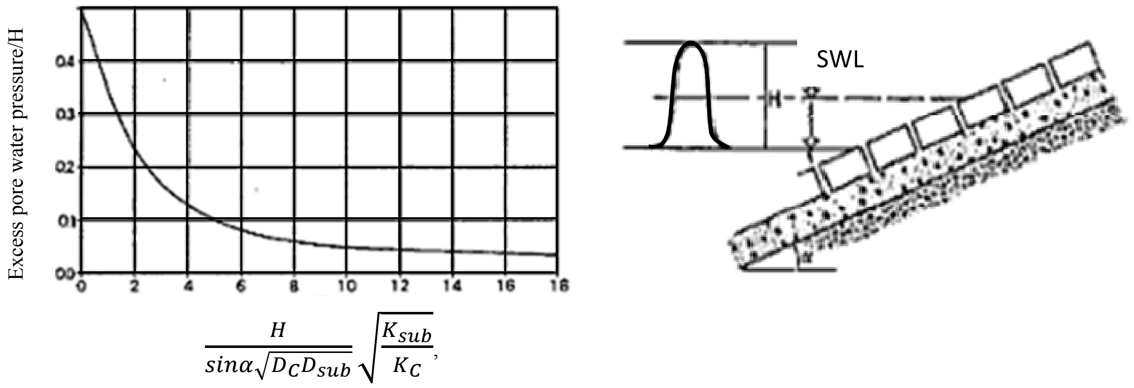

$$\frac{H}{sin\alpha\sqrt{D_C D_{sub}}}\sqrt{\frac{K_{sub}}{K_C}},$$

where H=wave height, D=thickness, K=permeability and sub indexes c=cover layer, sub=layer underneath.

Fig. 2-9: Excess pore pressure below a revetment due to sinusoidal waves (van Gent (1994)).

A further approach for revetments was presented by Wolsink (see Pilarczyk (1998)), which also calculates the uplift pressure gradient ($\Delta\Phi$) at different locations on and inside the revetment. This approach (s. eq. (2.35) and Fig. 2-10) was developed especially for concrete place block (CPB) revetments and it introduces the concept of leakage length which is defined as the length of a piece of protection in which the flow resistance through the revetment and through the filter layer are the same. In other words, the leakage length describes the relative permeability of the layers involved.

$$\Phi_w = \left(\frac{1}{2}\Lambda\cos\alpha\tan\theta\left(1-\exp\left[-\frac{\Phi_b}{\Lambda\cos\alpha\tan\theta}\right]\right)+\frac{\Lambda\sin\alpha}{2}\right)\left(1-\exp\left[\frac{-2z}{\Lambda\sin\alpha}\right]\right) \tag{2.35}$$

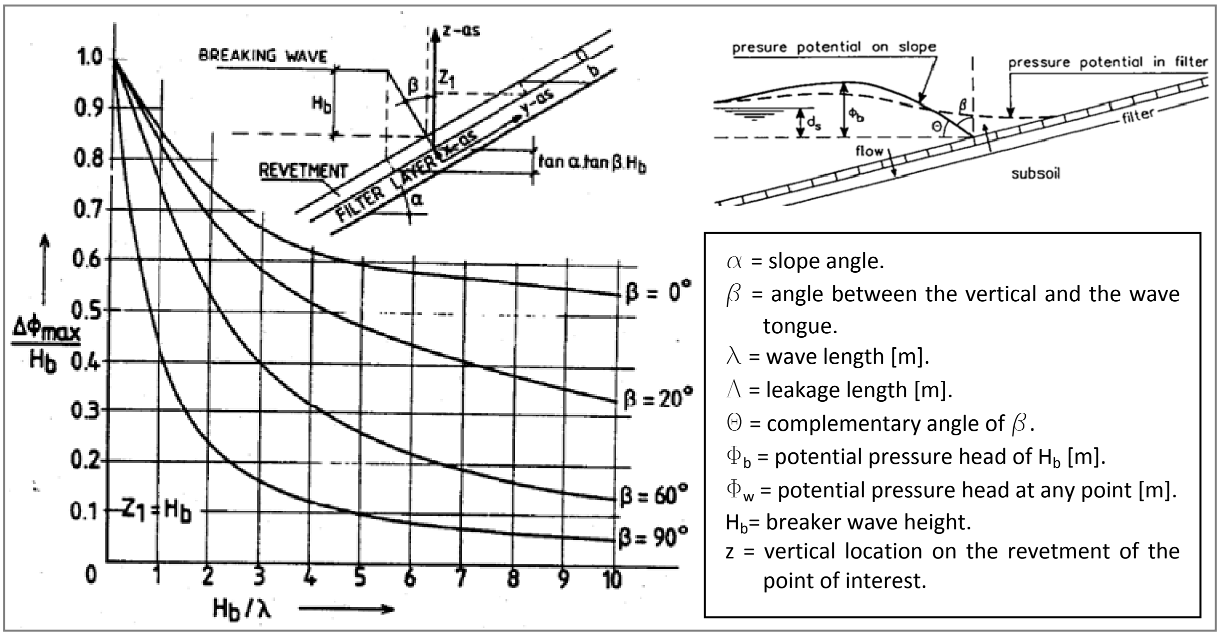

α = slope angle.

β = angle between the vertical and the wave tongue.

λ = wave length [m].

Λ = leakage length [m].

Θ = complementary angle of β.

Φ_b = potential pressure head of H_b [m].

Φ_w = potential pressure head at any point [m].

H_b= breaker wave height.

z = vertical location on the revetment of the point of interest.

Fig. 2-10: Schematized pressure conditions for wave load conditions based on the analytical Wolsink solution (Bezuijen et al. (1987)).

The assessment of uplift pressures in different revetments types is still a knowledge gap. None of the aforementioned approaches consider the wave breaking type and the influence of the slope steepness for the calculation of the uplift pressure. Particularly, PBA revetments have no design formulae for the development of uplift pressures or for the design of the optimum cover and filter thicknesses that can minimize the effects of this loading condition. Furthermore, limitations arise for the estimation of the uplift pressure in the embankment subsoil beneath the revetment. Thus, normally it is highly recommended to analyse and investigate the performance, stability and response of revetments through numerical and physical tests. For this purpose, comprehensive analyses based on systematic tests with PBA-revetments are required.

2.2.3 Cyclic wave loading

The cyclic loads can cause permanent displacements in the embankment subsoil of a revetment since residual or permanent strains could not be released and thus leading to a partial displacement of the soil skeleton (if it is not well compacted). The permanent deformations are produced mainly due to a volume change or because a shear distortion in the soil.

Some attempts to quantify the deformation of the soil due to wave motion have been made normally for those structures subject only to the wave loading cycles such as offshore structures or scour protections. Sangrey (2011) describes some developments in experimental and theoretical derivations to explain the effects of wave cycling loads. When the uplift forces are present during the cyclic wave load, higher and irreversible displacements can be expected. Furthermore, for a complete cycle important displacements could be accumulated and the final deformation due to several of these cycles could lead to a failure of the soil even that the ultimate capacity has not been reached. Therefore, some failures observed on coastal structures can be attributed to the cyclic loads and thus to the soil deformation.

Cyclic loading can lead to a build up of the excess of pore pressure that might reduce the effective stress to sufficiently low levels where liquefaction will develop (Sangrey (2011)). The wave-induced cyclic loads are in close relationship with the development of instantaneous liquefaction, and the drainage allowed. Furthermore, the cyclic loading induce an instantaneous or transient pore pressure that might be added to the build up of pore pressures in time (residual pore pressure) exemplarily shown in Fig. 2-11.

The instantaneous pore pressure is fluctuating with the load but not necessarily in the same phase and might be dominated by elastic soil behaviour (De Groot et al. (2006)). The excess of pore pressure are largest underneath the wave trough and thus liquefaction risk may be expected during the wave trough for porous sea beds (Fig. 2-11a). However, the largest excess of pore pressure for revetments may occur during the pass of the wave trough on the revetment but also where the wave run-down is found.

On the other hand, residual pore pressures increase or decrease gradually and are mainly caused due to the plastic deformation of the soil skeleton. For revetments, drainage and release of the excess of pore pressure is allowed trough the surface of the revetment, and residual pore pressure may develop causing an apparently permanent situation of partial liquefaction (De Groot et al. (2006)). However, the flow of pore water outside the soil leads to densification of the soil (causing settlements) and to increase the resistance to the generation of pore pressures unless the cyclic wave loading increases.

Wave-induced excess pore pressures in drained sand bed.

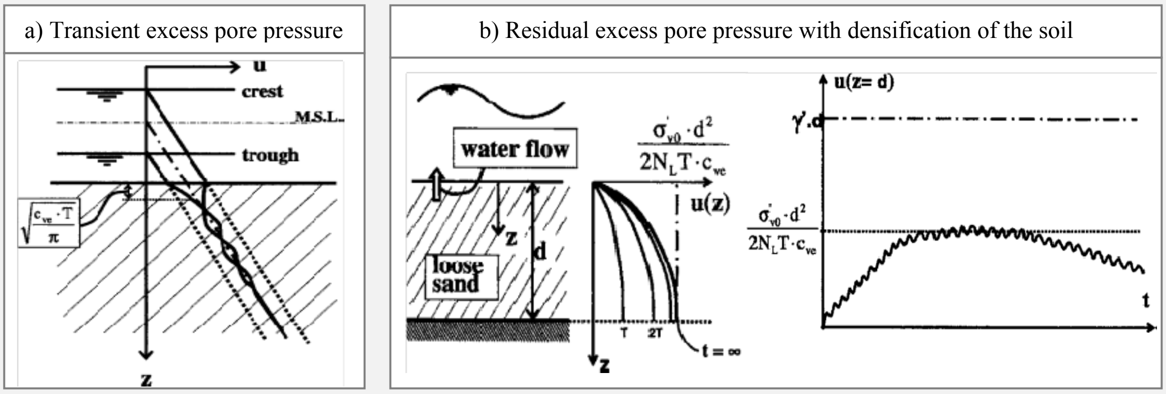
a) Transient excess pore pressure

b) Residual excess pore pressure with densification of the soil

where d is the thickness of the sand seabed; z is a location in the sand; T is the wave period, $c_{ve}=k/[\gamma_W(\beta_S+n\beta_w)]$ is the consolidation coefficient for elastic, horizontal constrained (de)compression; k is the permeability; γ_W(the specific weight of the water; n the porosity, β_S and βw are the compressibility of the water and soil, respectively; γ' the submerged specific weight of the soil; N_L is the number of cycles to liquefaction in undrained cyclic test and σ'_{v0} is the vertical effective stress before excess pore pressure starts.

Fig. 2-11: Wave-induced excess pore pressure in drained sand bed: a) transient excess of pore pressure, b) residual excess of pore pressure with densification of the soil (modified from De Groot et al. (2006)).

The pore pressure inside the embankment subsoil of revetments has been recently studied by Oumeraci et al. (2010) based on large-scale tests with PBA-revetments considering a slope 1:3. A failure of the PBA-revetment occurred within the laboratory tests (most likely caused by soil liquefaction) and an analysis for the stability of the embankment subsoil beneath PBA-revetments was performed but no methodology was developed for the assessment of liquefaction potential considering simultaneously different revetment configurations and wave load conditions.

The stability of the soil against liquefaction around marine structures has been reviewed by De Groot et al. (2006) but no direct guideline to account for the stability of the embankment subsoil for PBA-revetments against liquefaction is available. Moreover, the transient and the residual pore pressure have been investigated mostly for porous seabed and not for its application for subsoil embankments underneath revetments. Thus, a knowledge gap is recognized for the assessment of liquefaction risk as consequence of wave-induced cyclic loads and which has been identified as a key element for the stability of PBA-revetments.

Overall, the wave-induced load types have been analysed with focus on the revetment response. Impact and non-impact loads are wave-induced loads which may induce a different performance of the revetment. Furthermore, the peak pressure of the wave-induced loads and its location on the revetment are the key parameters considered in several studies (e.g., Oumeraci et al. (2010); Alcérreca-Huerta & Oumeraci (2012)) for the determination of the spatial pressure distribution on revetments together with the location of the peak pressure. Differences are present on the spatial pressure distribution for CPB- and PBA-revetments which are noticed particularly close to the location of the peak pressure: for a same peak pressure, the pressures around the impact area are smaller for porous and rough PBA-revetment than for the almost impervious and smooth CPB-revetments. Moreover, for impact and non-impact loads, the effect of a water layer on the revetment can provide a significant damping of the wave load. The damping effect of the water layer increases with flatter slope so that the peak pressure decreases accordingly. Moreover, the limit slope steepness for which plunging breakers impacts on a water free slope is found around 1:4 and 1:6.

Regarding uplift pressures, PBA revetments have no design formulae for the assessment of uplift pressures in the revetment and filter layers. Furthermore, limitations arise for the estimation of the uplift pressure in the embankment subsoil beneath the revetment. Moreover, approaches for the analysis of the cyclic wave-induced pore pressures are based on the results from the analysis of porous sea beds and the validity of their application for porous revetments has not yet been verified. Furthermore, up to now, no systematic methodology has been developed (as function of wave conditions and the revetment geometry) to assess the stability of PBA-revetments against soil liquefaction due to cyclic-loading

2.3 Flow, pore pressures and stresses in porous media

The porosity has an important effect on wave-structure interaction processes such as the decrease of the wave run-up and wave reflection. The flow through the structure allows wave energy dissipation and also reduces the total amount of wave energy reflected. Moreover, the flow propagation trough the pores decay in the same form as the energy does and consequently pressures acting on revetments may be reduced as they are transmitted inside the porous media. However, the pressures developed in the soil must be taken into account for the stability of the structures.

Therefore, this section will provide a review of the fundamentals involved on the description of the flow inside porous bonded revetments as well as elements concerning the development of pressures and stresses. Also, an introduction to the basic assumptions made in porous media modelling is provided.

2.3.1 Theory of flow in porous media

One of the first approaches concerning flow in porous media was provided by Henry Darcy in 1856, who studied steady laminar flow through sand sample measuring the rate of flow Q. The consequence of these experiments is known as Darcy's law and proportionality was found to exist between the hydraulic gradient (i) and the rate flow Q. The constant of proportionality was named by Darcy as hydraulic conductivity (K) and it represents the rate at which water flows through the porous media (m/s).

The validity of Darcy's law occurs for most type of fluid flow in soils, however, for fluids at very high velocities the law becomes invalid. When the velocity U is high enough, a non-linear relationship occurs between the flux and the pressure gradient. To consider where the non-linear effects appear it necessary to take into account the flow regimes (Bennethum & Giorgi (1997)): i) laminar regime, where the viscous forces dominates, ii) steady inertial flow regime, where the micro-velocity is still stationary but the pressure gradient stops to vary linearly with the velocity; iii) Turbulent transition regime, where the inertial forces are more important and the micro-velocities fluctuates at any experimental sample point; iv) Turbulent regime, where the micro-velocities randomly fluctuates about a mean. The non-linearity occurs from the second regime and therefore an extension of Darcy's law is described by the Darcy-Forchheimer equation (eq. (2.36)) which is valid for regimes i, ii and iii ($1\text{-}10<Re<200$ with $Re=(Ud_{30})/\nu$) also called Forchheimer flow (Burcharth & Christensen (1991)):

$$i = aU + b\left|U\right|U \tag{2.36}$$

where a and b are dimensional coefficients expressed in [s/m] and [s^2/m^2], respectively; U in [m/s] and i adimensional [-].

The first term in eq. (2.36) considers Darcy’s law with a linear relationship between the pressure gradient and the velocity (laminar contribution), while the second term of the equation considers the turbulent contribution and nonlinear effects. Since coefficients a and b in eq. (2.36) are dimensional, several studies have been conducted to determine their value (see Table 2-6 and also Sidiropoulou et al. (2006)). From this studies, it is concluded that coefficients a and b are dependent on the porosity, the particle size (or equivalent sphere diameter) and the density of the soil.

Table 2-6: Formulae for the determination of coefficients a and b in Darcy-Forchheimer equation (eq. (2.36)).

Author	***Coefficient a***	***Coefficient b***	***Considerations***
Ergun (1952)	$\alpha_f \frac{(1-n)^2}{n^3} \frac{\nu}{gD^2}$	$\beta_f \frac{1-n}{n^3} \frac{1}{gD}$	α_f=150, and β_f= 1.75
Engelund (1953)	$\alpha_f \frac{(1-n)^3}{n^2} \frac{\nu}{gD^2}$	$\beta_f \frac{1-n}{n^3} \frac{1}{gD}$	α_f=780, and β_f= 1.8-3.6
Ward (1964)	$\alpha_f \frac{\nu}{gD^2}$	$\beta_f \frac{1}{gD}$	α_f=360, and β_f= 10.44
Koenders (1985)	$\alpha_f \frac{(1-n)^2}{n^3} \frac{\nu}{gD_{15}^2}$	$\beta_f \frac{1}{n^5} \frac{1}{gD_{15}}$	α_f=290 (confidence levels 95%: 250-330), β_f= 1.4
den Adel (1987)	$\alpha_f \frac{(1-n)^2}{n^3} \frac{\nu}{gD_{15}^2}$	$\beta_f \frac{1}{n^2} \frac{1}{gD_{15}}$	α_f=160 (confidence levels 95%: 75-350), β_f= 2.2 (confidence levels 95%: 0.9-5.3)
Shih (1990)	$\alpha_f \frac{(1-n)^2}{n^3} \frac{\nu}{gD_{15}^2}$	$\beta_f \frac{1-n}{n^3} \frac{1}{gD_{15}}$	$\alpha_f=1684+3.12\text{x}10^{-3}(g/\upsilon^2)^{2/3}\ (D_{15})^2$ $\beta_f= 1.72+1.57\ \exp[-5.1\ \text{x}\ 12\text{x}10^{-3}(g/\upsilon^2)^{1/3}\ {}^{(}D_{15})]$ For wide grade material use $D_*=D_{15}\ (D_{15}/D_{50})^{-1.11}\ (D_{50}/D_{85})^{0.52}$

Through the Fochheimer's equation turbulence effects are considered but it is applicable only for steady flows. Thus, a time-dependent term is included so the extended Forcheimer's equation is valid also for non-stationary flows:

$$i = aU + b|U|U + c\frac{dU}{dt} \tag{2.37}$$

where c is a coefficient [s^2/m] that could be defined through eq. (2.38) which is theoretically derived from the Navier-Stokes/Reynolds equation (van Gent (1993)). The value of "c" considers the effect of a non-dimensional coefficient that takes into account the added mass (γ). The added mass or virtual mass is the inertia added to a system because an accelerating or decelerating body must move some volume of surrounding fluid as it moves through it, since the object and fluid cannot occupy the same physical space simultaneously.

$$c = \frac{1+\gamma\left(\frac{1-n}{n}\right)}{ng} \tag{2.38}$$

The contribution of each coefficient (a, b, c) was analyzed by van Gent (1993) for oscillating flow. The results for non-stationary conditions (Fig. 2-12) concluded that: i) the biggest contribution for the hydraulic gradient is the b-coefficient which takes into account the turbulence contribution, ii) the c-coefficient reaches its maximum contribution just after the zero crossings, however, its contribution is relatively short and iii) the a-coefficient has a large contribution than the c-term and it is distributed outside the zero crossings.

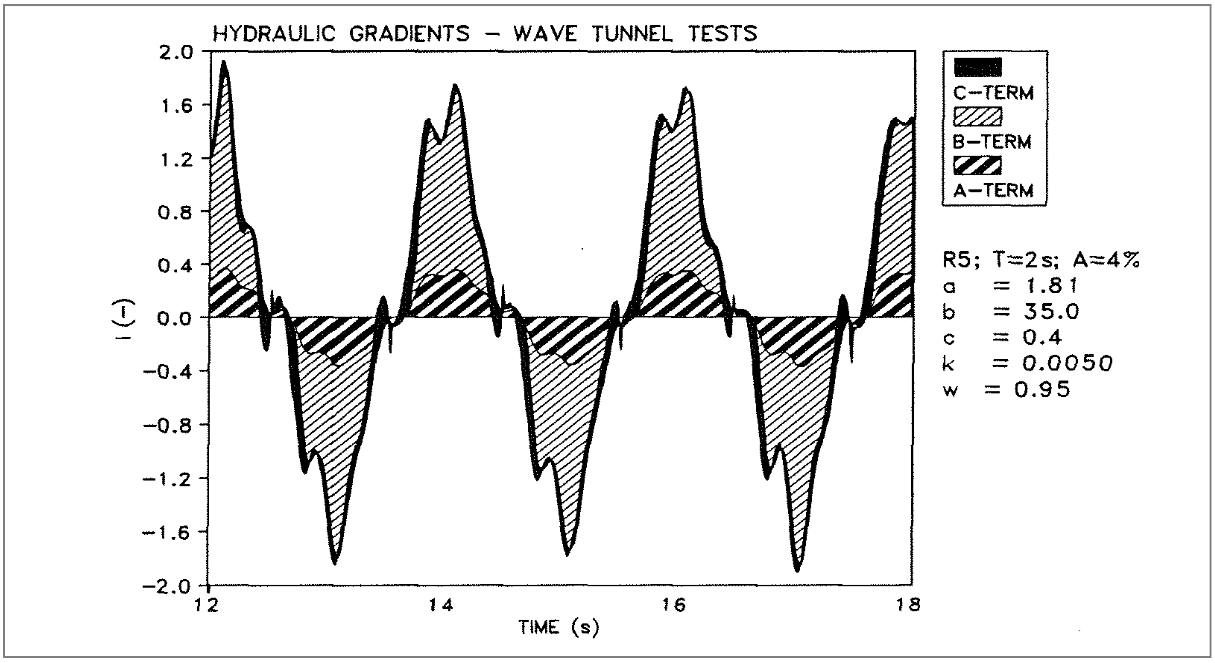

Fig. 2-12: Contribution of coefficients a, b and c into the extended Darcy-Forchheimer equation (eq. (2.38)). (van Gent (1993)).

Based on experimental studies and field observations, Barree & Conway (2004) suggested a new equation for describing the non-Darcy flow through porous media. The experiments performed showed that the coefficient b in the Darcy-Forchheimer equation should not be constant since the apparent permeability K_{app} may vary with the flow rate. Thus, as an alternative the authors suggested expression (2.39). If K_{app} is considered constant, eq. (2.39) leads to the Darcy-Forchheimer equation (eq. (2.36)).

$$i = \frac{\mu U}{K_{app}} = \mu U \frac{1}{K}\left(1 + \frac{bK|U|}{\mu}\right) \tag{2.39}$$

Barree and Conway's approach is valid to represent both single and multiphase non Darcy's flows by considering the apparent permeability $K_{app,\alpha}$ (for a single phase $K_{app,\alpha}= K_{app}$). For this purpose, the apparent permeability $K_{app,\alpha}$ is estimated as shown in eq.(2.40) where $\overline{T}$ [m^{-1}] is the transition constant ($\overline{T} = 1/(bK)$), $k_{r,\alpha}$ is the relative permeability for a fluid phase α, and coefficients F and E are empirically defined (F and E≈1).

$$K_{app,\alpha} = k_{r,\alpha} + \frac{K - k_{r,\alpha}}{\left(1 + Re_{\alpha}^{\ F}\right)^{E}} \tag{2.40}$$

An additional task on the multiphase flow modelling arises when the porous media is stratified and the properties of each layer differ. The presence of layers with different properties is common in revetments structures, since they are generally formed by the revetment itself, the filter and the underlying soil. Thus, the computation of multiphase flow through these different porous media layers has been simplified to produce classic design rules (eq. (2.41)). The permeability of a layered soil normal to the flow is always smaller than the permeability of the same layered soil but with a flow parallel to the layers (Venkatramaiah (2006)). For flow normal to the layers Sridharan & Prakash (2002) found that the theoretical permeability (eq.(2.41)) differs from direct measurements due to the influence of the exit layer which seems to control the final value of the hydraulic conductivity K.

$$\frac{1}{K_N} = h\sum_{i=1}^{n}\frac{1}{\left(h_i / K_i\right)} \text{ (flow normal to soil layers)} \qquad K_P = \frac{1}{h}\sum_{i=1}^{n} K_i h_i \text{ (flow parallel to soil layers)} \tag{2.41}$$

where, h_i and K_i are the thickness and permeability of soil layer i-, respectively, and K_n is the permeability due to flow normal to the soil layer and K_p is the permeability due to flow parallel to soil layers.

Finally, for the analysis and modelling of flow in porous media is should be considered that: i) not all the pores are interconnected and therefore the concept of effective porosity should be considered as better descriptor for flow motion applications (the volume of voids V_s is substituted by the volume of connected voids $V_{s,c}$), ii) sorting has an impact into the porosity and for this reason well sorted materials exhibit a higher porosity than poorly sorted, where the smaller particles fill the gaps between larger particles and iii) the consideration of a characteristic grain size to represent the porous media (e.g., D_{15}, D_{50}, D_*) as well as the permeability may induce a large effect on the stability and performance of coastal structures and their porous layers (e.g., rock armours (van der Meer (1988); van Gent et al. (2004); Reedijk et al. (2008)), placed block revetments (Bezuijen & Kruse (1998)), accropodes armours (Burcharth (1998)).

2.3.2 Stresses, strains and pore pressure in porous media

The behaviour of a porous media (such as the soil in a revetment) could be modelled by theory of elasticity and the conception of stresses, strains and pore pressures developed as a consequence of the application of actions and loads. The deformation of the soil due to an applied stress σ results in a strain ε (Fig. 2-13). The theory of elasticity, based on Hooke's Law, provides a linear relation between the stresses and strains established through the Young's modulus (E) and the Poisson's ratio (ν) as shown in the set of equations (2.42) considering an isotropic material. The first term in eq. (2.42) for describing strains ε_{xx}, ε_{yy}, ε_{zz} is the compression stress and reflects the assumption that the strain in a given direction depends linearly on the stress in the same direction, while the second term take into account he deformation due to the stresses in other directions.

$$\begin{aligned}
\varepsilon_{xx} &= \frac{1}{E}\left[\sigma_{xx} - \nu\left(\sigma_{yy} + \sigma_{zz}\right)\right] & \varepsilon_{xy} &= \frac{1+\nu}{E}\tau_{xy} \\
\varepsilon_{yy} &= \frac{1}{E}\left[\sigma_{yy} - \nu\left(\sigma_{zz} + \sigma_{xx}\right)\right] & \varepsilon_{yz} &= \frac{1+\nu}{E}\tau_{yz} \\
\varepsilon_{zz} &= \frac{1}{E}\left[\sigma_{zz} - \nu\left(\sigma_{xx} + \sigma_{yy}\right)\right] & \varepsilon_{zx} &= \frac{1+\nu}{E}\tau_{zx}
\end{aligned} \tag{2.42}$$

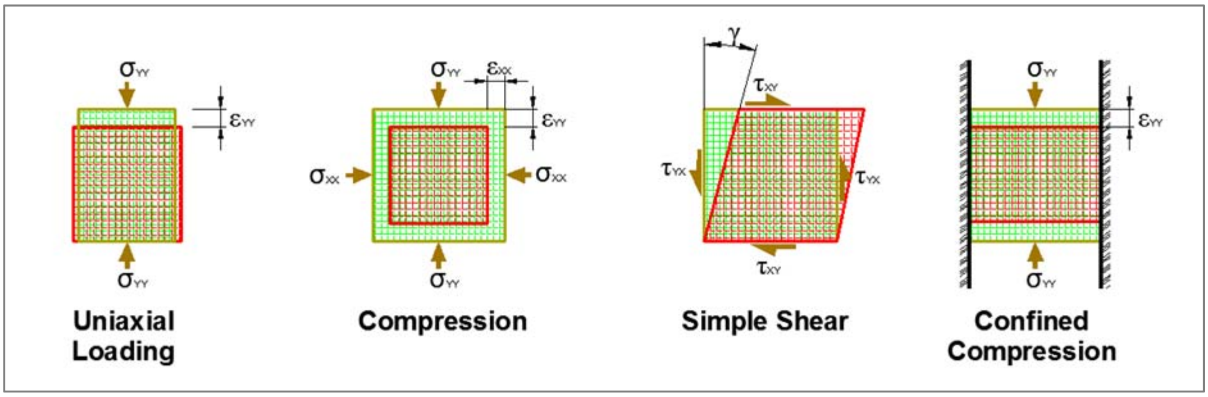

Fig. 2-13: Definition sketch of soil stresses and strains (Lambe & Whitman (1969)).

Additionally, the total stress σ in soils is integrated by two components: i) pore water pressure u, and ii) the effective stress σ' that represents the average stress between soil grains over a cross section area. The relationship between the stresses and the water pore pressure is expressed in eq. (2.43) and depicted in Fig. 2-14.

$$\sigma' = \sigma - u \tag{2.43}$$

The importance of the effective stress was stated by Terzaghi et al. (1996): "*...all the measurable effects of a change in stress, such as compression, distortion and a change in shearing resistance, are due exclusively to changes in the effective stress.*" The effective stress in coarse granular soil is transmitted particle to particle by the contact between them.

For steady flow the pore water pressure is equal to the hydrostatic pressure, however, coastal structures are subject to flow inside the structure, so the value of the pore pressure varies as an effect of wave motion and wave impact loads.

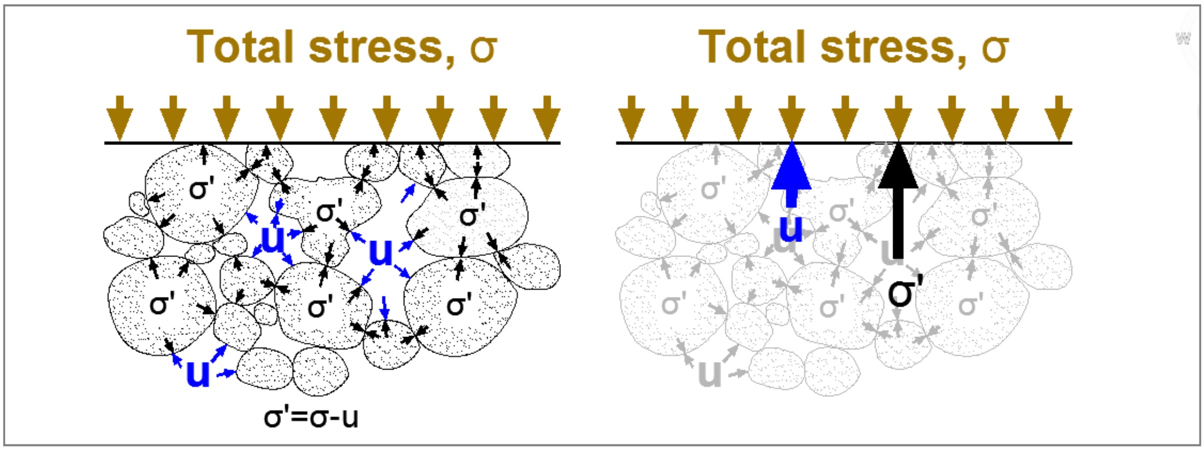

Fig. 2-14: Development of pore pressures and effective soil stresses in the soil.

The response of a partially saturated soil is related to the degree of saturation. The behaviour of a partially saturated soil during drainage and undrained conditions is schematized in Fig. 2-15 where the relationship between the pore pressure, the total and the effective stresses is also shown.

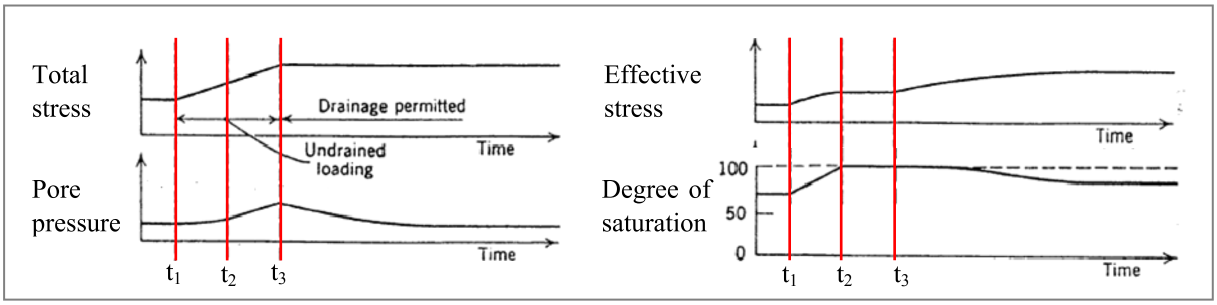

Fig. 2-15: Behaviour of pore pressure, soil effective and total stresses in partially saturated soils (Lambe & Whitman (1969)).

For partially saturated soils and when no drainage is allowed, an increment in the total stress corresponds to an increase in both effective stress and pore pressure. However, when the soil is fully saturated and the total stress is increased then the pore pressure increases but not the effective stress. When drainage is allowed and the soil is fully saturated then the effective stress increases but not the pore pressure.

Additionally to the variations of pore pressure due to saturation conditions on the soil, other variations could be induced because of the presence of oscillatory flows such as the ones generated by waves or because of an accumulation of the pore pressure. Two significant wave-induced pore pressures could be developed as a response to wave action: i) transient or oscillatory pore pressure and ii) residual pore pressure. Large-scale tests have been performed on coastal structures showing the development of such pore pressures (Fig. 2-16) for the case of a PBA revetment (Oumeraci et al. (2010)) and for the case of caissons (Kudella & Oumeraci (2006)).

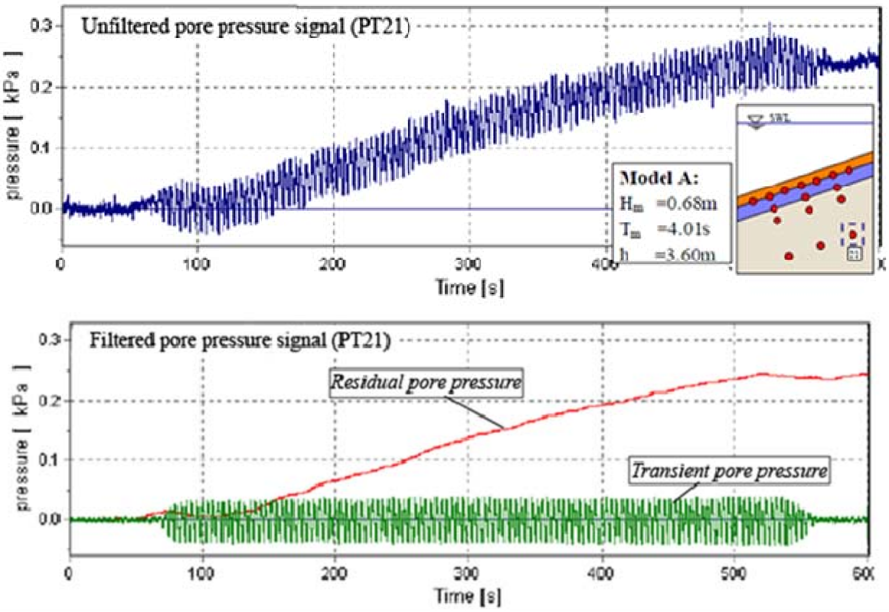

Fig. 2-16:Pore pressure recorded in large-scale laboratory tests with PBA-revetments (Oumeraci et al. (2010)), where the residual and transient pore pressure are developed simultaneously.

Analytical solutions have been derived for the analysis of transient pore pressures. Mei & Foda (1980), derived an approach (based on Biot's theory for soil consolidation under linear elasticity and Darcy's flow) that propose a boundary-layer approximation to get a simplified formulation for transient pore pressure valid for coarse sand. In the case of marine sediments and transient pore pressure, some analytical solutions for an infinite seabed have been proposed by Jeng (2008). Transient pore pressures have been investigated mostly for the case of seabed, however, the applicability of these studies for its use in coastal structures needs further validation. For the analysis of the residual pore pressures, models and approximations have been developed (e.g., Jeng (2008)) while observations of its occurrence has been observed in coastal structures such as caisson breakwaters (Kudella & Oumeraci (2006)).

2.3.3 Porous media flow modelling: basic assumptions

The objective of a good modelling is to reduce the complexity of the mathematical formulations for studying the physical process. Since the internal morphology of the porous media is too complex to be modelled in detail, the selection of the volume and time averaging techniques is a good implementation to describe the flow in the porous media.

The volume averaging technique is widely used for the simulation of multiphase flows. The technique is based on the consideration that the volume averaging of the microscopic equations over a representative elementary volume ΔV can provide the macroscopic governing equations for flow through a porous medium. The intrinsic volumetric average is described by eq. (2.44), in which the inclusion of the porosity concept is applied where V_f is the volume of fluid contained in V, and $\langle\varphi\rangle^i$ is the intrinsic average magnitude of property φ:

$$\langle\varphi\rangle^i = \frac{1}{\Delta V_f}\int_{\Delta V_f}\varphi dV, \qquad \langle\varphi\rangle^v = n\langle\varphi\rangle^i, \qquad n = \frac{V_f}{V} \tag{2.44}$$

The property φ can then be defined as the sum of $\langle\varphi\rangle^i$ and a term related to its spatial variation within the representative elementary volume (REV), ${}^i\varphi$, as in eq. (2.45) (s. Fig. 2-17b):

$$\varphi = \langle\varphi\rangle^i + {}^i\varphi \tag{2.45}$$

Similar to the volume averaging, the time average technique could also be applied and an instantaneous property φ can be defined by the sum of the time averaged value of this property plus its fluctuating component (Fig. 2-17a).

Based on these procedure and in order to obtain the governing equations to model the flow in porous media, some relationships have been developed for this purpose and are known as the theorem of local volume averaging (see Whitaker (1986) for further reference). The application of both volume and time averaging techniques to the Navier-Stokes equations leads to the derivation of the Volume-Averaged Reynolds Averaged Navier Stokes (VARANS) equations (Hsu et al. (2002); de Lemos & Pedras (2001); del Jesús Peñil (2011)), that have been implemented in several numerical models (s. Section 2.4) for the simulation of flow in porous media without representing the exact morphology of the porous media.

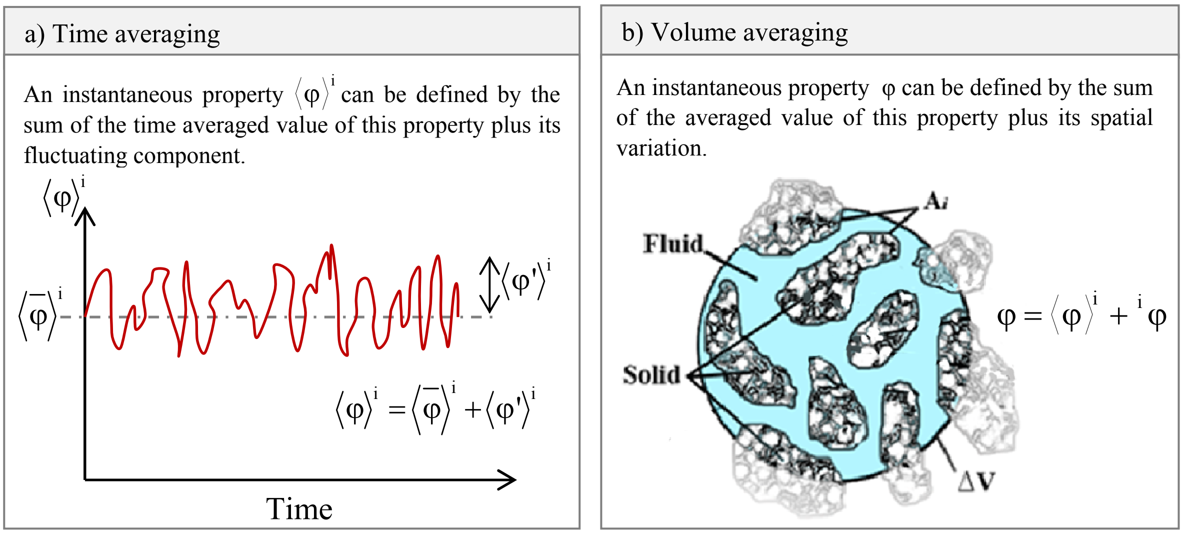

a) Time averaging

An instantaneous property $\langle\varphi\rangle^i$ can be defined by the sum of the time averaged value of this property plus its fluctuating component.

$$\langle\varphi\rangle^i = \langle\bar{\varphi}\rangle^i + \langle\varphi'\rangle^i$$

b) Volume averaging

An instantaneous property φ can be defined by the sum of the averaged value of this property plus its spatial variation.

$$\varphi = \langle\varphi\rangle^i + {}^i\varphi$$

Fig. 2-17: Averaging techniques applied to a variable φ: a) time averaging and b) volume averaging inside the representative elementary volume REV.

By applying the time and volume averaging techniques to the governing equations (Navier Stokes equations - NS) a new set of unknowns are introduced such as the turbulent stresses and turbulent fluxes, therefore, additional equations to model these unknowns are needed: for the time averaging technique the introduced unknowns are modelled through the turbulent models, while for the volume averaging the Darcy-Forchheimer equation is used.

The classification of the turbulence models in order of increasing complexity is: i) First Order Models (Zero-, One- and Two-Equation Models) and ii) Second Order Models (Algebraic Stress Models and Reynolds Stress Models). Particularly the Two-Equation models (e.g., k-ε, k-ω, SST models) are widely used due to the simplicity of implementation if compared to second order models and are able to model the turbulent kinetic energy (*k*) and the rate of energy dissipation. Further classifications of turbulence models may be found based on the scale for modelling the turbulence: i) RAS (Reynolds Averaged Simulation) which uses averaged form of the governing equations for turbulence, ii) LES (Large Eddy Simulation) solve the large turbulent structures in the flow while modelling the small eddies, iii) DES (Detached eddy simulation) is a hybrid method between RAS and LES models and iv) DNS (Direct numerical simulation) resolves all scales of turbulence by solving directly the NS equations (OpenFOAM (2013)).

Flow in porous media is described by Darcy-Forchheimer equation. It is used in the volume averaging technique as a basis for the numerical modelling of the flow in porous media. On the other hand, Terzaghi's principle is fundamental for the analysis of soil stresses and the development of pore pressure in porous media. Moreover, wave-induced transient and residual pore pressures have been recognized as key parameters for the stability analysis due to their close relation with soil deformations and soil liquefaction. Several studies have been conducted to understand the processes related to liquefaction and soil response due to wave-induced loads particularly for porous sea beds, while a small amount of analysis have been conducted with PBA-revetments. Therefore, for a comprehensive analysis of the response of a PBA-revetment and its soil foundation due to wave-induced loads, it is required to account for the basics of flow in porous media, soil stresses and pore pressures development as well as the assumptions commonly considered for its numerical modelling such as the volume and the time averaging of the Navier Stokes equations.

2.4 Numerical modelling

Numerical models are based on the resolution of the mathematical expressions that describe the physical process by replacing them with numbers and evaluating in space and/or time the variables involved in order to define (through iterative processes) the final numerical description of all variables that satisfy the equations. In this sense, numerical modelling is used to model systems for which simple closed analytical solutions are not available. In the case of modelling the physical processes of fluid mechanics, specific numerical methods algorithms and governing equations are available to reproduce and analyse problems that involve fluid flows and are normally called Computational Fluid Dynamics (CFD). Furthermore, computational methods capable to reproduce soil-pore fluid interaction have also been developed and are normally known as Computational Soil Dynamics (CSD).

For this purpose, in the present section a review of the numerical modelling with CFD and CSD for coastal engineering applications is performed. Moreover, a brief description and comparison between available numerical models for wave-structure interaction is addressed.

2.4.1 CFD and CSD numerical modelling

a) CFD numerical modelling

First works on CFD solutions appeared during 1950's and 60's as an attempt to solve the high velocity and temperature re-entry problem (Anderson et al. (2009)). A second generation of CFD solutions appeared at mid of the 1960's, when the full Navier-Stokes equations (NS) were numerically solved at Los Alamos National Labs for modelling a 2-D swirling flow around an object (Harlow & Welch (1965)). However, the introduction of the time averaging technique provided an important advance on the CFD solutions, making practical the use of this tool for several applications (Anderson et al. (2009)).

CFD numerical models based on solutions of the NS equations can provide accurate and detailed solutions of the wave-structure interaction. The NS equations are a set of non-linear partial differential equations that can describe fluid motions that in addition to the free surface boundary conditions are, in principle, the basic mathematical expressions that can model water wave motions (Liu & Losada (2002)).

Several numerical models are based on the solution of these equations but assumptions and considerations are normally implemented to simplify the NS equations (e.g., time and volume averaging techniques). The Reynolds Averaged Navier Stokes equations (RANS), the Volume-Averaged RANS equations (VARANS) are some of the set of equations derived by simplification of the original NS equations in order to solve practical problems.

For instance, the RANS equations are normally used to analyse wave motion and wave-structure interactions with great detail and accuracy by applying the time averaging technique to the NS equations based on the -Reynolds decomposition proposed by Osborne Reynolds in 1894. This decomposition allows the separation of the time -averaged and -fluctuating quantities: the time averaged quantities are calculated directly through the set of equations, while the fluctuating component is modelled by the turbulence models as closure of the RANS equations. The derivation of the RANS equations can be made by two different averaging processes: i) through the Reynolds decomposition (time averaging, s. section 2.3.3) and ii) by using a mass-weighted averaging suggested by Favre (1965). The two averaging conditions lead to the same RANS equations when fluctuations on the fluid density can be neglected (Tannehill et al. (1997)).

The application of the RANS equations for modelling the wave structure interaction has been developed by several authors during the last decades, mainly due to a higher qualitative and quantitative description of the hydrodynamics conditions developed close to a structure, particularly under wave-breaking conditions (Lara & Losada (2006)). The capability of the RANS has been tested in numerical models with impermeable structures (i.e. Kobayashi et al. (1992); Lin & Liu (1998); Li et al. (2004)).

The VARANS equations are a derivation based on the RANS equations to include the effects of porous media into flow motion applying for this purpose the volume averaging technique which considers that the properties inside a REV (representative element of volume) can be separated into averaged and fluctuations quantities. Under this consideration, time- and volume- averaging results in the VARANS equations and numerical simulations considering porous media and permeable structures could be made. The Darcy-Forchheimer equation (eq. (2.36)) is normally used to represent the closure of the VARANS. The derivation of the VARANS equations leads to two different approaches: i) through time- and volume-averaging of the NS equations (s. Liu et al. (1999); Hsu et al. (2002); del Jesús Peñil (2011)); ii) through volume- and then a time- averaging of the NS equations (s. de Lemos & Pedras (2001)). For a rigid medium, the volume of fluid is dependent on space and not in time if the time interval for all REV's is the same and thus, the order of application of the averaging operators can commute (de Lemos & Pedras (2001)).

In addition to the RANS/VARANS equations, the definition of the location of the water free surface should be determined in order to model wave-structure interactions. For this purpose, Eulerian methods such as the Volume of Fluid technique (VOF) or the level set methods are normally implemented in CFD simulations. These methods work with a fixed grid that remains constant during the numerical computation allowing in certain cases topological changes. Furthermore, robustness is achieved for large deformations of the free surface since the movement of the free surface is independent of the mesh cell locations. These features of the Eularian methods constitute the major advantage over Lagrangian methods since computational costs reductions are achieved due to the no calculation of the mesh at each time step (s. Sethian (1999)). Particularly the VOF method is used for several numerical models for wave-structure interaction simulation as well as CFD codes (Prosperetti & Tryggvason (2009)). Therefore, these models and codes are able to track the free-surface (i.e. ODIFLOCS (van Gent (1994)), VOFbreak (Troch (1997)), COBRAS-UC (Lin & Liu (1999)) Flow3D (Hirt (2012)), and moreover, to simulate multiphase flows with two or more fluids (i.e. OpenFOAM (2013)).

b) CSD numerical modelling

Most of the applications of soil dynamics are focused among others on machine foundations, earthquake engineering, pile driving, wave-loading on offshore structures, dynamic and vibratory compaction (Whitman (2000)). These applications have in common that (Dobry (2014)): i) the loads tend to act much faster than in typical soil mechanics problems, ii) the loads change direction periodically because they are associated to vibrations and ii) most of the problems are related with small shear strains in the soil.

Therefore, the computational soil dynamics represents an essential tool for dealing with soil dynamics and also with soil-pore fluid interactions. The governing equations applied for modelling this interaction are the Biot's equations (Biot (1956)) proposed for partly saturated soil based on the displacement of the soil and the fluid. These equations constitute the basis for CSD numerical modelling (Zienkiewicz & Chan (1988)) and provide a complete and general description of the mechanical behaviour of a pore-elastic medium based on the Navier-Stokes equations and on Darcy's Law.

Additionally to the governing equations, constitutive models are required an which may have a significant influence on numerical results (Liu et al. (2005)). These constitutive models have been developed for the simulation of elasto-plastic characterization of soil and the stress-strain relationship and several classes are distinguish among others: i) elastic (stresses are linearly proportional to strains), ii) plastic (non-linear stress-strain relationship), iii) visco elastic (they exhibit a time-dependent strain rate).

Numerical analysis of soil dynamics has experienced a constant progress in latest decades on specialized software capable of simulating complex problems where fluid-structure-soil interaction occurs (Lai (2013)). Most of the focus is made for earthquake engineering, landslides or dam analysis, however, as already mentioned the application of the governing equations and constitutive models can be extended to coastal engineering purposes for wave-structure-soil interaction under wave-induced loading conditions.

2.4.2 Available numerical models for wave-structure interaction based on RANS and VARANS equations

Considerable number of numerical models for CFD simulations based on the RANS and the VARANS equations are available. Most of the CFD models for coastal engineering applications are based on RANS-VOF equations and differences arouse as a consequence of the modelling of closure terms or in the techniques applied to finally solve the RANS equations such as the volume averaging or the numerical schemes used. On the other hand, VARANS-VOF numerical models have been investigated in the last decade for the simulation of the wave-structure interaction, e.g. COBRAS-UC, IH-3VOF, VOFbreak, 2D-HYDROTUR. Furthermore, numerical simulations have been performed in order to analyze and reproduce different wave-structure interactions such as wave and low-crested structures interaction (i.e.García et al. (2004), Losada et al. (1996)); wave shoaling and breaking on gravel slopes (Lara et al. (2006), Higuera et al. (2013a)); wave interaction of rubble mound breakwaters (Troch et al. (2002); Losada et al. (2008)).

Thus, a brief overview of selected available CFD and CSD numerical models is herein presented:

- ***COBRAS, COBRAS-UC and PORO-WSSI II***

  COBRAS (COrnell BReaking waves And Structures) is a 2-dimensional numerical RANS-VOF model based in the code RIPPLE (originally developed by Los Alamos National Laboratory and the NASA) which was developed and modified by Prof. Philip Liu (from the Cornell University) capable to describe the flow inside and outside of coastal structures including permeable layers. The calculations are based on the "finite differences" method and the use of a "source function" is described in Lin & Liu (1999) for wave generation considering Stokes waves theory. An updated version of COBRAS (called COBRAS-UC) was then developed at the University of Cantabria in order to provide a tool that can be easily used for practical application. Hsu et al. (2002) introduced an improvement in the model by implementing the VARANS equations into COBRAS-UC, also the extended model included the introduction of a set of volume average k-ε turbulence model equations considering the closure provided by Nakayama & Kuwahara (1999).

  The model PORO-WSSI II has been developed by Zhang et al. (2011). This numerical model, still under development, is based on the VARANS equations as COBRAS does, but it includes a strong coupling between these equations for flow motion and the Biot's poro-elastic theory. With this coupling, the PORO-WSSI II model is capable to correctly model the flow in porous media and to account for the stresses and pore pressures developed in the porous matrix, which cannot be solved alone with the VARANS equations.

- ***OpenFOAM CFD toolbox***

  OpenFOAM (Open Source Field Operation And Management) developed by OpenCFD Ltd. at ESI Group, is a free open source CFD library that has an ensemble of C++ classes in order to solve and simulate specific problems in engineering. It consists of more than 80 solver applications with the capability to solve incompressible, multiphase and compressible flows with the inclusion of turbulence models and also for its interaction with other mesh applications. For coastal engineering problems, 3-dimensional solvers for incompressible and multiphase flows are available using the RANS coupled with a VOF method. Recently, the VARANS equations have been implemented (Alcérreca-Huerta & Oumeraci (2013)) to model flow in porous media in addition to the calculation of stresses and pore pressure by means of the Biot's equations (El Safti & Oumeraci (2012)). Wave generation (Jacobsen et al. (2012)) is possible considering Stokes wave theory, stream function as well as irregular waves with Jonswap and Pierson-Moskowitz spectra. A numerical model based on the OpenFOAM framework for coastal engineering applications is IH-FOAM developed by the University of Cantabria (IH-Cantabria (2012)) which also include simulations with porous structures (Higuera et al. (2014)).

- ***IH-3VOF***

  IH-3VOF (del Jesús Peñil (2011)) is a 3-dimensional model based on the numerical method TRUCHAS developed in Los Alamos National Laboratory. For the representation of the porous media, the VARANS equations are used. The finite volume method (FVM) is implemented and therefore the momentum, mass and energy are always conserved even that variables may not be continuously differentiable (Eymard et al. (2003)). IH-3VOF is capable to support structured and unstructured meshes. Parallel computation techniques are applicable to the model in order to speed-up calculations

- ***ANSYS***

  ANSYS,Inc. provides CFD software ANSYS Fluent that can be integrated to other applications such as ANSYS Workbench to provide connection with CAD systems or with applications for mesh generation such as ANSYS Meshing (ANSYS (2014)). Normally the application of this software package is used for turbo-machinery problems, but it has not been extended for other applications such as the coastal engineering. Moreover, ANSYS provide a CSD software (CivilFEM with ANSYS) based on finite element for soil mechanics analysis with inclusion of the soil-fluid interaction.

- ***ComFLOW***

  ComFLOW is a 3-dimensional CFD numerical model designed for offshore and coastal protection developed by the Maritime Research Institute Netherlands (MARIN). The basic objective of ComFLOW is the prediction of hydrodynamic loads over structures considering compressible two-phase flow and the possibility of including moving bodies. Validations of the software have been performed considering dam-break experiments, simulations of snore tension-leg platforms, sloshing tanks (MARIN (2013)).

A comparison of the aforementioned numerical models for CFD simulation is shown in Table 2-7. As observed, several CFD software is available but it is limited in its extension or capabilities to solve coastal engineering problems or, on the other hand, it does not provide the interaction with porous media. Several of the previous mentioned CFD packages are commercial, so no changes can be performed inside the codes in order to fulfil the desired requirements. Therefore, open source CFD models are a suitable as a good alternative to enhance the available capabilities for the numerical simulation of different coastal engineering problems.

Table 2-7: Comparison of available numerical models for CFD simulations.

Numerical model	***Dimensionality***	***Development***	***Open source***	***Fluid phases***	***Governing equations***	***Inclusion***		***Validations***
						Porous media	Wave generation	
COBRAS/ COBRAS-UC	2D	Cornell/Cantabria University based on the code RIPPLE	No	1	RANS/ VARANS	No/ Yes	Yes	Simulation of break
PORO-WSSI II	?	Based on COBRAS and a geotechnical model	No	1	VARANS+ Biot's eqs.	Yes	Yes	Submerged permeable breakwater
OpenFOAM	3D	Developed by ESI Group (ensemble of C++ classes for CFD)	Yes	2	VARANS+ Biot's eqs.	Yes	Yes	Dam-break, wave-structure interactions
IH-3VOF	3D	Based on TRUCHAS	?	1	VARANS	Yes	Yes	Dam-break, wave-structure interactions
ANSYS	3D	Developed by ANSYS, Inc.	No	≥2	?	Yes	No	Applications by the industry in several fields.
ComFLOW	3D	Developed by MARIN	No	2	RANS	No	Yes	Dam-break, snore tension-leg platforms, sloshing tanks

As shown in Table 2.7, the OpenFOAM toolbox, possibly with PORO-WSSI II, represents an alternative that considers the implementation of the 3-dimensional VARANS and Biot's equations for the correct simulation of the hydrodynamic and hydro-geotechnical processes, respectively. The access to the free open source code from OpenFOAM provides an enormous advantage over other available software, so that improvements/modifications can be performed straightforward. In addition, the developed codes can be further extended considering the available solvers already implemented in OpenFOAM or those developed by different users. The latter aspect is particularly important as the community of OpenFOAM users has considerably increased in the last years and is continuing to increase. Moreover, the ensemble of C++ classes provides a code structure than can be easily controlled for focusing into those classes that needs to be improved/modified/enhanced.

Nowadays, the predictions and results provided by CFD/CSD tools are accepted and in some cases comparable to the results obtained from theoretical or experimental studies. The simulation of the wave-structure interaction considering porous VARANS-VOF and RANS-VOF models have the key advantage of reproducing the physical processes involved in the wave-structure interaction with high degree of detail and accuracy within an acceptable amount of time and computational costs. However, for the proper simulation of the soil dynamics, the Biot's equations together with the constitutive models should be considered in addition to the CFD models; thus a CFD-CSD model system is required for wave-structure-soil interactions.

OpenFOAM, ANSYS and PORO-WSSI II are among the available numerical models which are capable to perform both CFD and CSD simulations. Among these models, OpenFOAM is considered most appropriate for the numerical modelling of waves interacting with PBA-revetments and their soil foundation because it is an open source toolbox with full access to the source codes thus allowing modifications/improvements/extensions of the different modules to correctly simulate the wave-structure interaction.

2.5 Summary and implications for the PhD study

From the current knowledge review several conclusions are drawn for the PhD thesis. The interaction with porous and permeable structures is still not fully understood especially for PBA-revetments. The effects of the porous structure on processes such as wave breaking and wave reflection has been identified in several studies, however, their interaction with other processes such as the wave-induced loads has not been investigated in depth. The wave run-up, run-down and the wave set-up in front of a structure are normally analysed together, and recent studies on PBA-revetments (Foyer (2013)) showed that analysing them separately represents a better approach to understand these processes and their interaction.

The analysis of wave-induced loads has been reviewed in the literature for different structures. Features of the pressure signals considering also aeration during the wave-impact have been investigated. However, knowledge gaps are identified when analysing the pressure distribution on revetments, especially regarding the effects that the porous revetment structure may induce on the development of the pressure distribution. Moreover, approaches for the analysis of the wave-induced pore pressures developed inside porous media are based on results from the analysis of porous sea beds and their application for porous revetments has not been verified. Large-scale laboratory tests by Oumeraci et al. (2010) determined the pore pressures beneath revetments, but limitations and shortcomings are found when considering different revetment slopes or revetment-filter thicknesses. Therefore, a detailed description of the pressure distribution on and beneath PBA-revetments is required. Furthermore, the stability of PBA-revetments under wave-induced loads should be considered based on the development of pore pressure in the embankment subsoil.

The flow in porous media is based on Darcy-Forchheimer equation which has been used for the development of numerical models. For this purpose, several numerical models are available for the simulation of wave-structure interaction with porous media and its selection is dependent on its specific applicability. Thus, for a detailed analysis of the processes on and in PBA-revetments (e.g., wave breaking, wave reflection, wave run-up/down, wave set-up/down and wave-induced pressures), the numerical models based on solutions of the Navier-Stokes are necessarily required. From the available numerical models, those that include the use of the VARANS equations in combination to theory of elasticity or Biot's equations are more suitable for the numerical modelling of PBA-revetments and especially for the analysis of wave-induced pore pressures developed on and beneath the revetments. Therefore, the OpenFOAM CFD toolbox is considered in the present study since it is a 3-dimensional open-source software capable to perform the modelling of PBA-revetments as well as to reproduce properly wave-structure interactions.

2.6 Specification of objectives and methodology

The tentative objectives and methodology for the PhD research are defined in Section 1.3. Based on the state of the art review results, the specification of objectives and the methodology is presented in this section

2.6.1 Specification of objectives

(i) Development of a new CFD-CSD numerical model system to simulate the hydrodynamic and hydro-geotechnical processes in the wave-structure-subsoil interaction for PBA-revetments and their sand foundation:

- Identification of capabilities and limitations of the CFD/CSD numerical models available for wave-structure-subsoil simulation (e.g., wave generation methods, consideration of flow in porous media, assessment of pore pressures).
- Identification of shortcomings in previous studies with the numerical modelling of wave-structure-subsoil interaction, particularly those related to wave-induced pressures on PBA-revetments and wave-induced pore-pressures in the soil foundation.
- Improvement/extension/modification of the best available numerical codes for the numerical simulation of the wave-structure-subsoil.

(ii) Systematic validation of the CFD-CSD model system.

- Calibration of the empirical-defined parameters of the CFD-CSD model system and analysis of their influence for the simulation of PBA-revetments.
- Systematic validation with large- and small- scale laboratory tests with PBA-revetments using the data form GWK tests (Oumeraci et al. (2010)) and LWI tests (Liebisch & Oumeraci (2012)), respectively.

(iii) Comprehensive and systematic parameter study based on numerical simulations to extend the results from GWK tests and by Foyer (2013).

- Extension of the tested conditions from previous studies and overcome shortcomings reported on them.
- Definition of a test programme and performance of a systematic parameter study considering different wave conditions (i.e., wave height, wave period) and PBA-revetment configurations (i.e., slope steepness, revetment-filter thicknesses).

(iv) Development of simple semi-analytical formulae for the description of the hydrodynamic and hydro-geotechnical processes which can be applied for the stability analysis of PBA-revetments and their sand foundation.

- Systematic and comprehensive analysis of the hydrodynamic and hydro-geotechnical processes: a) processes on and in front PBA-revetments, b) wave-induced pressures on and beneath PBA-revetments.
- Development of prediction formulae for the aforementioned processes.

- Development of a process-based approach for the assessment of the stability of PBA-revetments and their sand foundation.

2.6.2 Specification of the methodology

The phases for the methodology for this research are illustrated in Fig. 2-18 and the phases are described as follows:

(i) In Phase I, a comprehensive analysis of the current knowledge is conducted with the aim to identify knowledge gaps, missing data and other limitations described in the literature. This phase also includes the analysis of the datasets of GWK tests with PBA-revetments as a basis for the understanding of the hydrodynamic and hydro-geotechnical processes. In addition, the capabilities and limitations of available numerical models are analysed for the simulation of the wave-structure-subsoil interaction.

(ii) Phase II is focused on the development of a new CFD-CSD numerical model based on the improvement/modification/extension of available numerical codes. For this purpose, the implementation of the VARANS-VOF equations in the CFD model and weakly coupling with the CSD model are performed. The later allows the proper simulation of the hydrodynamic and hydro-geotechnical processes in the wave interaction with PBA-revetments and their soil foundation. Validation of the new CFD-CSD model system is conducted considering the large- scale GWK tests (Oumeraci et al. (2010)) and the small-scale tests at LWI (Liebisch & Oumeraci (2012)).With the validated CFD-CSD model, a very systematic parameter study is performed in order to extend the results provided by the large-scale tests from GWK and those by Foyer (2013).

(iii) In Phase III, a comprehensive analysis of the results from the parameter study is conducted: processes on and in front of PBA-revetments and wave-induced pressures. Moreover, the development of a stability analysis of PBA-revetments against soil liquefaction is proposed.

(iv) In Phase IV, the key results are summarized and concluding remarks are drawn.

All these phases have been performed and are documented in several progress reports (Alcérreca-Huerta & Oumeraci (2012); Alcérreca-Huerta & Oumeraci (2013); Alcérreca-Huerta & Oumeraci (2014)). The overall results will be presented in this thesis: a) Phases I and II are described in Chapter 2 and Chapter 3, respectively, b) Phase III is described in Chapter 4 for those processes on and in front of PBA-revetments (mean water level, wave run-up/down, wave set-up, wave reflection), in Chapter 5 for the wave-induced pressures on and beneath PBA-revetments and in Chapter 6 for the stability analysis of PBA-revetments. The summary, discussion and concluding remarks (Phase IV) are addressed in Chapter 7.

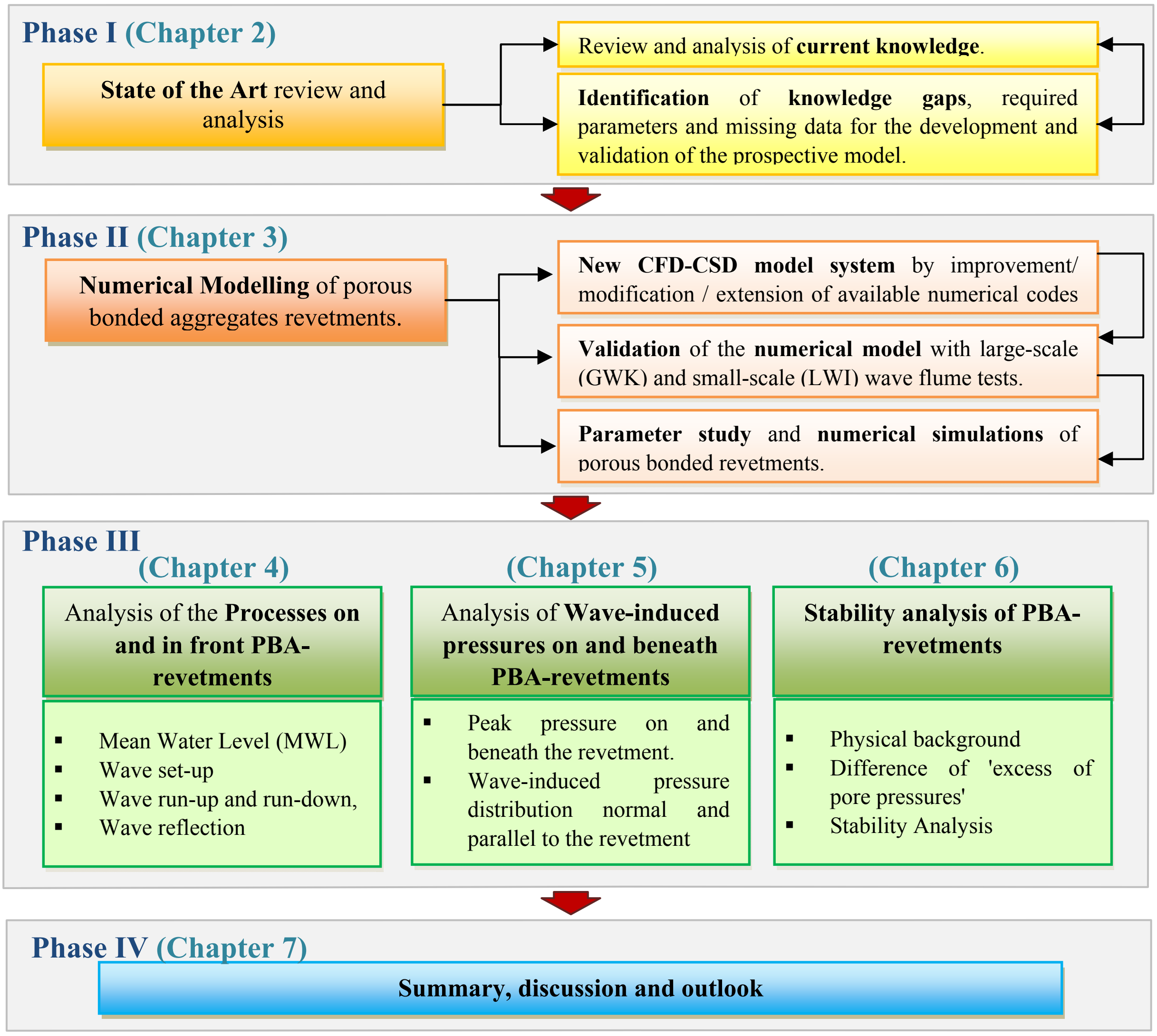

Phase I (Chapter 2)

State of the Art review and analysis

Review and analysis of **current knowledge**.

Identification of **knowledge gaps**, required parameters and missing data for the development and validation of the prospective model.

Phase II (Chapter 3)

Numerical Modelling of porous bonded aggregates revetments.

New CFD-CSD model system by improvement/ modification / extension of available numerical codes

Validation of the **numerical model** with large-scale (GWK) and small-scale (LWI) wave flume tests.

Parameter study and **numerical simulations** of porous bonded revetments.

Phase III

(Chapter 4)

Analysis of the **Processes on and in front PBA-revetments**

- Mean Water Level (MWL)
- Wave set-up
- Wave run-up and run-down,
- Wave reflection

(Chapter 5)

Analysis of **Wave-induced pressures on and beneath PBA-revetments**

- Peak pressure on and beneath the revetment.
- Wave-induced pressure distribution normal and parallel to the revetment

(Chapter 6)

Stability analysis of PBA-revetments

- Physical background
- Difference of 'excess of pore pressures'
- Stability Analysis

Phase IV (Chapter 7)

Summary, discussion and outlook

Fig. 2-18: Methodology of the PhD study and organisation structure of the thesis.

3 Implementation, validation and application of the new CFD-CSD model `"wavePoreGeoFoam"` for a parameter study

A new 3-dimensional CFD-CSD model system `"wavePoreGeoFoam"` was developed at the Leichtweiß-Institute (LWI) within the OpenFOAM® framework. For this purpose, the developed CFD solver `"wavePorousFoam"` (Alcérreca-Huerta & Oumeraci (2013)) and the developed CSD solver `"geotechFoam"` (El Safti & Oumeraci (2013)) were coupled (one-way coupling) in the numerical model system in order to simulate flow, stresses and pore pressure in porous media including wave-generation/absorption. The CFD solver was developed considering the implementation of the VARANS equations with inclusion of the VOF method for tracking the free surface elevation. It is able to handle two-fluid phases (water and air) and to explicitly define the location of several porous regions with different properties (i.e. d_{50}, porosity). On the other hand, the fully dynamic Biot's equations coupled with Darcy's law were implemented in the CSD solver which allows the determination of soil stresses as well as pore pressures inside the porous regions.

Therefore, in this chapter, a brief overview of the OpenFOAM framework is firstly presented. Second, the CFD and CSD governing equations used for the numerical modelling of PBA-revetments are reviewed. Third, validation of the weakly coupled CFD-CSD system `"wavePoreGeoFoam"` is described considering large-scale laboratory tests in GWK and small-scale model tests with PBA-revetments in the LWI wave flume. Fourth, a sensitivity analysis relative to the effect of the parameters empirically defined for `"wavePoreGeoFoam"` on the results of the numerical simulations with PBA-revetments is shown. Fifth, the model setup and the test programme for the parameter study conducted to enhance the understanding of the processes involved in the wave-structure-subsoil interaction for PBA-revetments is described. Finally, a summary of the results and their implications for the present study are provided.

3.1 OpenFOAM framework

As already mentioned in Section 2.4.2, OpenFOAM was developed by OpenCFD Ltd. at ESI Group. Its advantage over other numerical models is that it consists in a free open source library of C++ classes for which the user can have complete access to improve/modify/enhance the current codes. For the use of OpenFOAM in coastal engineering problems, solvers for incompressible and multiphase flows are available using the RANS equations coupled with a VOF method (`"interFoam"` solver). Furthermore, for the solution of flow in porous media a solver (named `"porousInterFoam"`) is already available. However shortcomings have been reported by Alcérreca-Huerta & Oumeraci (2013) and Higuera et al. (2014) which are especially related to: i) the incorrect inclusion of the VARANS equations and ii) the consideration of the total cell volume (V) instead of the volume that can actually be filled by the fluids within the porous media (V_v= volume of voids).

For wave generation/absorption within the numerical modelling with OpenFOAM three different alternatives are provided:

i. The "`groovyBC`" utility (for OpenFOAM v2.0 or higher, it is included in "`swak4Foam`") is based on the generation of a boundary condition where the gradients of the variables are specified as functions instead of fields, so it can set the initial conditions at each time step at this boundary which will be propagated to the computational domain.

ii. The "`waves2Foam`" library includes a wave generation/absorption method based on relaxation zones where an explicit relaxation technique is performed before the momentum equation is solved as follows: $U=(1-\omega)U_{target}+\omega\cdot U_{computed}$ and $\alpha=(1-\omega)\alpha_{target}+\omega\cdot\alpha_{computed}$ where $\omega\in[0,1]$ is a weighting function; U_{target} and α_{target} are the desired velocity and water content in a cell at the boundary, respectively, (e.g., incident wave height/period), while $U_{computed}$ and $\alpha_{computed}$ are the velocity and water content in a cell as calculated by the momentum and continuity equations. This method was implemented in OpenFOAM by Jacobsen et al. (2012) and it includes the wave generation and absorption of several wave types: 1st-, 2nd-, and 5th- order Stokes waves; stream function, solitary and 1st order cnoidal waves in addition to irregular waves based on Jonswap and Pierson-Moskowitz spectra.

iii. The wave generation is combined with active absorption and no relaxation zones are needed. This method was implemented by Higuera et al. (2013b) and the wave generation consists in a boundary condition based on analytical expressions of wave theories, while wave absorption is implemented by modifying the boundary condition considering the measurement of the velocity and water elevation fields of the reflected wave (feedback) so that the boundary generates the target incident wave. This approach is closer to the wave generation/absorption as implemented in laboratory wave flumes and wave basins. The wave types implemented with this method are: 1st-, 2nd-, and 5th- order Stokes waves; stream function; Boussinesq solitary wave, irregular waves and piston-type wave maker.

For the mesh generation, OpenFOAM includes the "`blockMesh`" utility which can provide structured meshes. It also allows the generation of "sub-meshes" with different cell size with consideration of the ratio cell size between adjacent "sub-meshes". Moreover, very complex geometries can be handled by the utility "`snappyHexMesh`" supplied with OpenFOAM which automatically generates 3-dimensional meshes containing hexahedra (hex) and split-hexahedra (split-hex) from triangulated surface geometries in Stereolithography (STL) format (OpenFOAM (2013)). Furthermore, mesh applications are available that are compatible with OpenFOAM such as Gmsh (Gezuine & Remacle (2009)) and for meshes generated for ANSYS CFX (ANSYS (2014)).

Also, for turbulence modelling several alternatives are already implemented and supplied by OpenFOAM: more than 15 models of RAS type (Reynolds Average Simulation: e.g., k-ε, k-ω, SST); more than 18 models of LES type (Large Eddy Simulation) and ~2 of DES type (Dettached Eddy Simulation). The reader is referred to OpenFOAM (2013) for further details in the available turbulence model already implemented and description of the models can be reviewed in the literature (e.g., Wilcox (2006); Baumert et al. (2011)).

OpenFOAM is thus a CFD toolbox suitable for numerical modelling of wide range of applications in coastal engineering due its capabilities for wave generation/absorption, mesh manipulation and turbulence modelling. However, limitations have been mentioned for the simulation of flow in porous media and thus corrections to the CFD governing equations (s. Section 3.2) are needed. Moreover, coupling with a CSD model (s. Section 3.3) is required for the proper simulation of the wave-structure-subsoil interaction. The latter has motivated the generation of a new CFD-CSD model system named "`wavePoreGeoFoam`" based on the OpenFOAM framework.

3.2 Governing equations for the CFD model

The governing equations defined for the numerical modelling of flow in porous media are the VARANS equations which include the continuity and the momentum balance equations (see Sections 3.2.1 and 3.2.2). These equations result from the integration of the RANS equation over a representative element of volume (REV) larger than the pore structure but smaller than the characteristic length of the flow. The Reynolds decomposition is applied over the RANS, so a variable is decomposed into an average and a spatial fluctuation. For a general fluid property φ, the intrinsic $\langle\varphi\rangle^i$ and the volumetric averages $\langle\varphi\rangle^f$ are related through the porosity n (Bear (1972)):

$$\langle\varphi\rangle^{i}=\frac{1}{\Delta V_{f}}\int_{\Delta V_{f}}\varphi dV,\qquad \langle\varphi\rangle^{f}=n\langle\varphi\rangle^{i},\qquad n=\frac{\Delta V_{f}}{\Delta V} \tag{3.1}$$

where ΔV is the volume of the REV and ΔV_f is the volume that can be filled by the fluid (volume of voids).

The VARANS equations can have different terms depending on the approach. Hsu et al. (2002) derived a set of equations that has been reference for more than 10 years (Higuera et al. (2014)) and recently, a new set of VARANS equations has been suggested by del Jesús Peñil (2011). However, discrepancies of del Jesús approach with previous works of Hsu and de Lemos & Pedras (2001) have been pointed out by Bjarne et al. (2014) especially related to: i) the continuity equation which in del Jesús Peñil (2011) was based on the intrinsic (pore) velocity as $\nabla\cdot\langle U\rangle^{i}=\nabla\cdot U/n=0$ and do not provide a correct physical representation as in Hsu's approach where $\nabla\cdot U=0$ and ii) the pressure gradient in the momentum equation is affected by the porosity in del Jesús approach leading to larger pressures inside the porous media. Further details on the differences between Hsu's and del Jesús' approaches are exemplarily described in Bjarne et al. (2014) considering stationary flux through a porous system for difference (i) and stationary water on a domain with clear fluid region and a porous media region for difference (ii).

Therefore, the implementation of the VARANS equations in the new numerical model "`wavePoreGeoFoam`" is based on the approach provided by Hsu et al. (2002). As a remark, these equations are not implemented in "`porousInterFoam`" (native solver in OpenFOAM for solving porous media) which just includes the effect of porous media by adding the Darcy-

Forchheimer equation in the momentum equation but without considering the effect of the porosity in the continuity equation as well as in the advection and convection terms of the momentum equation. Thus, the modifications/improvements were introduced to properly account for the VARANS equations in the model.

3.2.1 The continuity equation and the VOF method

The continuity equation is one of the governing equations within the set of VARANS equations. For the case of unsteady, incompressible, viscous and immiscible two-phase flow the continuity equation is given by:

$$\nabla \cdot U = 0 \tag{3.2}$$

In order to track the two-phase flow interface, the volume of fluid (VOF) method (eq. (3.3)) is used by OpenFOAM®. A scalar function γ is used to consider the fluid fraction in a computational cell. The values of γ range from 1 to 0, where a cell fully filled by one of the fluids (phase 1) is defined as γ=1, while a cell fully filled with the second fluid (phase 2) is defined as γ=0. Furthermore, in OpenFOAM® the interface between the two phases is compressed by the introduction of an extra artificial compression term in the VOF equation to keep a sharp interface between the phases:

$$\frac{\partial \gamma}{\partial t} + \nabla \cdot (\gamma U) + \nabla \cdot \left(\gamma (1-\gamma) U_r\right) = 0 \tag{3.3}$$

where U_r is a velocity field capable to compress the interface and defined as $U_r = U \cdot \hat{n}$ with $\hat{n}$ being a vector normal to the interface ($\hat{n} = \nabla\gamma$). The term $\partial\gamma/\partial t$ in the VOF equation is active only at the two-phase interface.

The effect of porosity was implemented in order to consider that, e.g.: if the porosity of a cell is 0.35 then only 35% of the cell is available to be filled by the fluids. Therefore, the porosity was included in the solver MULES[1] that mainly works with the VOF technique in OpenFOAM. The later is a very important consideration especially for those porous regions located in a dry-wet zone where the exchange of fluids between the free stream and the porous region is a highly predominant process (i.e. the dry-wet zone of a revetment or a breakwater where wave run-up and run-down take part). Additionally, the density ρ in the cells of the domain is calculated as a weighted average of the densities of the phases according to the volume fraction γ occupied by each phase in a cell:

$$\rho = \gamma \rho_{phase1} + (1-\gamma)\rho_{phase2} \tag{3.4}$$

---

[1] Multidimensional Universal Limiter with Explicit Solution (MULES) solver that supports multiple phases (i.e. air and water) and fields (i.e. the porosity field) while maintaining boundedness of individual phases and their sum using the limitSum functionality (OpenFOAM (2013))

3.2.2 The momentum balance equation

The momentum equation implemented in the new numerical model `wavePoreGeoFoam` developed within OpenFOAM® is slightly different to the one presented by Lin (1998) and Hsu et al. (2002) described in eq. (3.5) for the 2-dimensional VARANS equations:

$$\frac{1}{n}\frac{\partial\rho\langle\overline{U}_i\rangle}{\partial t}+\frac{\rho\langle\overline{U}_j\rangle}{n^2}\frac{\partial\langle\overline{U}_i\rangle}{\partial x_i}=\left[-\frac{\partial\langle\overline{P}\rangle^f}{\partial x_i}+\rho g_i\right]+\frac{1}{n}\left[\frac{\rho\partial\langle\overline{U_i'U_j'}\rangle}{\partial x_j}+\frac{\partial\langle\overline{\tau}_{ij}\rangle}{\partial x_j}\right]-[CT] \tag{3.5}$$

where p is the pressure; g the gravitational acceleration; n the porosity; ρ the weighted average density of the fluids; x the Cartesian coordinate axis, U the velocity and $\bar{\tau}_{ij}$ is the shear stress. Moreover, the term [CT] stands for the closure term that should be modelled and is obtained as consequence of the volume averaging procedure for the VARANS equations. This term is commonly modelled through the Darcy-Forchheimer equation (see Section 2.3.1 as reference). Also, the term $\rho\partial\langle\overline{U_i'U_j'}\rangle/\partial x_j$ on the right side of eq. (3.5) is modelled by the turbulence model. In OpenFOAM® the effects of the turbulence are included through the turbulence viscosity (μ_t), that is later considered in the definition of the effective dynamic viscosity ($\mu_{eff}=\mu_t+\mu_{phase,i}$) as shown in eq. (3.6). Moreover, the convective term in OpenFOAM® is described as $\rho\nabla\cdot(UU)$. Thus, the 3-dimensional momentum equation implemented in "`wavePoreGeoFoam`" is described by eq. (3.6):

$$\rho\left(\frac{1}{n}\frac{\partial U}{\partial t}+\frac{1}{n^2}\nabla(UU)\right)=-\nabla P+g\cdot X\nabla\rho+\frac{1}{n}\nabla\mu_{eff}\nabla U+\sigma\kappa\nabla\gamma-[CT] \tag{3.6}$$

where X is the position vector, P is the dynamic pressure. The extra term $\sigma\kappa\nabla\gamma$ accounts for the surface tension between the two phases (σ=surface tension, γ=volume fraction occupied by each phase and κ is the curvature of the interface $\kappa=\nabla\hat{n}/|\nabla\hat{n}|$) which is not considered in Lin and Hsu's approach, but it is already implemented in OpenFOAM. Finally, the closure term [CT] is modelled as in eq. (3.7) by considering Darcy-Forchheimer equation and the inclusion of the added mass effect described by Polubarinova-Kochina (1962) (PK-term).

$$[CT]=\underbrace{\rho\left(aU+b|U|U\right)}_{Darcy-Forchheimer}+\underbrace{c_A\frac{\partial}{\partial t}\rho U}_{PK-term} \tag{3.7}$$

Coefficients a and b in eq. (3.7) could be defined considering different approaches (see Table 2-6). These coefficients in `wavePoreGeoFoam` are user-defined and the input to the numerical model is described in detailed in Alcérreca-Huerta & Oumeraci (2013). The coefficient c_A is considered through eq. (3.8) with a coefficient γ_A normally taken as 0.34. This coefficient was derived theoretically by van Gent (1993) for stationary and oscillatory flow through coarse porous media.

$$c_A=\frac{1+\gamma_A\dfrac{(1-n)}{n}}{ng} \tag{3.8}$$

Thus, the momentum balance equation of the VARANS implemented in `wavePoreGeoFoam` is described by eq. (3.9).

$$\rho\left(\frac{(1-c_A)}{n}\frac{\partial U}{\partial t}+\frac{1}{n^2}\nabla(UU)\right)=-[\nabla P+g\cdot X\nabla\rho]+\frac{1}{n}\nabla\mu_{eff}\nabla U+\sigma\kappa\nabla\gamma-\rho\left(aU+b|U|U\right) \tag{3.9}$$

For the new CFD-CSD model system `wavePoreGeoFoam`, the VARANS equations based on Hsu et al. (2002) approach were implemented for the simulation of the hydrodynamic processes in porous and non-porous regions. However, for the assessment of pore pressures and soil effective stresses the coupling with the CSD model is still needed.

3.3 Governing equations for the CSD model

The VARANS equations (described in Section 3.2) consider volume averaged properties which in fact consider the solid skeleton and gaps in the porous region as a unique continuous and homogeneous medium. The flow velocity field and the water surface elevation at the porous region can be correctly and accurately calculated by considering the aforementioned assumption, but for the calculation of the pore pressures a CSD model must be used to distinguish between the soil effective stresses taken by the solid skeleton and the pore pressures developed in the pore fluid (Fig. 3-1).

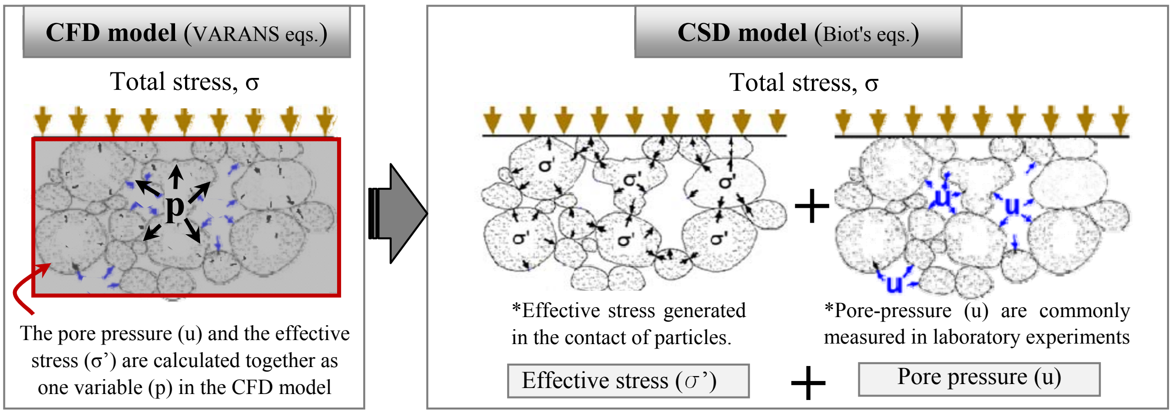

Fig. 3-1: Relationship between CFD model results at the porous structure using VARANS equations (where soil and gaps are considered as a continuum) and the actual pore pressures and effective stresses that are developed in the soil.

As already mentioned, in the CFD-CSD model system `wavePoreGeoFoam`, the CSD solution is based on `geotechFoam` (El Safti & Oumeraci (2013)) which considers the fully dynamic formulation of Biot's theory (Biot (1956)). This theory provides a complete and general description of the mechanical behaviour of a poro-elastic medium based on the Navier-Stokes equations and on Darcy's Law to include the effects of the porous medium in the flow motion for fluid-saturated porous media.

The discretization and implementation of the governing equations are described in detail in El Safti & Oumeraci (2012), El Safti et al. (2012) and El Safti & Oumeraci (2013). Therefore, only a brief summary of the governing equations is provided below.

3.3.1 Mass conservation equation

The mass conservation of the fluid is considered in the Biot's theory as described by the eq. (3.10) (Zienkiewicz et al. (1999)):

$$\nabla\cdot U+\frac{\partial\varepsilon_v}{\partial t}+\frac{1}{Q}\frac{\partial p}{\partial t}=0 \qquad (3.10)$$

where $\varepsilon_v=\mathrm{tr}(\varepsilon)$ is the volumetric strain of the solid matrix with tr(ε) as the trace of the strain tensor ε; U is the average Darcy's velocity vector of the percolating fluid and $Q=K_f/n$, with n as the porosity and [$K_f=\left(S_w/K_w+\left(1-S_w\right)/p_0\right)^{-1}$] as the bulk modulus of the pore fluid, where K_W is the bulk modulus for pure water and S_W is the degree of saturation rate ($S_W=V_W/V_V$, with V_W and V_v as the volume of water and voids, respectively) and p_0 as the absolute zero pore pressure ($\approx 10^5$ Pa under atmospheric pressure).

The mass conservation depends also on the degree of saturation of the porous medium and therefore, the equation is applicable also to partially saturated porous media.

3.3.2 Momentum balance equations

The fully dynamic formulation for the solid-fluid mixture is described in Zienkiewicz et al. (1999) and it is written as in eq. (3.11):

$$\nabla\sigma-\left(n\rho_f+\left(1-n\right)\rho_s\right)\left[\frac{\partial^2\ell}{\partial t^2}+b\right]-\rho_f\left[\frac{\partial U}{\partial t}+U\cdot\nabla U\right]=0 \qquad (3.11)$$

where σ is the total stress tensor, ℓ is the displacement vector, b is the body force per unit mass tensor (i.e. gravity), n is the porosity and ρ_f and ρ_s are the densities of the fluid and the solid particles, respectively.

The total stress can be correlated to displacements by use of the 'constitutive models' and thus, eqs. (3.10) and (3.11) can be solved simultaneously. Moreover, the calculation of the pore pressure (u) and the effective stresses (σ') is performed considering Terzaghi's principle (eq. (3.12)). The effective stresses are calculated based on the relationship between strains and stresses: $d\sigma'=E:d\varepsilon'$ and the strain-displacement relationship based on the assumption of small strains as $\varepsilon=0.5(\nabla\ell+(\nabla\ell)^T)$ where T is the transposition operator.

$$\sigma'=\sigma-u\,I \text{ , with I as the identity matrix} \qquad (3.12)$$

Therefore, the momentum balance equation of the fluid phase considering the solid phase as reference can be described as in eq. ((3.13)),where the sink term R is defined as $R=U\rho_f g/K$

and represents the viscous drag force according to Darcy's seepage law, with K as the isotropic hydraulic conductivity in m/s.

$$U - \nabla u - R - \rho_f \left[\frac{\partial^2 \ell}{\partial t^2} + b \right] - \frac{\rho_f}{n} \left[\frac{\partial U}{\partial t} + U \cdot \nabla U \right] = 0 \tag{3.13}$$

There are simplifications of the fully dynamic formulation, based on different assumptions that lead to new set of governing equations. The CSD solver includes the fully dynamic formulation but also the *u-p approximation* (where the acceleration due to pore fluid is neglected) and an approximation that neglects the pore fluid convective acceleration, also, a poro-elastoplastic approach is implemented (El Safti et al. (2012)).

Overall, the CSD model allows us to differentiate between the soil effective stresses taken by the solid skeleton and the pore pressures developed in the water. The later overcomes the limitation of the VARANS equations in the CFD model where just the effects of the porous structure are considered on the fluid motion. However, both CFD and CSD models are required for the proper simulation of wave-structure-subsoil interaction.

3.4 Model validation with PBA-revetment laboratory tests.

The CFD and CSD solvers ("`wavePorousFoam`" and "`geotechFoam`") have been validated separately and details are described in Alcérreca-Huerta & Oumeraci (2013) and El Safti et al. (2012).

Moreover, validation of the new weakly coupled CFD-CSD model system "`wavePoreGeoFoam`" was conducted especially for the assessment of pore pressure development beneath PBA-revetments. For this purpose, comparison was performed between numerical and experimental results from large-scale tests in GWK (Oumeraci et al. (2010)) and small-scale tests carried out within the DFG-BoPoRe project (Liebisch & Oumeraci (2012)). Thus, in the present section the results of the validation are described and further details are provided in Alcérreca-Huerta & Oumeraci (2013)

3.4.1 Validation with data from large-scale model tests in GWK

Two regular wave tests from the GWK study with PBA-revetments (Oumeraci et al. (2010)) were selected for the validation of "`wavePoreGeoFoam`". The wave conditions of the tests consisted on:

- Test 1: wave height H=0.6 m, wave period T=5.0 s, water depth h=3.7 m. with surf similarity parameter ξ=2.67 corresponding to non-impact wave load condition which allows a straightforward comparison between numerical and experimental results. This tests was used for calibration of the empirical-defined parameters of the numerical model.
- Test 2: wave height H=1.0 m, wave period T=3.0 s, water depth h=3.6 m with a surf similarity parameter ξ=1.25 (impact wave load condition).

The porosity of the revetment, filter and sand core layers as well as the coefficients α and β in Engelund's approach (see Table 2-6) are required by the numerical model for the assessment of the Darcy-Forchheimer equation. Prior calibration of these parameters was needed, however, the final values are within recommendations commonly provided in the literature (e.g., Morris & Johnson (1967), Engelund (1953)). For the particular calibration of the hydraulic permeability, no data was given by the GWK study, and it was found that for the sand core of the PBA-revetment the permeability is depth-dependent and thus it was set to $K=2.9\text{x}10^{-6}$ m/s for a depth $0<d<0.40$m and $K=4.5\text{x}10^{-6}$ m/s for a depth greater than $d>0.40$m.

The wave conditions (e.g., wave height H, wave period T, water depth h), the revetment features (e.g., slope steepness, revetment-thickness) as well as further parameters (e.g., porosity, hydraulic permeability) needed for the numerical setup are summarized in Table 3-1.

Table 3-1: Parameters and variables in the numerical model setup for validation with data from GWK regular wave tests (impact and non-impact load conditions.

Wave conditions Test 1 (non-impact waves, ξ=2.67)	Wave height H=0.6m	Wave period T=5.0s	Water depth h=3.7m		
Wave conditions Test 2 (impact waves, ξ=1.25*)*	Wave height H=1.0m	Wave period T=3.0s	Water depth h=3.6m		
PBA-revetment features	Slope steepness cotα=3 and Revetment-filter thickness d_{rev}=0.15m				
	D_{50} [mm]	ǂ Porosity n [%]	ǂ α_f	ǂ β_f	ǂ Hyd. Permeability K [m/s]
- Revetment parameters	30.0	0.28	1600	3.6	5x10^{-5}
- Sand core parameters	0.34	0.32	660	3.6	Depth 0-0.4m: 2.9x10-6 Depth >0.4m: 4.5x10-6
ǂ Parameter for which calibration was necessary.					

The comparison that is presented in the present section includes only the results for the column C3 of pressure transducers normal to the revetment slope (see Fig. 3-2). However, the systematic validation and comparison are described in Alcérreca-Huerta & Oumeraci (2013), where similar results are shown for the other columns of pressure transducers (C1, C2 and C4).

For the pressures on the revetment (PT05) almost no difference between the numerical simulation and the experimental data can be observed in Fig. 3-2a for non-impact waves. For impact waves (Fig. 3-2b), the differences are observed particularly in the shape of the pressure time series, but the magnitude is well capture. The difference in shape is mostly consequence of the turbulence induced by the plunging breaker which may induce variations even for regular waves in laboratory tests. For the pressure transducers on the revetment, the difference between the maximum peak pressures measured in GWK and those calculated by the numerical model provided a relative error RE≈7.9%. On the other hand, for the pressures inside the porous media (e.g., PT12, 16 and 20), slight differences are observed with a RE lower than 25% (RE<25%). However, these differences are expected particularly for layers deeper in the sand foundation, where the variation of the permeability may affect the magnitude of the pore pressure measured in the location by the pressure transducer. Moreover, calibration of empirical-defined parameters for the numerical model was conducted and thus uncertainties on their definition may induce differences with experimental data. The relative error herein reported considers all pressure transducers at a certain depth placed in the GWK tests and it was calculated as in eq. (3.14) defined also for the calibration and sensitivity analysis of the numerical model (section 3.5).

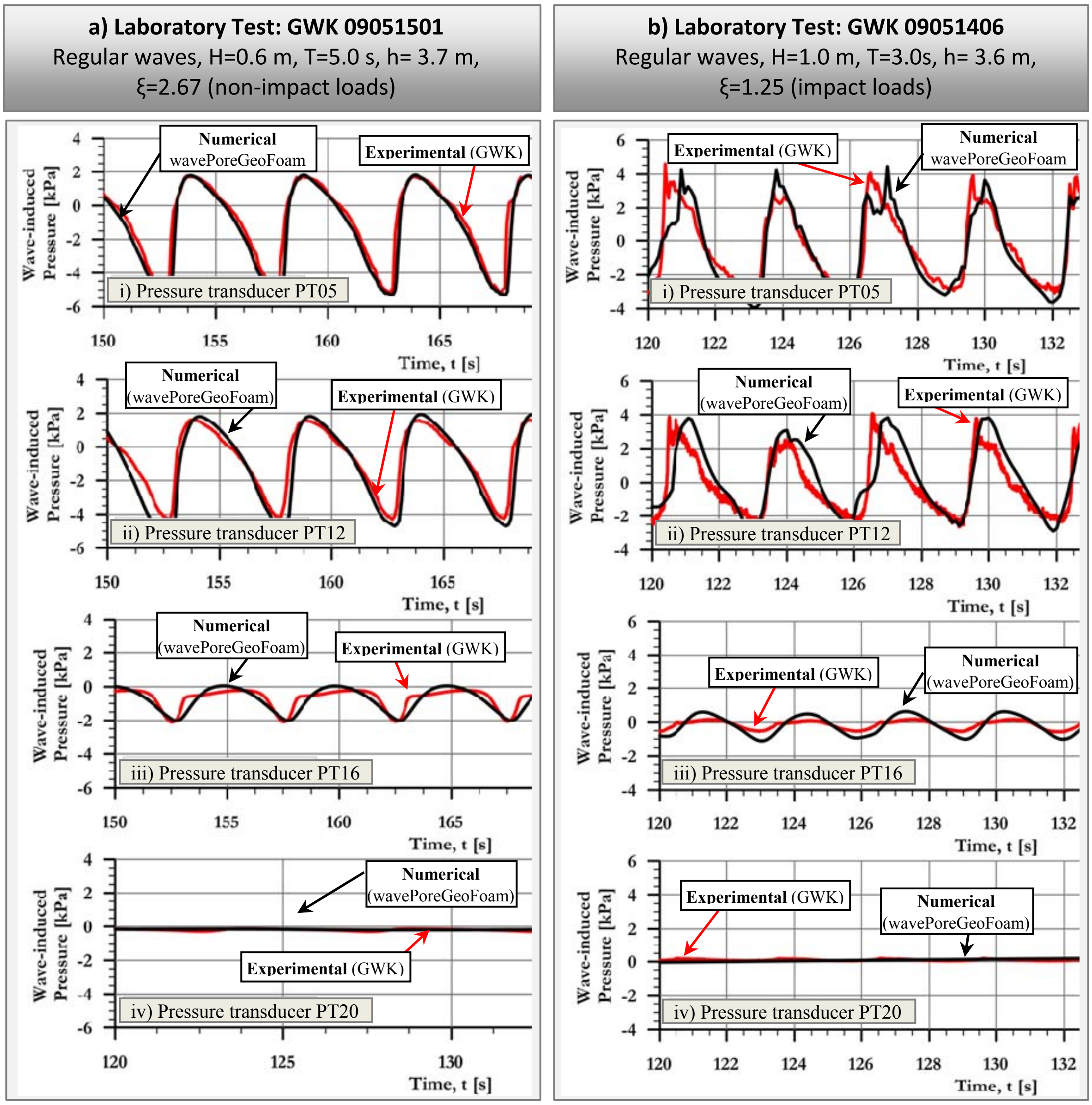

a) Laboratory Test: GWK 09051501
Regular waves, H=0.6 m, T=5.0 s, h= 3.7 m,
ξ=2.67 (non-impact loads)

b) Laboratory Test: GWK 09051406
Regular waves, H=1.0 m, T=3.0s, h= 3.6 m,
ξ=1.25 (impact loads)

PBA-revetment features	D_{50} *[mm]*	*Porosity [%]*	a_f	β_f
- Revetment parameters	30.0	0.28	1600	3.6
- Sand core parameters	0.34	0.32	660	3.6

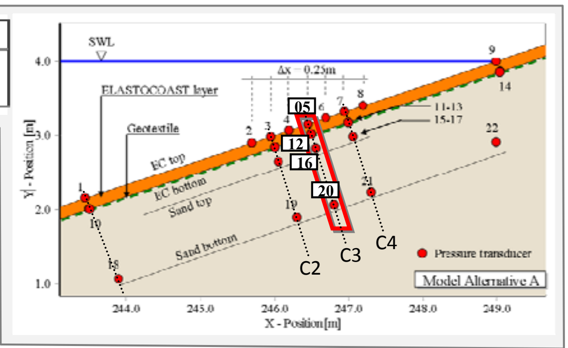

Fig. 3-2: Validation of the new weakly coupled CFD-CSD model "`wavePoreGeoFoam`" for PBA-revetments simulations: experimental data from GWK (Oumeraci et al. (2010)) vs. numerical results.

In general, a relatively good agreement is obtained in terms of shape and magnitude of the pressure time series for the layers underneath the revetment. Also, it was observed during the calibration process of the model setup that the hydraulic permeability is the key parameter to be determined since it has a great influence on the magnitude of the pore pressures and thus on the soil stresses and soil displacements.

3.4.2 Validation with data from small-scale model tests in the LWI wave flume

The validation of the weakly coupled CFD-CSD model "`wavePoreGeoFoam`" with model tests (scaled 1:5 from GWK tests) included two regular waves tests carried out in the LWI wave flume within the frame of the DFG BoPore project (Liebisch & Oumeraci (2012)). Thus, validation is made considering both impact and non-impact wave load conditions:

- Test 1 (non-impact wave loads): wave height H=0.16 m, wave period T=5.0 s, water depth h=0.778 m which results in a surf similarity parameter ξ_0= 5.214.
- Test 2 (impact wave loads): wave height H=0.25 m, wave period T=1.5 s, water depth h=0.578 m leading to a surf similarity parameter ξ_0= 1.355.

The characteristics of the revetment for the selected tests are: revetment slope 1:3, thin porous cover layer (n=22.7%) , gravel (8/16mm) filter layer of 0.05 m thickness and a porosity of about 40%, highly porous geotextile fabric Terrafix® B609, and sand core with a grain size D_{50}=0.14 mm and a porosity of about 35%.

The wave conditions and the revetment characteristics are summarized in Table 3-2. The porosity n, the hydraulic permeability K and the coefficients α_f and β_f of the Darcy-Forchheimer were calibrated for the numerical model setup based on preliminary simulations.

Table 3-2: Parameters and variables in the numerical model setup for validation with data from small-scale model tests in the LWI wave flume.

Wave conditions Test 1 (non-impact waves, ξ=5.21)	Wave height H=0.16m	Wave period, T=5.0s	Water depth, h=0.776m		
Wave conditions Test 1 *(impact waves, ξ=1.36)*	Wave height H=0.25m	Wave period T=1.5s	Water depth h=0.776m		
PBA-revetment features	Slope steepness $\cot\alpha$=3 and revetment-filter thickness d_{rev}=0.057m				
	D_{50} [mm]	ǂ Porosity n [%]	ǂ α_f	ǂ β_f	ǂ Hyd Permeability K [m/s]
- Revetment parameters	---	22.7	1600	3.0	$1.0\text{x}10^{-3}$
- Filter layer parameters	12.00	40.0	1600	3.0	$6.0\text{x}10^{-5}$
- Geotextile parameters	---	95.0	---	---	---
- Sand core parameters	0.14	35.0	780	3.0	$2.4\text{x}10^{-6}$
ǂ Parameters for which calibration was necessary.					

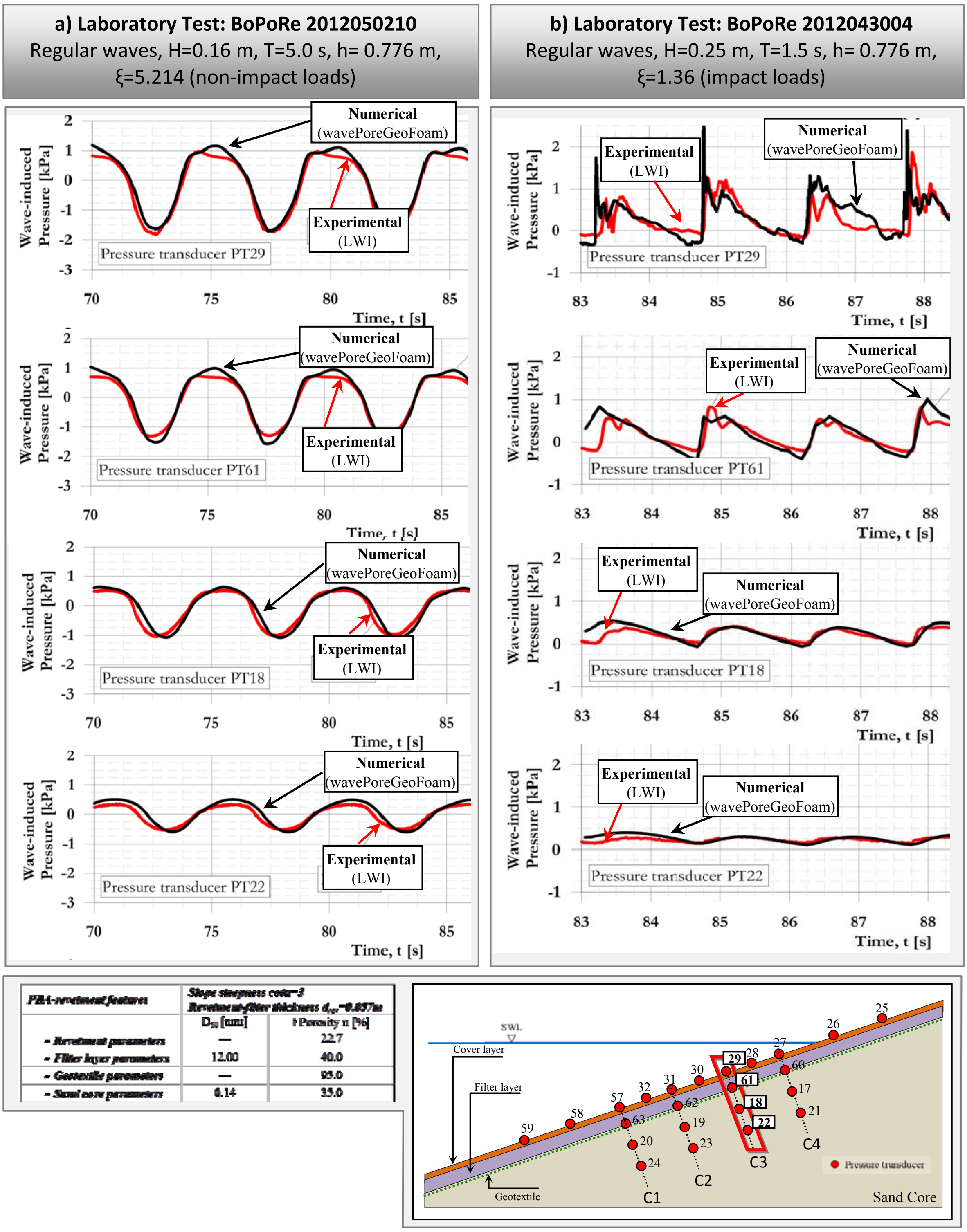

Fig. 3-3: Validation of the new weakly coupled CFD-CSD model "`wavePoreGeoFoam`" for PBA-revetments simulations: small-scale laboratory data (Liebisch & Oumeraci (2012)) vs. numerical results for a) non-impact wave loads and b) impact wave loads.

The results from the validation are shown in Fig. 3-3a for non-impact loads and in Fig. 3-3b for impact load conditions. The pressure on the revetment does not show large differences (relative error <8%) between numerical and experimental results for non-impact waves (Fig. 3-3a). For impact wave loads (Fig. 3-3b), slight differences (relative error <12%) of the pressure on the revetment between numerical and experimental results are noticed and are particularly related to the shape of the pressure time series which may be consequence of the wave-wave interactions or the influence of the turbulence model selected for the simulation (as also observed in the validation with GWK tests (Fig. 3-2b)). On the other hand, for both impact and non-impact loads almost no differences are observed in Fig. 3-3 between the laboratory data and the numerical simulations regarding the pore pressures beneath the filter layer and in the sand foundation. Therefore, the pore pressure magnitude as well as the shape of the time series are fully reproduced by the new weakly coupled CFD-CSD model "`wavePoreGeoFoam`".

Furthermore, the pressure development is directly related to the fluid motion in and outside the PBA-revetments. Therefore, considering the results depicted in Fig. 3-2 and Fig. 3-3, it can be concluded that the fluid motion is also correctly estimated as will be shown in Section 5.4 where the comparison of the wave breaking process provided by experimental and numerical tests is shown.

A relatively good agreement is obtained between the numerical simulation and the large- and small-scale laboratory tests in terms of the shape and magnitude of the pressure time series for all layers on and beneath the revetment. Slight differences are observed in the pressure time series, especially for impact wave loading which might be caused by wave-wave interactions and/or uncertainties on the determination of the empirical parameters required by the numerical model.

3.5 Sensitivity analysis for the numerical modelling of PBA-revetments

For the GWK tests used for the validation of the numerical model (see Section 3.4.1) prior calibration of the empirically-defined parameters was conducted. Details of the calibration are described in Alcérreca-Huerta & Oumeraci (2013), where the peak pressure on the revetment and the peak pore pressure in the sand core were used for the comparison between numerical and experimental results in the case of non-impact loads. The relative error according to eq. (3.14) is applied to quantify the errors at each pressure transducer location:

$$\text{Relative error}[\%] = \frac{|P_{\exp} - P_{num}|}{P_{\exp}} \times 100 \tag{3.14}$$

with P_{exp} and P_{num} as the peak pressures from experimental and numerical results, respectively.

For the validation with the data from the GWK tests and non-impact loads, an average relative error of 7.63% was obtained for those pressures on the revetment, and 17.43% for the pore pressures in the sand core (Test ID 14 in Table 3-3). The relative error for other test cases performed during the calibration become larger and a summary is provided in Table 3-3.

Table 3-3: Parameters and conditions during calibration tests.

Test ID	***Sand (input variables)***				***Gravel (input variables)***				***Relative error [%]***		***Turbulence model***
	n	S_w [%]	α_f	β_f	n	S_w [%]	α_f	β_f	P_{max} on revetment	P_{max} on sand core	
0	0.40	100	1950	2.4	0.388	100	2500	2.4	20.4	48.0	k-ω SST
1	0.32	100	2438	2.4	0.400	100	1600	2.4	18.3	37.7	k-ω SST
2	0.32	100	2438	3.6	0.400	100	1600	3.6	17.2	36.0	k-ω SST
3	0.32	100	24375	3.6	0.388	100	1600	3.6	10.5	22.0	k-ω SST
4	0.32	100	240	3.6	0.388	100	1600	3.6	12.3	20.8	k-ω SST
5	0.32	100	660	3.6	0.388	100	1600	3.6	11.6	21.0	k-ω SST
6	0.32	100	12500	3.6	0.388	100	1600	3.6	11.6	21.5	k-ω SST
7	0.32	100	660	3.6	0.388	100	1600	3.6	12.9	23.5	k-ω SST
8	0.32	100	660	3.6	0.388	100	1600	3.6	12.37	22.6	k-ω SST
9	0.32	95	660	3.6	0.388	100	1600	3.6	13.2	24.4	k-ω SST
10	0.32	100	660	3.6	0.388	100	1600	3.6	11.3	26.6	k-ω SST
11	0.32	100	660	3.6	0.280	100	1600	3.6	11.0	21.4	k-ω SST
12	0.32	100	660	3.6	0.388	100	1600	3.6	12.7	23.8	k-ω SST
13	0.32	100	660	3.6	0.280	100	2500	3.6	12.4	23.4	k-ω SST
14	0.32	100	660	3.6	0.280	100	1600	3.6	7.6	17.4	ǂ k-ε
19	0.32	100	660	3.6	0.388	100	1600	2.4	21.5	51.7	ǂ k-ε
23	0.32	100	660	0.0	0.388	100	1600	3.6	20.1	35.2	ǂ k-ε

Variables: n=porosity; S_W= degree of saturation of the porous media; α_f and β_f tare parameters for calculation of a and b coefficients in Darcy-Forchheimer equation.
ǂ The model was volume averaged as described in Nakayama & Kuwahara (1999) and del Jesús Peñil (2011)

Considering the calibration test conditions, a sensitivity analysis was therefore conducted to examine the effect on the results of numerical simulations by varying the empirically-defined parameters included in the governing equations such as porosity (n), "Darcy-Forchheimer coefficients" (α_f and β_f) and degree of saturation (S_w). The detailed sensitivity analysis is shown in Alcérreca-Huerta & Oumeraci (2013), and a summary is briefly described considering also the results shown in Table 3-3.

- ***Effects of the variation of coefficients α_f and β_f.*** They are used for the definition of Darcy-Forchheimer equation (section 2.3.1) which constitutes the closure term in the momentum equation of VARANS equations in the CFD solver (section 3.2) and are related to the permeability and porosity of the soil:
    - The gravel is less sensitive to a variation of these parameters than the sand material underneath.
    - A variation on β_f (e.g., Test 14 vs. 19) induces larger effects on the flow and pressure development in the porous media than the variation of α_f (e.g., Test 5 vs. 6). Similar results are described by van Gent (1993) (see Fig. 2-12). This may occur since the second term in the Darcy-Forchheimer equation (s. eq. (2.36)) is expressed by the square of the flow velocity.

  - A large increment of the parameter α_f for the revetment cover layer (Test 3 and 6) slightly increases the pressure on the revetment, as expected since the revetment becomes more impermeable.
  - Calibration of α_f and β_f is in close relation with the porosity, however, the porosity is a parameter that can be easily determined through laboratory tests.
- ***Effects of the variation of the porosity n:***
  - The variation of n results in an effect similar to that induced by a variation of α_f and β_f.
  - The difference between porosity ($n=V_v/V$=volume of voids/total volume) and effective porosity ($n=V_{IP}/V$=volume of interconnected pores/total volume) should be made since only the effective porosity will induce fluid motion and the development of pore pressures.
- ***Effects of the variation of the degree of saturation S_w in the sand core:***
  - An unsaturated sand core will lead to lower pore pressure than a fully saturated sand core. This is because for partially saturated soils, part of the load is supported by the water and the rest by the soil skeleton (s. section 2.3.2 and Fig. 3-1).
  - Considering a degree of saturation S_w=95% (Test 9) in the sand core and the porous cover layer, it was observed that the negative pore pressures (uplift) are reduced if compared with a case with S_w=100% (e.g., Tests 8 & 9). This effect was also described by De Groot et al. (2006) and is caused due to the air compressibility which allows the water to occupy part of the air volume, thus resulting in a slight reduction of the pore pressure.
- ***Effect of the applied turbulence model:***
  - The k-ω SST model showed a relatively good performance (Tests 1-13). However, for locations in the swash zone the pressures on the revetment from numerical simulation were normally higher than those from the laboratory tests. The k-ε model considering the volume averaged technique (Test 14, 19, 23) provided higher dissipation of the energy and therefore a reduction of the pressures on the revetment.
  - The k-ω SST and the k-ε models were found to be suitable especially for short duration numerical simulations considering non-impact waves. Otherwise, through the validation with the data from GWK tests (Fig. 3-2b) and that from the LWI wave flume tests (Fig. 3-3b), it was noticed that LES turbulence model is suitable for long duration simulations and particularly for impact wave loads.
  - For numerical simulations of PBA-revetments, it is recommended to use LES model which is applicable to impact-wave load condition and moreover for long duration simulations.

The sensitivity analysis performed has resulted in a rather qualitative assessment of the effects that the empirically-defined parameters may induce on the results of the numerical simulations. Among these parameters, α_f and β_f from Darcy-Forchheimer equation together with the porosity are the most relevant for the whole wave-structure-subsoil interaction. Also, during calibration of the model setup, the permeability was found to be the key parameter to be determined, since it has a large influence on the magnitude of the pore pressures. However, further research should be conducted in order to describe in more detail the aforementioned effects.

3.6 Parameter study and numerical simulations of PBA-revetments

A parameter study based on the numerical simulations was conducted as a basis for the process analysis of PBA-revetments using the validated model "`wavePoreGeoFoam`". The test programme and the numerical model setup are described in this section.

3.6.1 Test programme of previous parameter studies with PBA-revetments

The test programme was defined by considering those of previous parameter studies with PBA revetments such as: i) the large-scale tests in GWK with the PBA-revetment "Elastocoast" (Oumeraci et al. (2010)) and ii) the numerical simulations of PBA-revetments with COBRAS-UC (Foyer (2013)).

In the large-scale tests performed in GWK, three different revetment alternatives with a cover layer made of Porous Bonded Aggregates (PBA) were used (s. Fig. 3-4):

i) *Model Alternative A.* The Elastocoast revetment lies directly on a geotextile that can retain the finer fractions of the underlying sand. The thickness of the cover layer is of 0.15 m, and no filter layer is included for this alternative.

ii) *Model Alternative B.* The Elastocoast revetment lies over a filter layer with a thickness of about 0.10 m, composed of crushed limestone (20/40 mm). The gravel filter layer lies over a geotextile that covers the underlying sand.

iii) *Model Alternative C.* This alternative was provided with the same features as model alternative B, but with the difference that the filter layer thickness is about 0.20 m

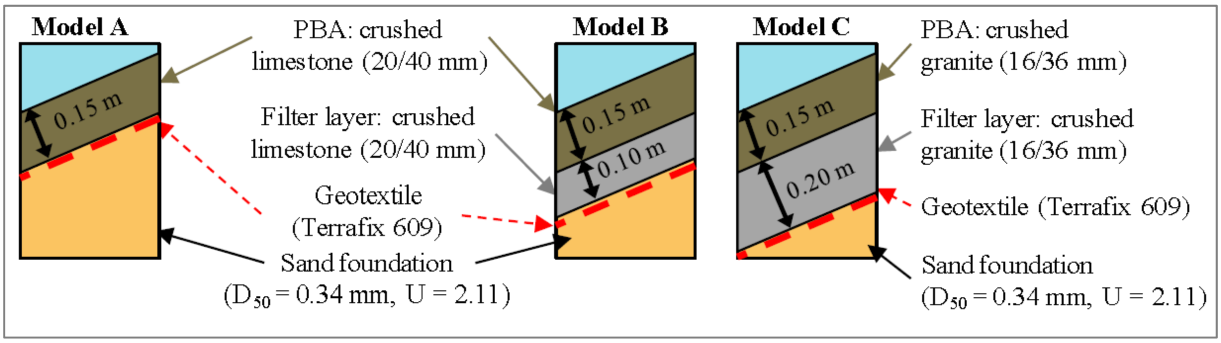

Fig. 3-4: Tested PBA-revetment alternatives in GWK (Oumeraci et al. (2010)).

The final test programme in GWK includes a total of 150 tests. Two phases were performed in order to test two model configurations simultaneously: i) Phase1 with model configurations A & B and ii) Phase2 with model configurations B & C. The first phase consisted of 16 tests with two model configurations (32 tests in total). For the second phase 59 tests were also performed with two model configurations (118 tests in total). Therefore, the total number of performed tests considering phase1 and phase2 were up to 150. Moreover, regular and irregular wave conditions were tested and the test programme as well as the wave breaker types are described in Fig. 3-5.

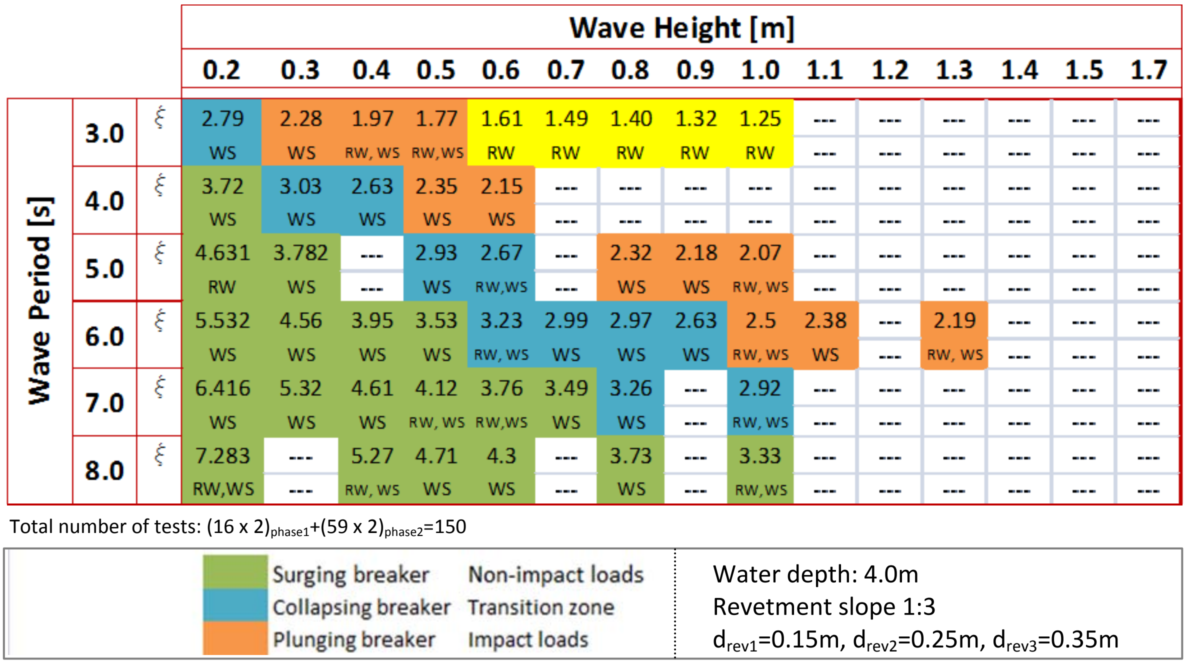

Wave Period [s]		Wave Height [m]														
		0.2	0.3	0.4	0.5	0.6	0.7	0.8	0.9	1.0	1.1	1.2	1.3	1.4	1.5	1.7
3.0	ξ	2.79	2.28	1.97	1.77	1.61	1.49	1.40	1.32	1.25	---	---	---	---	---	---
		WS	WS	RW, WS	RW,WS	RW	RW	RW	RW	RW	---	---	---	---	---	---
4.0	ξ	3.72	3.03	2.63	2.35	2.15	---	---	---	---	---	---	---	---	---	---
		WS	WS	WS	WS	WS	---	---	---	---	---	---	---	---	---	---
5.0	ξ	4.631	3.782	---	2.93	2.67	---	2.32	2.18	2.07	---	---	---	---	---	---
		RW	WS	---	WS	RW,WS	---	WS	WS	RW, WS	---	---	---	---	---	---
6.0	ξ	5.532	4.56	3.95	3.53	3.23	2.99	2.97	2.63	2.5	2.38	---	2.19	---	---	---
		WS	WS	WS	WS	RW, WS	WS	WS	WS	RW, WS	WS	---	RW, WS	---	---	---
7.0	ξ	6.416	5.32	4.61	4.12	3.76	3.49	3.26	---	2.92	---	---	---	---	---	---
		WS	WS	WS	RW, WS	RW,WS	WS	WS	---	RW, WS	---	---	---	---	---	---
8.0	ξ	7.283	---	5.27	4.71	4.3	---	3.73	---	3.33	---	---	---	---	---	---
		RW,WS	---	RW, WS	WS	WS	---	WS	---	RW,WS	---	---	---	---	---	---

Total number of tests: $(16 \times 2)_{phase1}+(59 \times 2)_{phase2}=150$

🟩	Surging breaker	Non-impact loads
🟦	Collapsing breaker	Transition zone
🟧	Plunging breaker	Impact loads

Water depth: 4.0m
Revetment slope 1:3
d_{rev1}=0.15m, d_{rev2}=0.25m, d_{rev3}=0.35m

Fig. 3-5: Programme for the GWK tests by Oumeraci et al. (2010).

The test programme in GWK was focused mainly on the generation of surging, collapsing and plunging waves, that result in impact and non-impact loads. However, due to limitations associated with wave generation, just few tests were carried out considering plunging breakers with a surf similarity parameter $\xi<1.9$.

Moreover, due to the limitations associated with time and costs of constructing different revetment slopes in combination with several revetment-filter thicknesses (d_{rev}) of the filter layer, and of testing different wave conditions (limited mainly to $\xi>1.9$), it was necessary to conduct numerical simulations using the validated model COBRAS-UC model in the frame of the PhD study by Foyer (2013). The advantages of testing several alternatives of PBA-revetments in a numerical model enabled to extend the range of structure and wave parameters over the conditions tested in GWK.

In order to reduce time and computational costs a total number of 40 combinations of wave height, wave period and revetment slopes were selected for the numerical parameter study with COBRAS-UC model. Furthermore, 5 different revetment slopes and 3 different revetment-filter thicknesses were selected providing a total number of 120 tests (s. Fig. 3-6).

Despite this extensive parameter study, the pressures developed on and beneath the revetment as well as inside the sand core were not considered due to limitations of COBRAS-UC to properly reproduce them (Foyer (2013)). The parameter study by Foyer was therefore focused only on the reflection performance of the structure and on the analysis of wave run-up/down and wave set-up/down on the PBA revetment.

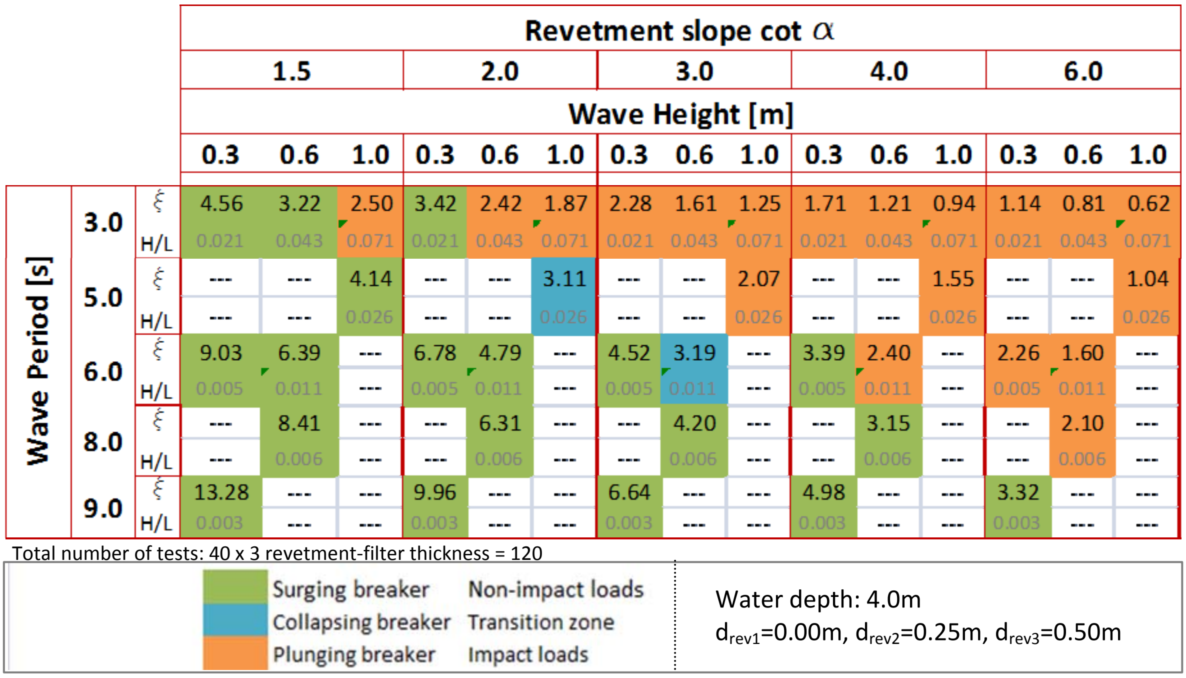

			Revetment slope cot α														
			1.5			2.0			3.0			4.0			6.0		
			Wave Height [m]														
			0.3	0.6	1.0	0.3	0.6	1.0	0.3	0.6	1.0	0.3	0.6	1.0	0.3	0.6	1.0
Wave Period [s]	3.0	ξ	🟩 4.56	🟩 3.22	🟧 2.50	🟩 3.42	🟧 2.42	🟧 1.87	🟧 2.28	🟧 1.61	🟧 1.25	🟧 1.71	🟧 1.21	🟧 0.94	🟧 1.14	🟧 0.81	🟧 0.62
		H/L	0.021	0.043	0.071	0.021	0.043	0.071	0.021	0.043	0.071	0.021	0.043	0.071	0.021	0.043	0.071
	5.0	ξ	---	---	🟩 4.14	---	---	🟦 3.11	---	---	🟧 2.07	---	---	🟧 1.55	---	---	🟧 1.04
		H/L	---	---	0.026	---	---	0.026	---	---	0.026	---	---	0.026	---	---	0.026
	6.0	ξ	🟩 9.03	🟩 6.39	---	🟩 6.78	🟩 4.79	---	🟩 4.52	🟦 3.19	---	🟩 3.39	🟧 2.40	---	🟧 2.26	🟧 1.60	---
		H/L	0.005	0.011	---	0.005	0.011	---	0.005	0.011	---	0.005	0.011	---	0.005	0.011	---
	8.0	ξ	---	🟩 8.41	---	---	🟩 6.31	---	---	🟩 4.20	---	---	🟩 3.15	---	---	🟧 2.10	---
		H/L	---	0.006	---	---	0.006	---	---	0.006	---	---	0.006	---	---	0.006	---
	9.0	ξ	🟩 13.28	---	---	🟩 9.96	---	---	🟩 6.64	---	---	🟩 4.98	---	---	🟩 3.32	---	---
		H/L	0.003	---	---	0.003	---	---	0.003	---	---	0.003	---	---	0.003	---	---

Total number of tests: 40 x 3 revetment-filter thickness = 120

🟩	Surging breaker	Non-impact loads
🟦	Collapsing breaker	Transition zone
🟧	Plunging breaker	Impact loads

Water depth: 4.0m

d_{rev1}=0.00m, d_{rev2}=0.25m, d_{rev3}=0.50m

Fig. 3-6: Test programme for the numerical simulations with COBRAS-UC (Foyer (2013)).

3.6.2 Test programme of the present parameter study with PBA-revetments

The parameter study using the new CFD-CSD model system `wavePoreGeoFoam` considered the wave-induced pressure on and beneath the revetment as well as in the sand core. Moreover, a focus was set on the impact-load condition as the results reported by Oumeraci et al. (2010) have clearly shown that the failure of the revetment (registered during the tests) was induced by pore pressure in the sand core beneath the revetment under impact loads.

Like in the study by Foyer (2013) with COBRAS-UC, 5 revetment slopes were considered (cotα=1.5, 2.0, 3.0, 4.0 & 6.0) in order to supplement the cotα=3.0 alternative tested in GWK. Moreover, 3 revetment-filter thicknesses d_{rev}=0.15 m, 0.25 m and 0.35 m are investigated as compared to d_{rev}=0.00 m, 0.25 m and 0.50 m in the study using COBRAS-UC and d_{rev}=0.15 m, 0.25 m and 0.35 m in the GWK tests.

The wave conditions in the present parameter study include more tests with plunging and collapsing wave breakers in comparison to the parameter study in GWK and with COBRAS-UC. For this purpose, 5 wave periods (T=3.0, 4.0, 5.0, 7.0 & 9.0s) and 3 wave heights (H=0.3, 0.6 and 1.0m) were considered. Thus, the test programme as well as the wave breaker types for the present parameter study are described in Fig. 3-7 and a total number of 135 tests were considered.

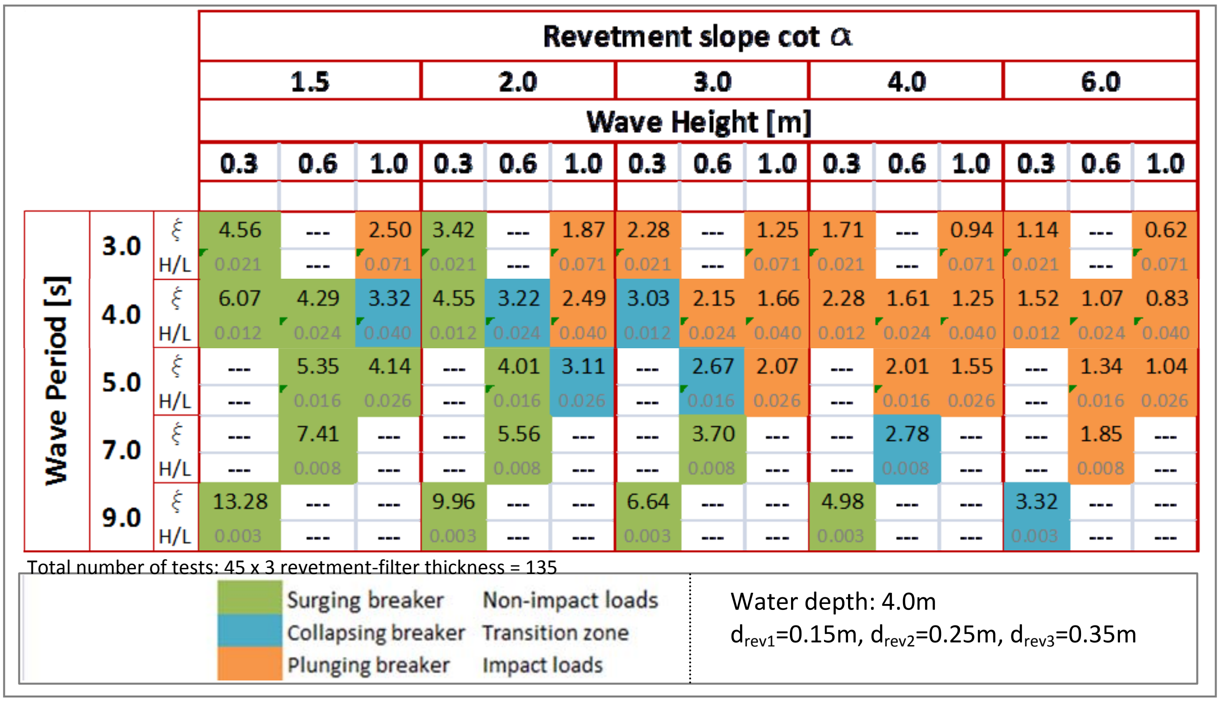

Wave Period [s]			Revetment slope cot α														
			1.5			2.0			3.0			4.0			6.0		
			Wave Height [m]														
			0.3	0.6	1.0	0.3	0.6	1.0	0.3	0.6	1.0	0.3	0.6	1.0	0.3	0.6	1.0
	3.0	ξ	4.56	---	2.50	3.42	---	1.87	2.28	---	1.25	1.71	---	0.94	1.14	---	0.62
		H/L	0.021	---	0.071	0.021	---	0.071	0.021	---	0.071	0.021	---	0.071	0.021	---	0.071
	4.0	ξ	6.07	4.29	3.32	4.55	3.22	2.49	3.03	2.15	1.66	2.28	1.61	1.25	1.52	1.07	0.83
		H/L	0.012	0.024	0.040	0.012	0.024	0.040	0.012	0.024	0.040	0.012	0.024	0.040	0.012	0.024	0.040
	5.0	ξ	---	5.35	4.14	---	4.01	3.11	---	2.67	2.07	---	2.01	1.55	---	1.34	1.04
		H/L	---	0.016	0.026	---	0.016	0.026	---	0.016	0.026	---	0.016	0.026	---	0.016	0.026
	7.0	ξ	---	7.41	---	---	5.56	---	---	3.70	---	---	2.78	---	---	1.85	---
		H/L	---	0.008	---	---	0.008	---	---	0.008	---	---	0.008	---	---	0.008	---
	9.0	ξ	13.28	---	---	9.96	---	---	6.64	---	---	4.98	---	---	3.32	---	---
		H/L	0.003	---	---	0.003	---	---	0.003	---	---	0.003	---	---	0.003	---	---

Total number of tests: 45 x 3 revetment-filter thickness = 135

🟩	Surging breaker	Non-impact loads
🟦	Collapsing breaker	Transition zone
🟧	Plunging breaker	Impact loads

Water depth: 4.0m
d_{rev1}=0.15m, d_{rev2}=0.25m, d_{rev3}=0.35m

Fig. 3-7: Test programme for numerical simulations in the present parameter study.

The conditions tested in GWK, COBRAS-UC and the present parameter study are compared in Table 3-4 considering only tests with regular waves. As a remark, the numerical simulations with COBRAS-UC considered the sand core as an impermeable layer, due to the limitations of the model. Moreover, it is noticed that the numerical simulations can provided a wider number of slope steepnesses and ξ_0-values ($0.62<\xi_0<13.28$) than GWK tests.

Table 3-4: Comparative table for structure and wave parameters considered within the parameter studies of GWK (Oumeraci et al. (2010)), COBRAS-UC (Foyer (2013)) and this study.

	GWK Oumeraci et al. (2010)	*COBRAS-UC* Foyer (2013)	*Present study*	*Remarks*
Wave depth (m)	3.40 - 4.20	4.0	4.0	Nominal values for the wave generation in the laboratory tests and in the numerical simulations
Wave conditions				
- Wave height, H_0(m)	0.20 - 1.40	0.3, 0.6, 1.0	0.3, 0.6, 1.0	
- Wave period, T(s)	3.0 - 8.0	3.0, 5.0, 6.0, 8.0 & 9.0	3.0, 4.0, 5.0, 7.0 & 9.0	
- Surf similarity par., ξ_0(-)	1.25 - 7.28	0.62 - 13.28	0.62 - 13.28	
PBA-revetment features				
- Slope steepness, cotα (-)	3.0	1.5, 2.0, 3.0, 4.0 & 6.0	1.5, 2.0, 3.0, 4.0 & 6.0	For COBRAS-UC, the sand core of the PBA-revetment is considered impermeable
- Revetment-filter thickness, d_{rev}(m)	0.15, 0.25, 0.35	0.00, 0.25, 0.50	0.15, 0.25, 0.35	
Total number of tests	74	120	135	Considering only tests with regular waves

3.6.3 Numerical model setup

As the main objective of this parameter study is to extend the range of tested conditions in GWK (Oumeraci et al. (2010)) in order to improve the knowledge of the hydro-geotechnical processes involved in the interaction between waves, revetment and soil foundation, it is important that the numerical setup should also be similar to the experimental setup for the reference test in GWK which will be used directly for comparison. This procedure was also adopted in the previous parameter study by Foyer (2013). However, in contrast to the later study, where the sand core was considered to be impermeable, this numerical setup accounts for the sand core as a porous medium.

For the numerical model setup, different aspects were defined before conducting the test programme: i) mesh generation, ii) wave generation, iii) definition of empirical parameters needed by the governing equations, iv) turbulence models and v) location for data extraction of the numerical simulations. A brief summary of the numerical model setup is described in this section and further details for the definition of the aforementioned features are provided in Alcérreca-Huerta & Oumeraci (2014).

a) Mesh generation

The mesh generation was performed for the 15 different revetment configurations (5 slope steepnesses and 3 revetment-filter thicknesses). The complete GWK- wave-flume, the revetment, the filter, the sand core and a sandy slope 1:20 placed in front of the revetment structure (220<x<240m) were considered (Fig. 3-8a) to be numerically simulated by the CFD solver of "`wavePoreGeoFoam`" (Fig. 3-8b). For this purpose, the number of cells within the unstructured meshes ranged from 332 265 to 375 187 cells for the different configurations. With these meshes, 50-80s were simulated on 2-6 days for a single computer core.

Moreover, for the simulation with the CSD solver of "`wavePoreGeoFoam`", a smaller domain was set since it is only needed for the estimation of stresses and pore pressures beneath the revetment. Therefore, only the revetment, filter and sand core were simulated (Fig. 3-8c). Due to the one way coupling, different meshes than those used for the CFD simulations were generated with approximately 57600 cells. For the CSD solver, 50-80s are simulated on 7-20 minutes for a single computer core.

The velocity and water surface in the free stream region and in porous media regions are correctly estimated through the CFD solver of "`wavePoreGeoFoam`". The pressures in the free stream region and on the revetment are also calculated by the CFD solver, however, the pore pressures and stresses in porous media are defined by using the CSD solver of "`wavePoreGeoFoam`".

To produce the coupling in "`wavePoreGeoFoam`", common points on the revetment are defined for both CFD and CSD solvers. At these point locations, the wave-induced pressures are extracted from the CFD simulations and then introduced as boundary conditions for the CSD simulations. Further details are described in Alcérreca-Huerta & Oumeraci (2014).

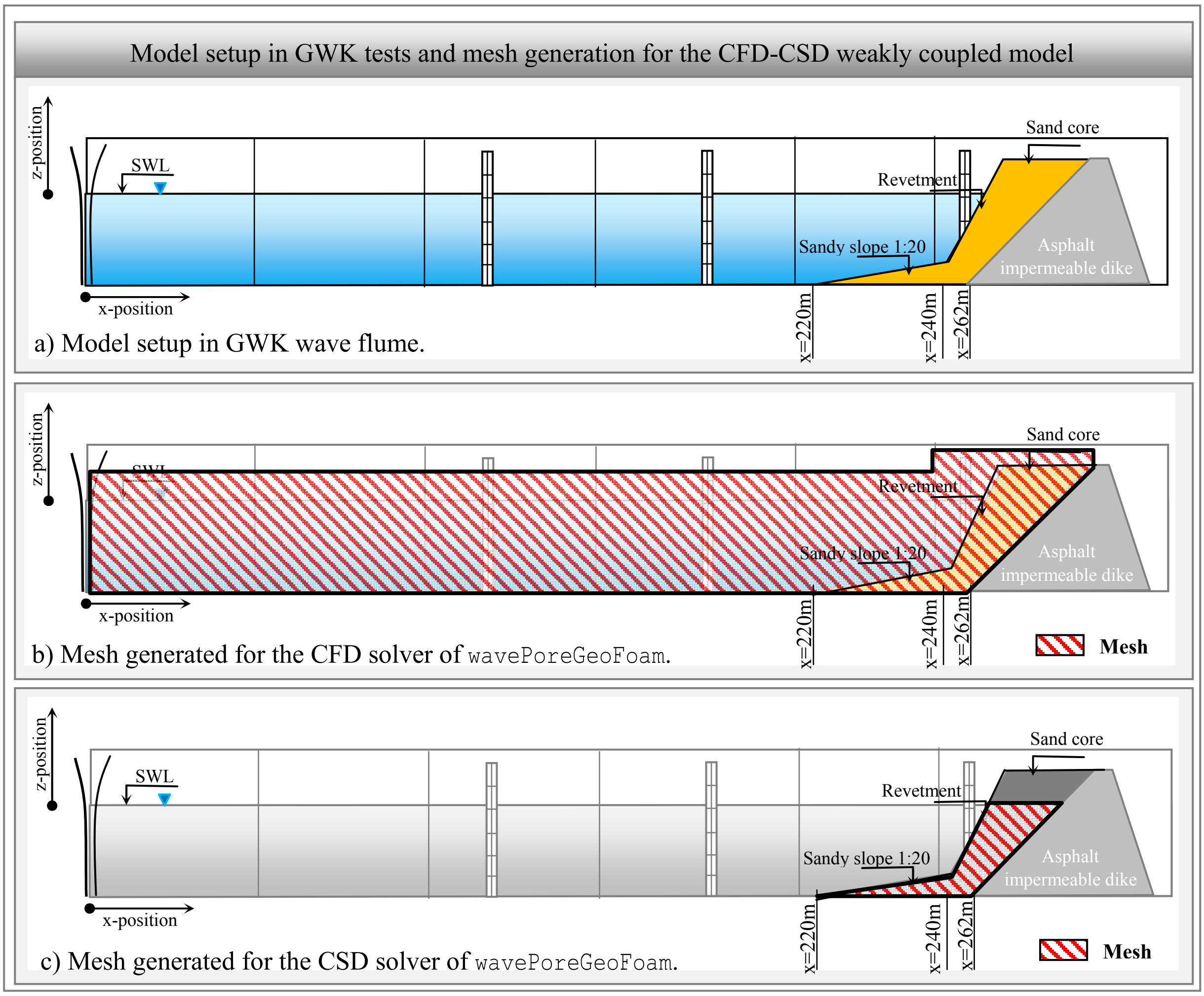

a) Model setup in GWK wave flume.

b) Mesh generated for the CFD solver of `wavePoreGeoFoam`.

c) Mesh generated for the CSD solver of `wavePoreGeoFoam`.

Fig. 3-8: Model setup in GWK tests (a) and meshes generated for the CFD (b) and CSD (c) numerical modelling with `wavePoreGeoFoam`.

b) Wave generation

The wave generation in the numerical wave flume was made considering the "`waves2Foam`" library which includes a wave generation/absorption method based on relaxation zones (s. Section 3.1 and Jacobsen et al. (2012)). The wave theories that best fits for this parameter study considering the wave conditions and water depth defined in the test programme (Fig. 3-7) are Stokes II and Stokes V (s. Table 3-5).

Table 3-5: Wave theories used for the wave generation in the numerical simulations of this parameter study.

		Wave Period [s]				
		3.0	4.0	5.0	7.0	9.0
Wave height [m]	0.3	Stokes II	Stokes II	---	---	Stokes II
	0.6	---	Stokes II	Stokes II	Stokes II	---
	1.0	Stokes V	Stokes V	Stokes V	---	---
						Water depth, h=4.0m

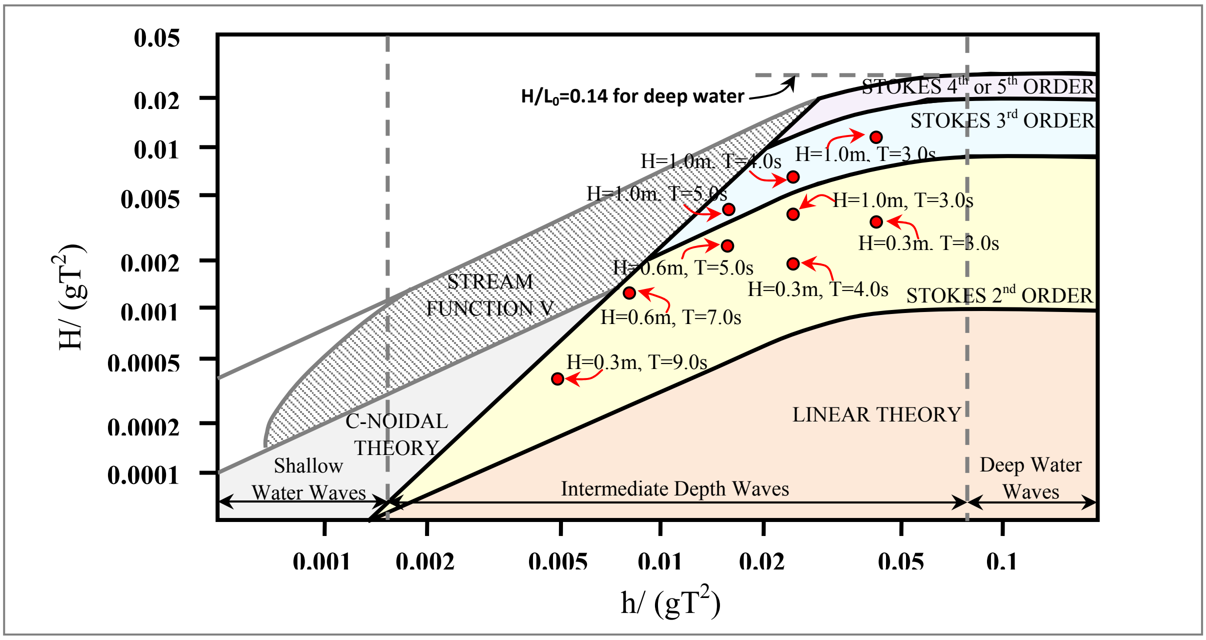

Fig. 3-9 Ranges of validity of wave theories and wave conditions (H,T) to be tested (modified from USACE (2002)).

c) Definition of empirical parameters needed by the governing equations

The empirical parameters to be defined for the numerical simulations are mainly the porosity of the porous regions, coefficients α_f and β_f of Darcy-Forchheimer equation and permeability. For this purpose, the results from the validation and calibration (Section 3.4 & 3.5) are considered, as already mentioned, the aim of this parameter study is to extend the range of tested conditions in GWK. Therefore, the empirical parameters used within the numerical simulations are shown in Table 3-2.

d) Turbulence models

Performance of the numerical model using the k-ε and LES turbulence models for impact and non-impact waves was observed during the validation and calibration tests with data from GWK tests (section 3.4.1) and with small-scale model tests in the LWI wave flume (section 3.4.2). Thus, it was concluded that the k-ε model modified to work with VARANS equations (Nakayama & Kuwahara (1999) is suitable for numerical simulation of non-impact loads for short duration tests, while the LES turbulence model is a better alternative for the simulation of impact loads and long duration tests. Therefore, the k-ε model is considered for the numerical modelling of waves with $\xi_0>3.0$, while the LES model is implemented for $0.62<\xi_0<3.0$.

e) Location for data extraction in the numerical simulations

For the location of probes for data extraction within the numerical simulations, the coordinate system shown in Fig. 3-8 is used. The zero x-position is located at the beginning of the numerical wave flume, while the zero z-position is set to the SWL. An overview of the data extraction is described in the following. Further details as well as the location of all the probes for data extraction from the numerical simulations are provided in Alcérreca-Huerta & Oumeraci (2014).

Numerical wave gauges were set in the numerical model to extract the water surface elevation at certain locations. Two numerical wave gauges arrays (WG1-4 & WG5-8) were placed at two locations (the same as those in GWK tests for comparison) for measuring the wave reflection. Moreover, five numerical wave gauges were distributed over the sandy slope 1:20 (s. Fig. 3-8) to provide a measurement of the MWL in the free stream region. Other four wave gauges were located inside the sand core to measure the MWL beneath the revetment. Particularly for the later, the advantages of numerical simulations over laboratory tests becomes crucial since the free surface can be "measured" without disturbances provided by the porous media.

Numerical wave run-up gauges were set in the model parallel to the revetment slope at three different locations: i) on the revetment, ii) at the revetment-filter interface and iii) at the filter-sand core interface. The wave run-up gauges at locations ii) and iii) allow the estimation of the maximum wave run-up and run-down beneath the revetment which has not been measured in laboratory tests with PBA-revetments (e.g., Oumeraci et al. (2010)).

Numerical pressure transducers were located on and beneath the PBA-revetment as well as in the sand core. The number of numerical pressure transducers depends on the slope steepness. The distance between numerical pressure transducers in the impact zone was set to Δx=0.25m. Two more pressure transducers with similar spacing were located close to the impact zone. Outside this area, the spacing of the numerical pressure transducers parallel to the revetment was increased to Δx=0.5 m, 1.0 m and 2.0 m depending on the length of the PBA-revetment slope as well as the proximity to the toe of the structure. Furthermore, in order to obtain the pore pressure distribution normal to the revetment slope, the same number of pressure transducers set on the revetment were also deployed at each layer interface in the direction normal to the revetment slope (Fig. 3-10). Also, 4 layers of pressure transducers were set at different depths within a spacing 0.20m for the first three layers and of 0.40m between the third and fourth layers.

It should be mentioned that the numerical pressure transducers located on the revetment are used for the one-way coupling of the CFD and CSD solvers in "`wavePoreGeoFoam`".

A numerical model setup with the location of the numerical wave gauges and pressure transducers is shown in Fig. 3-10, exemplarily for a slope 1:3 for model configuration 3-C with d_{rev}=0.35m.

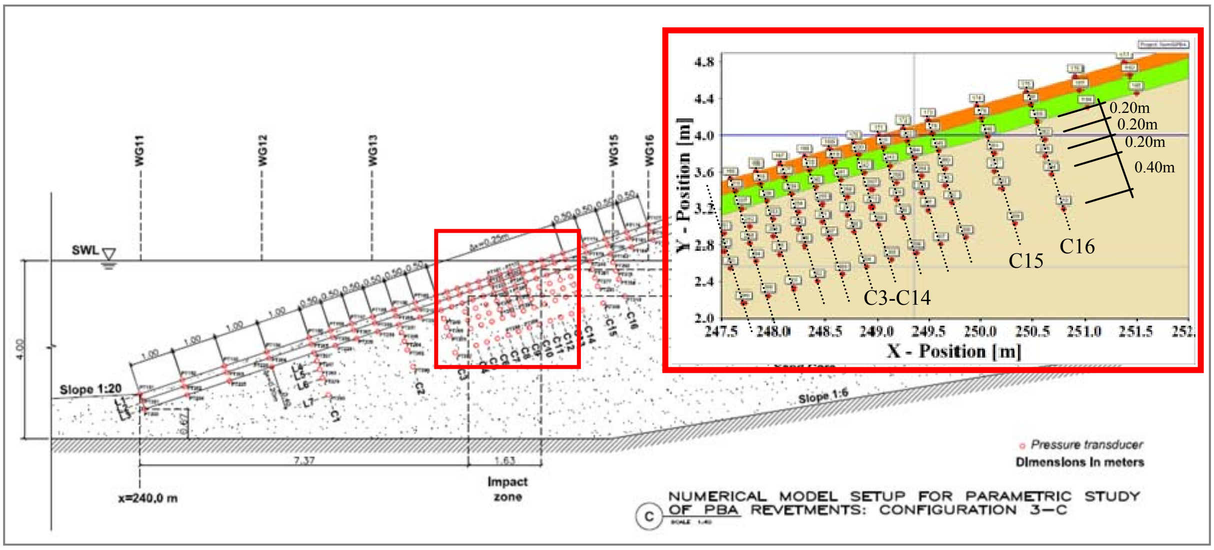

Fig. 3-10: Location of pressure probes, numerical wave gauges in the model set-up for the numerical simulation of a PBA-revetment with slope 1:3 and d_{rev}=0.35m.

Thus, a test programme was developed for the numerical parameter study based on previous laboratory and numerical studies. Furthermore, the model setup was defined considering 100 to 165 locations for data extraction (depending on the revetment configuration) with a special focus on those related to the pressure and pore-pressure. The large amount of locations for data extraction together with the possibility of considering different configurations of PBA-revetments is recognized as the key advantages of numerical modelling over laboratory tests.

3.7 Applicability and limitations of the CFD-CSD model `wavePoreGeoFoam`

Different factors can be defined in the numerical modelling that may affect the accuracy and validity of the results provided by the numerical simulations. According to Shah (2002), these factors might classified as follows:

i. *User factors* associated with the definition of the empirical user-defined parameters required by the model (e.g., porosity, permeability) or with the specification of the initial and boundary conditions for the numerical simulation, including the selection of an appropriate turbulence for the specific problem to be modelled.
ii. *Assumptions and simplifications implemented in the model* which are required in order to avoid complex governing equations which might be difficult to solve with the available hardware and software resources.
iii. *Quality of the mesh*, as an insufficient mesh discretization may lead to inaccuracies in the numerical results. Also, an excessive fine mesh may result in high computational resources.

Therefore, the limitations for the application of the new developed numerical model system "`wavePoreGeoFoam`" for the simulation of porous structures are described in this section considering the aforementioned factors.

a) User factors

Regarding the user factors, the definition of the porosity and permeability is highly important for the CFD-CSD model "`wavePoreGoeFoam`" as exposed in Section 3.5 where a sensitivity analysis was conducted to qualitatively describe the influence of the user-defined parameters on the numerical results. The initial and boundary conditions are set dependending on the problem to be modelled. For further information related to possible conditions that can be implemented in the simulations the reader is referred to OpenFOAM (2013). The boundary where the wave generation/absorption is performed (together with the domain of the relaxation zone) is particularly limited for the consideration of turbulence. For this boundary, the velocity, pressure and water surface elevation fields are described based on a specified wave theory which does not allow any variation of these fields due to turbulence effects. However, it should be considered that the relaxation zone constitutes a region where the imposed inlet wave field interacts with the wave field calculated through the governing equations (s. Jacobsen et al. (2012)), so that the turbulence effects are fully considered in the mesh domain outside the relaxation zone.

The turbulence model selected within the numerical simulations might depend on the type of application. For this PhD research and for the simulation of PBA-revetments, it is highly recommended to use the LES turbulence model, particularly for impact loads and long duration tests. However, the LES is recommended only for 3-dimensional cases and high Reynolds numbers, since turbulence (and the large eddies simulated by the LES model) is inherently a 3D phenomenon. Nevertheless, in the PhD study, the LES model was implemented considering the results from the comparison between the numerical simulations and the large- and small-scale laboratory tests. Therefore, a detailed sensitivity analysis of the effect of turbulence models on the results is recommended prior to the final selection of a turbulence model.

b) Assumptions and simplifications in the model

Within the assumptions considered in the CFD-CSD model, the implementation of the volume averaged RANS equations in the CFD model considers the bulk properties of a porous medium as representative for a defined control volume (REV) within the mesh domain (see Section 2.3.3). The later provides the link between the microscopic physical properties and the macroscopic properties. However, a limitation of the model is related to how the overall porous medium can be represented as homogeneous within a well-defined geometry (Jakobsen (2008)). In other words, the application of the model is limited when representing non-homogeneous porous media (e.g., rocks embedded in sand) or porous media interfaces with a large variation of the porous medium properties (e.g., large rocks laying on fine sand). Furthermore, due to the volume averaging process, the mesh refinement in porous regions within the numerical simulations is limited by the length of the control volume where the bulk properties are set. That is, the cell size in the porous regions is restricted by the REV that has to account for the macroscopic (bulk) properties and consequently, it should consider a volume larger than the particle size (see Fig. 2-17 for reference).

Moreover, the assumption of incompressibility of the fluids implemented in the VARANS equations might represent a further limitation for the applicability of the CFD-CSD model. However, this limitation could be evaluated by considering the Mach number which stands for the relative velocity of a fluid compared to that of the sound speed. When the Mach number is lower than $M<0.3$ then the fluids may be considered as incompressible, thus considerably simplifying the time calculation solution of the governing equations. For most coastal engineering applications, the Mach number is normally $M<0.3$, so that the new model can be applied for a wide range of problem types, except for problems such as highly aerated wave-induced impact loads where compressibility effects may be crucial for the results.

Further research is required on the effects of the aforementioned assumptions on the accuracy of the results from simulations os structures made of other porous material than that of PBA-revetments (e.g., rubble mound breakwaters).

On the other hand, the CFD-CSD model "`wavePoreGeoFoam`" was validated considering the experimental data from large- and small-scale laboratory tests. However, this validation is only indicative for the accuracy that can be achieved when simulating all hydrodynamic and hydro-geotechnical processes on and beneath PBA-revetments (e.g., wave breaking, wave reflection, wave run-up/run-down, wave-induced pressures and pore pressures). Further validation is suggested for the CFD-CSD coupled model, but particularly for the CFD-model by considering comparison with e.g. analytical solutions of flow through porous media, similar to that performed with the CSD-model by El Safti et al. (2012) and El Safti & Oumeraci (2013). This may enhance the reliability of the model to reproduce the hydrodynamic and hydro-geotechnical processes for a wider range of porous structures.

Additionally, it should be mentioned that the one-way coupling of the CFD and CSD involves a limitation of the model "`wavePoreGeoFoam`" to properly simulate those areas which may include large air-water exchange and mixture. As the CSD model considers only one-fluid phase, the one-way coupling of the solvers is restricted to those porous regions located below the water level. This shortcoming can be overcome by considering a two-way coupling of the CFD and CSD solvers.

c) *Quality of the mesh and mesh discretization*

The accuracy on the numerical simulation results also depends on the mesh quality. For this purpose, an utility named "`checkMesh`" (OpenFOAM (2013)) can be applied to analyze the quality of the mesh in terms of its statistics (e.g., number of cells, points, faces, etc), topology (e.g., boundary definition and connection between boundaries), and geometry (e.g., non-orthogonality, cell and boundary openness, skewness). For this PhD research, the "`checkMesh`" utility was applied resulting in no mesh quality errors. Furthermore, comparison was made between the laboratory tests and the numerical simulations to ensure that the results were within the order of magnitude expected by also considering the mesh discretization implemented in the 15 meshes used in the parameter study. For further studies, it is highly recommended to perform convergence studies in order to reduce the possible errors due to mesh quality and mesh discretization. These convergence studies provide a sensitivity analysis considering a critical output parameter (e.g., pressure, velocity) in a specific location compared to some measure of the mesh discretization (NAFEMS (2014)). Possible restrictions on the cell size as described in the use of the VARANS equations should be considered during the mesh generation.

Overall, the limitations for the application of the model as well as the accuracy and validity of the results are closely related to the three factors that were in this section described particularly for the CFD-CSD model "`wavePoreGeoFoam`". The governing equations as well as the considerations made for the numerical simulations within the parameter study were essentially calibrated for PBA-revetments. Nevertheless, the recommendations and the limitations herein described may be considered for further analysis with the model "`wavePoreGeoFoam`". Moreover, sensitivity analysis may be required to quantitative account for the possible errors induced by the different factors in the numerical modelling.

3.8 Summary of key results and implications for the study

A brief overview of the OpenFOAM framework has been presented and it is recognized as a CFD toolbox suitable for the numerical modelling of different coastal engineering problems. However, modification to the solvers in this framework were performed in order to improve the shortcomings existing, especially for the simulation of flow in porous media. Therefore, it was recognized that the coupling of a CFD "`wavePorousFoam`" and a CSD solver "`geotechFoam`" into a new numerical CFD-CSD model system "`wavePoreGeoFoam`" is needed for the correct analysis of wave-structure interaction.

The governing equations implemented in "`wavePoreGeoFoam`" were described and the CFD and CSD models were weakly coupled (one-way coupling). Therefore, to enhance the results of the numerical simulations, further research may be required for the development of a fully coupled CFD-CSD model system for coastal engineering, particularly for the solution of 3-dimensional problems. The fully coupled CFD-CSD model system may be extremely valuable when solving the pore pressures and soil stresses inside porous media at locations where an important variation of the water surface takes place (such as in the swash area in the revetment and filter layers of PBA revetments, or the armour units of breakwaters) and thus, the pore pressure can be measured also in areas where air-water mixture varies with time.

The CFD-CSD model system `wavePoreGeoFoam` was validated considering large and small-scale laboratory tests with PBA-revetments. Calibration of the numerical model was conducted for the validation and as a result a sensitivity analysis was provided with the following key results:

- The porosity, permeability and the α_f and β_f coefficients which are needed in the Darcy-Forchheimer equation were identified as the most crucial parameters for the numerical modelling of the wave-structure-subsoil interaction.
- Regarding the turbulence models applied in the numerical simulation of PBA-revetments, the LES models provide better results for wave impact-loading and large duration tests, while the volume-averaged k-ε turbulence model performs better for non-impact waves and short duration simulations.

- Further studies with systematic analysis to determine the effects of the input parameters for the numerical model (e.g., porosity, turbulence model, coefficients α_f and β_f) should be conducted considering a systematic analysis of the numerical results for each of the input variables.

The numerical model setup calibrated and validated with GWK tests was used for the parameter study in order to better understand the hydro-geotechnical processes which may affect the stability of PBA-revetments and their foundation. Therefore, a test programme was developed for the parameter study based on previous laboratory and numerical studies. Furthermore, the advantages of numerical simulations over laboratory tests were identified: i) possibility of a larger number of locations for data extraction (e.g., pore pressures in the sand core, wave run-up/down at PBA-revetment layers interface) and ii) simulation of several structure configurations (e.g., slope steepness, revetment-filter thickness) and wave conditions that for laboratory tests may result in significantly higher time and costs. Nevertheless, numerical modelling should always be employed together with laboratory tests for a systematic calibration and validation. Only under such condition, numerical modelling can be considered as a valuable tool to reliably analyse the hydro-geotechnical processes involved in the wave-structure-foundation interaction beyond the tested conditions in the laboratory.

In addition, the limitations for the application and validity of the new CFD-CSD model "`wavePoreGeoFoam`" should be considered for further research related to different types of porous structures (e.g., conventional rubble mound structures, berm breakwaters). Also, a sensitivity analysis should be conducted for the quantification of possible errors induced by different factors in the numerical modelling (i.e., user factors, assumptions in the model, mesh quality). Further improvements of "`wavePoreGeoFoam`" are suggested, particularly including the implementation of a two-way coupling of the CFD and CSD solvers which may notably enhance the results from the numerical model for porous regions where large air-water exchange/mixture occurs.

4 Analysis of the wave breaking, wave reflection and swash processes on and beneath the revetment

In this chapter, the hydrodynamic processes involved in the wave-structure interaction are analysed based on the results of the parameter study (s. section 3.6) using the new validated CFD-CSD model "`wavePoreGeoFoam`". For this purpose, the wave breaking and wave reflection are firstly presented. Second, the analysis of the wave set-up (Mean Water Level-MWL) outside and inside the PBA-revetments is conducted. Third, the analysis of the wave run-up and run-down is performed considering also the wave run-up and run-down related to the MWL. A focus is set on the effect of the revetment-filter thickness on the aforementioned processes and on the comparison with results from GWK tests.

4.1 Wave breaking and wave reflection

4.1.1 Wave breaking

Comprehensive studies based on numerical and physical modelling have been conducted on the classification of wave breaking types for PBA-revetments (e.g., Oumeraci et al. (2010), Foyer & Oumeraci (2013b)). However, differences were noticed in the results particularly concerning the limits of the wave breaker types. Therefore, the present parameter study was also applied for the classification of wave breaker types in front of PBA-revetments with consideration of these previous studies. The main types of breakers considered are exemplarily shown in Fig. 4-1: plunging, collapsing and surging breakers. Spilling breakers hardly occur for steep slopes such as those of PBA-revetments and were not included also because they are highly dependent on the air-water interaction, so their numerical simulation is highly sensitive to the turbulence model and the mesh geometry (due to possible numerical diffusion) that may strongly affect the results of the wave-structure interaction.

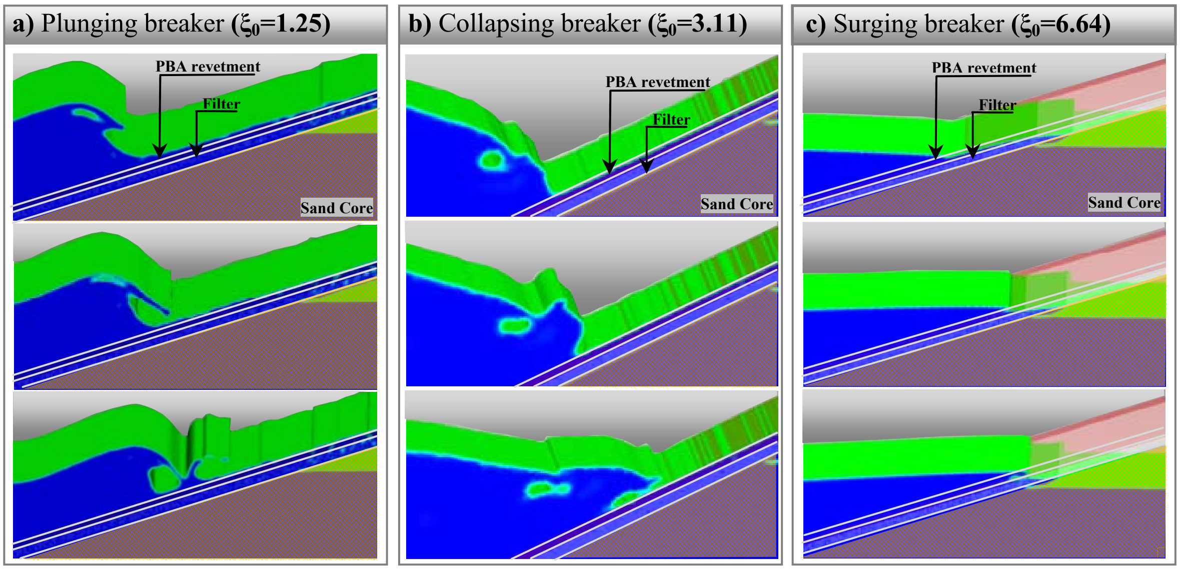

Fig. 4-1: Typical breaker types in the numerical simulations: a) plunging, b) collapsing and c) surging breakers.

A visual ("video") analysis of the numerical simulations was performed in order to classify the types of wave breaking in terms of the surf similarity parameter leading to the breaker type classification summarized in Fig. 4-2 which shows that for all values of the revetment-filter thickness (d_{rev}) a similar distribution of the breaker types takes place. Although for d_{rev1}=0.15m the limit between plunging and collapsing breakers is not as clear as with the d_{rev2}=0.25m and d_{rev3}=0.35m, the results on Fig. 4-2 suggest the following classification: plunging ($0.6 < \xi_0 < 2.4$), collapsing ($2.4 < \xi_0 < 3.4$) and surging ($\xi_0 > 3.4$).

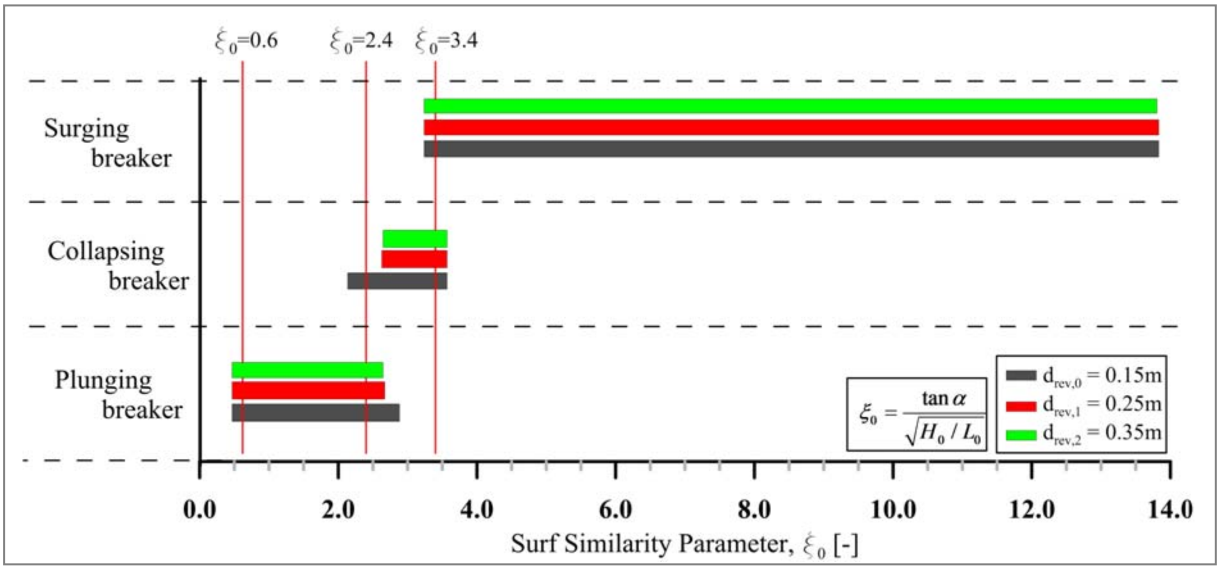

Fig. 4-2: Breaker type classification based on a "video" analysis of the numerical results from the parameter study.

A comparison of the classification obtained from the numerical results of the parameter study using `wavePoreGeoFoam` and those in the large-scale tests with PBA-revetments performed at the GWK (Oumeraci et al. (2010)), including those of Foyer & Oumeraci (2013b) by applying the model COBRAS-UC is given in Table 4-1.The most important differences between the results of the three studies is observed for the upper range of ξ_0-values defining the collapsing breaker.

Table 4-1:Comparison of breaker type classification obtained from different studies in terms of the surf similarity parameters.

		Spilling	*Plunging*	*Collapsing*	*Surging*
GWK-tests (Oumeraci et al. (2010))	ξ_0	-	< 2.2	2.2 - 4.5	> 4.5
Parameter study by Foyer & Oumeraci (2013b)	ξ_0	< 1.0	~ 1.0 - 2.4	~ 2.4 - 5.2	> 5.2
This parameter study	ξ_0	-	0.6 - 2.4	2.4 - 3.4	> 3.4
Average		**<0.8**	**0.8 - 2.4**	**2.4 - 4.3**	**> 4.3**

Previous studies (e.g. Dean & Dalrymple (1991); Okazaki & Sunamura (1991); Svendsen (2006)) concluded that the boundary between collapsing and surging breakers cannot be properly defined. This is confirmed by the differences shown in Table 4-1. The differences for the definition of the limits of wave breakers types can be due to several reasons:

- Wave-wave interaction, including that between incident and reflected waves, so that plunging, collapsing or surging breakers might unexpectedly occur.
- Influence of the revetment roughness and revetment-filter thickness into the run-up/down that can modify the aforementioned wave-wave interaction.
- Differences in the models setup of each of the studies that can modify the wave conditions such as revetment geometry, filter layer thicknesses, roughness of the cover layer.

In the numerical simulations, these differences might also be caused by the turbulence model implemented (highly important in air-water-structure interaction) or due to the refinement of the mesh close to the revetment structure (relevant for the accuracy of the simulation). Further reasons might be the different numerical models used (`wavePoreGeoFoam` in this parameter study and COBRAS-UC in the parameter study of Foyer & Oumeraci (2013b)) as well as the different model setups considered (entire GWK wave flume in this study and only part of the flume in Foyer & Oumeraci (2013b), due to limitations of COBRAS-UC).

All these considerations and uncertainties suggest that the most appropriate alternative at present is to adopt averaged ξ_0-values from those provided by the three studies as shown in Table 4-1, so that the following classification of breaker types is tentatively proposed: plunging breakers ($0.8 < \xi_0 < 2.4$), collapsing breakers ($2.4 < \xi_0 < 4.3$) and surging breakers ($\xi_0 > 4.3$).

4.1.2 Wave reflection

In this section, a comparative analysis of the numerical data provided by the parameter study and those obtained from the large-scale tests in GWK (Oumeraci et al. (2010)) is described. The effect of the revetment-filter thickness of PBA-revetments on wave reflection is first discussed and prediction formulae are then developed.

For the analysis of the wave reflection in the numerical wave flume and comparison of results, the water surface elevation was sampled at the same locations as those of the wave gauges deployed in GWK (Oumeraci et al. (2010)).

a) Effect of revetment-filter thickness on wave reflection

The comparison of the results from the numerical simulations and those from the GWK tests is shown in Fig. 4-3, including the tentatively proposed breaker type classification according to Table 4-1 where it was noticed that only for collapsing breakers the numerical simulations provide slightly lower reflection coefficients. This might be due to the change of the turbulence model because the LES model better reproduces the plunging waves, while the k-ε model shows a better performance for surging waves (Alcérreca-Huerta & Oumeraci (2014)). The LES model has a tendency to dissipate less energy than the k-ε model does. Therefore, for collapsing waves that are close to the limit with plunging waves, some breakers were subject to excessive dissipation of energy by the k-ε turbulence model rather than being reflected by the PBA-revetment structure. For this purpose, it is recommended to perform further studies to analyse the effect of turbulence models in numerical modelling of wave-structure interaction.

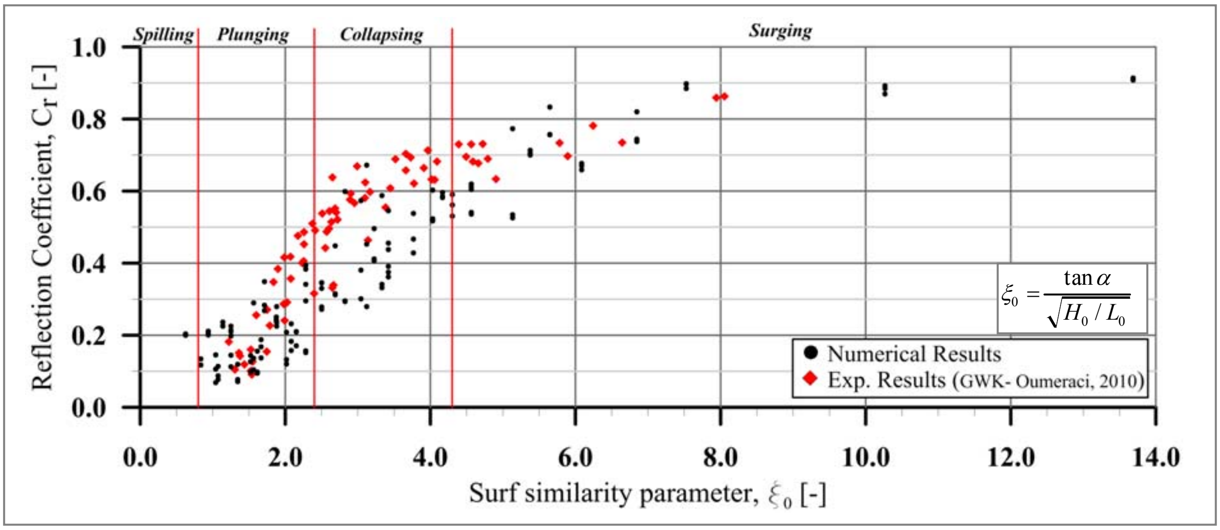

Fig. 4-3: Reflection coefficient obtained from numerical results and GWK data by Oumeraci et al. (2010).

The reflection performance of the revetment for different values of thickness d_{rev} and surf similarity parameters ξ_0 is shown in Fig. 4-4. The revetment-filter thickness d_{rev} indeed affects the wave reflection, especially when comparing the dataset for d_{rev1}=0.15 m and that for d_{rev3}=0.35 m. However, this effect is less pronounced if the dataset for d_{rev1}=0.15 m is compared with data for d_{rev2}=0.25 m.

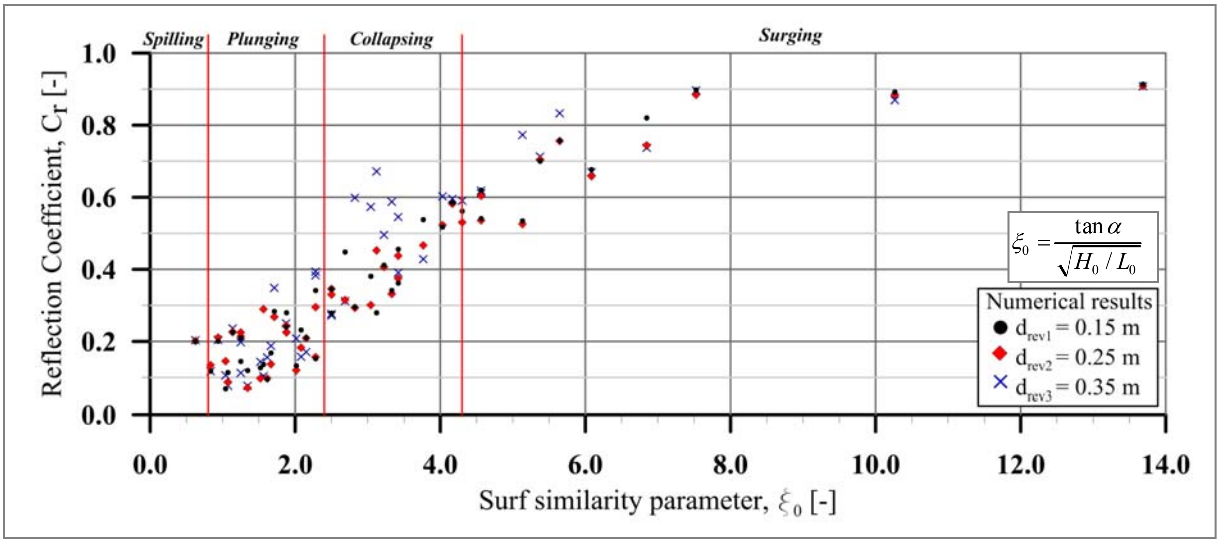

Fig. 4-4: Reflection coefficient vs. surf similarity parameter: effect of revetment-filter thicknesses d_{rev}.

The effect of the revetment-filter thickness d_{rev} was identified in previous studies (e.g. Seelig & Ahrens (1981)). Therefore, it is expected that a thicker revetment will reduce the wave reflection but the reflection coefficient C_r, for any revetment thickness may tend to 1.0 for $\xi_0 > 12$ (Foyer (2013)). However, the results provided by the present parameter study are not always in full agreement with this expected effect. Consequently, the wave reflection analysis was performed as function of both surf similarity parameter (breaker type) and thickness d_{rev}:

- The effect of the revetment-filter thickness d_{rev} on wave reflection is relatively small within the range $0.15<d_{rev}<0.25$ m, but increases when $d_{rev} > 0.25$ m for any value of the surf similarity parameter.
- Increasing thickness d_{rev} for $0 <d_{rev}<0.25$ m results in less reflection at any value of surf similarity parameter. The same occurs when increasing d_{rev} for $0.25 <d_{rev}<0.35$ m, but only for small range of plunging waves ($0.8 < \xi_0 < 1.5$).
- The revetment-filter thickness does not affect the reflection coefficient for surging waves with $\xi_0 > 6.5$.
- The wave reflection increases particularly for collapsing breakers ($2.4 < \xi_0 < 4.3$) and $d_{rev}= 0.35$m.
- The reflection coefficient in this PhD study tends to $C_r \sim 1.0$ for $\xi_0 > 14$ and for any revetment-filter thickness. A similar result was found by Foyer (2013). The ξ_0-value at which C_r=1.0 is reached may be dependent on d_{rev} but also on other variables, such as the permeability and porosity of the revetment and filter layers.

The increase of wave reflection for $d_{rev} > 0.25$m and collapsing breakers ($2.4 < \xi < 4.3$) is non-expected (s. also Fig. 4-5). This may be explained as a consequence of the infiltration and exfiltration process that occurs in the swash zone (s. as reference Fig. 4-18): i) during wave run-up, water infiltrates and is stored within the revetment and filter layers, ii) the stored water exfiltrates during run-down (a thicker d_{rev} will tend to store a larger amount of water and to induce more seepage) and iii) the next incident wave is reflected by the structure itself but also by the seepage flow during the exfiltration phase.

b) Prediction formulae for wave reflection

Prediction formulae for wave reflection are developed based on the results of this parameter study on the effects of d_{rev} and on previous studies with permeable slopes (e.g. Seelig & Ahrens (1981); Zanuttigh & van der Meer (2008)) and PBA-revetments (Foyer & Oumeraci (2013b)).

The revetment-filter thickness d_{rev} affects the wave reflection as already mentioned, and explicit account for this has been considered by Foyer (2013) through the use of a modified surf similarity parameter ξ_{ad} defined by eq. (4.1). However, the use of ξ_{ad} with the results from the numerical parameter study did not result in a clear improvement for the assessment of the wave reflection since the scatter of the data was similar to that shown in Fig. 4-4 (further details are described in Alcérreca-Huerta & Oumeraci (2014)).

$$\xi_{ad} = \frac{\tan\alpha}{\sqrt{\frac{H_0}{L_0}\left(1-\frac{d_{rev}}{H_0}\right)}} \tag{4.1}$$

Moreover, large-scale (Oumeraci et al. (2010)) and small-scale laboratory tests (Liebisch et al. (2014)) have shown that the effects of the wave height and wave period are more important than considered in the surf similarity parameter ξ_0. Nevertheless, this was not found in the results of the parameter study. Therefore, further analysis is needed in order to determine the dependency of the wave reflection on the wave height and the wave period which both might not be sufficiently weighted in ξ_0 especially for PBA-revetments, since this effect has not been reported to occur for smooth impermeable revetments.

The prediction formulae in this study were developed considering the tanh-model in equation (4.2), which provides an improvement as compared to the prediction formula by Seelig & Ahrens (1981) by considering wide number of structures, dataset and representing physical bounds (for $\xi_0 \rightarrow 0$, Cr=0 and for $\xi_0 \rightarrow \infty$, Cr=1), with coefficients A and B dependent on the roughness (Zanuttigh & van der Meer (2008)):

$$C_r = \tanh\left(A \cdot \xi_0^{\,B}\right) \tag{4.2}$$

By fitting eq. (4.2) to the dataset of the parameter study and considering the different values of d_{rev}, equations (4.3), (4.4) and (4.5) were obtained.

$$C_{r,drev=0.15m} = \tanh\left(0.105 \cdot \xi_0^{1.202}\right) \tag{4.3}$$

$$C_{r,drev=0.25m} = \tanh\left(0.109 \cdot \xi_0^{1.150}\right) \tag{4.4}$$

$$C_{r,drev=0.35m} = \tanh\left(0.128 \cdot \xi_0^{1.165}\right) \tag{4.5}$$

The fitting equations (4.3), (4.4) and (4.5), are plotted in Fig. 4-5, while, the values of A and B are provided in Table 4-2. Since the roughness of the PBA-revetment slope was kept constant in the parameter study, it can be concluded from Table 4-2, that coefficients A and B are not only dependent on the roughness but also on the revetment-filter thickness d_{rev}.

Table 4-2: Coefficients A and B in eq. (4.2) for PBA-revetments with different revetment-filter thickness d_{rev}.

$C_r = \tanh\left(A \cdot \xi_0^{\,B}\right)$	***Impermeable revetment (Zanuttigh & van der Meer (2008))***	***PBA-revetment (this study)***			
		d_{rev}=0.15m	d_{rev}=0.25m	d_{rev}=0.35m	Average for d_{rev}=0.15-0.35m
Coefficient A	0.160	0.105	0.109	0.128	0.114
Coefficient B	1.430	1.202	1.150	1.165	1.17
Coeff. of determination (r^2)	---	0.924	0.915	0.876	0.894

A general estimation of the wave reflection for PBA-revetments without considering the effect of the revetment-filter thickness d_{rev} is described by eq. (4.6) where coefficients A=0.114 and B=1.17 were obtained as an average of the values provided in Table 4-2.

$$C_r = \tanh\left(0.114 \cdot \xi_0^{1.17}\right) \tag{4.6}$$

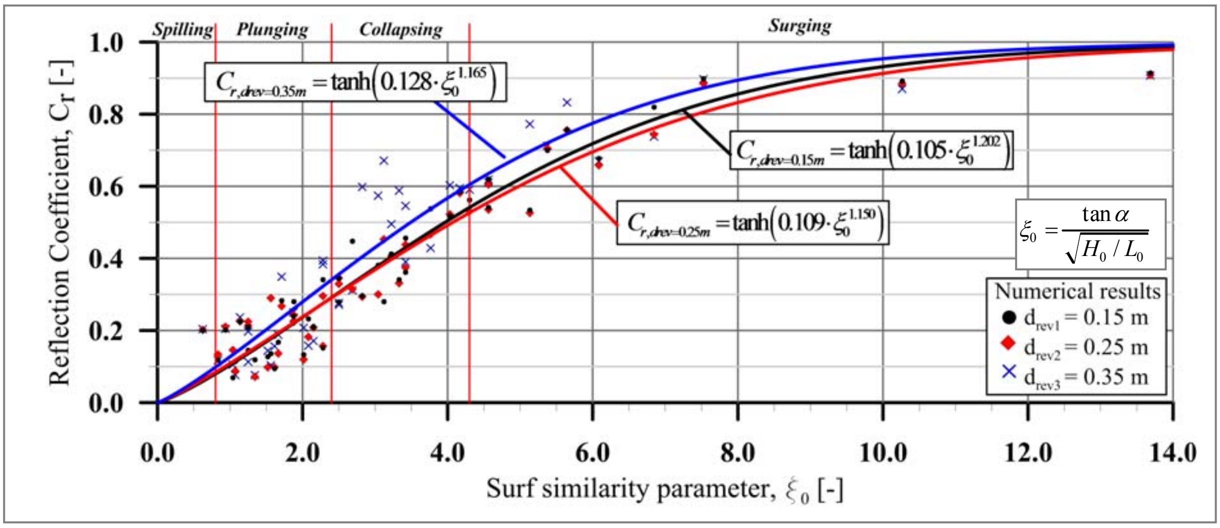

Fig. 4-5: Prediction formulae wave reflection of PBA-revetments with different revetment-filter thicknesses d_{rev}.

Wave reflection of PBA-revetments as described by eq. (4.6) and the comparison with impermeable smooth revetments is shown in Fig. 4-6. The benefits of the PBA-revetment over impermeable ones for the reduction of the wave reflection are clearly illustrated. For $\xi_0 < 1.1$, the impermeable revetment and the PBA revetment exhibit almost the same performance, which means that for spilling breakers and the transition to plunging waves, the difference between impermeable and porous revetments of different revetment-filter thickness is not relevant for wave reflection.

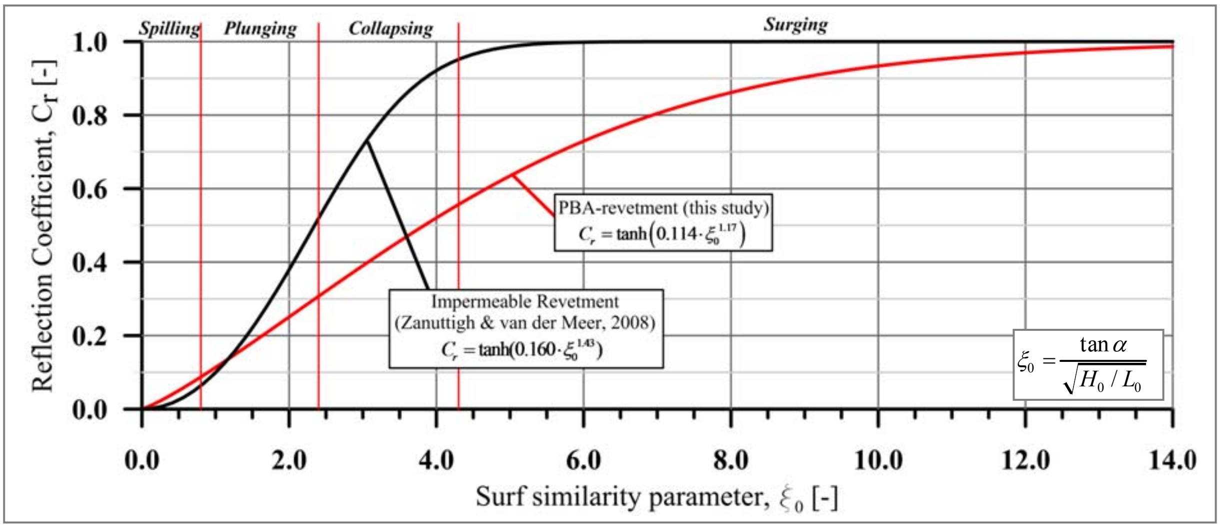

Fig. 4-6: General prediction formulae for wave reflection of PBA-revetments and comparison with impermeable smooth revetments.

The classification of wave breaker types proposed considers the averaged ξ_0-values from those provided by three different studies (present parameter study; parameter study by Foyer (2013); and GWK tests, Oumeraci et al. (2010)). The classification of the breaker type is important for the process analysis of the wave-structure interaction. Prediction formulae for the wave reflection were defined considering the revetment-filter thickness, however, it was noticed to provide a slight effect. Also, an unexpected result with collapsing waves was found where an increment of the wave reflection occurs when $d_{rev} > 0.25$m.

4.2 Mean water level and wave set-up

One of the key findings of the study of Foyer (2013) is that the wave set-up affects all other processes on and beneath the revetment, including the hydro-geotechnical processes in the sand core. As shown in Fig. 4-7, the wave set-up at the slope will induce an increase of the SWL so that a Mean Water Level (MWL) will result in front and on the revetment (external MWL) as well as inside the revetment (internal MWL). Therefore, the wave set-up together with the internal and external MWL are analysed in the present section.

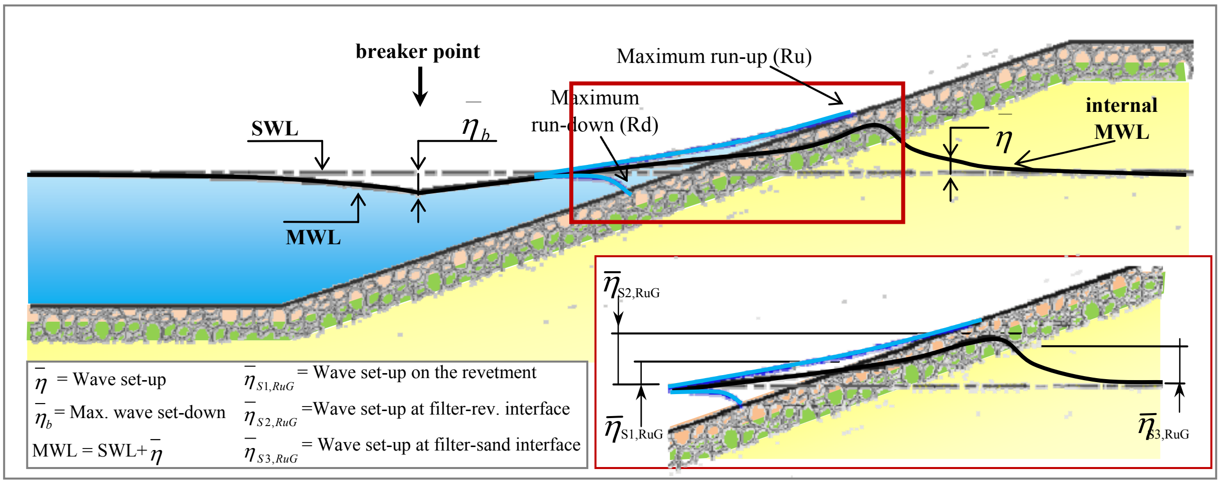

Fig. 4-7: Definition sketch for the external and internal Mean Water Level as consequence of the change in the SWL due to the wave set-up ($\bar{\eta}$).

4.2.1 Mean water level under impact and non-impact waves

The development of the external MWL (eMWL) and the internal MWL (iMWL) due to the presence of a PBA-revetment will be described for two wave loading conditions:

(i) Non-impact loads (collapsing and surging waves with $\xi_0 > 3.4$).
(ii) Impact loads (plunging and collapsing waves with $0.8 < \xi_0 < 3.4$).

a) Mean water level for non-impact wave loads

Among the conditions tested in the parameter study, the steeper slopes 1:1.5, 1:2 and 1:3 are the most likely to result in non-impact waves and therefore were considered in the analysis of the MWL. For non-impact waves ($\xi_0 > 3.4$), the MWL was found to be highly dependent on the wave height while the wave period has only a slight effect; no noticeable effect of the revetment-filter thickness on MWL could be identified (Fig. 4-8). Furthermore, the MWL increases with the wave height reaching its maximum elevation at the interface between the filter and the sand core.

The permeability difference at the interface between the revetment-filter and the sand core was found to produce a large gradient of the MWL at this location, result that was also observed by Foyer & Oumeraci (2012).

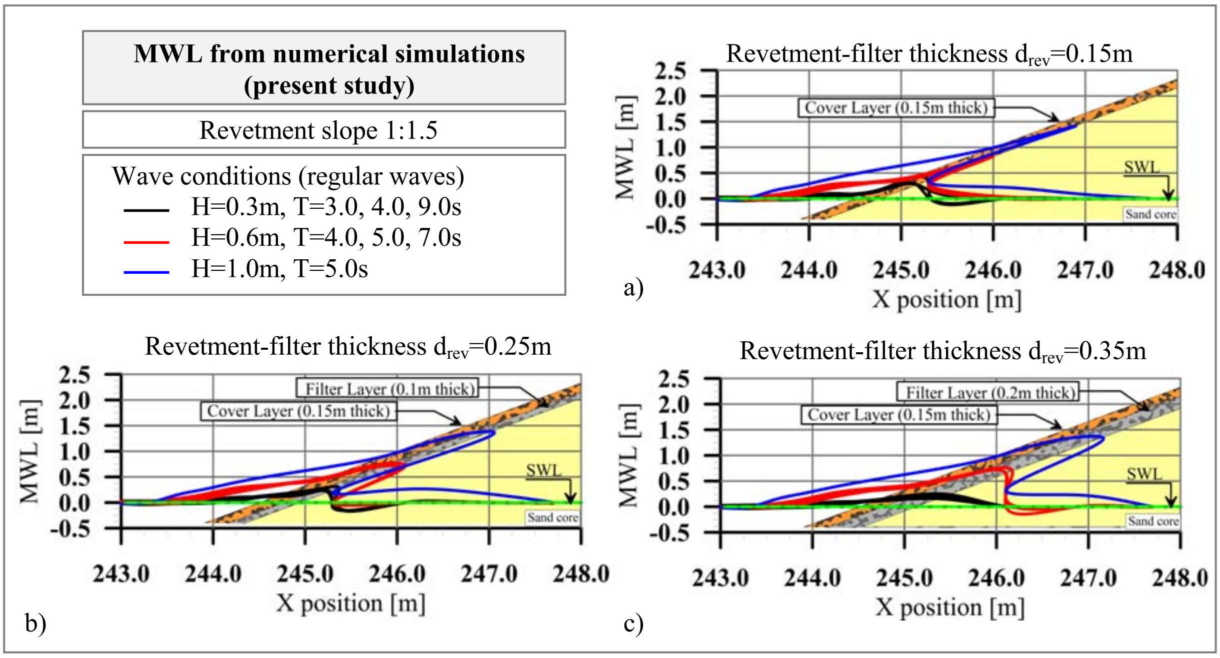

Fig. 4-8: External and Internal MWL for ***non-impact wave loads*** (ξ_0>3.4) on a PBA-revetment (slope 1:1.5) with different revetment-filter thicknesses d_{rev}: a) d_{rev}=0.15m, b) d_{rev}=0.25m, c) d_{rev}= 0.35m.

Furthermore, it was observed during the numerical simulations that the revetment-filter thickness does not has any noticeable influence on the stationary internal MWL (iMWL) for non-impact wave loads but a larger thickness causes a decrease of the time to achieve the stationary iMWL which was observed to occur for a time t >30 T (T: wave period) after the first wave reaches the revetment structure (Roca Barceló (2014)).

b) Mean water level for wave impact loads

Among the conditions tested in the parameter study, the flatter slopes 1:4 and 1:6 are the most likely to result in impact wave loads. The external MWL (eMWL) and the internal MWL (iMWL) on a PBA-revetment with a slope steepness 1:6 are shown Fig. 4-9 for different revetment-filter thicknesses d_{rev}.

In contrast to the non-impact wave conditions (ξ_0>3.4), the MWL induced by impact wave loads (ξ_0<3.4) is dependent not only on the wave height but also on the wave period (s. Fig. 4-9). The eMWL for impact waves is affected by the wave height, the wave period and also by the revetment-filter thickness. The wave set-up on the revetment slope is higher when the revetment-filter thickness decreases and thus the eMWL is higher (Fig. 4-9).

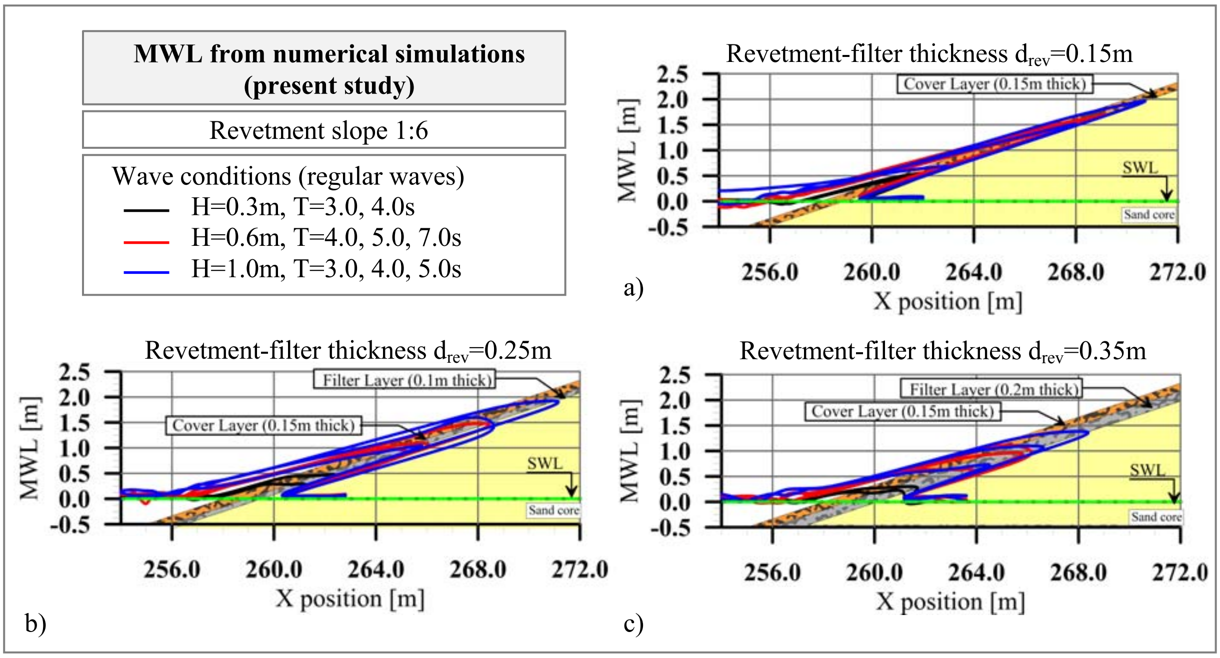

Fig. 4-9: External and Internal MWL for ***impact wave loads*** on a PBA-revetment (slope 1:6) with different revetment-filter thicknesses d_{rev}: a) d_{rev}=0.15m, b) d_{rev}=0.25m, c) d_{rev}= 0.35m.

The revetment-filter thickness significantly affects the iMWL for impact waves, especially at the revetment/filter layers. Thus, similar to the eMWL, the iMWL is higher when the revetment-filter thickness decreases. Furthermore, the iMWL in the revetment and the filter is also higher for impact wave loads (Fig. 4-9) than for non-impact wave loads (Fig. 4-8).

4.2.2 Wave set-up on and beneath the revetment

The external wave set-up on the revetment $\overline{\eta}_{S1,RuG}$ (s. Fig. 4-7) related to the wave length in deep water ($\overline{\eta}_{S1,RuG}/L_0$ with $L_0= gT^2/2\pi$) and to the wave height H_0 is firstly analysed in this section. The relationship between $\overline{\eta}_{S1,RuG}$ and the internal wave set-up just beneath the revetment ($\overline{\eta}_{S2,RuG}$) and on top of the sand core ($\overline{\eta}_{S3,RuG}$) is also considered within the analysis. Furthermore, prediction formulae are developed for the estimation of $\overline{\eta}_{S1,RuG}$, $\overline{\eta}_{S2,RuG}$ and $\overline{\eta}_{S3,RuG}$. Distinction between impact and non-impact wave loads will be considered during the analysis of $\overline{\eta}_{S1,RuG}$, $\overline{\eta}_{S2,RuG}$ and $\overline{\eta}_{S3,RuG}$ in case it is necessary for better understanding of the process.

a) External wave set-up on the revetment $\eta_{S1,RuG}$

The results of the relative wave set-up ($\overline{\eta}_{S1,RuG}/L_0$) as function of the surf similarity parameter (ξ_0) given by the parameter study showed that $\overline{\eta}_{S1,RuG}/L_0$ is inverse proportional to the surf similarity parameter and, especially for $\xi_0<4.0$ (plunging and collapsing breakers), it is dependent on the slope steepness (Fig. 4-11), result that has also been found by Foyer (2013). Furthermore, $\overline{\eta}_{S1,RuG}/L_0$ results larger for steeper slopes than for the flatter slopes for the same surf similarity parameter. Similar findings have been described in previous studies (e.g., Bowen et al. (1968); Lo (1988); Foyer (2013)). The effect of the revetment-filter thickness

d_{rev} was found in the parameter study not to define a clear tendency (s. Alcérreca-Huerta & Oumeraci (2014)). However, the effect of d_{rev}, though not clear, is lower than that of the slope steepness.

A set of curves ($\bar{\eta}_{S1,RuG}/L_0$ vs. ξ_0) were first tentatively fitted to the dataset considering the different slope steepness of the PBA-revetment. These curves are described by eq. (4.7) where the tentative coefficients A and B are found in Table 4-3.

Table 4-3: Tentative coefficients A and B for the prediction of the external relative wave set-up $\bar{\eta}_{S1,RuG}/L_0$, considering different slope steepnesses using eq. (4.7).

	PBA-revetment slope				
	cot α_1=1.5	cot α_2=2.0	cot α_3=3.0	cot α_4=4.0	cot α_5=6.0
Coefficient A	0.690	0.528	0.158	0.107	0.032
Coefficient B	-2.517	-2.648	-2.296	-2.276	-1.820
Coeff. of determination (r^2)	0.958	0.919	0.918	0.925	0.855
Coeff. of variation ($CoV=\sigma_x/\bar{x}$)	31.6%	33.3%	32.9%	32.0%	31.0%

$$\frac{\bar{\eta}_{S1,RuG}}{L_0} = A \cdot \xi_0^{\ B} \tag{4.7}$$

Coefficients A and B were found to be function of the slope steepness cot α as shown in eqs. (4.8), (4.9) and in Fig. 4-10 (valid for $\xi_0>0.8$ and for $1.5<\cot\alpha<6.0$). The coefficient of determination and of variation were $r^2=0.98$ and CoV=16.0% for coefficient A and $r^2=0.91$ and CoV=3.5% for coefficient B. Therefore, the prediction formula for the relative external relative wave set-up ($\bar{\eta}_{S1,RuG}/L_0$) with explicit account for the slope steepness is shown in Fig. 4-11 (eq. (4.7) with A and B from eq. (4.8) and eq. (4.9)).

$$A = 2.03(\cot\alpha)^{-2.245} \tag{4.8}$$

$$B = 0.168 \cdot \cot\alpha - 2.867 \tag{4.9}$$

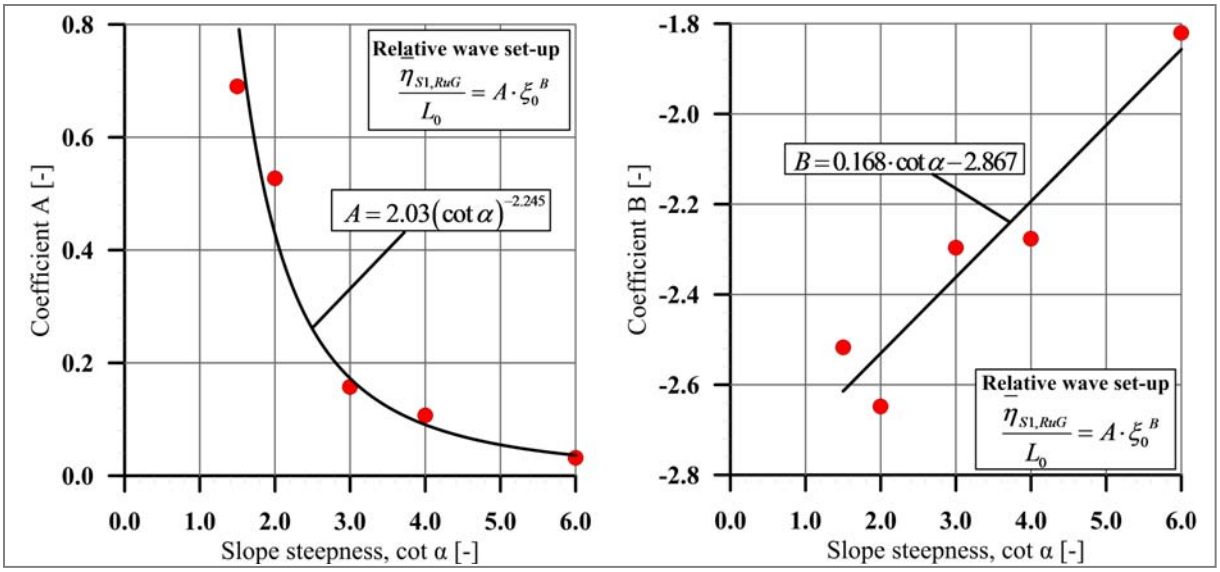

Fig. 4-10: Coefficients A and B for the prediction of the external relative wave set-up ($\bar{\eta}_{S1,RuG}/L_0$) using eq. (4.7).

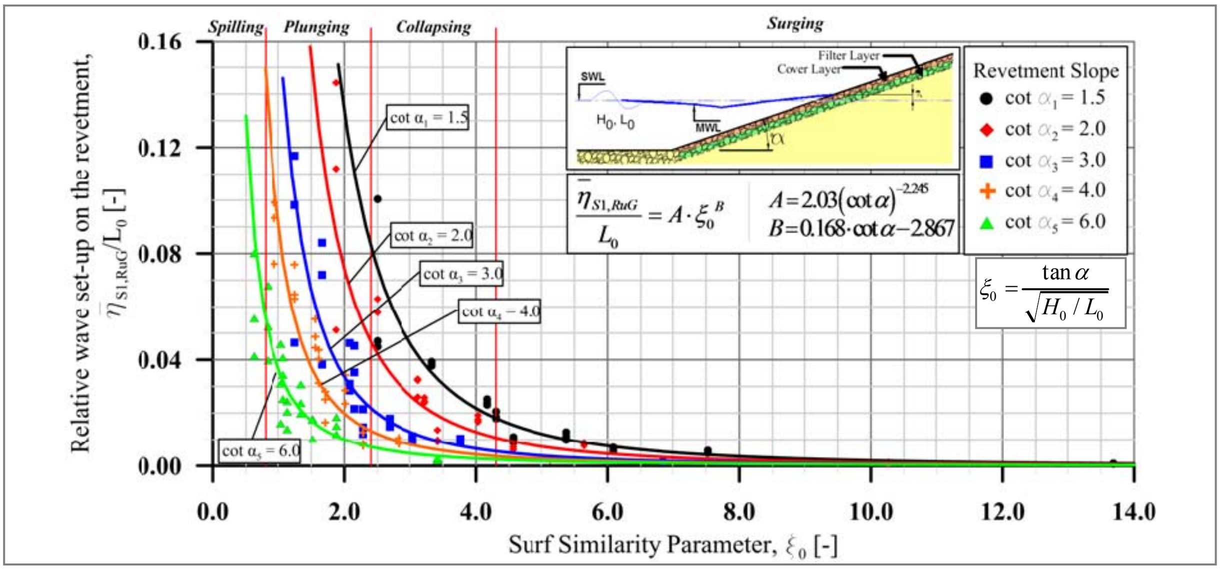

Fig. 4-11: Prediction formulae for the external relative wave set-up ($\overline{\eta}_{S1,RuG}/L_0$) vs. surf similarity parameter.

The relative wave set-up on the revetment $\overline{\eta}_{S1,RuG}/H_0$ is affected by the slope steepness as expected but, due to the scatter in the data against the surf similarity parameter (Fig. 4-12), the dependency of the wave set-up on the wave height is not clear. However, the scatter of the data is clearly limited by an upper envelope (which for impact wave loads is dependent on the revetment-filter thickness d_{rev}) and a lower envelope (Fig. 4-12) for the wave set-up, result also observed on data from Foyer (2013). These envelopes are related to the steady component of the wave set-up which is produced due to the increment of the water level in order to balance the onshore component of the momentum flux. The dynamic component also named dynamic wave set-up or surf beat (Lo (1988); Hedges & Mase (2004); Dean & Walton (2010)) is described by infragravity waves which could have periods of 0.4 to 4 minutes (Herbers et al. (1995)) and consequently could not be recorded in the parameter study where the simulation test duration was set only to 10-20 waves.

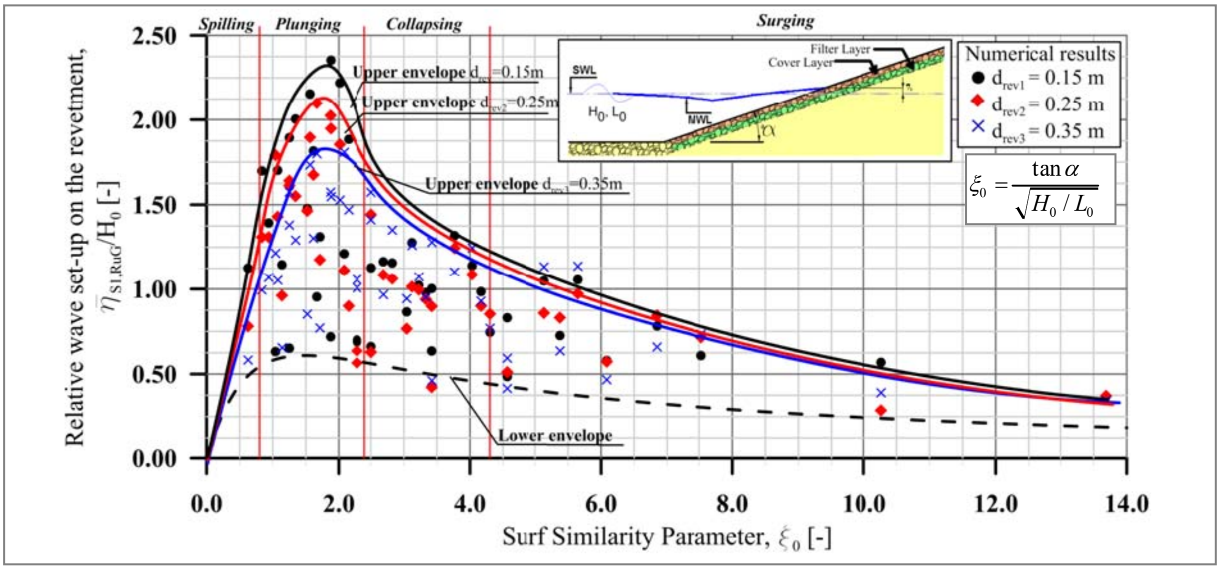

Fig. 4-12: Relative wave set-up $\overline{\eta}_{S1,RuG}/H_0$ vs. surf similarity parameter: effect of revetment-filter thicknesses d_{rev}

The minimum value of the steady wave set-up is given by the lower envelope of the wave set-up related to the wave height $\overline{\eta}_{S1,RuG}/H_0$ (Fig. 4-12) and described by eq. (4.10). On the other hand, the maximum value of the steady wave set-up related to the wave height $\overline{\eta}_{S1,RuG}/H_0$ is given by the upper envelope for a revetment-filter thickness d_{rev}=0.15m (Fig. 4-12) which can be described by eq. (4.11).

$$\left(\frac{\overline{\eta}_{S1,RuG}}{H_0}\right)_{\min}=\frac{1.35\cdot\xi_0}{1+0.864\cdot\xi_0+0.454\cdot\xi_0^{\,2}} \tag{4.10}$$

$$\left(\frac{\overline{\eta}_{S1,RuG}}{H_0}\right)_{\max}=\frac{1.58\cdot\xi_0}{1-0.442\cdot\xi_0+0.359\cdot\xi_0^{\,2}} \tag{4.11}$$

Furthermore, $\overline{\eta}_{S1,RuG}/L_0$ in eq. (4.7) can be also expressed in terms of the wave height. For this purpose, equation (4.7) is multiplied by H_0/L_0 and afterwards, since coefficient A is function of the slope steepness, it is possible to obtain eq. (4.12) which is described in terms of the surf similarity parameter:

$$\frac{L_0}{H_0}\left[\frac{\overline{\eta}_{S1,RuG}}{L_0}=A\cdot\xi_0^{\,B}\right]\rightarrow\frac{\overline{\eta}_{S1,RuG}}{H_0}=\frac{L_0}{H_0}\cdot A\cdot\xi_0^{\,B}=\frac{L_0}{H_0}\cdot\frac{2.03}{(\cot\alpha)^2(\cot\alpha)^{0.245}}\cdot\xi_0^{\,B}=\xi_0^{\,2}\frac{2.03}{(\cot\alpha)^{0.245}}\cdot\xi_0^{\,B}$$

$$\rightarrow\frac{\overline{\eta}_{S1,RuG}}{H_0}=2.03(\cot\alpha)^{-0.245}\,\xi_0^{\,B+2}=2.03(\cot\alpha)^{-0.245}\,\xi_0^{\,0.168(\cot\alpha)-0.867} \tag{4.12}$$

The relative wave set-up related to the wave height $\overline{\eta}_{S1,RuG}/H_0$ (eq. (4.12)) as function of the surf similarity parameter, as well as its minimum (eq. (4.10)) and maximum value (eq. (4.11)) are shown in Fig. 4-13. The validity of these prediction formulae for $\xi_0 < 0.8$ should be verified with further studies since no results from the parameter study were obtained within this ξ_0-range.

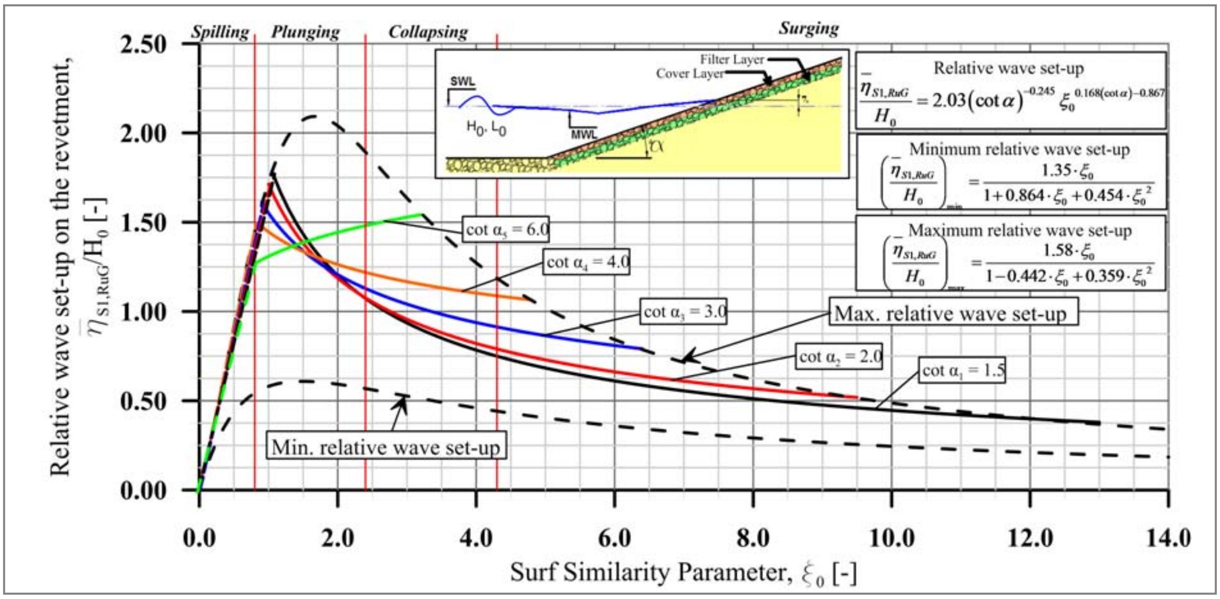

Fig. 4-13: Prediction formulae for the external relative wave set-up ($\overline{\eta}_{S1,RuG}/H_0$) vs. surf similarity parameter (eq. (4.12)) and its lower (eq. (4.10)) and upper envelope (eq. (4.11)).

Overall, the analysis has shown that, especially for plunging and collapsing breakers, the revetment-thickness has a significant effect on the relative wave set-up related to the wave height ($\overline{\eta}_{S1,RuG}/H_0$). However, the slope steepness is the key parameter affecting the wave set-up on the revetment with a larger influence than the revetment-filter thickness.

b) *Internal wave set-up*

The internal wave set-up at the revetment-filter interface $\overline{\eta}_{S2,RuG}$ and at the filter-sand core interface $\overline{\eta}_{S3,RuG}$ (s. Fig. 4-7) were analysed through comparison with the external wave set-up on the revetment $\overline{\eta}_{S1,RuG}$ and the results from all numerical tests are described in Fig. 4-14, showing that the internal set-up is linearly dependent on the external set-up. Therefore, the internal wave set-up at the revetment-filter interface ($\overline{\eta}_{S2,RuG}$) can be expressed as in eq. (4.13) and the wave set-up on the sand core ($\overline{\eta}_{S3,RuG}$) as in eq. (4.14). The prediction formulae in eq. (4.13) and eq. (4.14) provided a coefficient of determination and a coefficient of variation r^2=0.982, CoV=24.05% and r^2=0.996, CoV=27.9%, respectively.

$$\overline{\eta}_{S2,RuG} = 1.218 \cdot \overline{\eta}_{S1,RuG} \tag{4.13}$$

$$\overline{\eta}_{S3,RuG} = 0.993 \cdot \overline{\eta}_{S2,RuG} \quad \rightarrow \overline{\eta}_{S3,RuG} = 1.210 \cdot \overline{\eta}_{S1,RuG} \tag{4.14}$$

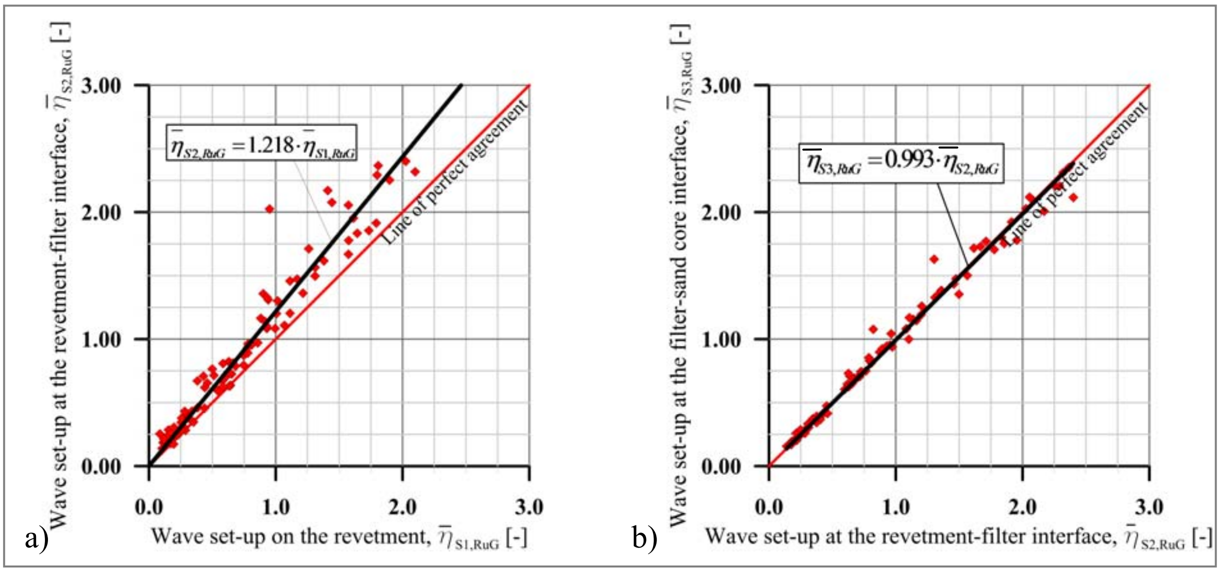

Fig. 4-14: Prediction formulae for the internal set-up at different layers of the PBA-revetment: a) wave set-up at the revetment-filter interface $\overline{\eta}_{S2,RuG}$ vs. $\overline{\eta}_{S1,RuG}$ and b) wave set-up on the sand core $\overline{\eta}_{S3,RuG}$ vs. $\overline{\eta}_{S2,RuG}$.

The behaviour of the internal set-up based on the results of the parameter study can be described as follows: the wave set-up increases its magnitude in the PBA-revetment until it reaches its maximum at the interface with the filter layer. If the filter layer has a similar permeability to that of the PBA-revetment, then the wave set-up remains similar up to the interface with the sand core (Fig. 4-15). Afterwards, the wave set-up decreases considerably inside the sand core thus resulting in high gradients at the filter-sand core interface (s. Fig. 4-8 and Fig. 4-9).

The development in time of the wave set-up is exemplarily shown in Fig. 4-15 considering the time series of numerical run-up gauges on the revetment, at the revetment-filter interface and on the filter-sand core interface for a numerical simulation with non-impact wave loads (H=0.6m, T=5.0s, h=4.0m, d_{rev}=0.25m & ξ_0=2.67).

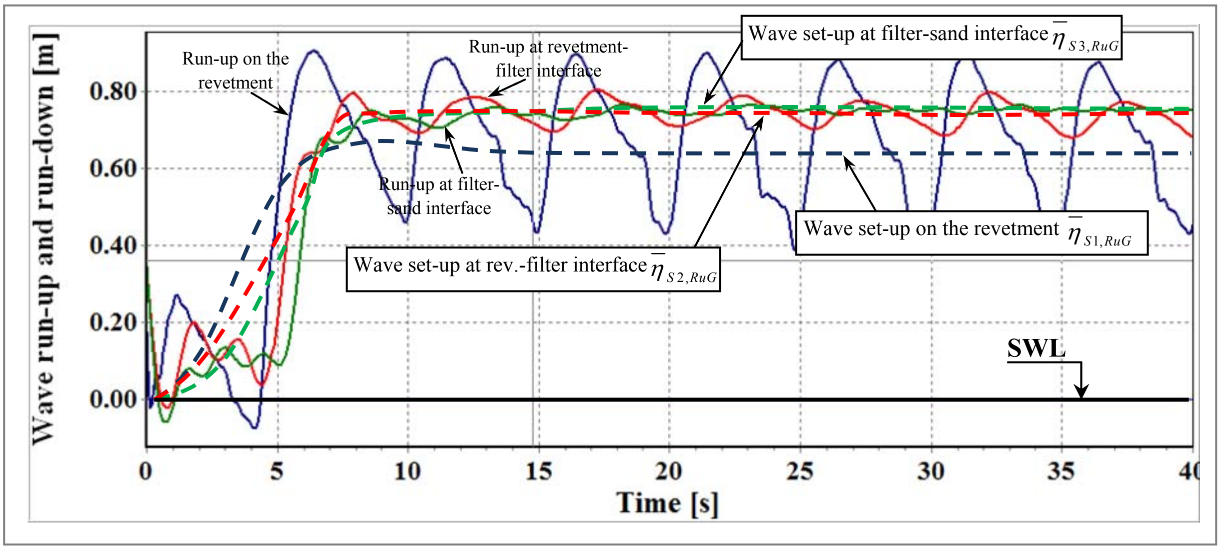

Fig. 4-15: Wave run-up and run-down time series with variation of the wave set-up at different locations: on the revetment ($\overline{\eta}_{S1,RuG}$), at the revetment-filter interface ($\overline{\eta}_{S2,RuG}$) and at the filter-sand core interface ($\overline{\eta}_{S3,RuG}$) of PBA-revetments.

The eMWL and the iMWL are higher when the revetment-filter thickness decreases. Moreover, the iMWL in the revetment and the filter layer is higher for impact waves (Fig. 4-9) than for non-impact waves (Fig. 4-8). A variation of the wave period affects the iMWL for both impact and non-impact waves, but particularly for impact waves, the wave height is also relevant. The slope steepness is the key parameter affecting the wave set-up on the revetment with a large influence than the revetment-filter thickness. Also, the wave set-up at the revetment-filter interface ($\overline{\eta}_{S2,RuG}$) is larger than the wave set-up on the revetment $\overline{\eta}_{S1,RuG}$ (Fig. 4-14a and Fig. 4-15), while the wave set-up at the filter-sand core interface $\eta_{S3,RuG}$ has a similar magnitude to that on the revetment $\overline{\eta}_{S1,RuG}$ (Fig. 4-14b and Fig. 4-15).

4.3 Wave run-up and run-down

The numerical data of the wave run-up and run-down obtained from the parameter study are analysed with a focus on the effect of the revetment-filter thickness on both parameters as well as on the associated hydrodynamic processes on the revetment, inside the revetment-filter layers and in the sand core beneath the revetment. Moreover, results of the wave run-up/ run-down related to the SWL as well as to the MWL are described, and prediction formulae are developed.

4.3.1 Wave run-up and run-down on and beneath the revetment: analysis related to the SWL

A definition sketch of the run-up (Ru) and run-down (Rd) on the revetment related to the SWL is shown in Fig. 4-16, where also the definition of the run-up and run-down at the revetment-filter interface (Ru_{Lay2} & Rd_{Lay2}, respectively) and on the sand core of the embankment (Ru_{Lay3} & Rd_{Lay3}, respectively) is depicted.

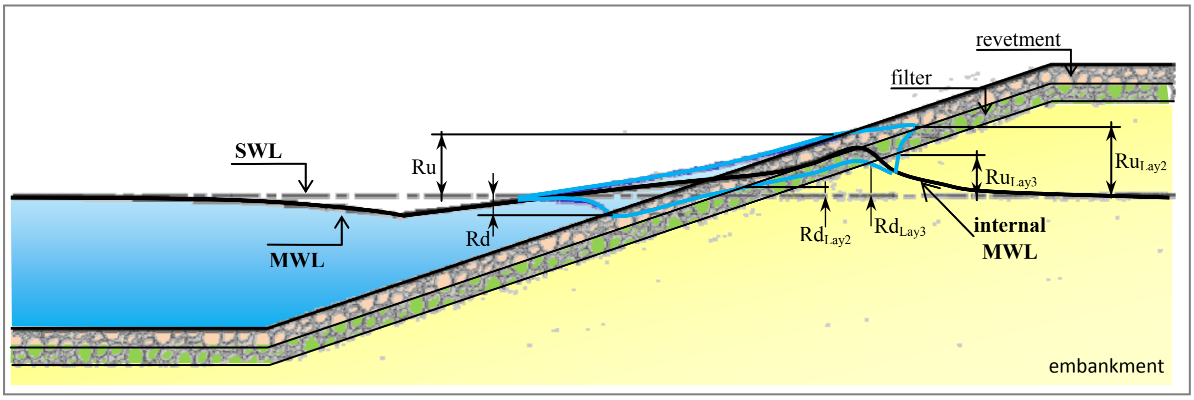

Ru = Wave run-up on the revetment
Ru_{Lay2} = Wave run-up at the revetment-filter interface
Ru_{Lay3} = Wave run-up at the filter-sand interface
Rd = Wave run down on the revetment
Rd_{Lay2} = Wave run down at the revetment-filter interface
Rd_{Lay3} = Wave run down at the filter-sand interface

Fig. 4-16: Wave run-up and run-down on the revetment related to the SWL: definition sketch.

The results of the analysis for the relative run-up and run-down on the PBA-revetments are shown in Fig. 4-17a and Fig. 4-17b, respectively, for different revetment-filter thicknesses (d_{rev}) and compared with the existing formulae (commonly related to SWL) for smooth impermeable slopes as a reference. For the run-up and run-down on smooth impermeable slopes, the formula of EurOtop (2007) (eq. (4.15)) and the formula by Schüttrumpf (2001) (eq.(4.16)) are considered for comparison with the numerical results (Fig. 4-16).

$$\frac{Ru_{2\%}}{H_{m0}} = \min\left(1.65 \cdot \xi_{m-1,0}\ ,\ 4 - \frac{1.5}{\sqrt{\xi_{m-1,0}}}\right) \tag{4.15}$$

$$\frac{Rd_{2\%}}{H_S} = -0.7\left[1 + \tanh\left(\xi_0 - 2.1\right)\right] \tag{4.16}$$

Lower run-up values for the PBA-revetment than for the smooth impermeable slopes are generally obtained (see Fig. 4-17), and as expected, an increase of d_{rev} results in lower run-up value. The maximum run-up occurs for $1.5<\xi_0<2.5$ (mostly plunging waves) and afterwards the run-up tends to a value $Ru/H_0 \approx 1.8$ for $\xi_0>6.0$ where the revetment filter thickness has no noticeable effect. Therefore, the maximum run-up in PBA-revetments occurs for plunging and collapsing breakers, while the run-up for surging breakers is smaller. The later indicates an opposite trend to that of smooth impermeable revetments as shown in Fig. 4-17a.

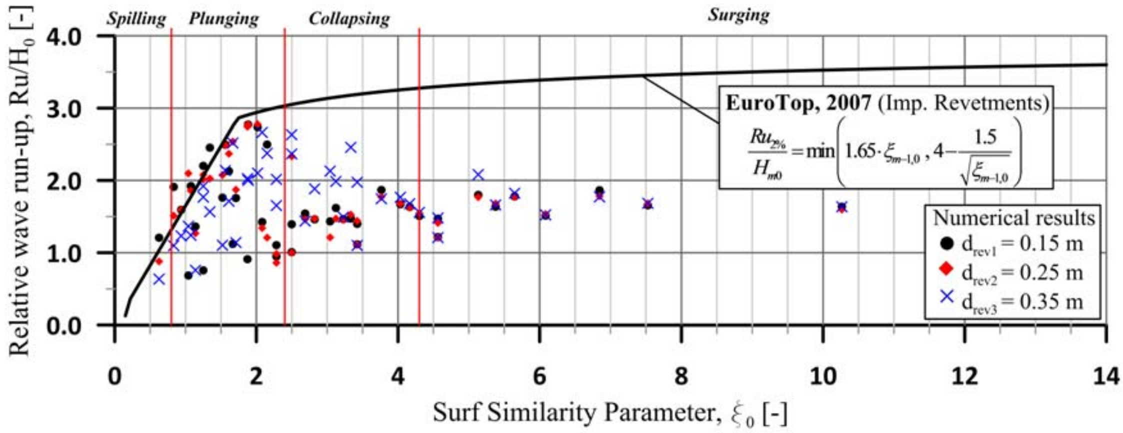

a) Relative wave run-up vs. surf similarity parameter referred to SWL

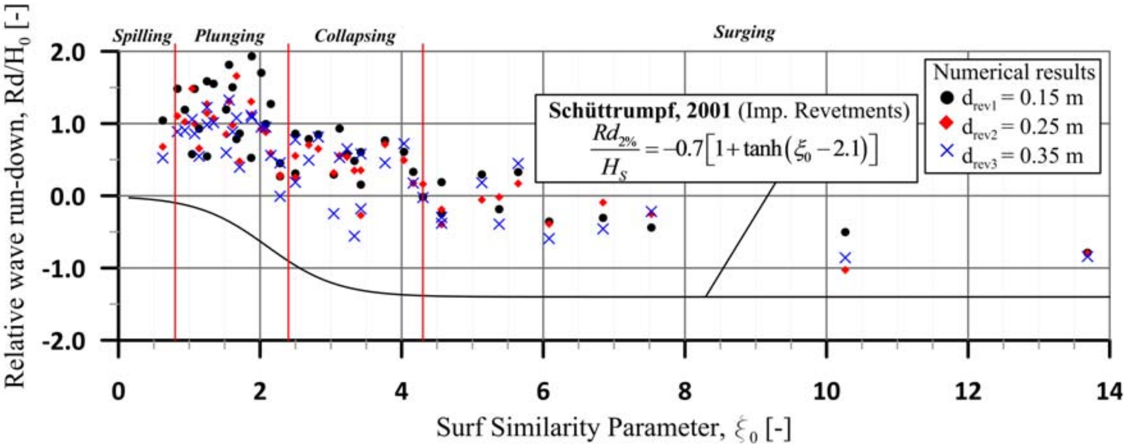

b) Relative wave run-down vs. surf similarity parameter referred to SWL

Fig. 4-17: Relative wave run-up (a) and run-down (b) vs. surf similarity parameter referred to SWL for different PBA-revetment-filter thicknesses d_{rev} and comparison with smooth impermeable revetments.

For collapsing waves with $2.4 < \xi_0 < 3.5$ and particularly with $d_{rev}=0.35$m, the wave run-up is higher than that with $d_{rev}=0.15$m and $d_{rev}=0.25$m. A similar behaviour has also been observed in the results from the regular wave tests in GWK (s. Oumeraci et al. (2010)) where the maximum run-up is found for $\xi_0=2.0\text{-}4.0$: larger wave run-up occurs for $d_{rev}=0.25$ than for $d_{rev}=0.15$m.

The aforementioned result could be consequence of the interaction between the incident wave and the previous run-down (Fig. 4-18): i) once wave run-up reaches its maximum, wave rush-down occurs on the revetment (forming a water layer on the revetment) and inside the revetment and filter layers, ii) the water layer on the revetment during the rush-down cannot easily infiltrate through thinner revetment-filters and consequently, a water layer thickness can be found on the slope, iii) the incident wave run-up collides with the remaining water layer on the revetment which velocity moves in opposite direction, iv) with smaller d_{rev}, the interaction increases as the water layer on the revetment increases which may induce a smaller wave run-up.

The aforementioned interaction is of great importance particularly for collapsing breakers, since the breaker glides through the revetment slope in direct contact with it at any time, while plunging breakers can role and splash on the slope. Surging breakers are not affected by the revetment-filter thickness as observed in the results (Fig. 4-17a) and in previous studies (e.g., Oumeraci et al. (2010); Foyer (2013)).

Collapsing breaker: velocity field (ξ=3.32) with different d_{rev}*
Regular waves: H=1.0m, T=4.0s, h=4.0m, Slope 1:1.5

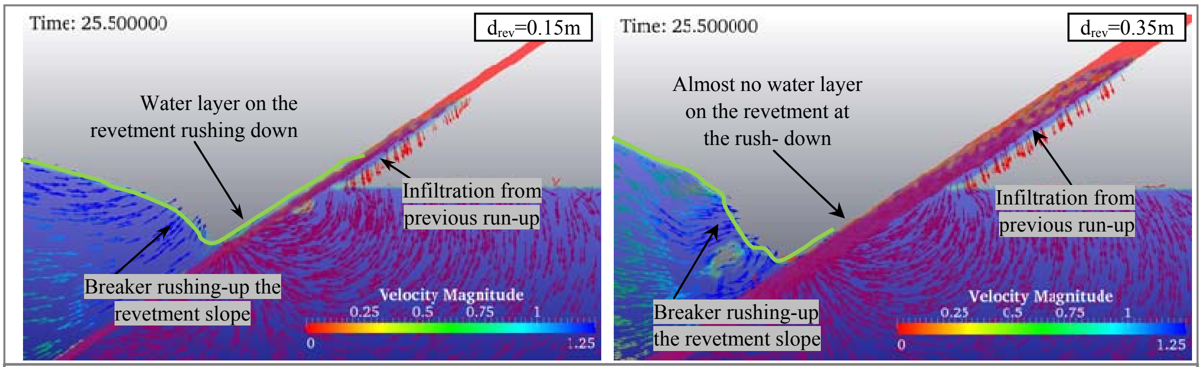

a) Once wave run-up is reached its maximum (Fig. 4-18c), wave rush-down occurs on and inside the revetment and filter layers. The water layer cannot easily infiltrate trough thinner revetment-filters forming a water layer on the revetment.

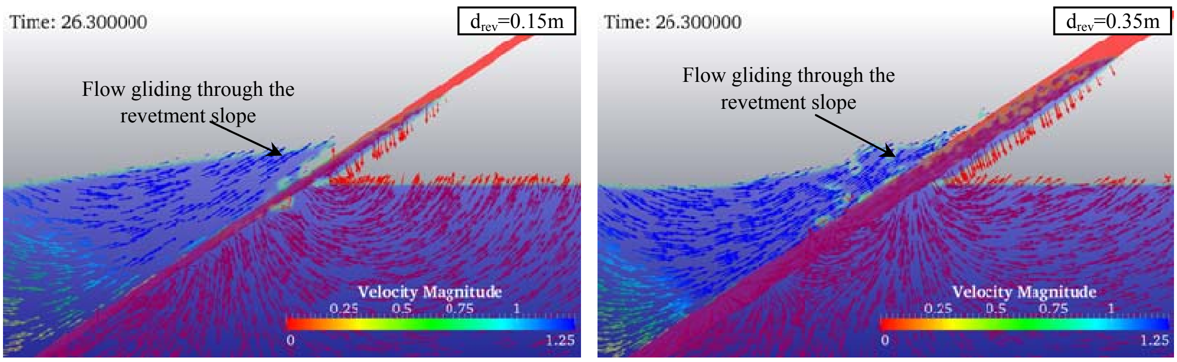

b) The incident wave run-up collides with the remaining water layer on the revetment which flows in opposite direction and therefore, the run-up is affected since the flow for collapsing waves is almost at any time gliding the revetment surface.

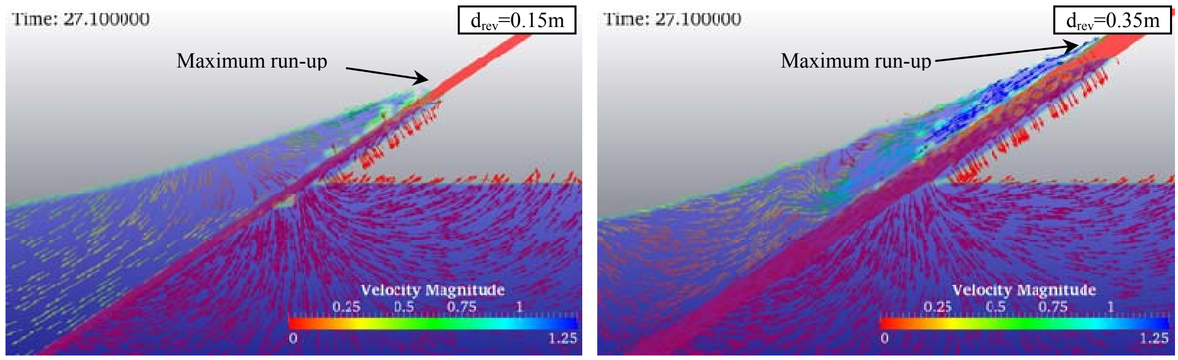

c) With thinner revetment-filter thickness d_{rev}, the interaction increases with increasing water layer on the revetment which may result in a smaller wave run-up.

**Velocity vector length not scaled (the colour indicates its magnitude according to scale).*

Fig. 4-18: Effects of the interaction between the incident wave and previous wave run-down on the wave run-up for collapsing breaker comparatively for revetment-filter thickness d_{rev}=0.15m and d_{rev}=0.35m.

Regarding the wave run-down, the PBA-revetments shows a shift upwards, referred to the SWL (Fig. 4-17b), in comparison to smooth impermeable revetments. The wave run-up is not shifted upwards to the SWL and thus, the swash zone for permeable revetments is smaller than for impermeable slopes. For $\xi_0<3.0$, the run-down mainly takes place above the SWL, result that has also been observed in other studies (e.g. Oumeraci et al. (2010); Foyer & Oumeraci (2013b)).

The maximum run-down location on the revetment moves upwards with decreasing revetment-filter thickness d_{rev} because the water layer over the revetment during the rush-down cannot easily infiltrate through thinner revetment-filters. Consequently, a water layer thickness develops on the revetment slope as shown exemplarily in Fig. 4-19 for plunging breakers and also in Fig. 4-18 for collapsing breakers.

Plunging breaker: velocity field (ξ=1.25) with different d_{rev}*
Regular waves: H=1.0m, T=3.0s, h=4.0m, Slope 1:3

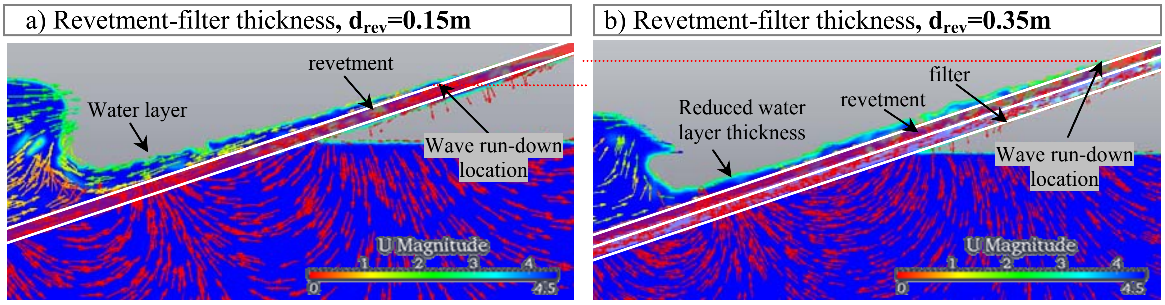
a) Revetment-filter thickness, $\mathbf{d_{rev}=0.15m}$

b) Revetment-filter thickness, $\mathbf{d_{rev}=0.35m}$

The water layer over the revetment before breaking is larger for a d_{rev}=0.15m, than for d_{rev}=0.35m. Also, the maximum wave run - down location is modified due to the presence of this layer.

**Velocity vector length not scaled (the colour indicates its magnitude according to scale). Same geometry scale*

Fig. 4-19: Development of the water layer over the PBA-revetment and modification of the wave run-down location for different d_{rev}.

The wave run-up at the revetment-filter interface Ru_{Lay2} has nearly the same magnitude as that on the revetment (Ru). Similar to the wave run-up on the revetment Ru, an increase in d_{rev}, also results in a reduction of Ru_{Lay2}, except for collapsing breakers and d_{rev}=0.35m. However, when larger surf similarity parameters, similar to wave run-up on the revetment, these effects become smaller and negligible for $\xi_0>6.0$. Beyond this value, the relative wave run-up remains approximately constant with $Ru/H_0\approx1.8$ on the revetment and $Ru_{Lay2}/H_0\approx1.3$ at the revetment-filter interface. Moreover, the maximum Ru_{Lay2} takes place around $\xi_0\approx1.9$ for d_{rev}=0.25 m and with $\xi_0\approx2.1$ for d_{rev}=0.35 m; i.e., an increase in thickness d_{rev} causes the maximum Ru_{Lay2} to shift to higher ξ_0–values. For the wave run-down, in contrast to the wave run-up, larger differences are observed between the run-down on the revetment Rd and that at the revetment-filter interface Rd_{Lay2}. The main difference is that for $\xi_0<10$, the run-down at the revetment-filter interface Rd_{Lay2} is always located above the SWL as consequence of the increase of the internal water table. Further details can be consulted in Alcérreca-Huerta & Oumeraci (2014).

The wave run-up Ru_{Lay3} and run-down Rd_{Lay3} at the filter-sand core interface were also analysed. The results lead to the conclusion that an increase of d_{rev} induces a significant reduction in both Ru_{Lay3} and Rd_{Lay3}. The values of Ru_{Lay3} and Rd_{Lay3} referred to the SWL are quite similar and therefore, the "swash" zone at the filter-sand core is strongly reduced through the revetment and the filter layer (s. Alcérreca-Huerta & Oumeraci (2014)). This reduction of the swash zone is favourable for the stability of the top layers of the sand core since the water motion which can cause turbulence and erosion is also reduced.

4.3.2 Wave run-up and run-down on and beneath the revetment: analysis related to the mean water level (MWL)

The wave run-up and run-down related to MWL was investigated in previous studies (Hedges & Mase (2004); Dean & Walton (2008)) and more recently by Foyer & Oumeraci (2013b). Particularly, the later showed more systematically how the wave set-up affects most of the hydrodynamic processes on and beneath the revetment, including the wave run-up and run-down.

The relative wave run-up and run-down in the revetment related to MWL are defined as $(Ru\text{-}\eta_{S1,RuG})/H_0$ and $(Rd\text{-}\eta_{S1,RuG})/H_0$, where Ru and Rd are respectively the run-up and run-down, on the revetment related to SWL, H_0 is the wave height and $\eta_{S1,RuG}$ is the wave set-up on the revetment. Similarly, the relative wave run-up and run-down related to MWL at the revetment-filter interface ($(Ru_{Lay2}\text{-}\eta_{S2,RuG})/H_0$ and $(Rd_{Lay2}\text{-}\eta_{S2,RuG})/H_0$)) and at the filter-sand core interface ($(Ru_{Lay3}\text{-}\eta_{S3,RuG})/H_0$ and $(Rd_{Lay3}\text{-}\eta_{S3,RuG})/H_0$)) are defined with $\eta_{S2,RuG}$ and $\eta_{S3,RuG}$ as the wave set-up at the corresponding layer (s. Section 4.2.2). A definition sketch of the internal and external wave run-up and run-down related to the MWL is shown in Fig. 4-20.

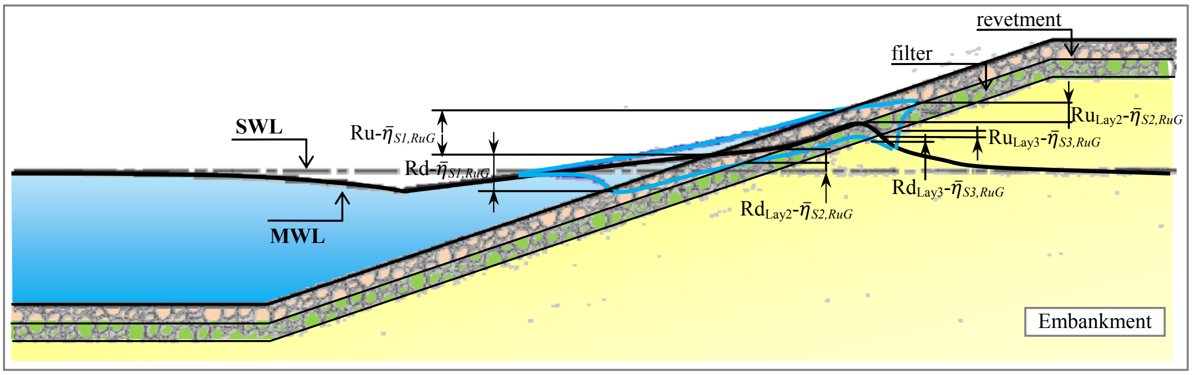

$\bar{\eta}_{S1,RuG}$= Wave set-up on the revetment
$\bar{\eta}_{S2,RuG}$ =Wave set-up at filter-rev. interface
$\bar{\eta}_{S3,RuG}$ = Wave set-up at filter-sand interface

Ru = Wave run-up on the revetment
Ru_{Lay2} = Wave run-up at the rev.-filter interface
Ru_{Lay3} = Wave run-up at the filter-sand interface

Rd = Wave run down on the revetment
Rd_{Lay2} = Wave run down at the rev.-filter interface
Rd_{Lay3} = Wave run down at the filter-sand interface

Fig. 4-20: Definition sketch for the wave run-up and run-down related to MWL at the revetment-filter interface ($Ru\text{-}\eta_{S2,RuG}$ and $Rd\text{-}\eta_{S2,RuG}$) and at the filter-sand core interface ($Ru\text{-}\eta_{S3,RuG}$ and $Rd\text{-}\eta_{S3,RuG}$).

a) Wave run-up and run-down on the revetment related to the MWL

The relative wave run-up and run-down on the revetment related to MWL are plotted in Fig. 4-21 against the surf similarity parameter for three different values of revetment-filter thickness d_{rev} and compared to the formulae developed by Foyer & Oumeraci (2013b). It is clearly observed from Fig. 4-21 that the revetment-filter thickness d_{rev} affects the wave run-up and run-down, depending on the prevailing breaker type: larger thicknesses d_{rev} unexpectedly result in larger run-up and run-down values and this effect is more pronounced for plunging and collapsing breakers than for surging breakers.

This unexpected behaviour was also observed in the results of the wave run-up related to SWL especially for collapsing breakers and, as already mentioned (see section 4.3.1), it might be explained as a consequence of the water layer rushing down the revetment slope and colliding with the incident breaker rushing-up, where the thickness of the present water layer is dependent on the revetment-filter thickness d_{rev} (larger d_{rev} increases the water layer thickness). Further reasons for this unexpected behaviour might be also summarized as follows:

i. Thicker revetment-filter layers have a larger absorption capacity, so that a higher amount of air-water mixture from the entrapped air during the wave breaking process is introduced into the revetment-filter layer and a reduced water layer on the revetment will result (see Fig. 4-18 and Fig. 4-19).
ii. Due to the increase of the air-water mixture inside the revetment-filter, higher turbulence is produced, and thus the water motion increases to ensure a momentum balance. The water flow velocity inside the revetment and filter layers is limited due to their permeability, and consequently the momentum balance is achieved by increasing and decreasing the water elevation (i.e. larger run-up and run-down related to MWL).

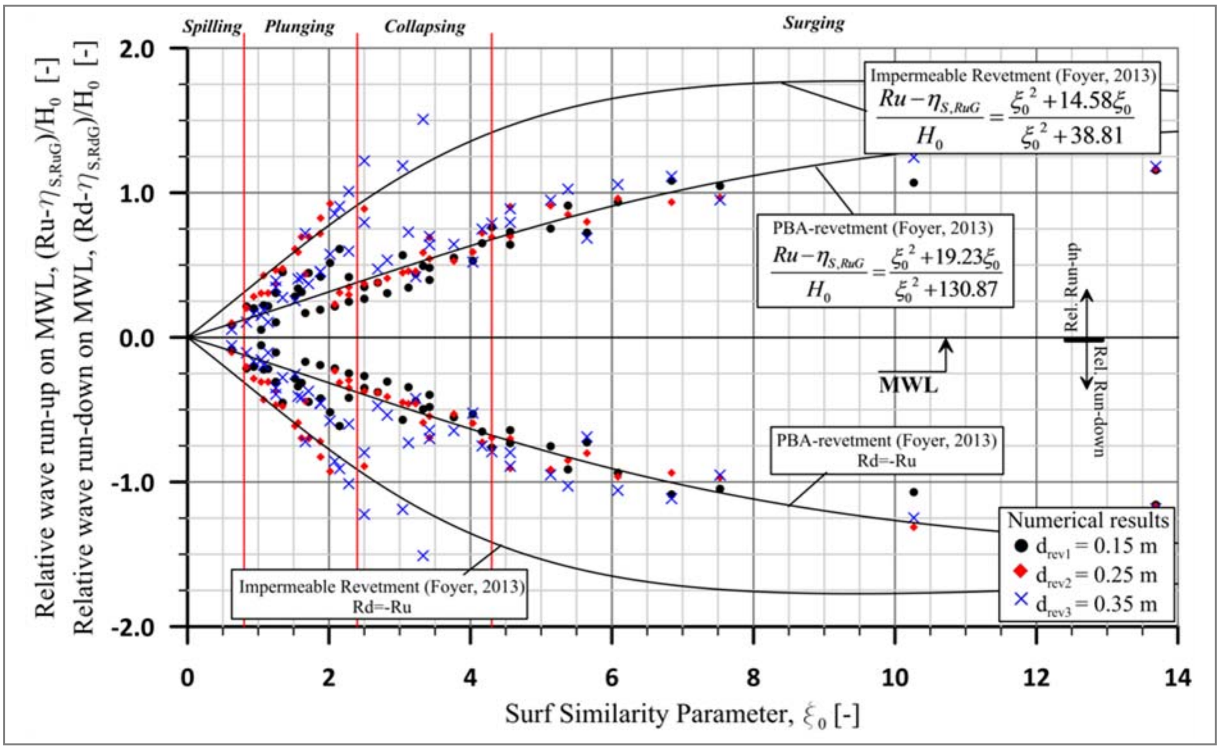

Fig. 4-21: Relative wave run-up and run-down on the revetment related to MWL vs. surf similarity parameter: effects of revetment-filter thickness and comparison with exiting formulae from Foyer (2013), for PBA- and smooth impermeable revetments.

A similar behaviour to that of the present parameter study has also been observed in: a) the GWK tests and b) results from the numerical simulations from Foyer & Oumeraci (2013b). Further details can be found in Alcérreca-Huerta & Oumeraci (2014).

Also, larger revetment-filter thicknesses are more likely to provide the occurrence of a so called "resonance effect" as described by Bruun (1974) and Bruun & Günbak (1977) for waves on slope revetments: "*Such as situation may occur if the down-rush period is equal to the wave period, assuming that down-rush is at its lowest position at the toe of the breaking wave so that every down-rush meets a breaking wave at the lowest position of the down-rush"*. Therefore, the resonance effect found within $2.0<\xi_0<4.0$ is closely related to the thickness of a water layer on the revetment during wave breaking: the increase of this water layer (also dependent on the revetment-filter thickness d_{rev}) produces a wave damping which may decrease the wave run-up and run-down, the wave reflection and also the wave-induced pressure on the revetment.

Prediction formulae for the relative wave run-up and run-down related to MWL on and beneath the revetment are developed below based on results of Foyer & Oumeraci (2013b) as well as on the findings described in this section. For this purpose, prediction formulae are proposed for the lower and upper envelope in order to consider that the maximum relative wave run-up and run-down is dependent on the revetment-filter thickness and related also to MWL.

The prediction formulae for the lower and upper envelope were calculated through OriginPro9 considering the following procedure: i) the data points sorted in terms of the independent variable (i.e., in terms of ξ_0 for this case) are linearly connected, ii) the derivative is calculated and the minima and maxima events are obtained, iii) a cubic spline interpolation with a smoothing Adjacent-Averaging method (OriginLab (2014)) is performed considering the minima/maxima events and iv) a fitting function is applied considering the minima events to obtain the lower envelope and the maxima events for the upper envelope. Therefore, the lower envelope of the relative run-up and run-down related to MWL on the revetment is provided by the prediction formula from Foyer (2013) expressed in eq. (4.17) and as shown in Fig. 4-22. Eq. (4.17) becomes zero when $\xi_0=0$ and becomes asymptotic to 1.0 when $\xi_0 \rightarrow \infty$. A maximum is obtained when $\xi_0=19.23$ where the relative wave run-up and run-down related to MWL is larger than 1.0 before becoming asymptotic to this value.

Lower envelope:
$$\left(\frac{Ru-\eta_{S,RuG}}{H_0}\right)_{LE}=\frac{\xi_0^{\,2}+19.23\cdot\xi_0}{\xi_0^{\,2}+130.87} \qquad (4.17)$$

The prediction formula for the upper envelope is described by eq. (4.18) which is dependent on coefficient A that varies as function of the revetment-filter thickness d_{rev}. Moreover, eq. (4.18) will become asymptotic to the lower envelope (eq. (4.17)) when $\xi_0 \rightarrow \infty$ which is the result expected for surging breakers where the d_{rev} does not affect the relative wave run-up and run-down related to MWL. For this purpose, coefficient A as function of the revetment filter thickness d_{rev} is given in Table 5.1.

Upper envelope:
$$\left(\frac{Ru-\eta_{S,RuG}}{H_0}\right)_{UE} = A\left(\xi_0 - A\right)\cdot\exp\left[-\frac{\left(\xi_0-A\right)^2}{4A}\right] + \left(\frac{Ru-\eta_{S,RuG}}{H_0}\right)_{LE}$$
$$\rightarrow \left(\frac{Ru-\eta_{S,RuG}}{H_0}\right)_{UE} = A\left(\xi_0 - A\right)\cdot\exp\left[-\frac{\left(\xi_0-A\right)^2}{4A}\right] + \frac{\xi_0^{\,2}+19.23\cdot\xi_0}{\xi_0^{\,2}+130.87} \quad (4.18)$$

Table 4-4: Coefficients A in for prediction eq. (4.18) of the relative wave run-up on MWL on top of a PBA-revetment.

	PBA-revetment		
Revetment-filter thickness	d_{rev1}=0.15m	d_{rev2}=0.25m	d_{rev3}=0.35m
Coefficient A	0.55	0.77	0.97

The upper envelope may account for the wave run-up/run-down related to both impact and quasi-static components of the wave loading (eq. (4.19) and s. also section 5.1 for reference).

Upper envelope:
$$\left(\frac{Ru-\eta_{S,RuG}}{H_0}\right)_{UE} = \left(\frac{Ru-\eta_{S,RuG}}{H_0}\right)_{Impact} + \left(\frac{Ru-\eta_{S,RuG}}{H_0}\right)_{Quasi-static} \quad (4.19)$$

The relative run-up and the run-down related to MWL are almost symmetric to the MWL, as also described by Foyer (2013) and thus, the run-down can be estimated by eq. (4.20).

$$\frac{Ru-\eta_{S,RuG}}{H_0} = -\frac{Rd-\eta_{S,RuG}}{H_0} \quad (4.20)$$

The prediction formulae developed for the upper and lower envelope of the relative run-up and run-down related to MWL are shown in Fig. 4-22.

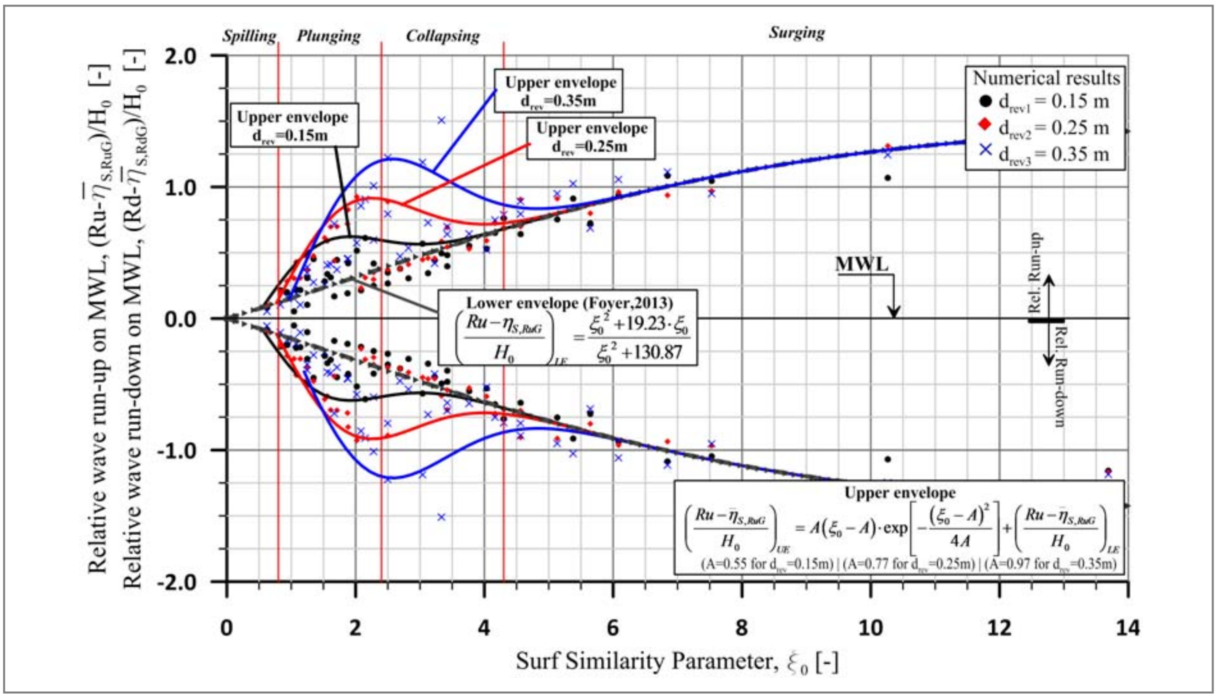

Fig. 4-22: Prediction formulae for the upper and lower envelope for the relative wave run-up and run-down related to MWL on top the revetment as function of the revetment-filter thicknesses d_{rev}.

b) *Wave run-up and run-down beneath the revetment related to the MWL*

The findings related to the analysis of the results from the parameter study regarding the relative run-up and run-down on MWL at the revetment-filter interface and on top of the sand core are summarized as follows: i) the revetment-filter thickness does not affect the relative wave run-up and run-down, ii) a steady increase is observed up to $\xi_0 \approx 14$ and iii) it is expected that for $\xi_0 \rightarrow \infty$, the relative run-up and the run-down on MWL are equal to 1.0. Further details are described in Alcérreca-Huerta & Oumeraci (2014).

As no noticeable effect of the revetment-filter thickness was identified, the latter is not taken into account in the proposed formulae for the relative wave run-up and run-down at the revetment-filter interface (eq. (4.21) and Fig. 4-23) and on top of the sand core (eq. (4.22) and Fig. 4-24). Both eq. (4.21) and eq. (4.22) are valid for any ξ_0-value and the value of the relative run-up and run down on MWL is equal to 1.0 for $\xi_0 \rightarrow \infty$ and equal to zero for $\xi_0 = 0$.

$$\frac{Ru_{Lay2} - \eta_{S2,RuG}}{H_0} = \tanh\left(0.05 \cdot \xi_0^{1.09}\right) \text{ and } \frac{Ru_{Lay2} - \eta_{S2,RuG}}{H_0} = -\frac{Rd_{Lay2} - \eta_{S2,RuG}}{H_0} \tag{4.21}$$

(r^2=0.83, σ=5.8%)

$$\frac{Ru_{Lay3} - \eta_{S3,RuG}}{H_0} = \tanh\left(0.005 \cdot \xi_0^{1.82}\right) \text{ and } \frac{Ru_{Lay3} - \eta_{S3,RuG}}{H_0} = -\frac{Rd_{Lay3} - \eta_{S3,RuG}}{H_0} \tag{4.22}$$

(r^2=0.81, σ=4.1%)

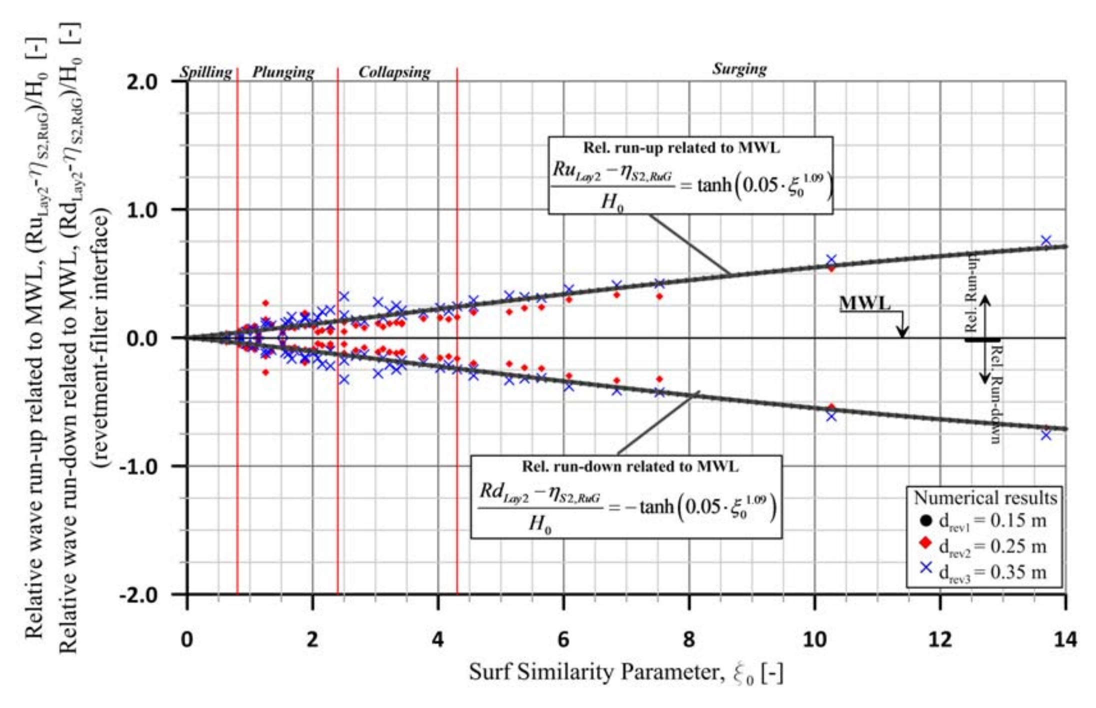

Fig. 4-23: Prediction formulae for relative wave run-up/down on MWL (at revetment-filter interface).

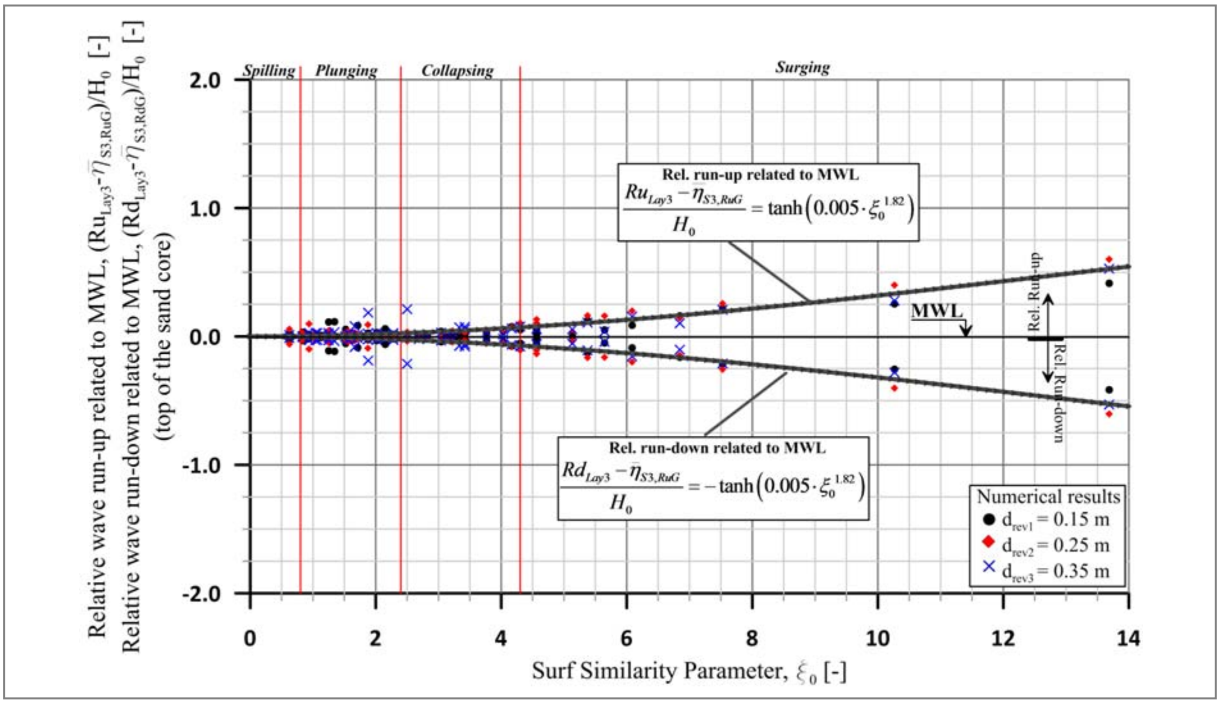

Fig. 4-24: Prediction formulae for relative wave run-up/down on MWL (at the filter-sand core interface).

The run-up and run-down analysis related to the MWL provides a better understanding of the wave run-up/run-down process which was found to be affected by the presence of a water layer on the revetment surface closely related to the revetment-filter thickness. The latter occurs especially for plunging and collapsing waves. For plunging and surging waves, an increase of the revetment-filter leads to a decrease of the wave run-up/run-down but not necessarily for collapsing waves. Moreover, a comparison of Fig. 4-23 and Fig. 4-24 with Fig. 4-22 shows that the relative wave run-up and down on the revetment are considerably damped by the revetment and filter layers, namely by 63% and 85% at the revetment-filter interface and at the filter-sand core interface, respectively.

4.4 Summary of key results

A comparative analysis was performed between three different classifications of breaker types (this parameter study, parameter study by Foyer & Oumeraci (2013b) and GWK tests by Oumeraci et al. (2010)). Differences and uncertainties on the definition of the limits of wave breaker types were found and thus, a classification of wave breaker types is proposed considering the averaged ξ_0-values from those provided by the three aforementioned studies: plunging breakers ($0.8<\xi_0<2.4$), collapsing breakers ($2.4<\xi_0<4.3$) and surging breaker ($\xi_0>4.3$).

The wave reflection was also analysed and prediction formulae for its assessment were provided which considers the general performance of PBA revetments (eq.(4.6)) or including the effects of the revetment-filter thickness d_{rev} (eq.(4.3)-(4.5)). The wave reflection was noticed to unexpectedly increase when $d_{rev}>0.25$ m (compared to $d_{rev}=0.15$ m) under collapsing wave breakers ($2.4<\xi_0<4.3$) which might be the consequence of a significant interaction between the incident wave and the seepage induced by the previous wave breaker. On the other hand, the findings of experimental studies with irregular waves (i.e.,Oumeraci et al. (2010) and Liebisch et al. (2014)) regarding the insufficient weighting of the wave height and wave period in the surf similarity parameter were not in agreement with the present parameter study results. The insufficient weighting has been reported to occur for PBA-revetments particularly subject to irregular waves and it may be caused due to wave grouping effects. For regular waves the wave phase velocity and the wave group velocity are equal in shallow waters while this relation is less clear for wave spectra.

Regarding the mean water level (MWL), the key results due to the presence of a PBA-revetment are summarised by distinguishing between impact and non-impact wave loading conditions as follows:

- *Non-impact wave loads*: i) an increase of the wave height also increases the MWL; ii) at the filter-sand core interface a large gradient of the MWL occurs due to the permeability change between the layers (similar finding by Foyer & Oumeraci (2012)) and iii) no clear effect caused by the change of revetment-filter thickness was noticed.
- *Impact wave loads*: i) the wave height and the wave period are both important for the MWL, and ii) the MWL slightly decreases when the revetment-filter thickness increases. This effect is smaller in comparison to the wave height and the wave period.

Furthermore, the wave set-up is of great importance for the better understanding of the run-up/down as demonstrated by the results of Foyer (2013). Therefore, both the internal and external set-up were analysed and the key findings are summarized as follows:

- *For the external wave set-up*: i) the PBA-revetment slope steepness has a significant effect on the relative set-up related to the wave length ($\eta_{S,RuG}/L_0$) especially for $\xi_0<4.0$ (as described in Foyer (2013)); ii) the effect of the revetment-filter thickness, though not clear, is lower than that of the slope steepness.
- For the internal wave set-up: i) a linear relationship between the internal and the external wave set-up exists, and ii) the internal wave set-up is larger than the external wave set-up as already observed by Foyer (2013).

For the description of the relative external wave set-up, prediction formulae expressed in terms of $\eta_{S,RuG}/L_0$ (eq.(4.7)) and $\eta_{S,RuG}/H_0$ (eq. (4.12)) were developed in addition to the formulae for the minimum and maximum expected values of $\eta_{S,RuG}/H_0$. Furthermore, prediction formulae for the internal wave set-up at the revetment-filter and filter-sand core interface were developed.

The external and internal wave run-up and run-down on and beneath the revetment (at both revetment-filter interface and filter-sand core interface) were analysed. For this purpose, the approach using the MWL as a reference water level instead of SWL as proposed by Foyer (2013) was investigated. Overall, the findings of Foyer (2013) were generally confirmed, but unexpected results (particularly regarding the effect of revetment-filter thickness on the run-up and run-down on the revetment) were obtained for $2.0<\xi_0<4.0$ which were also noticed in GWK tests (Oumeraci et al. (2010)) and briefly described in Foyer (2013). For this purpose, the following new key findings are worth to be mentioned:

- Increase of the revetment-filter thickness was found: i) to reduce the wave run-up and run-down on the revetment except for $2.0<\xi_0<4.0$ where both run-up and run-down increase, ii) to reduce the thickness of the water layer on the revetment, iii) to increase the wave run-up/run-down and iv) to slightly affect the internal wave run-up and run-down related to MWL.
- The maximum run-up and run-down on the revetment might occur for ξ_0-values $2.0<\xi_0<4.0$ and not necessarily for surging breakers.
- The wave run-up/run-down on the revetment is considerably damped beneath the revetment: by 63% at the revetment-filter interface and 85% at the filter-sand core interface.
- Prediction formulae were developed for the relative wave run-up and run-down beneath the revetment related to MWL as well as for the upper and lower envelopes of the run-up and run-down on the revetment related to MWL.

Finally, the following implications and recommendations for further analysis and future work studies may be drawn:

- The wave set-up consists of two components: the static and the dynamic (Dean & Walton (2010)). Only the static component was analysed in the present study since the numerical simulation of the dynamic component implies long duration tests which are limited due to the computational requirements and that could be better analysed in the laboratory. Therefore, the implications of the dynamic component of the wave set-up should be investigated to define its contribution to the total wave set-up as a function of the surf similarity parameter.
- It is suggested to conduct a study to understand the wave set-up and other processes for spilling breakers with $\xi_0<0.8$.
- Further analysis are required for the understanding of the wave run-up/run-down, wave reflection and wave set-up considering irregular waves and the effects caused by a variation of the revetment-filter thickness. Furthermore, the simultaneous variation of the revetment-filter thickness with the porosity and the revetment roughness should be investigated. Moreover, the implementation of the roughness in numerical modelling of PBA-revetments should be examined.

5 Wave-induced pressures on and beneath PBA-revetments

A comprehensive analysis of the pressures developed on the revetment, the pore pressures beneath the revetment and its soil foundation is presented in this chapter. The analysis is focused on the determination of the wave-induced peak pressure and pressure distribution on and beneath the revetment as well as the pore pressure distribution in the sand core normal to the revetment slope.

First, a brief overview on the wave load classification and parameterization is shown to define the elements and notations for the wave-induced pressure analysis. Second, the magnitude of the peak pressure magnitude and its location as well as the pressure distribution on the revetment are analysed. Third, the wave-induced pore pressures on top of the sand core are also investigated; including the peak pore pressure magnitude and location as well as pore pressure distribution. In a further section, the wave-induced pore pressures beneath the revetment and their distribution normal to the revetment slope are examined. Moreover, prediction formulae are developed for all the aforementioned processes.

The wave-induced pressures in this parameter study are referred to the SWL. Therefore, only the pressure due to wave motion is considered, excluding the hydrostatic pressure.

5.1 Wave load classification and parameterization

As observed in previous studies (e.g., Führböter et al. (1976); Neelamani (2005); Oumeraci et al. (2010)), two main wave loading cases are recognized: impact and non-impact (Fig. 5-1). There is a transition zone between the two main loading cases which limits cannot be clearly defined since they are dependent on wave-wave interactions.

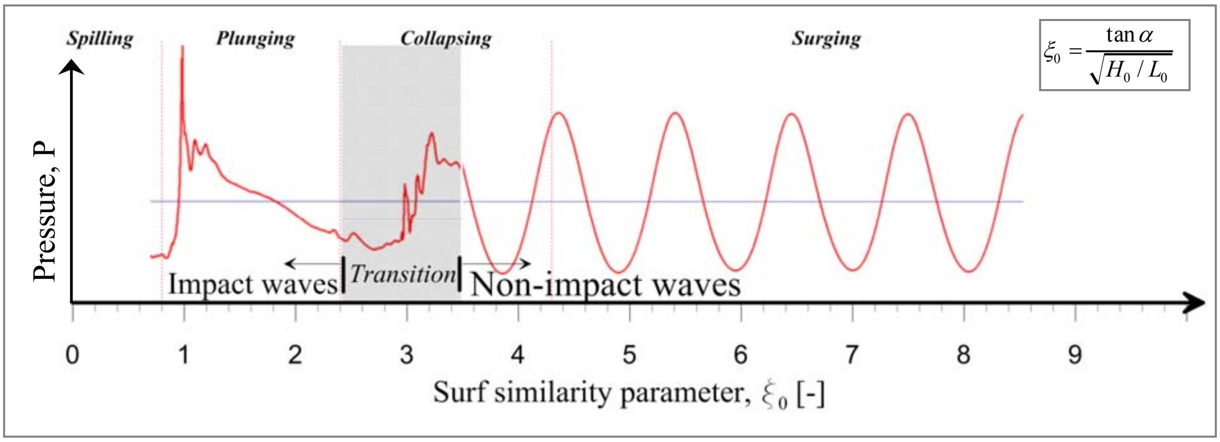

Fig. 5-1: Wave load classification.

The impact loads normally occur with plunging waves ($0.8 < \xi_0 < 2.4$), while non-impact load cases occur with surging waves ($\xi_0 > 4.3$). The transition zone between impact and non-impact load cases was found to mainly occur with collapsing waves close to the boundary with plunging waves (Fig. 5-1). Thus, the transition zone is defined within the range $2.4 < \xi_0 < 3.3$, where the quasi-static component has a larger magnitude than the impact component, but both loading cases take place.

For the parameterization of wave loading, only the impact and non-impact cases are described in this section. However, the transition zone can be parameterized in a similar way as the impact load, with the only difference that the impact component has a smaller magnitude than the quasi-static component.

a) Parameterization of wave-induced impact loads

The impact load is described by a pressure peak of short duration (impact component) superimposed over a quasi-static component as shown in Fig. 5-2a. The quasi-static component is related to the cyclic variation of the wave motion with wave period T, while the impact component is related to the transient load induced by waves plunging on the slope with a load duration $t_d << T$ (Oumeraci et al. (2010)).

The impact load is composed by the impact and the quasi-static components (both identified by triangles) and as already shown by Oumeraci et al. (2010) can be characterized (Fig. 5-2b) by:

- Three parameters for the impact component: i) peak pressure P_{max}, ii) rise time t_a and iii) impact duration t_d (~ 80-200ms for low aerated impacts, ~ 100-450ms for high aerated impacts (Bullock et al. (2007))).
- Three parameters for the quasi-static component: i) quasi-static peak pressure P_{stat}, ii) rise time t_{stat} and iii) the duration time that is equal to the wave period T.

After reaching P_{max} within the impact component, the pressure decreases to P_{min} at a time t_d increasing again up to P_{stat} due to the quasi-static component. The difference between P_{max} and P_{stat} is defined as P_{diff}. The magnitude of P_{max} and P_{stat} are analyzed and described in detail in section 5.2.

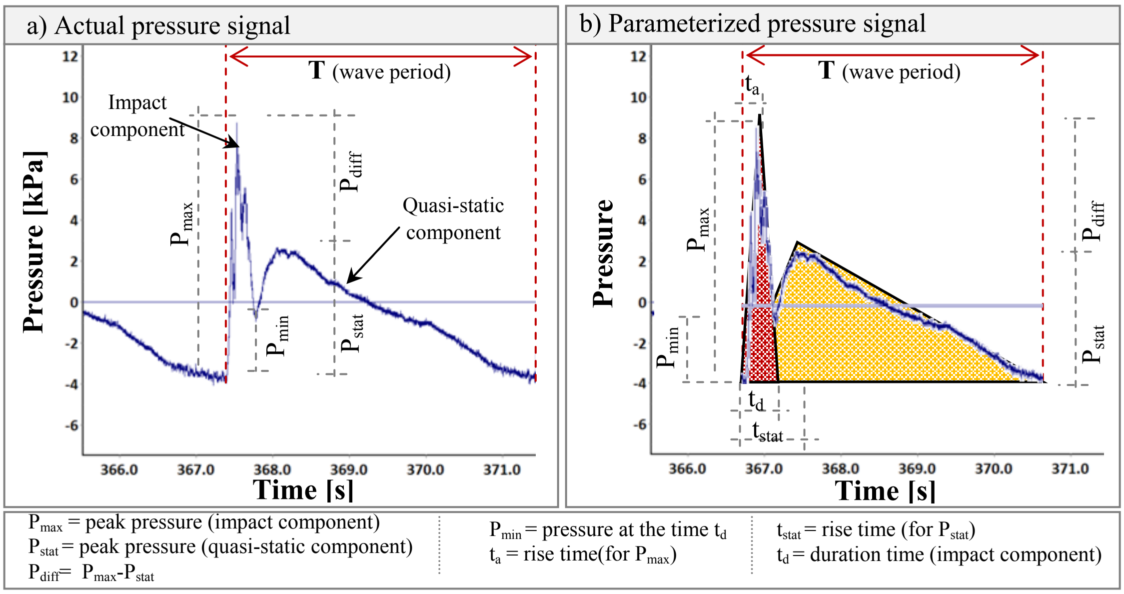

Fig. 5-2: Parameterization of entire impact wave load (Alcérreca-Huerta & Oumeraci (2012)).

The time parameters of the impact load (t_a and t_d) were analysed based on results from the numerical simulations within the parameter study. This analysis is also complemented with results from large-scale tests with PBA revetments (Oumeraci et al. (2010)). Comparison with large-scale tests with impermeable smooth block revetments has been considered (Alcérreca-Huerta & Oumeraci (2012)). For this purpose, the rise time t_a is plotted against the dimensionless peak pressure ($P_{max}/\rho g H_0$) in Fig. 5-3 where the scatter increases when $P_{max}/\rho g H_0 \rightarrow 0$. The upper envelopes computed by using of Origin Pro[1] lead to the estimation of the maximum rise time t_a as shown in eqs.(5.1) and (5.2) for PBA-revetments and for smooth impermeable block revetments, respectively:

Rise time for PBA-revetments
$$\frac{t_a}{T} = 0.12\left(\frac{P_{max}}{\rho g H_0}\right)^{-0.94} \tag{5.1}$$

Rise time for impermeable block revetments
$$\frac{t_a}{T} = 0.54\left(\frac{P_{max}}{\rho g H_0}\right)^{-1.48} \tag{5.2}$$

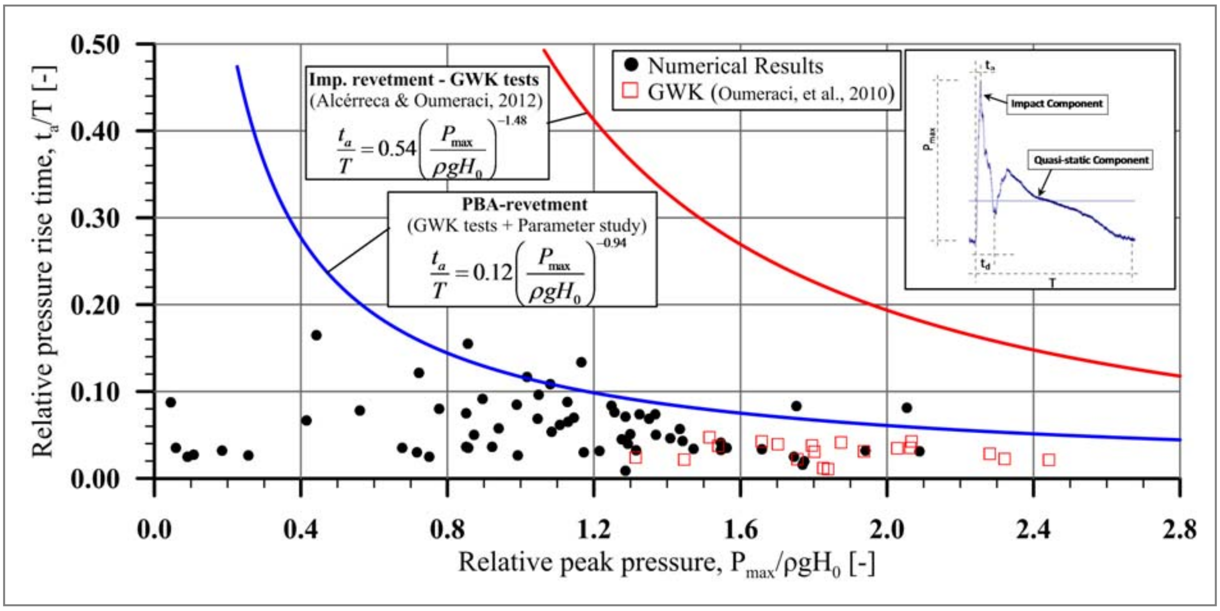

Fig. 5-3: Relative rise time vs. relative peak pressure for impact loads.

For the same relative rise time (t_a/T), a much larger relative pressure $P_{max}/\rho g H_0$ is obtained for impermeable smooth revetments than for porous rough PBA-revetments, but for both types of revetments $P_{max}/\rho g H_0$ increase with decreasing t_a/T.

The relative duration t_d/T of the impact component in the numerical simulations was generally lower than 30% the wave period T for all cases tested, but large scatter in the dataset was

---

[1] The envelopes are defined by: i) providing a linear connection between the points sorted in terms of the x-axis variable, ii) the derivative is then calculated and maxima/minima events are obtained, iii) a cubic spline interpolation with a smoothing Adjacent-Averaging method is performed within the events and iv) a fitting function is calculated for representing the envelope performance.

found, possibly caused by the influence of a water layer on the revetment at the impact location or due to the air content during the plunging process that might modify the impact duration (see further details in Alcérreca-Huerta & Oumeraci (2014)). Additional studies focused on the parameterization of the wave induced impact load may be needed for a better description of the load also considering differences due to changes in the porosity and roughness of the revetment.

b) Parameterization of wave-induced non-impact loads

The (quasi-static) non-impact load related to the cyclic variation of the wave motion with wave period T may be idealized by a trapezoid (Oumeraci et al. (2010); Alcérreca-Huerta & Oumeraci (2012)) characterized as follows (Fig. 5-4): i) peak pressure $P_{max} \hat{=} P_{stat}$, ii) steady rise time t_{stat}, iii) load duration t_d which is equal to the wave period, $T=t_d$ and iv) t_{stat1} and t_{stat2} which respectively represent the initial and final location where the concavity of the pressure signal is negative. In general, the rise time is expected to be approximately 50% the wave period T. The performance of t_{stat1} and t_{stat2} should be determined with further analysis of the non-impact wave loading.

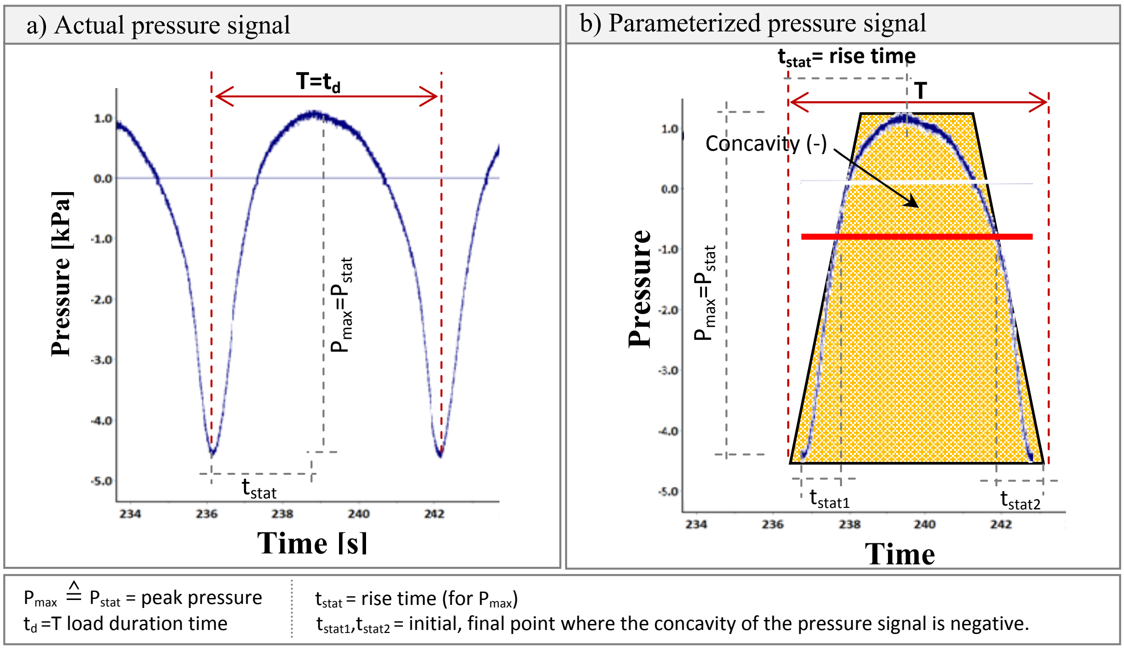

Fig. 5-4: Parameterization of non-impact wave load (Alcérreca-Huerta & Oumeraci (2012)).

From the parameterization and for the present study, the key parameters for the pressure analysis due to impact loads are the peak pressures P_{max}, P_{stat} (quasi-static component) and P_{diff} (difference between P_{max} and P_{stat}). For non-impact wave loading the key parameter is the peak pressure $P_{max} \hat{=} P_{stat}$. Regarding the time parameters, the rise time t_a is relevant since the response and resistance of the revetment also depends on the time at which P_{max} is being applied, especially for impact loads. On the other hand, the wave period T is related to the duration time t_d of the quasi-static wave loading and thus it is important for the development of the pressure P_{stat} for impact and non-impact wave loads.

5.2 Wave-induced pressures on the revetment

The analysis of the wave-induced pressure on the revetment considers the following elements: i) the peak pressure on the revetment slope; ii) the location of this peak pressure (referred to the SWL) and iii) the spatial distribution of the pressures along the revetment slope. Prediction formulae are developed based on the results of this analysis. Only the dynamic pressure induced by wave motion is considered without the hydrostatic pressure due to the local water depth h(x) under SWL conditions (eq.(5.3))

$$P_{total} = P_{hydrostatic} + P_{dynamic}\text{, where } P_{hydrostatic}(x) = \rho g h(x) \tag{5.3}$$

The peak of the dynamic pressure distribution on the revetment is denoted as P_{max1}, while its location measured vertically from the SWL being positive in upwards direction is denoted as z_{max1}. The pressure distribution on a PBA-revetment and the variables involved are schematically described in Fig. 5-5 where the coordinate system used for the analysis is also shown.

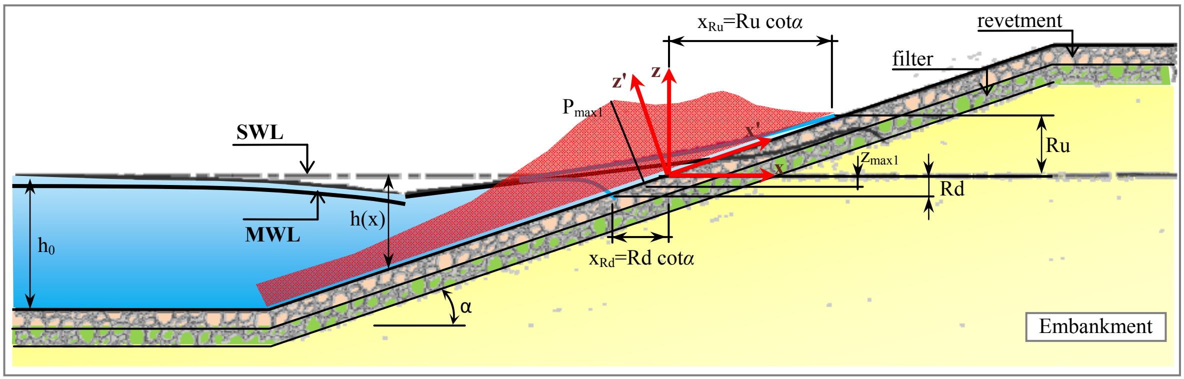

P_{max1}= Peak pressure on the revetment
z_{max1}= Location of the peak pressure on the revetment
Ru = Wave run-up on the revetment
Rd = Wave run-down on the revetment
α = Slope angle
x_{Ru} = Horizontal projection of wave run-up
x_{Rd} = Horizontal projection of wave run-down

Fig. 5-5: Pressure distribution on a PBA-revetment and coordinate system (definition sketch).

5.2.1 Peak pressure on the revetment

a) Process analysis

The peak pressure P_{max1} according to the parameterization in Fig. 5-2 is analysed. A comparison of the results from the numerical simulations with those from the large scale tests in GWK is shown in Fig. 5-6, where the relative peak pressure $P_{max1}/\rho g H_0$ (ρ is the density water, g the gravity acceleration and H_0 is the wave height) is plotted against the surf similarity parameter ξ_0.

The experimental and numerical results are in the same range of magnitude for plunging and collapsing breakers ($0.62<\xi_0<4.3$). The numerical results, however, also provide larger values than those from GWK tests, which may be a consequence of the extension of cases tested in GWK and included within the parameter study, leading to some wave conditions with larger $P_{max1}/\rho g H_0$. For surging breaker ($\xi_0>4.3$), the numerical simulations provide lower values than those from the GWK tests. Possible reasons for these differences might be among others: i) re-reflection problems in the GWK tests caused by insufficient absorption of long waves by the wave paddle and/or ii) larger dissipation of energy by the turbulence model in the numerical simulations for surging waves. The SST turbulence model was used for surging breakers (LES for plunging and collapsing breakers), and it might provide higher turbulence and energy dissipation for the case of PBA-revetments.

The largest scatter is observed within the range of plunging breakers ($1.0<\xi_0<2.4$) and the transition to collapsing breakers ($2.4<\xi_0< \sim 3.3$) which is a consequence of the impact component (see Fig. 5-1).

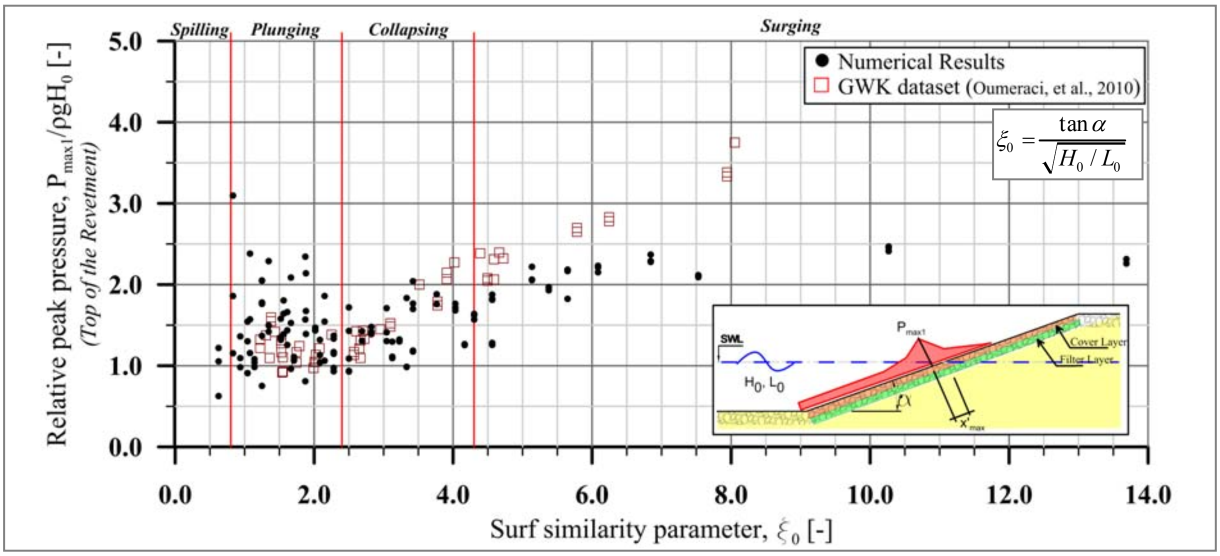

Fig. 5-6: Relative peak pressure on the revetment. Comparison between numerical simulations from the parameter study and results from the large-scale model tests in GWK with PBA-revetments (all tested revetment-filter thicknesses d_{rev}).

b) Prediction formulae

The prediction formulae revetment are developed considering the lower and upper envelopes which may represent, respectively, the quasi-static and the impact components according to the parameterization in Fig. 5-2:

$$\frac{P_{\max 1}}{\rho g H_0} = \frac{P_{diff}}{\rho g H_0} + \left(\frac{P_{stat}}{\rho g H_0}\right)_{quasi-static} \tag{5.4}$$

In the parameter study, P_{diff} is assumed to be positive $P_{diff} \geq 0$ (s. Fig. 5-2), and consequently P_{stat} is considered as the peak pressure if no impact component is found ($P_{max1} \triangleq P_{stat}$ for non-impact loads) or if the pressure induced by the impact component is smaller than that of the quasi-static component (e.g., transition loads). Furthermore, the lower envelope should fulfil the following physical requirements:

- When $\xi_0 \rightarrow 0$, then the relative peak pressure $P_{max1}/\rho g H_0 \rightarrow 0$.

- When $\xi_0 \rightarrow \infty$, the relative peak pressure tends to a value close to $P_{max1}/\rho g H_0=2.0$. This is because for a very steep slope and/or very long waves, the peak pressure is only produced by wave motion and considering full reflection for these conditions the water elevation will contain the incident and the reflected waves of the same magnitude superimposed at the structure.

The prediction formula for the quasi-static component (calculated through the software OriginPro9 (OriginLab (2014))) of the relative pressure is given by eq. (5.5) which fulfils the aforementioned physical requirements:

$$\left(\frac{P_{stat}}{\rho g H_0}\right)_{quasi-static} = 2\frac{\xi_0^{\,2}+6.7\cdot\xi_0}{\xi_0^{\,2}+38.5} \tag{5.5}$$

The upper envelope determines the relative peak pressure $P_{max1}/\rho g H_0$ and is defined by the sum of the relative pressure $P_{diff}/\rho g H_0$ (given by an expression with a shape similar to that of a Rayleigh density function, eq. (5.6)) and the quasi-static component $P_{stat}/\rho g H_0$ (eq. (5.5)). Furthermore, this upper envelope is described by eq. (5.7) and it is given for different revetment-filter thickness since it has an important effect on the impact-component.

Furthermore, the characteristics of the Rayleigh density function for $P_{diff}/\rho g H_0$ is that for $\xi_0 \rightarrow 0$ it increases rapidly until it reaches a peak which then decreases to be asymptotically to zero. Therefore, these features are considered in the fitting function to describe $P_{diff}/\rho g H_0$ for different revetment-filter thicknesses d_{rev} since the trend observed is described as follows:

- For $\xi_0 \rightarrow 0$ the peak pressure is zero $P_{max1}/\rho g H_0=0$.
- For the spilling breakers and the transition to plunging breakers, the impact component of the relative peak pressure on the revetment increases rapidly from zero (at $\xi_0=0$) until it reaches a peak that always occurs for plunging waves ($1.0<\xi_0<2.4$).
- Once the peak is reached, the decrease of the impact component takes place, and the quasi static component becomes more important. In other words, after the peak is reached, as ξ_0 increases, $P_{diff} \rightarrow 0$. For surging breakers, the impact component becomes zero.

One of the main advantages of fitting P_{diff} with the Rayleigh density function is that the approach is valid for all the entire range of surf similarity parameter considered and that the mathematical representation of the fitting formulae is simple. Thus, P_{diff} has the shape described in eq. (5.6):

$$\frac{P_{diff}}{\rho g H_0} = A\cdot\xi_0\cdot\exp\left(-\frac{\xi_0^{\,2}}{B}\right) \tag{5.6}$$

where coefficients A and B are dependent on the revetment-filter thickness (see Table 5-1). Coefficient A is related to magnitude of the peak P_{diff} (higher the peak, larger values of A). Coefficient B is a shape factor in the Rayleigh function and for this case is related to the magnitude of the peak P_{diff} but also to the domain (ξ_0) at which P_{diff} is larger than P_{stat}: higher magnitude of the peak P_{diff} results in lower values of B and a lower ξ_0-domain influenced.

Table 5-1: Coefficients A and B for the impact component of the relative peak pressure on the PBA-revetment.

Revetment filter-thickness	***d_{rev1}=0.15***	***d_{rev1}=0.25***	***d_{rev1}=0.35***
Coefficient A	3.25	2.27	1.24
Coefficient B	2.27	3.25	5.20

Thus, considering the superposition of $P_{diff}/\rho gH_0$ (eq. (5.6)) and the quasi-static component $P_{stat}/\rho gH_0$ (eq. (5.5)) into eq. (5.4), the prediction formula for the relative peak pressure on the revetment is obtained in eq.(5.7) with A and B shown in Table 5-1 for different revetment-filter thicknesses:

$$\frac{P_{\max 1}}{\rho g H_0} = A \cdot \xi_0 \cdot \exp\left(-\frac{\xi_0^{\ 2}}{B}\right) + 2\frac{\xi_0^{\ 2} + 6.7 \cdot \xi_0}{\xi_0^{\ 2} + 38.5} \tag{5.7}$$

This new proposed formula accounts a better description of the wave-induced loads since it is able to describe simultaneously the quasi-static P_{stat} and impact component P_{max1} of the wave-induced load as well as the difference existing between these two components (P_{diff}). Furthermore, the consideration of an upper envelope for the prediction of the peak pressure instead of a fitting function is made in order to account for the large scatter induced by the impact component of the peak pressure.

The fitting curves for the relative peak pressure on the revetment are described for different revetment-filter thicknesses in Fig. 5-7. Both, relative peak pressure $P_{max1}/\rho gH_0$ and the relative pressure due to the quasi-static component $P_{stat}/\rho gH_0$ are shown in this figure.

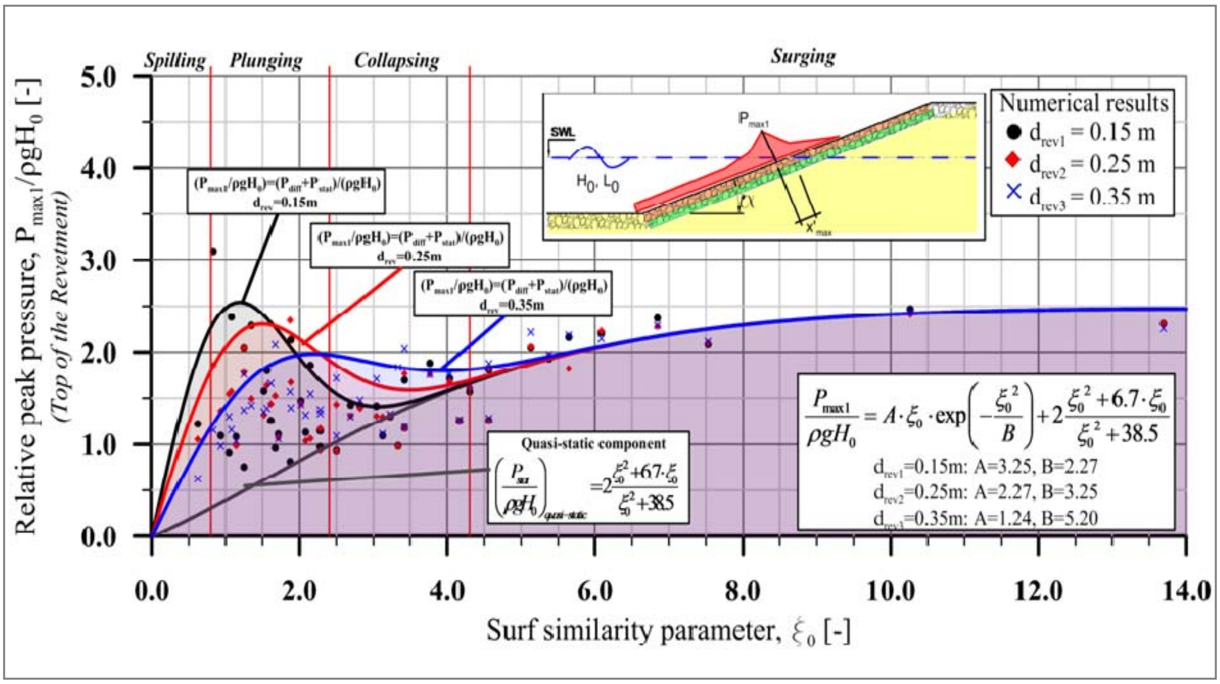

Fig. 5-7: Prediction formulae for relative peak pressure on the revetment for different revetment-filter thickness d_{rev}, including the relative pressures: $P_{max1}/\rho gH_0$, $P_{diff}/\rho gH_0$ and $P_{stat}/\rho gH_0$ (quasi-static component).

The revetment-filter thickness affects significantly the impact component of the peak pressure (Fig. 5-7). An increase of the revetment-filter thickness does not necessarily results in a general reduction of the peak pressure, this rather depends on the value of the surf similarity parameter ξ_0:

- For plunging breakers ($0.8<\xi_0<2.4$), thicker revetments develop lower peak pressures than thinner revetments.
- For collapsing breakers ($2.4<\xi_0<4.3$), the opposite behaviour is observed: thicker revetments develop larger peak pressures.
- For surging breakers ($\xi_0>4.3$), the revetment-filter thickness does not affect the wave-induced load.

The previous behaviour may be explained due to the revetment-filter thickness where a large thickness allows larger infiltration and avoid the presence of a water layer on the revetment that can damp the wave-induced load. However, this effect may occur especially for $2.4<\xi_0<4.3$ (collapsing breakers) where the development of the water layer thickness is highly sensitive to several factors such as the revetment-filter thickness, slope steepness and porosity of the revetment.

Overall, an increase of the revetment-filter thickness provides a smooth variation of the impact component as a function of ξ_0 (Fig. 5-7). Therefore, since a PBA-revetment is subject to a large diversity of storm conditions during its life time, a thicker revetment-filter will be able to support a wider range of wave conditions, and especially to resist larger plunging waves than a thinner revetment.

5.2.2 Location of the peak pressure on the revetment

The variable z_{max1} is defined as the location where the peak pressure on a PBA-revetment takes places. The value of z_{max1} is measured vertically from the SWL, where the positive direction is upwards (see Fig. 5-5).The analysis of the results given by the numerical simulations of the parameter study is described in this section and prediction formulae for z_{max1} are defined.

It was noticed that the numerical simulations and the experimental results for PBA-revetments show a relatively large scatter of z_{max1} over the entire range of surf similarity parameters considered ($\xi_0<14$), as shown in Fig. 5-8. Since the scatter occurs in both numerical and experimental results, the reason might be related to wave-wave interactions that modify (even with regular waves) the location of the impact point. Additionally, the revetment-filter thickness (d_{rev}) does not show any influence on the location of the peak pressure on the revetment (see Fig. 5-9).

Among the models already available in the literature to predict the location of the peak pressure (e.g., Schüttrumpf (2001); Klein Breteler (2007) and Oumeraci et al. (2010)). The hyperbolic tangent approach proposed by Schüttrumpf (2001) (eq. (5.8)) for smooth impermeable revetments is favoured due to the following reasons: i) it provides a continuous function over all the domain of surf similarity parameter values which cannot be observed in

Breteler's formulae; ii) because Oumeraci's formulae developed for PBA-revetments is based on Schüttrumpf's tanh- approach which was modified by the introduction of a factor to account for the effects of porous revetments.

$$\frac{z_{\max 1}}{H_0} = -\left[0.8 + 0.6 \tanh\left(\xi_0 - 2.1\right)\right] \tag{5.8}$$

However, for $\xi_0=0$, $z_{\max1}/H_0=0$ should be expected and which is not the case in eq. (5.8). Thus, a new prediction formula (eq. (5.9) with $\sigma'=32.6\%$) is developed based on a tanh-model that fulfil the physical conditions at $\xi_0=0$.

$$\frac{z_{\max 1}}{H_0} = -1.62 \cdot \tanh\left(0.46 \cdot \xi_0^{\,0.47}\right) \tag{5.9}$$

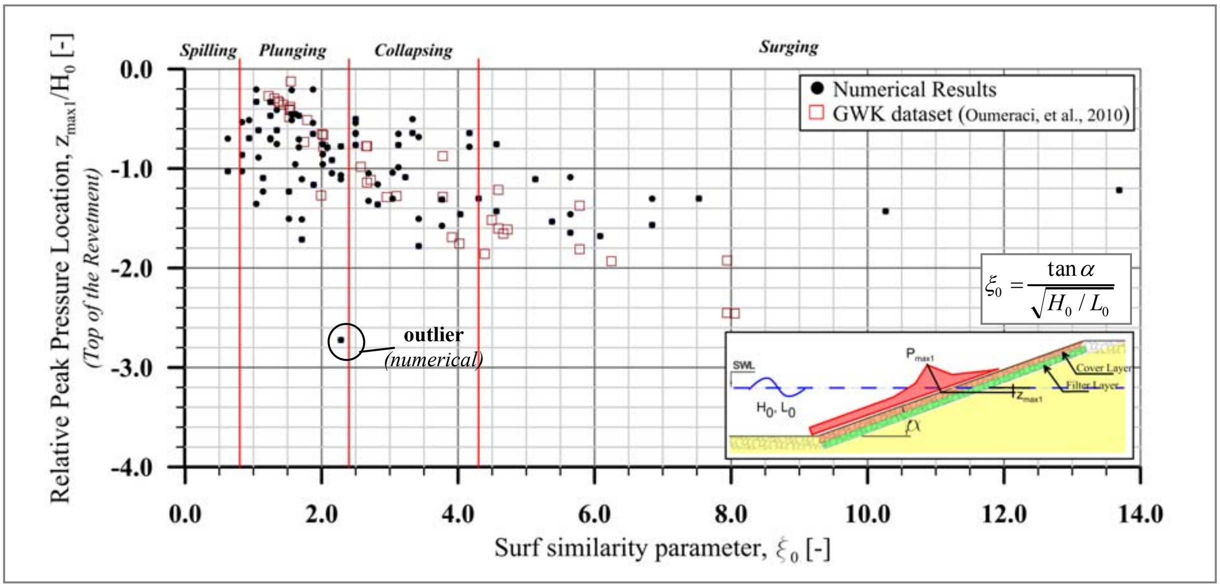

Fig. 5-8: Location of the peak pressure $P_{\max1}$ on a PBA-revetment vs. surf similarity parameter. Comparison between numerical simulations and GWK-large scale tests.

In addition to the mean location of the peak pressure on the revetment $z_{\max1}$ and because of the scatter found for both numerical and experimental results (Fig. 5-8), the lower and upper envelopes of $z_{\max1}/H_0$ are also provided. The lower and upper envelopes are given by eq. (5.10) and eq. (5.11), respectively. In these equations, the coefficients 1.61 and 1.34 are related to the value of $z_{\max1}/H_0$ when $\xi_0 \rightarrow \infty$. Furthermore, the two envelopes becomes zero when $\xi_0=0$ which is the behaviour expected.

Lower Envelope $$\frac{z_{\max 1}}{H_0} = -1.64 \tanh\left(1.04 \cdot \xi_0^{\,1.59}\right) \tag{5.10}$$

Upper Envelope $$\frac{z_{\max 1}}{H_0} = -1.34 \tanh\left(0.07 \cdot \xi_0^{\,1.58}\right) \tag{5.11}$$

As shown in Fig. 5-9, a large variability of z_{max1}/H_0 is observed for plunging and collapsing breakers, while for surging waves this variability is reduced. Approaches given by Oumeraci et al. (2010) for PBA-revetments and regular waves are found within the domain limited by the envelopes proposed in equations (5.10) and (5.11) (see Fig. 5-9).

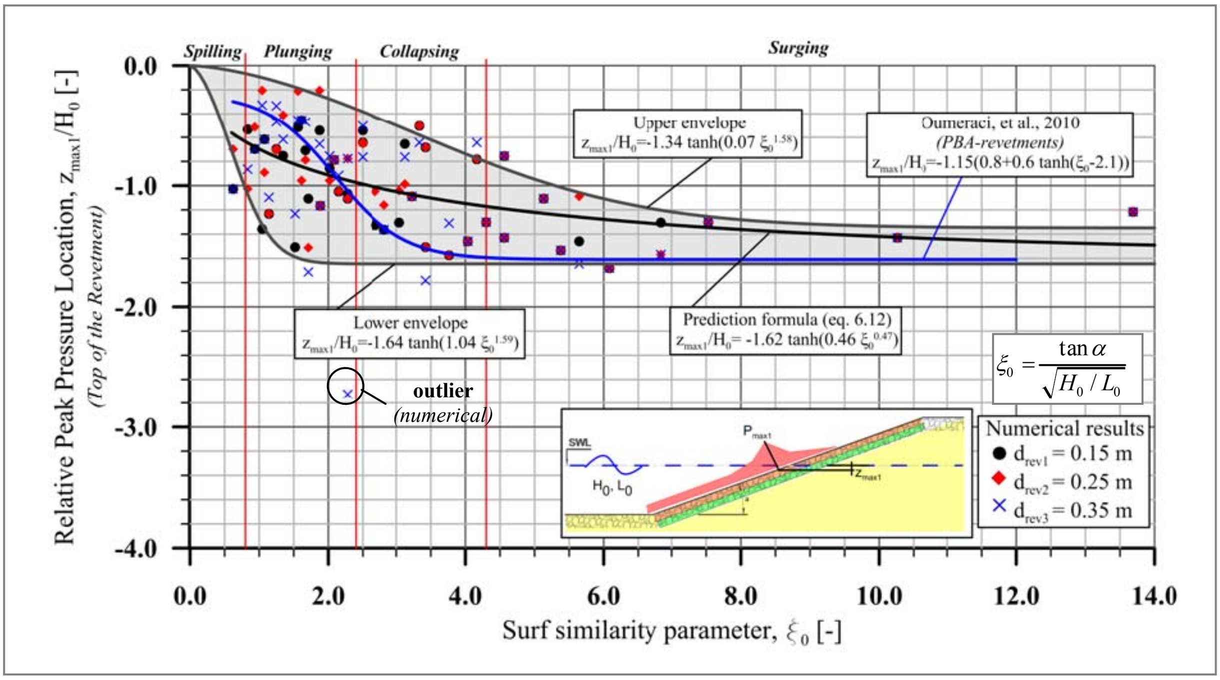

Fig. 5-9: Prediction formula for the location of the peak pressure (z_{max1}/H_0) on PBA-revetments, including upper and lower envelopes.

5.2.3 Wave-induced pressure distribution parallel to the revetment slope

For the analysis of the spatial distribution of the wave-induced pressure on the revetment the coordinate system adopted consists on an x'-axis oriented parallel to the revetment slope and positive upwards as well as a z' axis perpendicular to slope and positive in upwards direction (see Fig. 5-5).

Normalization was performed for the analysis of the spatial pressure distribution on the revetment. The spatial pressure distribution is described in terms of the relative pressure (P/P_{max1}) induced at a location ($x'_{rel}=x'/|x'_{max1}|$); where, P is the wave-induced pressure at a location x' (see for reference Fig. 5-5). P_{max1} is the peak pressure on the revetment (section 5.2.1 and eq. (5.7)) and x'_{max1} is function of z_{max1} and the revetment slope (cot α) as described by eq. (5.12). Any location x' on the revetment is defined by eq. (5.13).

$$x'_{max1} = \sqrt{\left(z_{max1}\right)^2 + \left(z_{max1} \cdot \cot\alpha\right)^2} \tag{5.12}$$

$$x' = \sqrt{\left(z\right)^2 + \left(z \cdot \cot\alpha\right)^2} \tag{5.13}$$

The impact and non-impact loads will be distinguished in the analysis of the spatial pressure distribution since, particularly in the swash zone, was found to depend on the wave loading (Alcérreca-Huerta & Oumeraci (2014)).

a) Non-impact loads: process analysis

The results from the parameter study for the spatial pressure distribution on the revetment for non-impact loads is shown in Fig. 5-10. The revetment-filter thickness has only a slight effect on the pressure distribution (Alcérreca-Huerta & Oumeraci (2014) and thus for the present analysis it is neglected. Furthermore, the spatial pressure distribution has a large scatter for depths lower than the location of the peak pressure x'_{max1}. However, for locations above x'_{max1} (where the peak pressure is induced), a clearer trend is observed: i) the pressure decreases after reaching P_{max1}, and ii) when the location x' is close to the run-down location, the pressure starts to rise producing a second peak in the spatial distribution of the pressure, iii) once the second peak is reached, the pressure continuously decreases until it reaches zero at the location x'_{Ru} of the maximum run-up ($x'_{Ru}= \surd(x_{Ru}{}^2+Ru^2)$; s. also Fig. 5-5).

An analysis of the non-impact wave motion was performed in order to provide a better understanding of the spatial pressure distribution especially in the swash zone where a second pressure peak occurs. In laboratory tests of PBA-revetments (e.g., Oumeraci et al. (2010); Liebisch & Oumeraci (2012)), a special focus was set on the wave impact area, so that only a small amount of pressure measurements were available to identify clearly the second pressure peak induced in the swash zone. This analysis also considers the comparison with the results from small-scale model tests with porous bonded revetments of Liebisch & Oumeraci (2012), so more confidence on the analysis is provided, especially with the results related to the wave kinematics on the revetment.

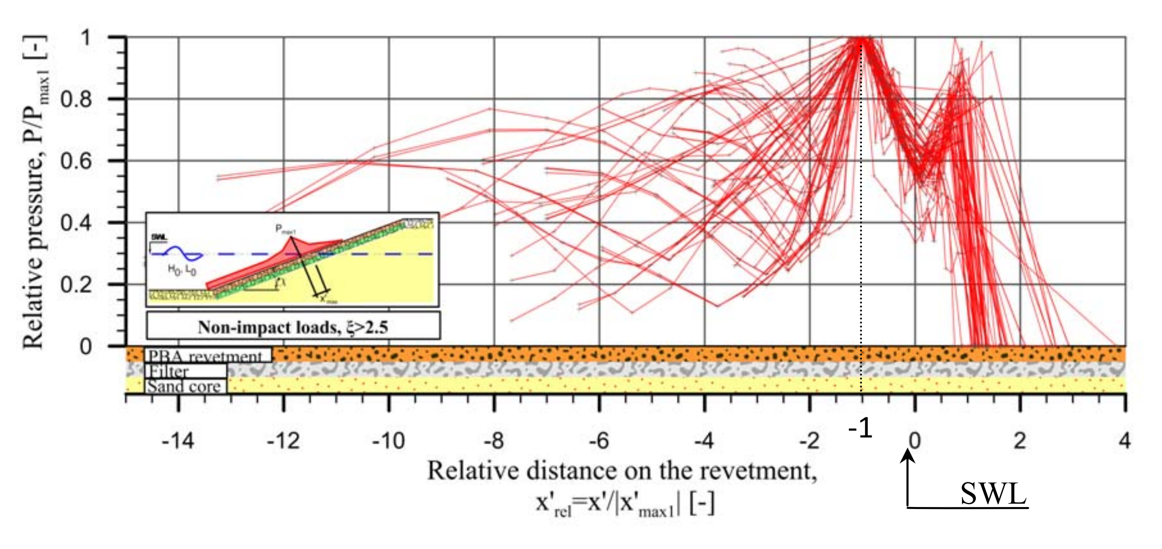

Fig. 5-10: Spatial distribution of the pressure on the revetment for **non-impact** loads for all tested revetment-filter thicknesses.

Based on the analysis of the surging breakers (illustrated in Fig. 5-11), the shape of the spatial pressure distribution on the revetment may be affected by the following processes:

- When the rush-down occurs, interactions between the incident wave and the rush-down take place (t/T=0.0 in Fig. 5-11a & b). This interaction may generate high turbulence as well as high pressures: during the rush-down, the water velocity moves downwards the revetment slope and collides with the incident wave which velocity is in opposite direction, the change in velocity direction leads to an increase and a focus of the pressure at location z_{max1} (Fig. 5-10).
- After the aforementioned interaction, the maximum run-down is reached and the incident wave starts to rush up the revetment (t/T=0.09 in Fig. 5-11b). From the interaction point (where the rush-down meets the incident wave) until the location of the maximum run-down, a small water layer thickness remains on the revetment slope and thus, it should be expected that the location of the peak pressure z_{max1} takes place below the maximum run-down.
- As the incident wave moves upwards the slope, the pressure decreases due to the water layer remaining on the revetment from the previous run-down. This is related to the pressure decrease once the highest pressure peak is achieved (Fig. 5-10). However, when the water layer is not present (in the swash zone), the pressure could increase again (second peak in the pressure distribution) due to two reasons:
  - The water layer provides a damping effect of the wave pressures and, when no water layer is present (e.g., t/T=0.41-0.59 in Fig. 5-11), no damping of the pressure occurs.
  - While the waves surges on the revetment, the energy of the wave is concentrated in the front part of the wave, leading to an increase of the pressure. In other words, the presence of the PBA-revetment represents an obstacle that does not allow the energy to be fully transmitted (despite the porosity of the structure). Subsequently, the wave energy is accumulated at the front of the wave in contact with the revetment.
- The pressure in the swash zone increases until it reaches a second peak (Fig. 5-10), which produces the infiltration of the water inside the revetment (t/T=0.59-0.67 in Fig. 5-11).

Finally, from the second peak (close to the maximum run-up location) the pressure decreases to zero. Finally, it should be stressed that the effect of the wave height H_0 and wave period T cannot be observed directly in Fig. 5-10, since the pressure distribution is normalized with P_{max1}, but as shown in Fig. 5-7, P_{max1} is dependent on the wave height, the wave period and the revetment slope, thus modifying the magnitude of all pressures on the revetment slope.

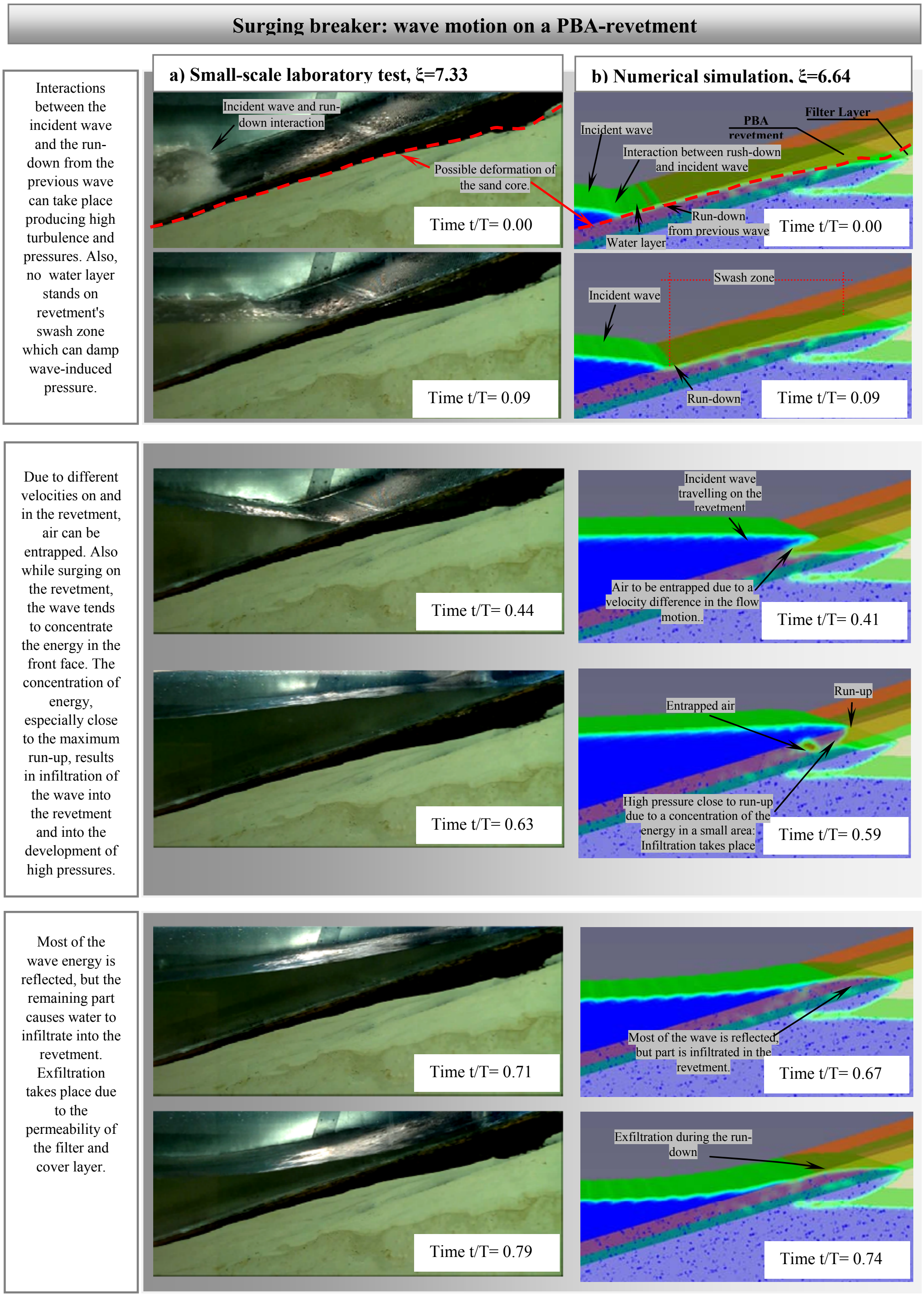

Surging breaker: wave motion on a PBA-revetment

a) Small-scale laboratory test, ξ=7.33

b) Numerical simulation, ξ=6.64

Interactions between the incident wave and the run-down from the previous wave can take place producing high turbulence and pressures. Also, no water layer stands on revetment's swash zone which can damp wave-induced pressure.

Due to different velocities on and in the revetment, air can be entrapped. Also while surging on the revetment, the wave tends to concentrate the energy in the front face. The concentration of energy, especially close to the maximum run-up, results in infiltration of the wave into the revetment and into the development of high pressures.

Most of the wave energy is reflected, but the remaining part causes water to infiltrate into the revetment. Exfiltration takes place due to the permeability of the filter and cover layer.

Fig. 5-11: Surging breaker on PBA-revetment based on a) physical small-scale tests by Liebisch & Oumeraci (2012) and b) numerical simulations.

b) Impact loads: process analysis

For impact loads, the spatial distribution of the pressure on the revetment (Fig. 5-12) is slightly different to that of non-impact loads in Fig. 5-10. The effect of the revetment-filter thickness can be neglected and, for locations above x'_{max1}, the second peak in the pressure distribution observed in non-impact waves is also present for impact loads. Larger scatter occurs all along the revetment slope and especially at locations above the impact point x'_{max1} for impact waves, while for non-impact waves those locations are associated with less scatter (s. Fig. 5-10).

A similar comparative analysis to that in Fig. 5-11 for non-impact loads is also performed in Fig. 5-13 for impact loads, so that the spatial pressure distribution on the revetment may be affected by the following processes:

- The crest of the incident wave becomes steeper and curls over. Due to the wave rush-down of the previous wave (and depending on the revetment-filter thickness) a water layer thickness is observed at the location of the peak pressure (Fig. 5-13a &b).
- When the crest of the incident wave curls over, a large amount of air is trapped.
- Once the wave plunges on the revetment (or on a water layer over the revetment), a splash-up is immediately generated (Fig. 5-13). The magnitude and motion of the splash-up depends on the thickness of the water layer over the revetment as well as on the breaker height.

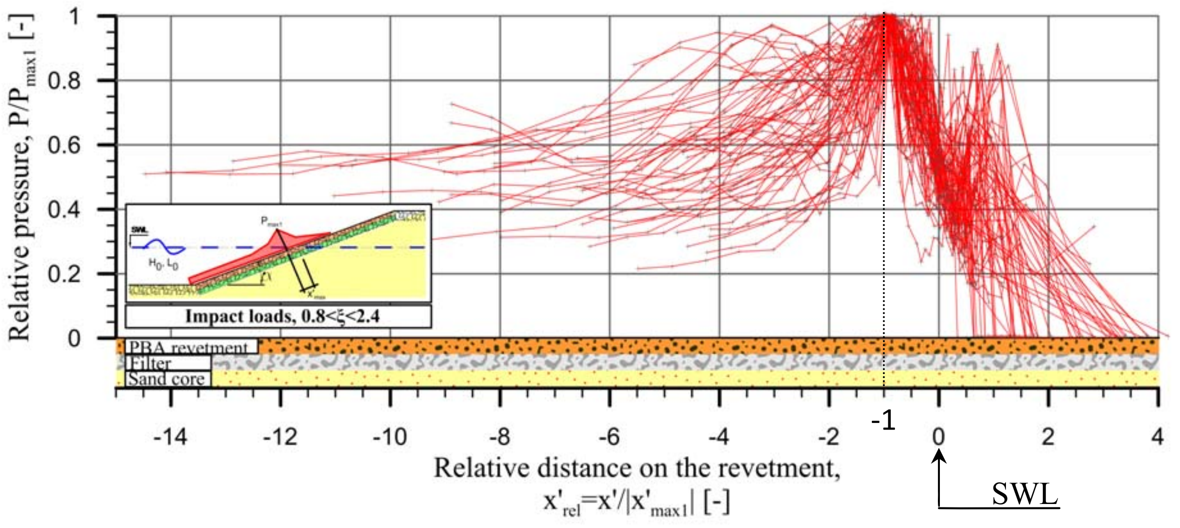

Fig. 5-12: Spatial distribution of the dynamic pressure on the revetment for impact waves for all revetment-filter thicknesses.

Plunging breaker: wave motion on a PBA-revetment

The crest of the wave becomes steeper and curls over. A water layer on the revetment results from the previous wave run-up. The presence of this water layer and its thickness depend on the revetment-filter thickness (section 5.1.1).

After the first plunge on the revetment, a splash-up is immediately observed. The interaction with an existing water layer on the revetment can modify the magnitude of the splash-up which will later impact on the revetment.

The breaker projects forward the splash-up. The splash-up will then generate an impact load and subsequent splash-ups. Therefore, impact loads of smaller magnitude are induced on the revetment.

During the breaking process, entrapped air and bubbles are observed.

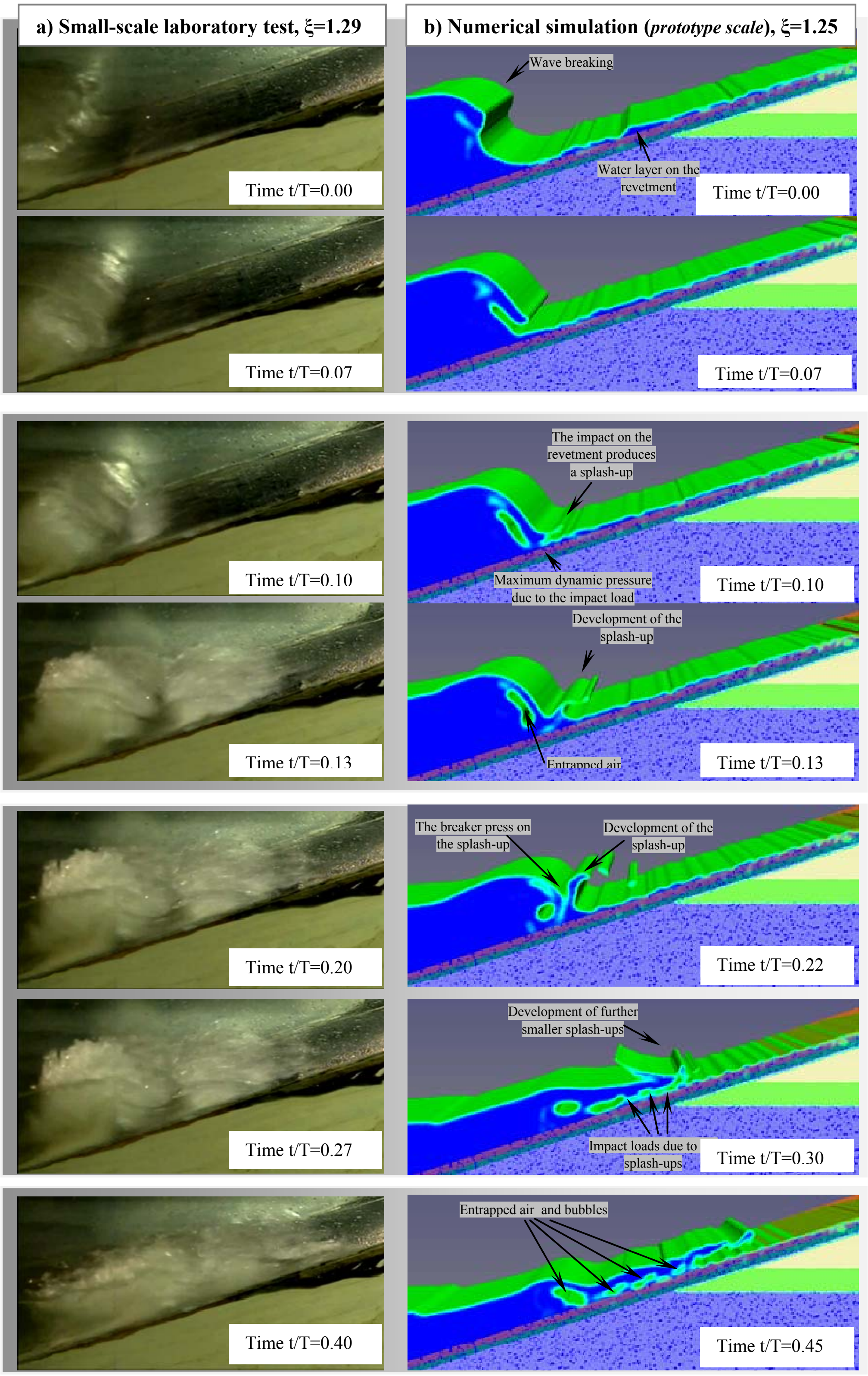

Fig. 5-13: Plunging breaker on PBA-revetment based on a) physical small-scale tests by Liebisch & Oumeraci (2012) and b) numerical simulations.

- The induced splash-up is projected forward by the breaker resulting in a further impact on the revetment slope. This generates a new peak within the spatial pressure distribution (s. Fig. 5-12). Furthermore, due to the impact of the splash-up on the revetment, new splash-ups develop and impact loads of smaller magnitude are generated on the revetment. These impacts are described by peaks of smaller magnitude in the spatial dynamic pressure distribution (Fig. 5-12). This may explain the large scatter observed above the location $x_{\max 1}$ in the pressure distribution for impact waves characterized by the presence of small peaks (Fig. 5-12), which are not observed with non-impact waves (Fig. 5-10). This behaviour is also described in the literature (e.g., Ghosh et al. (2007); Pedrozo-Acuña et al. (2011)).
- Finally, the quasi-static component of impact loads behaves similarly to the non-impact load. Therefore, a final peak is generated before the dynamic pressure becomes zero at the location of the maximum wave run-up.

c) Prediction formulae

The development of the prediction formulae is based on the processes analysis in sections 5.2.3a&b for the spatial pressure distribution for both impact and non-impact waves. The effect of the revetment filter thickness is not considered for the analysis of the relative pressure $P/P_{\max 1}$ because $P_{\max 1}$ already accounts for the variation of d_{rev} (s. Section 5.2.1). Moreover, the prediction formula in eq. (5.14) developed by Alcérreca-Huerta & Oumeraci (2012) for the pressure distribution on concrete placed blocks (CPB) revetment will be used since it provides the following advantages over other approaches (e.g., Oumeraci et al. (2010)): i) it represents a continuous function for the entire domain of application and ii) it can fulfil the requirement that $P/P_{\max 1}=1.0$ at $x'_{rel}=x'/|x'_{\max 1}|=-1.0$. Therefore, the formulae are developed for the upper envelope of the spatial pressure distribution due to the scatter found in the results of PBA-revetments which could be also noticed for CPB-revetments (Alcérreca-Huerta & Oumeraci (2012)).

$$\frac{P}{P_{\max 1}} = \frac{A + B \cdot x'_{rel}}{1 + C \cdot x'_{rel} + D \cdot \left(x'_{rel}\right)^2} \quad \text{with} \quad x'_{rel} = \frac{x'}{\left|x'_{\max 1}\right|} \tag{5.14}$$

To fulfil the requirement $P/P_{\max 1}=1.0$ at $x'_{rel}=-1.0$, the relationship $A=1+B-C+D$ should be fulfilled. Moreover, the first derivative of eq. (5.14) should be zero at $x'_{rel}=-1.0$ in order to represent the highest peak in the pressure distribution. Therefore, $A/B=(1-D)/(C-2D)$ should be fulfilled and thus: $A=1-D \rightarrow D=1-A$, $B=(C-2D)=C-2(1-A)$. Finally, if $D=1-A$ and $B=C-2(1-A)$ then the first requirement is also fulfilled. Therefore, eq. (5.14) can be rewritten:

$$\frac{P}{P_{\max 1}} = \frac{A + \left(C - 2(1-A)\right)\left(x'_{rel}\right)}{1 + C\left(x'_{rel}\right) + (1-A)\left(x'_{rel}\right)^2} \tag{5.15}$$

In the following, the prediction formulae are given based on eq. (5.15), first for non-impact loads and then for impact loads, where the only difference is found on the different values of coefficients A and C.

i) For non-impact waves, the spatial pressure is defined by eq. (5.16). This equation is valid only for locations below the maximum run-down ($x'\leq x'_{Rd}$) since a second peak develops within the swash zone.

$$\frac{P}{P_{\max 1}}=\frac{0.705-5.172\left(x'_{rel}\right)}{1-4.581\left(x'_{rel}\right)+0.295\left(x'_{rel}\right)^2}, \qquad \text{valid for } x'\leq x'_{Rd} \tag{5.16}$$

The second peak on the spatial distribution of the dynamic pressure on the revetment was found to have a mean value of $P/P_{\max 1}=0.761$ and a location above the run-down approximately 0.83% the swash height (Rd-Ru). Eq. (5.17) describes the magnitude and the location of the second peak which is important for the determination of the spatial pressure distribution in the swash zone.

$$\text{Second peak:} \frac{P}{P_{\max 1}}\approx 0.761 \qquad at \qquad x'_{rel}=\left[x'_{Rd}+0.83\left(x'_{Ru}-x'_{Rd}\right)\right]/\left|x'_{\max 1}\right| \tag{5.17}$$

with x'_{Rd} and x'_{Ru} calculated with eq. (5.13) with z=Rd and z=Ru, respectively.

ii) For impact waves, the prediction formula for the spatial distribution parallel to the revetment is defined by eq. (5.18) for locations below the maximum run-down level ($x'\leq x'_{Rd}$). Similar to non-impact waves, this formula is the envelope of the maximum pressures that can be found on the revetment. Furthermore, the second peak of the spatial pressure distribution for impact waves can be located trough the point described by eq. (5.19)

$$\frac{P}{P_{\max 1}}=\frac{0.789-3.330\left(x'_{rel}\right)}{1-2.908\left(x'_{rel}\right)+0.211\left(x'_{rel}\right)^2}, \qquad \text{valid for } x'\leq x'_{Rd} \tag{5.18}$$

$$\text{Second peak:} \frac{P}{P_{\max 1}}\approx 0.715 \qquad at \qquad x'_{rel}=\left[x'_{Rd}+0.723\left(x'_{Ru}-x'_{Rd}\right)\right]/\left|x'_{\max 1}\right| \tag{5.19}$$

with x'_{Rd} and x'_{Ru} calculated with eq. (5.13) with z=Rd and z=Ru, respectively.

The spatial distribution of the pressure on the revetment for non-impact (Fig. 5-14) and impact loads (Fig. 5-15) is given respectively by eq. (5.16) and eq. (5.18) until the location of the wave run-down x'_{Rd}. From this point and until the location of the second peak (eq. (5.17) and eq. (5.19) respectively), a linear interpolation can be made. Finally, from the second peak, the pressure decreases linearly to a value of zero at x'_{Ru} (for the prediction of the maximum Ru and Rd see eqs. (4.18) and (4.20), respectively, in section 4.3.2). For impact waves, this second peak is lower than for non-impact waves, however, for both loading cases, the pressure peaks are within the range of 0.70 to 0.80 $P_{\max 1}$.

A comparison of the coefficients A and C in the formulae for both impact and non-impact loads is given in Table 5-2.

Table 5-2: Coefficients for the prediction formulae of the spatial pressure distribution on PBA-revetments for impact and non-impact loads.

Wave loading	***Spatial pressure distribution on a PBA-revetment***			
	For locations < x_{Rd} (eq. (5.15))		Location second peak	
	Coeff. A	Coeff. C	x'_{rel}	P/P_{max1}
Non-impact loads	0.705	-4.581	$x'_{Rd}+0.83(x'_{Ru}-x'_{Rd})\ /\ \lvert x'_{max1}\rvert$	0.706
Impact loads	0.789	-2.908	$x'_{Rd}+0.72(x'_{Ru}-x'_{Rd})\ /\ \lvert x'_{max1}\rvert$	0.715
Average	0.747	-3.745	$x'_{Rd}+0.775(x'_{Ru}-x'_{Rd})\ /\ \lvert x'_{max1}\rvert$	0.710

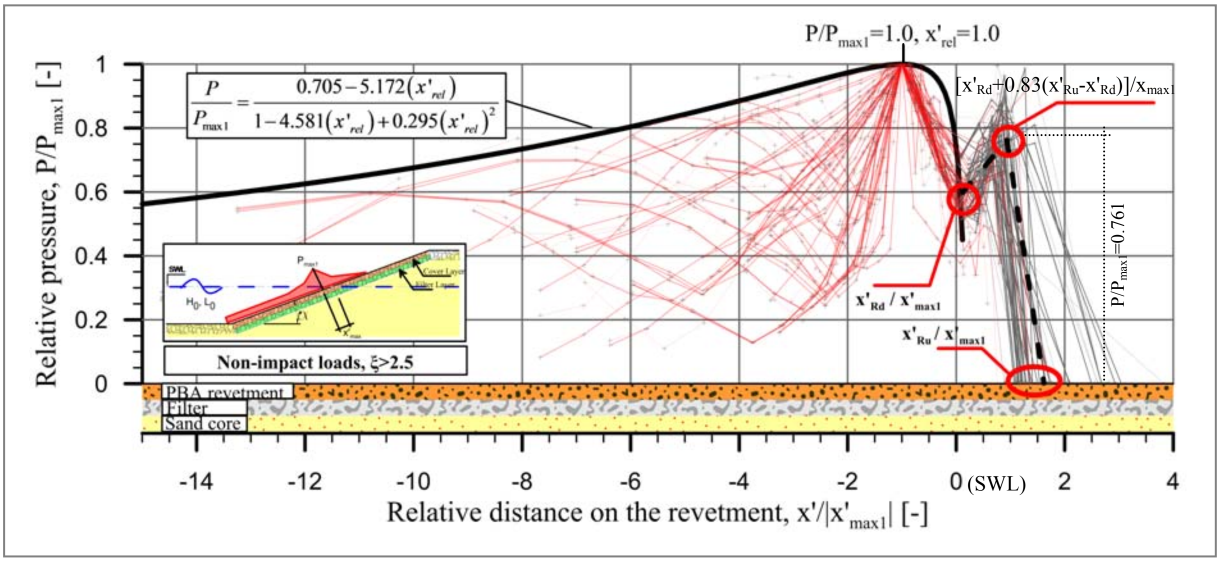

Fig. 5-14: Prediction formula for the spatial distribution of the pressure on the revetment for **non-impact** loads.

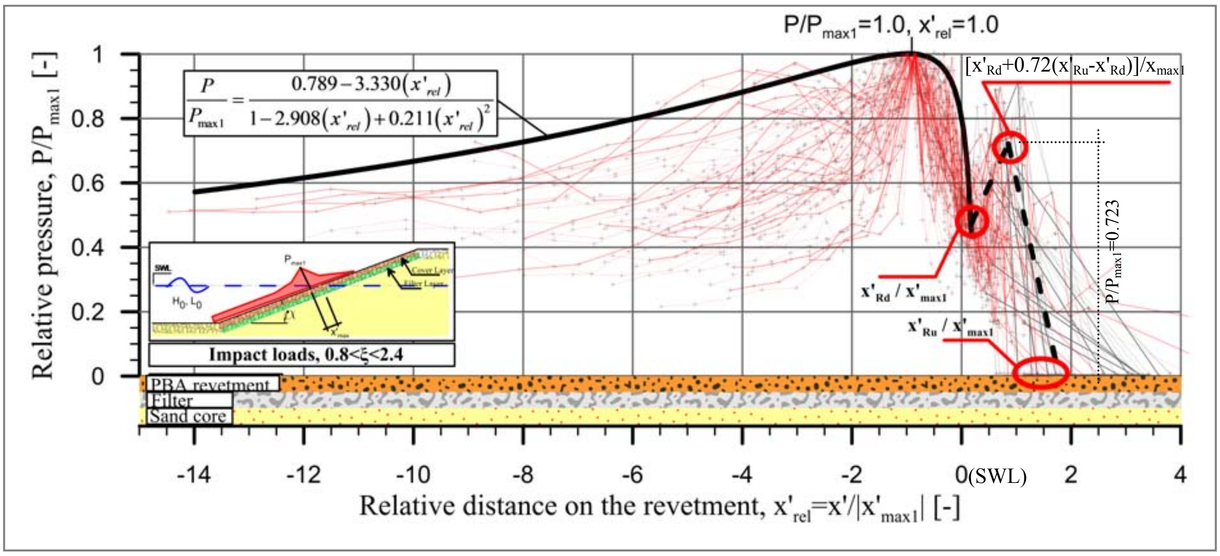

Fig. 5-15: Prediction formulae for the spatial distribution of the dynamic pressure on the revetment for impact loads.

It can be observed in Table 5-2 that the coefficients of the prediction formulae for both impact and non-impact loads are similar and thus, a single equation for the description of the spatial pressure distribution is proposed considering the average of the coefficient values:

$$\frac{P}{P_{\max 1}} = \frac{0.747-4.251\left(x'_{rel}\right)}{1-3.745\left(x'_{rel}\right)+0.253\left(x'_{rel}\right)^{2}}, \qquad \text{valid for } x' \leq x'_{Rd} \tag{5.20}$$

$$\text{Second peak: } \frac{P}{P_{\max 1}} \approx 0.710 \qquad at \qquad x'_{rel} = \left[x'_{Rd}+0.775\left(x'_{Ru}-x'_{Rd}\right)\right]/\left|x'_{\max 1}\right| \tag{5.21}$$

The comparison between the spatial pressure distributions on the revetment obtained from the prediction formulae for impact (eqs. (5.18) & (5.19)) and non-impact loads (eqs. (5.16) & (5.17)) is also shown in Fig. 5-16. From Fig. 5-16 it is seen that that there is only a slight difference in the spatial pressure distribution between impact and non-impact loads. The difference mainly occurs at locations in deeper water far away from the peak pressure $P_{\max 1}$ and also in the swash zone where the second peak is slightly smaller for impact waves than for non-impact waves. It is stressed that the location of the maximum run-up and run-down are of high relevance for the spatial pressure distribution in the swash zone since a second peak on the pressure distribution is achieved within this zone (Fig. 5-16).

Furthermore, it can be noticed that the spatial pressure distribution for impact and non-impact loads can be described by eq. (5.20) with the second peak pressure located according to eq. (5.21). The previous allows a straightforward calculation of the spatial pressure distribution.

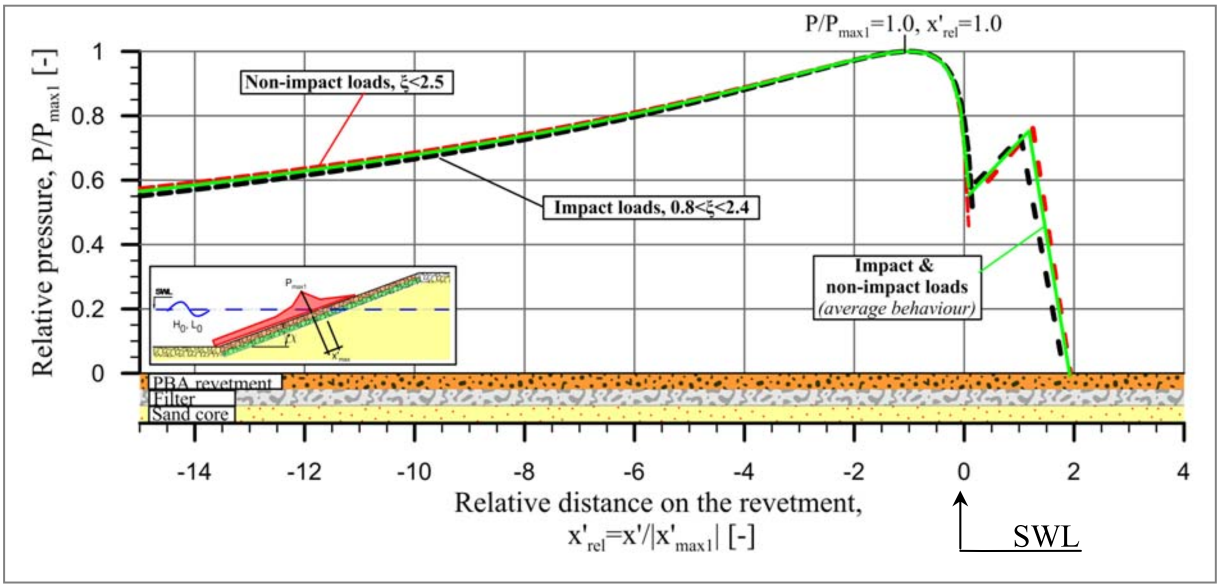

Fig. 5-16: Comparison of the spatial pressure distribution on the revetment for impact and non-impact waves provided by the prediction formulae and average behaviour.

The similar trend of the spatial pressure distribution for both impact and non-impact loads may occur since the mechanisms for the transmission of $P_{\max 1}$ along the revetment are almost similar. For impact loads, the effect of the impact component $P_{\max 1}$ may not only affect the location $z_{\max 1}$ where the impact occurs, rather it affects an area on the revetment, thus providing a peak pressure which smoothly decreases with the distance (the transmission of the impact load may be caused by the low compressibility of the water). Moreover, the quasi-static component of the impact load (with similar distribution as non-impact loads) slightly decreases within the distance in a similar way to the impact component (Alcérreca-Huerta & Oumeraci (2014)).

The trend of the pressure distribution on the revetment shows two pressure peaks occurring at the location of the impact point and close to the location of the maximum run-up over the swash zone. Just slight differences of this trend are noticed between impact and non-impact loads. Moreover, the definition of the pressure distribution on the revetment is highly dependent on the magnitude of the peak pressure P_{max1} and its location on the revetment (z_{max1}). Furthermore, the peak pressure is strongly affected by the revetment-filter thickness d_{rev} in such a way that for plunging breakers a larger d_{rev} decreases P_{max1} and for collapsing breakers a larger d_{rev} increases P_{max1}. However, no effect of d_{rev} was observed for the quasi-static component and surging breakers. The peak pressure varies depending on the presence of a water layer on the revetment at the impact location which changes due to the slope steepness, the porosity and d_{rev}. Furthermore, the location of the peak pressure z_{max1} strongly varies for plunging and collapsing breakers which is important for the estimation of the spatial pressure distribution on the revetment according to the prediction formulae here proposed.

5.3 Wave-induced pore pressures on top of the sand core

In the numerical parameter study, the wave-induced pore pressures on top of the sand core beneath the revetment were also investigated in order to determine the benefits of increasing the revetment-filter thickness for the damping of the wave pressure. It is expected that a thicker revetment-filter layer will induce a reduction of the wave-induced pore pressure that is transmitted to the top of the sand core. This is of high relevance for PBA-revetments since a higher pressure on top of the sand core may induce foundation failure modes, such as soil liquefaction, and consequently the failure of the whole revetment (as observed in GWK large-scale tests, Oumeraci et al. (2010)).

In the following sections, the results of the analysis and the development of prediction formulae are presented for the wave-induced peak pore-pressure and its location on top of the sand core of PBA-revetments, also including the pore pressure distribution along the slope of the sand core.

5.3.1 Peak pore-pressure on top of the sand core

a) Process analysis

The peak pore-pressure on top of the sand core is denoted as P_{max3}, in order to differentiate with the peak pressure on the revetment P_{max1}.

The results from the numerical simulations are first compared to the results from the large-scale tests in GWK (Oumeraci et al. (2010)) as shown in Fig. 5-17. Comparing the relative peak pressure on top of the revetment (Fig. 5-6) and the peak pore-pressure on top of the sand core (Fig. 5-17), it was noticed that the non-impact loads as well as the quasi-static component of impact loads are only slightly damped through the revetment and filter layers. This dissipation is small even for large revetment-filter thicknesses. In contrast, the revetment-filter thickness significantly damps the impact component of the wave-induced pressure of impact loads.

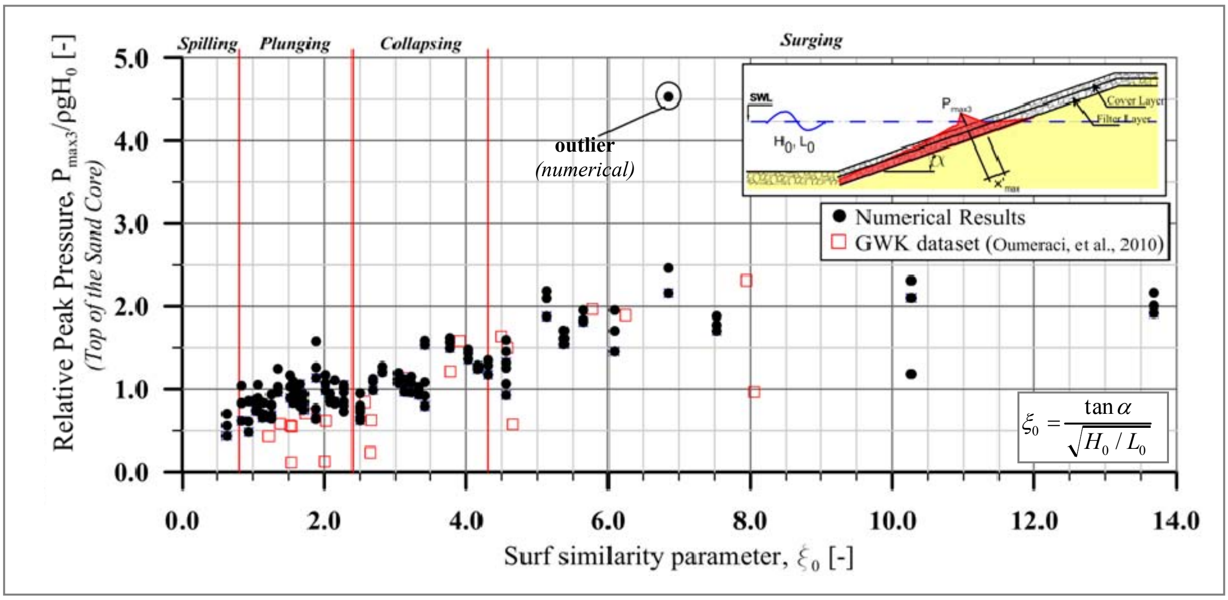

Fig. 5-17: Relative peak pressure on top of the sand core: numerical simulations vs. GWK tests with PBA-revetments.

The ratio of the peak pore pressure on top of the sand core (P_{max3}) and the peak pressure on top of the revetment (P_{max1}) is described as a function of the surf similarity parameter in Fig. 5-18. It can is observed that P_{max1} may decrease significantly through the revetment and filter layers depending on the ξ_0-range and the d_{rev}-value. It is observed that d_{rev2}=0.25m and d_{rev3}=0.35m provide higher dissipation than d_{rev1}=0.15m. For the quasi-static component (clearly observed for surging breakers), the peak pressure P_{max1} is reduced by only 15% for d_{rev}=0.35m compared to 10% for d_{rev}=0.15m. Also, the scatter is reduced for surging breakers, since less turbulence is produced inside the porous media due to an increase of the time scale needed for developing waves with large wave periods (T), which becomes closer to the time scale of the fluid motion inside the revetment and filter layers (defined mainly by the permeability).

For a revetment-filter thickness d_{rev}=0.15m and ~2.0 < ξ_0 < ~8.0, the peak pore pressure on top of the sand core in some cases was higher than that registered on top of the revetment. This might be due to several reasons that should be investigated in further studies:

- A thinner revetment-filter does not allow a large water motion than a thicker revetment-filter. Thus, due to the limited water motion and because of the momentum balance, the dynamic pressure inside these layers should increase.

- The change of the fluid motion direction of the internal run-down inside the revetment-filter layers due to the new incident wave produces high turbulence and the increment of the pore pressure. This effect did not occur for larger revetment-filter thicknesses (d_{rev} > 0.15m) since the space for the turbulence generation and the direction of the fluid motion is larger, decreasing the possibility for the development of high pressures on top of the sand core.

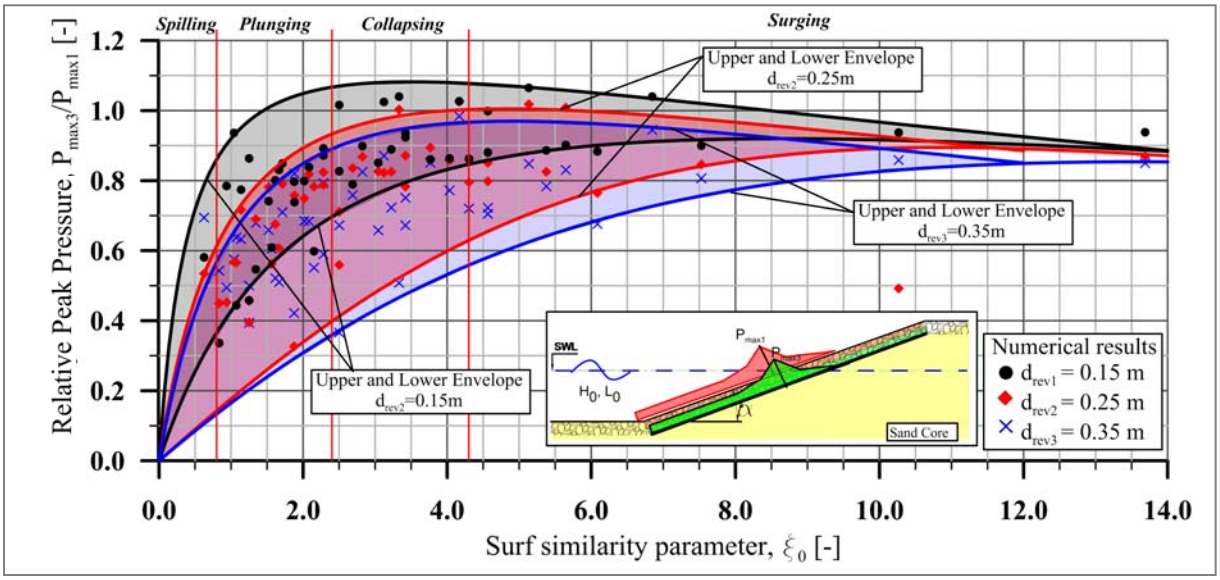

Fig. 5-18: Ratio of the peak pressure on top of the sand core and on the revetment (P_{max3}/P_{max1}) vs. surf similarity parameter for different revetment-filter thicknesses (d_{rev}).

b) *Prediction formulae*

As shown by eq. (5.4) for the pressure on the revetment, the peak pressure P_{max} is described as the sum of P_{stat} (quasi-static component) and P_{diff} (pressure difference between the peak pressure P_{max} and P_{stat}). As mentioned in section 5.3.1a, approximately 10 to 15% of the quasi-static component is dissipated through the revetment-filter layer depending on the revetment-filter thickness (d_{rev}). Thus, an average dissipation of 12.5% is assumed (i.e., 87.5% of P_{max1} is transmitted to the top of the sand core).

Thus, the prediction formulae for the quasi-static component of the peak pressure on the revetment (eq. (5.5)) can be multiplied by a reduction factor of 0.875 to provide the quasi-static component of the peak pore pressure on top of the sand core, leading to eq. (5.22).

$$\left(\frac{P_{stat3}}{\rho g H_0}\right)_{Quasi-static} = 1.75\frac{\xi_0^{\,2}+6.7\cdot\xi_0}{\xi_0^{\,2}+38.5} \tag{5.22}$$

The peak pore-pressure on the sand core P_{max3} can be estimated as shown in eq. (5.23), where a constant factor (denoted as γ_{RF} and dependent on the revetment-filter thickness) is considered to take into account the effect of the dissipation of the impact component P_{max1} through the revetment and filter layers.

$$\frac{P_{max3}}{\rho g H_0} = \gamma_{RF} A \cdot \xi_0 \cdot \exp\left(-\frac{\xi_0^2}{B'}\right) + \left(\frac{P_{max3}}{\rho g H_0}\right)_{Quasi-static} \tag{5.23}$$

In order to consider both the effect of the revetment-filter thickness on P_{max3} and its dissipation through the layers, coefficients A and γ_{RF} are merged into a single coefficient A' (A'= γ_{RF} A). Therefore, eq. (5.23) can be simplified and expressed as in eq. (5.24) which represents the upper envelope of the relative peak pore-pressure P_{max3}.

$$\frac{P_{max3}}{\rho g H_0} = A' \cdot \xi_0 \cdot \exp\left(-\frac{\xi_0^2}{B'}\right) + 1.75\frac{\xi_0^2 + 6.7 \cdot \xi_0}{\xi_0^2 + 38.5} \tag{5.24}$$

where coefficients A', B' as well as A and γ_{RF} are described in Table 5-2. Coefficient B' is related to the ξ_0-range where the impact component has an influence on top of the sand core. The prediction formula eq. (5.24) for different revetment-filter thickness is shown in (Fig. 5-19).

Table 5-3: Coefficients A' , A, γ_{RF} and B for the estimation of the impact component of the relative peak pressure on top of the sand core beneath PBA-revetment (see also Table 6-1).

Revetment filter thickness	***d_{rev1}=0.15m***	***d_{rev1}=0.25m***	***d_{rev1}=0.35m***
Coefficient A'= γ_{RF} A	0.908	0.539	0.300
- Coefficient A	*3.25*	*2.27*	*1.24*
- Coefficient γ_{RF}	*0.28*	*0.24*	*0.24*
Coefficient B'	4.72	7.67	10.80

Overall, the effect of the revetment-filter thickness is larger for the impact component of the peak pressure P_{max3} than for the quasi-static component. Furthermore, increasing the revetment-filter thickness reduces the peak pressure on top of the sand core for impact loads. However, a change of the revetment-filter thickness from d_{rev}=0.15m to d_{rev}=0.25m has a larger effect than a further increase from d_{rev}=0.25m to d_{rev}=0.35m. (see also Fig. 5-18). Considering only coefficient γ_{RF}, it is estimated that 72% of P_{max1} (under impact load conditions) can be dissipated for d_{rev}=0.15m, and 76% for d_{rev}=0.25m and d_{rev}=0.35m.

Finally, further studies are required in order to correlate properly the dissipation of P_{max1} with the revetment-filter thickness d_{rev} and to establish and explicit relationship between both P_{max1} and d_{rev}. Furthermore, a change in permeability of the revetment-filter layer should be investigated since it is expected to affect the dissipation of the peak pressures on and beneath the revetment.

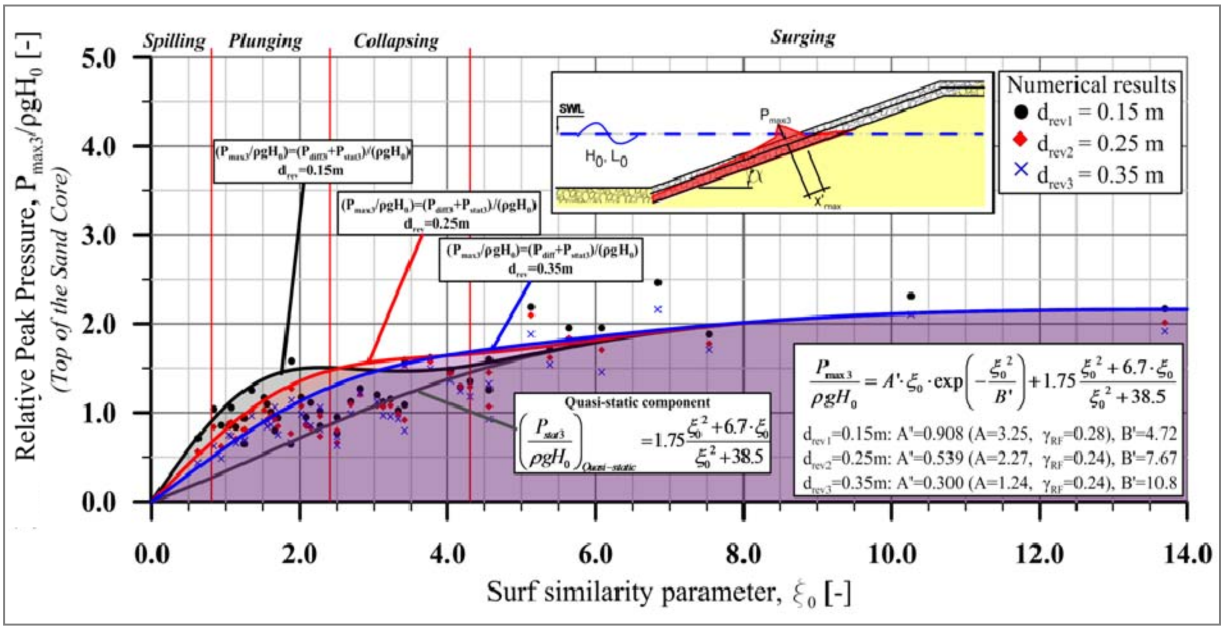

Fig. 5-19: Prediction formulae for relative peak pore pressure on top of the sand core for different revetment-filter thickness d_{rev}, including the relative pressures: $P_{max3}/\rho g H_0$, $P_{diff3}/\rho g H_0$ and $P_{stat3}/\rho g H_0$ (quasi-static component).

5.3.2 Location of the peak pore pressure on top of the sand core

The location z_{max3} of the peak pressure on top of the sand core (P_{max3}) was analysed and like for the location z_{max1} of P_{max1} on the revetment, z_{max3} is measured vertically from the SWL and is positive in upwards direction (see Fig. 5-5).

The revetment-filter thickness does not affect the location z_{max3} of the peak pore pressure P_{max3} (Fig. 5-20). Furthermore, few numerical data points within the domain of plunging breakers provide a different trend to the one described by the rest of the data set. This particularly occurs for a surf similarity parameter $\xi_0 \approx 2.3$, which is close to the condition where the resonance effect described by Bruun & Günbak (1977) takes place. However, for the development of the prediction formulae for z_{max3} (and similar than for z_{max1}), the points at $\xi_0 \approx 2.3$ and outside the data trend are considered as outliers. Further analysis is required to verify if these points are physically justified or only numerically produced since no large amount of data can be found for ξ_0-values close to $\xi_0 \approx 2.3$.

The prospective prediction formula is based on the mean value given by the hyperbolic tangent approach for the estimation of z_{max1}/H_0 shown in eq. (5.9). A constant factor has been applied to eq. (5.9) to predict the location of the peak pore pressure on top of the sand thus resulting in eq. (5.25) with standard deviation σ=34%.

$$\frac{z_{max3}}{H_0}=1.19\left[-1.62\tanh\left(0.46\cdot\xi_0^{\,0.47}\right)\right] \tag{5.25}$$

Considering that z_{max3} and z_{max1} are measured as the vertical distance from the SWL, then the constant factor equal to 1.19 in eq. (5.25) lead to the following conclusions related to the direction of the pressure transmission: i) the location of z_{max3} where P_{max3} occurs is deeper (in the vertical) than z_{max1} where P_{max1} takes place, ii) since the revetment-filter thickness does not provide a clear effect on z_{max1} and z_{max3}, the variation of the peak pressures location in the different layers may be dependent on other variables such as the wave impact angle together with the slope steepness.

Due to the scatter found in the dataset for the location of the peak pore-pressure on top of the sand core, the extreme values z_{max3}/H_0 are defined as in eq. (5.26) for the upper envelope and eq. (5.27) for the lower envelope (Fig. 5-20). These envelopes were obtained with a similar procedure than that described in sections 5.2.1b and 5.2.2 for P_{max1} and z_{max1}, respectively.

Upper Envelope
$$\frac{z_{\max 3}}{H_0} = -1.77 \tanh\left(0.18 \cdot \xi_0^{\,0.78}\right) \tag{5.26}$$

Lower Envelope
$$\frac{z_{\max 3}}{H_0} = -1.77 \tanh\left(2.07 \cdot \xi_0^{\,2.09}\right) \tag{5.27}$$

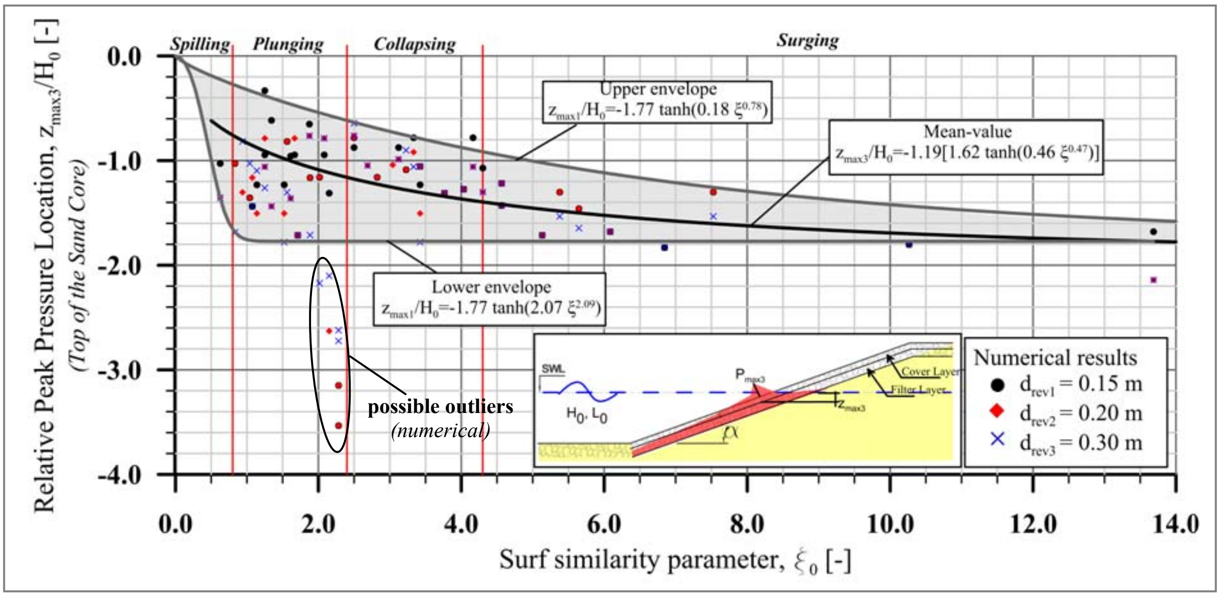

Fig. 5-20: Envelopes and prediction formulae for the location (z_{max3}/H_0) of the peak pressure P_{max3} on top of the sand core of PBA-revetments.

The lower location of z_{max3} compared to that of z_{max1} is a finding that was also reported in previous studies on PBA-revetments (Oumeraci et al. (2010)) and on concrete placed blocks revetments (Alcérreca-Huerta & Oumeraci (2012)). Both z_{max1} and z_{max3} may be influenced by the revetment geometry and the wave kinematics. However, further studies focused on the wave breaking over slopes and the kinematics should be conducted to determine their influence on z_{max1} and z_{max3}.

5.3.3 Pore pressure distribution on top of the sand core parallel to the revetment slope

For the description of the spatial pore pressure distribution, the coordinate system defined in Fig. 5-5 is used. Furthermore, the normalization of the pore pressure distribution on top of the sand core is analogous to the one used for the spatial pressure distribution on the revetment P/P_{max1} (Section 5.2.3). Thus, the normalized spatial pore pressure distribution on top of the sand core beneath the revetment is described in terms of the relative pressure P/P_{max3} induced at a location $x'_{rel3}=x'/|x'_{max3}|$; where, P is the pore pressure at a location x' (see Fig. 5-5), P_{max3} is the peak pore pressure on top of the sand core and x'_{max3} is (like for x'_{max1} in eq. (5.12)) function of the slope steepness and the location of P_{max3} as described by eq. (5.28):

$$x'_{\max 3} = \sqrt{\left(z_{\max 3}\right)^2 + \left(z_{\max 3} \cdot \cot \alpha\right)^2} \tag{5.28}$$

where z_{max3} is the location of P_{max3} on top of the sand core measured vertically from the SWL and positive in upwards direction (see Section 5.3.2).

The results of the spatial distribution of the pore pressure on top of the sand core for impact and non-impact loads are similar to those for the spatial distribution on the revetment, especially at locations below the maximum run-down. However, the second peak in the pressure spatial distribution on the revetment (Fig. 5-10) is reduced through the revetment and filter layers as shown in Fig. 5-21a & b. The internal swash on top of the sand core (s. Section 4.3) may induce a decrease of the second peak of the spatial pore pressure distribution. Therefore, the prediction formulae are given first for non-impact loads and then for impact loads:

i) For *non-impact waves* and since the spatial pressures on the revetment and on top of the sand core are normalized in a similar manner, the prediction formula given in eq. (5.16) can be applied just modifying the sub-indices to refer to the spatial pore-pressure distribution on top of the sand core as in eq. (5.29) with x'_{Rd3} calculated with eq. (5.13) and $z=Rd_{Lay3}$.

$$\frac{P}{P_{\max 3}} = \frac{0.705 - 5.172\left(x'_{rel3}\right)}{1 - 4.581\left(x'_{rel3}\right) + 0.295\left(x'_{rel3}\right)^2} \quad \text{valid for } x' \le x'_{RdLay3} \tag{5.29}$$

The second peak of the spatial dynamic pressure distribution can be located through the point described by eq. (5.30). Therefore, the spatial distribution of the pore pressure on top of the sand core is given by eq. (5.29) until x'_{Rd3} (location where the maximum run-down on the sand core Rd_{Lay3} is achieved). A linear interpolation can then be made until the second peak is achieved (eq. (5.30)). Finally, from the second peak, the pressure decreases linearly to a value of zero where the maximum run-up on the sand core (Ru_{Lay3}) is found.

$$\text{Second peak: } \frac{P}{P_{\max 3}} \approx 0.761 \qquad at \qquad x'_{rel3} = \left[x'_{Rd3} + 0.723\left(x'_{Ru3} - x'_{Rd3}\right)\right] / \left|x'_{\max 3}\right| \tag{5.30}$$

ii) For *impact waves*, the prediction formula for the spatial pressure distribution on top of the sand core is given in a similar way than for non-impact waves. However, the second peak of the spatial pressure distribution on the revetment decreases considerably to the top of the sand core (see Fig. 5-12 and Fig. 5-21b for comparison, respectively). This reduction might be explained by the turbulence produced by the impact which also interacts with the porous structure of the revetment and filter layers. Thus, the prediction formula for the spatial pore-pressure distribution on top of the sand core can be estimated through eq. (5.31). Since the second peak is not clearly developed, the pressure is assumed to linearly decrease from x'_{Rd3} to the x'_{Ru3} (at which the pore pressure becomes zero).

$$\frac{P}{P_{\max 3}} = \frac{0.789 - 3.330\left(x'_{rel3}\right)}{1 - 2.908\left(x'_{rel3}\right) + 0.211\left(x'_{rel3}\right)^2} \quad \text{valid for } x' \leq x'_{RdLay3} \qquad (5.31)$$

a) Spatial distribution of the pore pressure on the sand core for **non-impact** loads.

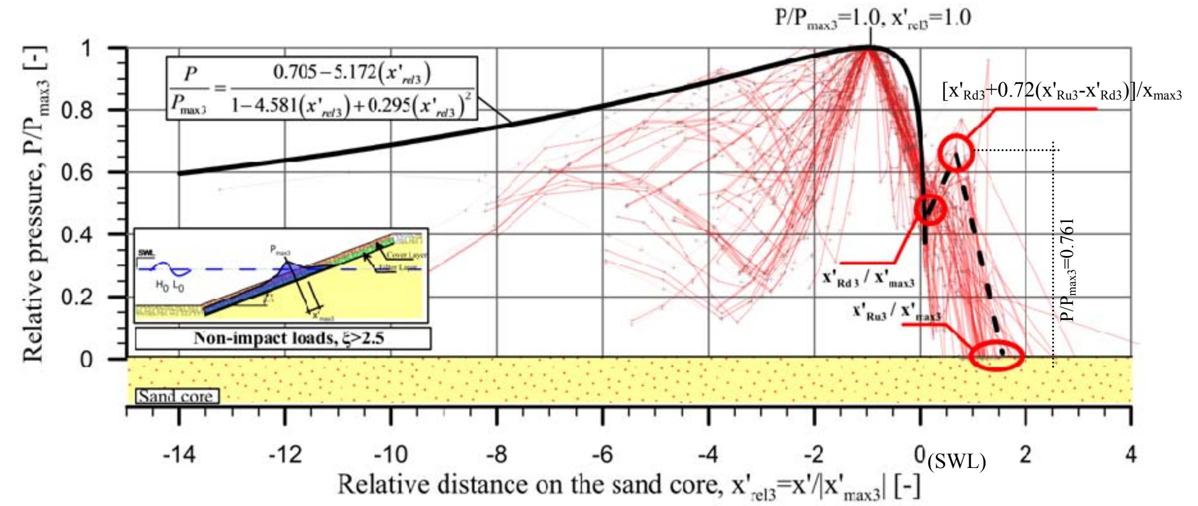

b) Spatial distribution of the pore pressure on the sand core for **impact** loads.

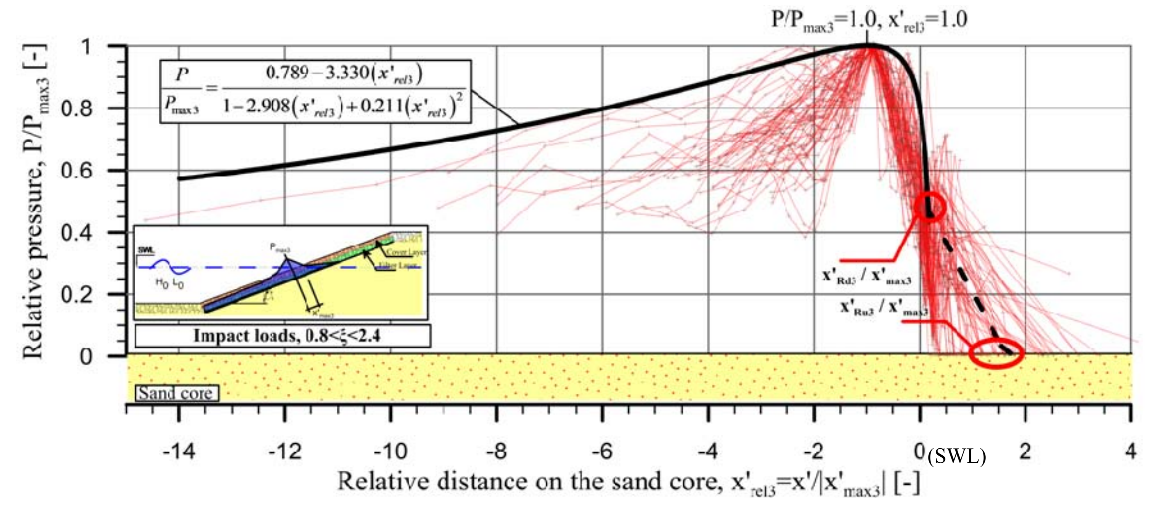

Fig. 5-21: Prediction formulae for the spatial distribution of the pore-pressure on top of the sand core beneath PBA-revetment for a) non-impact and b) impact loads.

The prediction formula for the spatial pressure distribution on top of the sand core for locations below x'_{RdLay3} are similar than that on the revetment. Moreover and as already mentioned, the spatial pressure distribution at these locations is similar between impact and non-impact waves. Therefore, it is recommended to use the proposed average formulae given in eq. (5.32) for both impact and non-impact loads. Nevertheless, for the description of the second peak in the spatial pressure distribution, eq. (5.30) should be implemented for non-impact loads while for impact loads no second peak pressure is presented.

$$\frac{P}{P_{\max 3}} = \frac{0.747 - 4.251\left(x'_{rel}\right)}{1 - 3.745\left(x'_{rel}\right) + 0.253\left(x'_{rel}\right)^2}, \qquad \text{valid for } x' \leq x'_{RdLay3} \qquad (5.32)$$

Overall, the difference between the spatial pore pressure distribution on top of the sand core between impact and non-impact loads is mostly related to the second peak within the internal swash zone. For impact loads, the second peak is not observed, probably due to the associated high turbulence.

Moreover, the presence of the revetment and filter layers is highly important since the impact component of the peak pressure on the revetment P_{max1} for $1.0<\xi_0<4.3$ (plunging and collapsing breakers) significantly decreases its magnitude through the revetment and filter layers: up to 72% for d_{rev}=0.15m and 76% for d_{rev}>0.25m. For comparison, the quasi-static component is reduced only by 10-15%. Finally, the location of z_{max3} where P_{max3} occurs is vertically deeper than z_{max1} where P_{max1} takes place, result that was expected and in agreement with previous studies.

5.4 Wave-induced pore-pressure in the sand core beneath the revetment

The wave-induced pressure distribution normal to the revetment in the sand core was investigated in order to determine the damping of the transmitted pore-pressure in different layers of the sand core. Due to the large amount of numerical data obtained from the parameter study, a preliminary analysis was first performed with the objective of determining the most appropriate approach for a more detailed process analysis and the development of prediction formulae. Therefore, the preliminary analysis is first shown and the process analysis and the development of the prediction formulae are then presented. Moreover, it will be shown that the prediction formulae derived from the results of the parameter study are in agreement with the findings and the approach provided by De Groot et al. (2006).

5.4.1 Preliminary analysis

Columns normal to the slope containing points (numerical pressure probes) were placed in each revetment configuration tested in the parameter study in order to extract the pore-pressure inside the sand core. The number of columns of pressure probes was dependent on the revetment surface subject to wave attack and thus higher for larger cotα: at least 8 columns for slope steepnesses 1:1.5, 1:2 and up to 16 columns for slope steepnesses 1:3, 1:4 and 1:6. Moreover, each of the columns contains 5 pressure probes (see Fig. 5-22) so that the pressure normal to the revetment can be described with a considerable spatial resolution.

The pore pressure distribution along these columns for the different revetment configurations tested is exemplarily shown in Fig. 5-22 (further details and revetment configurations are described in detail in Alcérreca-Huerta & Oumeraci (2014)).

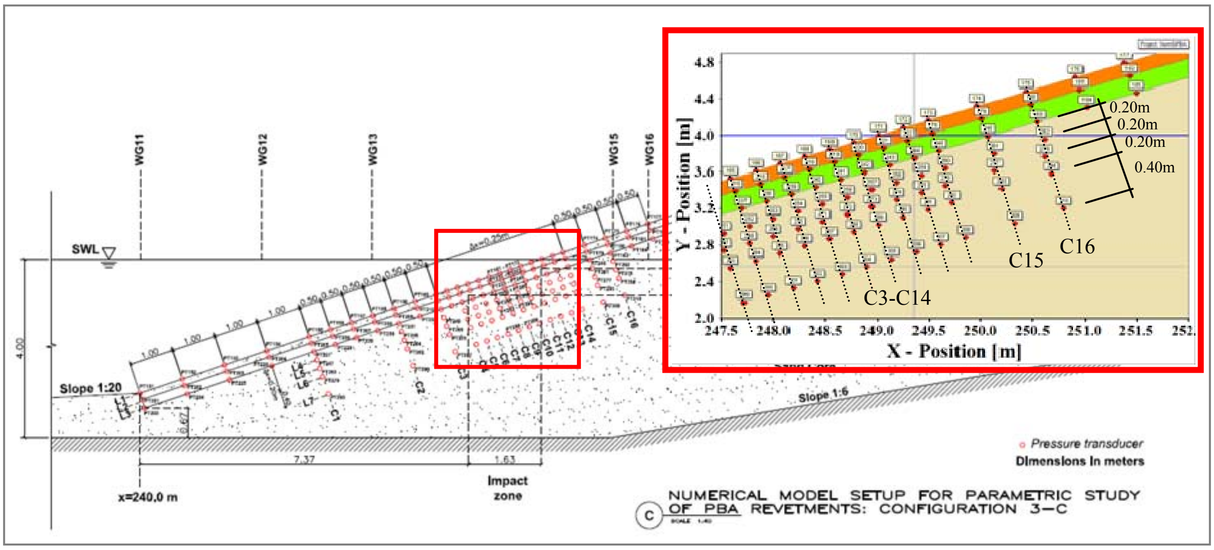

Fig. 5-22: Location of pressure probes in the model set-up for the numerical simulation of a PBA-revetment with slope 1:3 and d_{rev}=0.35m.

Therefore, due to the large amount of data from the numerical simulations, the preliminary analysis of the dataset from the numerical parameter study consisted on:

i. Extraction of the peak pore-pressure (P) in the time series from each of the numerical pressure probes where the pore pressure was calculated.
ii. Identification of the columns of numerical pressure probes normal to the revetment slope.
iii. For each column of pressure probes, the pore-pressures P are normalized considering as reference the pore pressure on top of the sand P_{topSC}: P/P_{topSC}.

It should be stressed that P_{topSC} is the pore-pressure registered by a pressure probe on top of the sand core while P_{max3} is the peak pore-pressure of all pressure probes on top f the sand core. Furthermore, this type of analysis can be performed due to the homogeneous porous media represented by the sand core, and also because all columns of numerical pore pressure probes were located below the water table avoiding the pore-pressure change due to the presence of water-air mixture.

5.4.2 Process analysis and prediction formulae

In Fig. 5-23, the pore pressure damping in the sand core as function of the depth is exemplified for both impact (Fig. 5-23b) and non-impact loads (Fig. 5-23a) and for two different columns of pressure probes (C2 and C10) in the revetment configuration shown in Fig. 5-22. It can be noticed that for the two columns of pressure probes, the pore pressure is damped with the depth similarly and despite the different location of the columns in the revetment embankment. Moreover, for the impact loads (with smaller wave period), the pore pressure on top of the sand core is rapidly damped in the first layers of the sand core while for non-impact loads (with larger wave periods) larger depths inside the sand core are needed to induce a similar pore pressure damping (s. Fig. 5-23). The later, indicates a dependency on the wave period of the pore pressure distribution normal to the revetment.

a) Pore pressure time series for non-impact waves: H=0.3m, T=9.0s, d_{rev}=0.35m, ξ_0=6.64

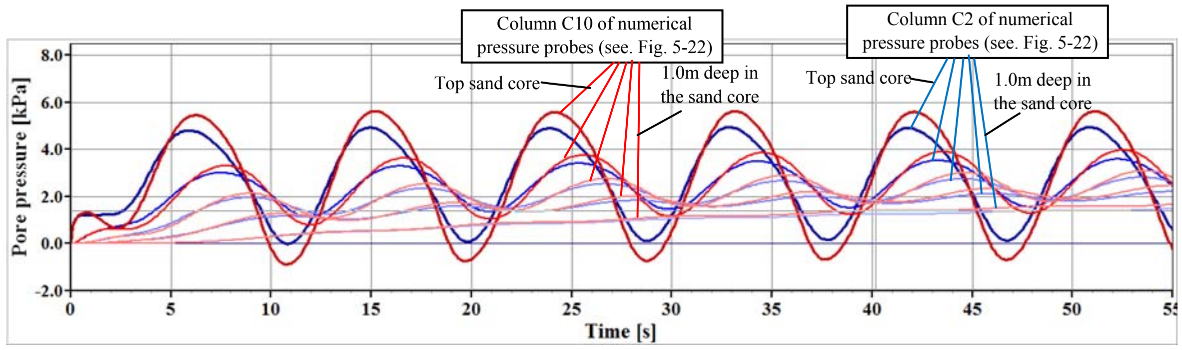

b) Pore pressure time series for impact waves: H=1.0s, T=3.0s, d_{rev}=0.35m, ξ_0=1.25

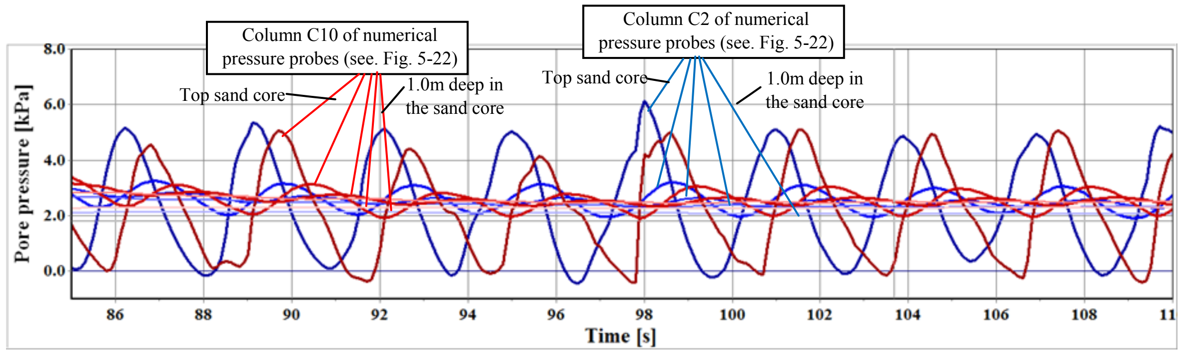

Fig. 5-23: Pore pressure time series of numerical pressure probes along columns C2 and C10 of a revetment with slope 1:3 and revetment-filter thickness d_{rev}=0.35m (described in Fig. 5-22): a) for non-impact loads and b) for impact loads.

Therefore, the pore pressure distribution normal to the revetment will be described in terms of the normalized depth against the normalized pressure P/P_{topSC}. The normalized depth z'/L_0 is given by the depth z' divided by the deep water wavelength L_0, with z'=0 located on top of the sand core and z'>0 positive in upwards direction (Fig. 5-24).

Considering all the revetment configurations, revetment-filter thicknesses and wave conditions tested, 9810 columns of numerical pressure probes were analysed. The results from the analysis of the columns of numerical pressure probes are shown in Fig. 5-25 where the reduction of the relative pore pressure (P/P_{TopSC}) is compared through the normalized depth z'/L_0 for different revetment-filter thickness. In this figure, the relative pore pressure P/P_{TopSC} obtained for each pressure probe in the numerical model is represented by a dot, while pressure probes in the same column (in order to represent the pore pressure distribution in the column normal to the revetment) are connected by a line.

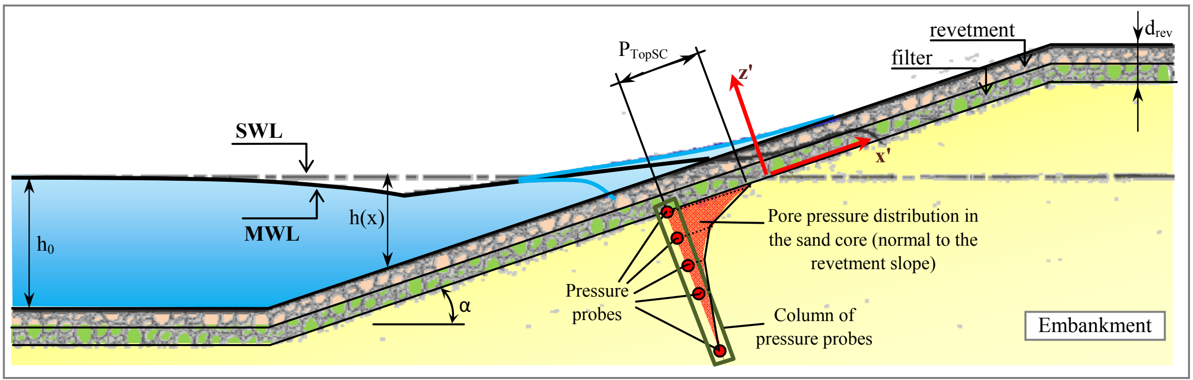

P_{TopSC} = Initial pore pressure on top of the sand core
d_{rev} = Revetment-filter thickness
SWL = Still water level
MWL = Mean water level
α = Slope angle

Fig. 5-24: Definition sketch for the analysis of the pore pressure distribution normal to the revetment inside the sand core.

Despite some scatter found in Fig. 5-25, a clear trend of the data can be defined and it is highly dependent on the wave period T, since the wave length L_0 is defined as $gT^2/2\pi$, and also because the data is clearly grouped in terms of the different wave periods tested. The pressure distribution in the sand core beneath the revetment is similar for all columns along x'-axis as expected since the damping is only produced by the porous media.

The pore pressure distribution normal to the revetment in the sand core for the different revetment-filter thicknesses tested is shown in Fig. 5-25. The revetment-filter thickness has an important effect on the pore pressure on top of the sand core (section 5.3.3) and consequently on the initial pore pressure P_{TopSC} of the normal pore pressure distribution in the sand core, but as shown by the comparison of Fig. 5-25a, b and c no noticeable additional effect occurs on the normalized distribution itself.

The relative pore pressure (P/P_{TopSC}) decreases exponentially with depth z'/L_0 and the highest rate of decrease of the pore pressure occurs in the upper layers. Similar findings are found in the literature for porous sea beds without revetments (Zen & Yamazaki (1990); Zen & Yamazaki (1991); De Groot et al. (2006)). Thus, for the development of the prediction formulae of the pore pressure distribution in the sand core normal to the revetment slope, the following results must be considered: i) the pore pressure decreases exponentially with the depth and ii) the wave period is of high relevance and iii) it is expected that the pore pressures induced by shorter waves are damped faster than those by larger waves. Thus, the prediction formulae should fulfil the following requirements:

- When the wave period (and consequently the wave length) tends to infinite ($T\rightarrow\infty$), the relative pressure should tend to one ($P/P_{TopSC}\rightarrow 1$). This is due to the fact that an infinitively long wave is not damped by the porous media.
- When the wave period (and consequently the wave length $L_0=gT^2/2\pi$) tends to zero ($T\rightarrow 0$), it is expected that no pressure is transmitted inside the sand core. Thus the relative pressure P/P_{topSC} tends to zero ($P/P_{TopSC}\rightarrow 0$).

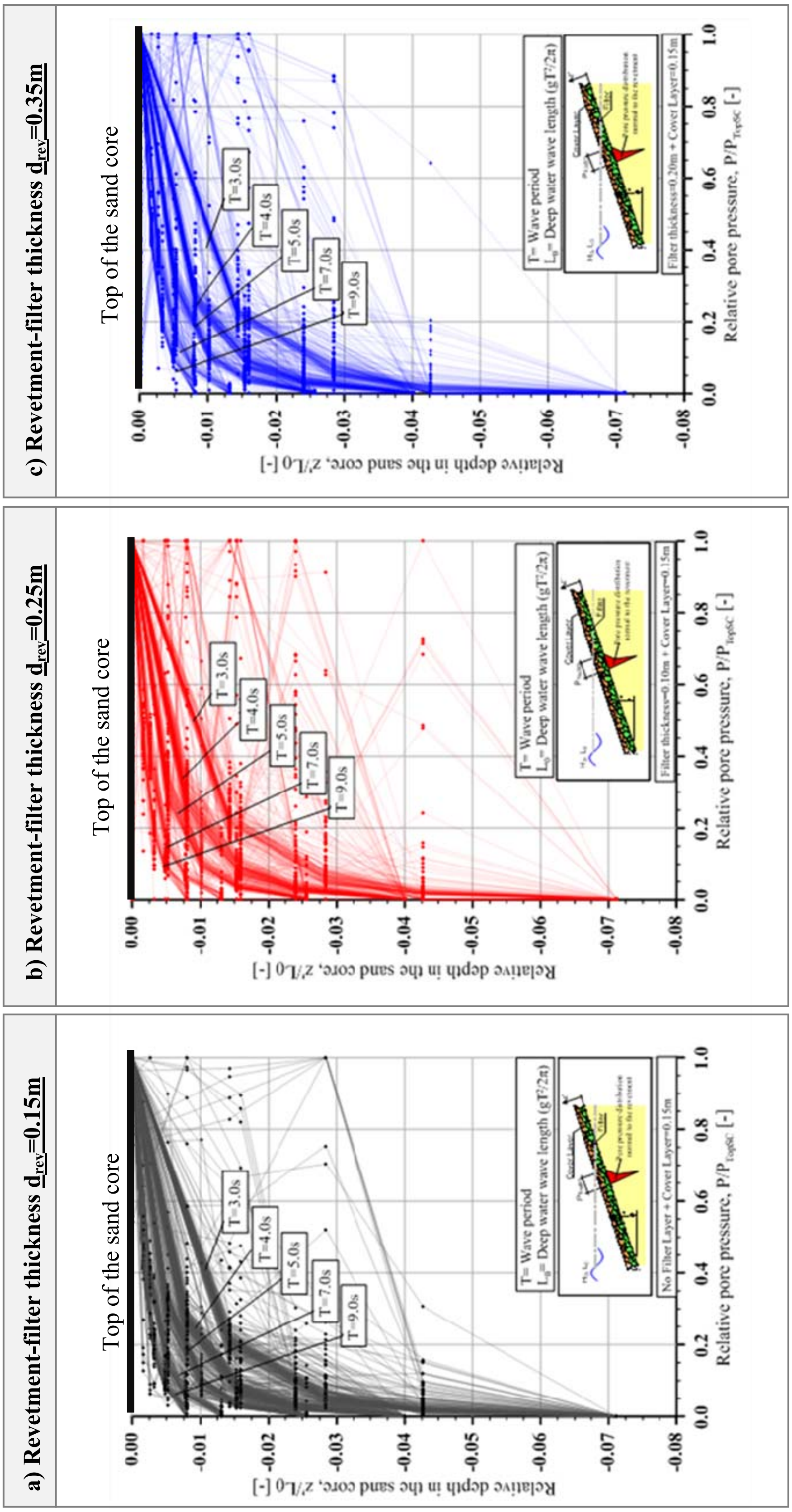

Fig. 5-25: Pore pressure distribution inside the sand core and normal to the revetment slope for different revetment-filter thickness (d_{rev}). The pore pressure measured by a single probe is represented by a dot, while probes in a column are connected by a line.

The exponential function in eq. (5.33) fulfils these requirements and describes the relative pore-pressure decreasing exponentially with the depth based on the behaviour depicted in Fig. 5-25. Furthermore, the non-dimensional coefficient A_T in eq. (5.33) depends on the wave period T.

$$\frac{z}{L_0} = A_T \cdot \ln\left(\frac{P}{P_{TopSC}}\right) \quad \rightarrow \left(\frac{P}{P_{TopSC}}\right) = \exp\left(\frac{z'}{A_T \cdot L_0}\right) \tag{5.33}$$

A preliminary regression analysis was made in order to define the values of coefficient A_T in eq. (5.33) (further details in Alcérreca-Huerta & Oumeraci (2014)). Therefore, non-dimensional coefficient A_T was found to be described as function of the wave period T as shown in the non-homogeneous eq. (5.34) where T is given in seconds (r^2= 0.9995 and a standard deviation σ'= 0.0001).

$$A_T = 0.0514 \cdot T^{-1.47} \text{, with T in [s]} \tag{5.34}$$

With eq. (5.34), the pore-pressure distribution inside the sand core and normal to the revetment slopes is determined for different wave periods T in Fig. 5-26.

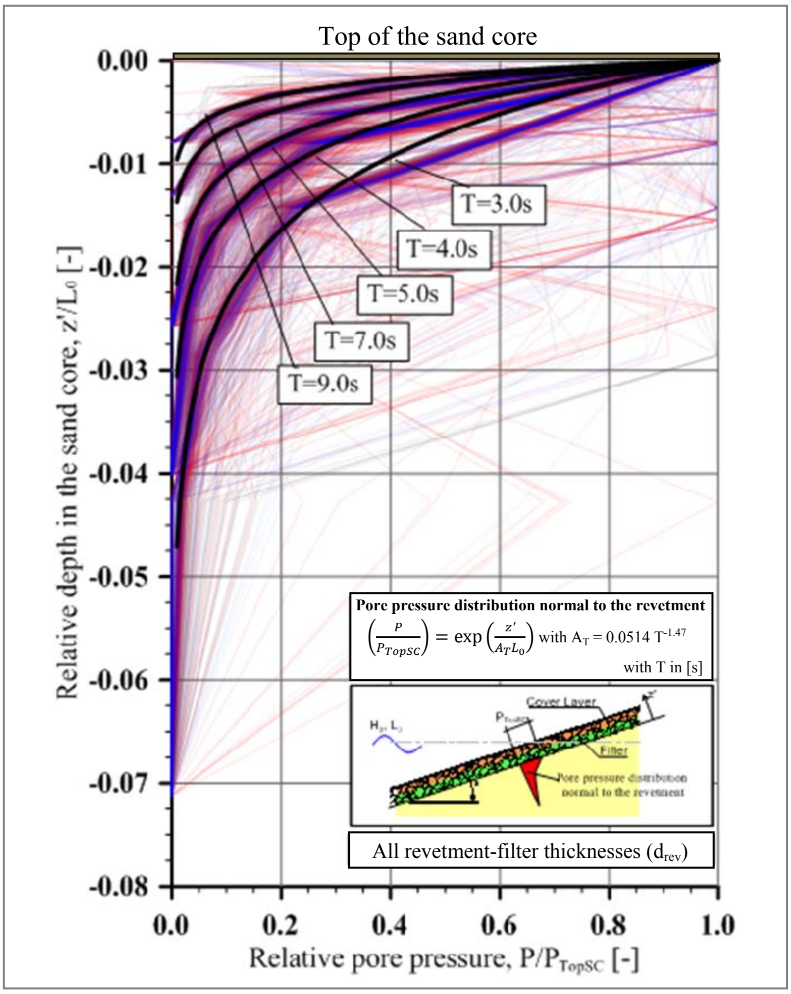

Fig. 5-26: Prediction formulae for the pore pressure distribution in the sand core and normal to the revetment slope.

When substituting eq.(5.34) into eq. (5.33), the following equation is obtained, with T in [s], z' and L_0 in [m], and the coefficient 0.0514 is dimensional [$s^{1.47}$]:

$$\left(\frac{P}{P_{TopSC}}\right)=\exp\left(\frac{z'}{0.0514\cdot T^{-1.47}\cdot L_0}\right) \tag{5.35}$$

Since eq. (5.35) is non-homogeneous, it was also examined whether eq. (5.35) can be related to the approach proposed by De Groot et al. (2006) (eq.(5.36)) which describes the damping of the pore-pressure amplitude considering pore water to be compressible due to gas content in the pores:

$$\left(\frac{P}{P_{TopSC}}\right)=\exp\left(\frac{z'}{z_2}\right)\quad ,\qquad where\quad z_2=\sqrt{c_{ve}\frac{T}{\pi}}\quad with\ c_{ve}=\frac{K}{\gamma_w\left(\beta_S+n\beta_w\right)} \tag{5.36}$$

with K as the Darcy permeability coefficient (~ 10^{-2}-10^{-5} m/s for sand); $\gamma_W=\rho_W g$ the unit weight of water; n the porosity (~0.25-0.50 for sand); β_S the elastic compressibility of the soil and β_w the elastic compressibility of water.

When linear elastic and homogeneous soil is considered, the parameter c_{ve} (consolidation coefficient for elastic, horizontally constrained (de)compression) could be defined as $c_{ve}\approx k/(\gamma_w n\beta_w)$. In the numerical simulations, the following values were set: permeability k=3.7 x 10^{-6} m/s, porosity n=0.32 while the elastic compressibility of water can be assumed as β_w = 0.05 MPa for a gas content of 1%. Thus, substituting these values in eq. (5.36), the non-homogeneous eq. (5.37) is obtained:

$$\left(\frac{P}{P_{TopSC}}\right)=\exp\left(\frac{z'}{A'_T\sqrt{T}}\right)=\exp\left(\frac{z'}{0.087\sqrt{T}}\right) \tag{5.37}$$

with $A'_T=(c_{ve}/\pi)^{0.5}=0.087$ [$m/s^{0.5}$], T in [s], z' in [m].

Now, if it is assumed that the exponent -1.47 of the wave period is rounded to -1.5 in eq. (5.35), then the equation can be re-written as follows:

$$\left(\frac{P}{P_{TopSC}}\right)=\exp\left(\frac{z'}{0.0514\cdot T^{-1.47}\cdot L_0}\right)\approx\exp\left(\frac{z'}{0.0514\cdot T^{-1.5}\cdot\left(gT^2/2\pi\right)}\right)=\exp\left(\frac{z'}{0.0514\frac{g}{2\pi}\sqrt{T}}\right) \tag{5.38}$$
$$\Rightarrow\left(\frac{P}{P_{TopSC}}\right)=\exp\left(\frac{z'}{0.080\sqrt{T}}\right)$$

with $A'_T=0.080$ [$m/s^{0.5}$], T in [s], z' in [m].

Overall, by comparing eq. (5.37) obtained by applying De Groots' formulae and eq. (5.38) obtained from the analysis of results of the numerical simulations within the parameter study, the following conclusions can be drawn:

- De Groot's approach described by eq. (5.36) can be applied as a prediction formulae to correctly estimate the pore pressure distribution normal to the revetment slope inside the sand core of PBA revetments due to the following reasons:
    - It is in complete agreement with the findings of the numerical parameter study.
    - It provides a physical interpretation of all the variables in the pore pressure damping within the sand core. This is of high relevance since in the equation provided by the numerical parameter study, some constants of the fitting function couldn't be physically interpreted with the data from the numerical simulations.
    - It fulfils the physical requirements that for $T \rightarrow 0$, $P/P_{topSC} \rightarrow 0$ and for $T \rightarrow \infty$ then $P/P_{topSC} \rightarrow 1$ (no dissipation of the pore pressure).
- The results obtained from porous seabed without any revetment can be applied for porous bed protected by porous revetment.

For the assessment of the pore-pressures developed in the sand-core, the use of De Groot's approach (eq. (5.36)) is highly recommended. However, for the definition of P_{topSC} the findings described in Section 5.3 for the pressure distribution on top of the sand core should be considered for the complete analysis of the pressures inside the embankment underneath a PBA-revetment. Moreover, it is stressed that the formulae proposed in this section are valid for locations below the water table and further research is required for those locations where the water table is modified and water-air mixtures may occur. Finally, the formulae proposed in this section can be applied as a preliminary assessment of the pore pressure distribution in the sand core normal to the slope of PBA-revetment.

5.5 Summary of key results

A comprehensive analysis of the pressures on top of the revetment and inside the porous layers of a PBA-revetment was performed in this chapter. Furthermore, prediction formulae for the wave-induced pressure distribution and the peak pressures on and beneath PBA-revetments were developed, including also the pore pressure distribution in the sand core beneath the revetment.

For the peak pressure on the revetment, the key results are summarized as follows:

- The revetment-filter thickness d_{rev} affects the magnitude of the impact component of the wave-induced pressure, especially for $1.0<\xi_0<4.3$ (plunging and collapsing breakers): a larger d_{rev} causes a decrease of the relative peak pressure $P_{1max}/\rho g H_0$ for $0.8<\xi_0<2.4$ (plunging breaker) and an increase for $2.4<\xi_0<4.3$ (collapsing breaker).
- The magnitude of the peak pressure for impact loads is damped by the presence of a water layer on the revetment. The thickness of this water layer is affected by the revetment slope, the porosity and the thickness of the revetment slope. Further analyses are required to define the relative importance of these effects.
- The quasi-static component of the wave-load is almost independent of the revetment-filter thickness.

- A large variability of the location of $P_{1max}/\rho g H_0$ on the revetment (z_{max1}/H_0) is observed for plunging and collapsing breakers, while for spilling and surging breakers, this variability is reduced.

In addition, the peak pore pressure on top of the sand core beneath a PBA-revetment (P_{max3}) was analysed in comparison to the peak pressure on the revetment (P_{max1}) resulting in the following findings:

- The peak pressure of the impact load on the revetment for $1.0<\xi_0<4.3$ (plunging and collapsing breakers) significantly decreases through the revetment and filter layers: up to 72% for $d_{rev} = 0.15$m and 76% for $d_{rev} > 0.25$m.
- An increase of the revetment-filter thickness d_{rev} results in a decrease of the ratio P_{max3}/P_{max1}, but not linearly.
- The quasi-static component of the pressure on the revetment for all the ξ_0-domain is only slightly affected by d_{rev}. It is damped through the revetment and filter layers only by 15% for a $d_{rev} = 0.35$m compared to 10% for $d_{rev} = 0.15$m.
- For a revetment-filter thickness $d_{rev} = 0.15$m and $\sim 2.0 < \xi_0 < \sim 8.0$, the peak pore pressure on top of the sand core can be higher than that on the revetment probably as a consequence of the limited space for fluid motion and turbulence development. Further research is required to study this effect experimentally.

The location of z_{max3} where the peak pore pressure on top of the sand core P_{max3} occurs is vertically deeper than z_{max1} where P_{max1} takes place (similar result found by Oumeraci et al. (2010) and Alcérreca-Huerta & Oumeraci (2012)). This may be caused by variables such as: wave impact angle and also by the revetment slope steepness. Moreover, it was found that for values of $\xi_0 \approx 2.3$, the location z_{max3} of P_{max3} presents a large deviation from the data trend within the numerical simulations of the parameter study. Further studies are required to verify if this could be physically justified or is only caused due to numerical effects.

The upper envelopes of the normalized pressure distributions on the revetment and on top of the sand core were found to have a similar behaviour particularly for locations below the maximum run-down. The presence of two peaks within the pressure distributions on and beneath the revetment were found for both impact and non-impact loads: i) below the maximum run-down and ii) within the swash zone closer to the maximum wave run-up. Only the pressure distribution on the sand core due to impact loads does not present the second peak probably due to the associated high turbulence. Further studies based on laboratory tests should be performed in order to define the occurrence and magnitude of the second peak of the pressure distribution on the revetment found through the numerical simulations of the parameter study, but also observed in previous laboratory studies (e.g., Pedrozo-Acuña et al. (2011)) and numerical studies (Ghosh et al. (2007)).

The pore pressure distribution in the sand core normal to the revetment slope was also analysed and the findings from the numerical simulations of the parameter study (s. Section 5.4.2) are in agreement with De Groot's approach (eq. (5.36)) for the pore pressure damping within the sand core. Therefore, the results obtained from porous seabed without any revetment can be applied for a porous bed protected by porous revetment by considering the pore pressure on top of the sand core as initial pressure of the pressure distribution normal to the revetment slope. In Oumeraci et al. (2010), the prediction formulae for the estimation of the pore pressure distribution were described in terms of the surf similarity parameter. However, results from the present parameter study and by De Groot, lead to the conclusion that the surf similarity should not be used to describe the pore pressure damping through the sand core, rather the permeability, the porosity, as well as the air content (even in a few amount such as 1% in the pores) are more relevant. Also, the prediction formulae proposed in this chapter for the pore pressure distribution normal to the revetment was defined considering a specific properties of the sand core beneath the revetment. Therefore, further research might be needed for considering different soil properties of the embankment subsoil beneath PBA-revetments.

Further research is needed for defining the pore-pressure distribution at locations with water-air mixtures, such as those close to the water table. For this purpose, limitations of the present model need to be overcome (see Section 3.7) by implementing a two-way coupling of the CFD and CSD solvers and by performing a parameter study with the improved model.

For subsequent analyses, it is also recommended to investigate in detail the effects that a water layer thickness over the revetment has on the wave kinematics during the breaking process and also on the development of the wave-induced pressure on and beneath PBA-revetments. Furthermore, the influence of the porosity, permeability and roughness of the revetment and filter layers on the development of the wave-induced pore-pressures should be also investigated.

Finally, all the formulae proposed in this chapter were developed considering regular waves and thus, results may be different when considering wave spectra as noticed in results from GWK-tests (Oumeraci, 2010). However, the numerical simulation of wave spectra is limited by the available computational resources to reproduce a statistically representative wave spectra sea state.

6 Stability analysis against soil liquefaction beneath PBA-revetments

No information is available from the field regarding failures and stability analyses of PBA-revetments as this type of revetment was introduced only in the last years as an innovative alternative to conventional revetments. A failure of a PBA-revetment observed in the large-scale tests (performed in the GWK) and a first stability analysis were reported in detail in a final report for the industry by Oumeraci et al. (2010). The proposed methodology for the stability analysis in this detailed report can be verified by using the extended results of the parameter study performed with the new CFD-CSD model proposed in this PhD study.

For this purpose, the physical background of soil liquefaction and stability of PBA-revetments is first briefly described in this chapter. In a further section, the uplift pressure development in the sand core beneath a PBA-revetment is examined. A generic expression to define the uplift pressures in a PBA-revetment in terms of the wave conditions is also described. In a third section, the methodology for the stability analysis of the soil beneath the revetment against soil liquefaction is described and implemented to reproduce the failure observed in the GWK tests.

6.1 Physical background of soil liquefaction and stability of PBA-revetments

Soil liquefaction is a process in which the effective stress (σ') and consequently the shear strength of the soil (τ) becomes zero (for non-cohesive soils, $\tau=(\sigma'-u)\tan\varphi$, with φ as the friction angle) due to the development of large excessive pore pressures (u). The soil behaves then like a viscous fluid resulting in large soil deformations and motions. The mechanism to induce liquefaction in a PBA-revetment is recognized as the wave-induced loads on the structure. Cyclic wave loading may induce the following two types of soil liquefaction:

a) Instantaneous or transient liquefaction

The most important parameters for the description of the instantaneous liquefaction are: i) the amplitude and the period of the cyclic loading; ii) the ratio between the elastic compressibility of the soil and the compressibility of water; iii) the absolute value of the highest of both compressibilities and iv) soil permeability and drainage (De Groot et al. (2006)).

The instantaneous liquefaction might occur during the passage of the wave trough where the pore pressure on the upper boundary (u_{0*}) of the sand core becomes negative. As the amplitude of the transient pore pressure (u_{t*}) decreases with the depth, a pressure difference ($u_{0*}-u_{t*}$) in upwards direction is induced which might cause the uplifting of the soil particles. If ($u_{0*}-u_{t*}$) at a certain location z' inside the sand core is higher than the total stress (σ) given by the submerged weight of the soil, then liquefaction will take place as described by eq.(6.1) and shown in Fig. 6-1.

Liquefaction if $$\sigma' = \sigma - u \leq 0 \quad \Rightarrow \underbrace{\left[\rho_r g d_{rev} + \rho_s' g(-z')\right]}_{\textit{Weight of soil over } z_1'} - \underbrace{\left|u_{0*} - u_{t*}\right|}_{\text{Pr}\textit{essure difference at } z_1'} \leq 0 \qquad (6.1)$$

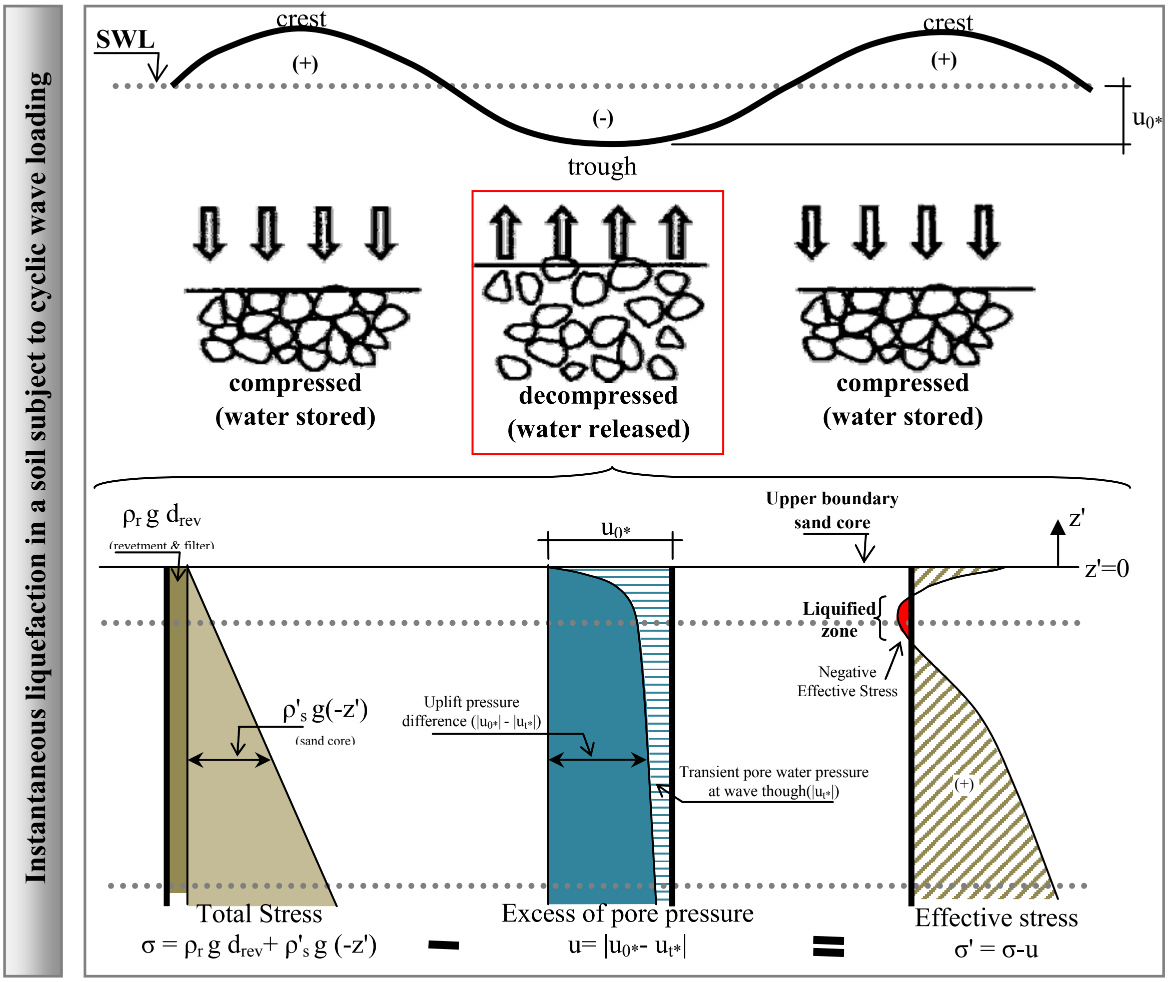

Fig. 6-1: Instantaneous liquefaction due to the cyclic wave loading and physical process description (modified from Oumeraci et al. (2010).

The total stress σ in eq. (6.1) includes: i) the submerged weight of the revetment and filter layers (given as $\rho_r g d_{rev}$ where ρ_r is the bulk density and d_{rev} the thickness of the revetment-filter layers together) and ii) the submerged weight of the sand over the location point of analysis z' (given by $\rho'_s g z'$ whit ρ'_s as the bulk submerged density of the sand).

Thus, the liquefaction might occur when the resistance force (due to the submerged weight of the porous media) is lower than the driving force (upward pressure difference).

b) *Liquefaction due to residual pore pressures*

The liquefaction due to residual pore pressures (u_r) occurs when the pressure difference $u_{r,0}-u_r$ (with $u_{r,0}$ and u_r as the residual pore pressures at depth z'=0 and z', respectively) gradually increases as a consequence of the plastic deformation of the soil skeleton (De Groot et al. (2006)). The positive residual pore pressure can be dissipated through drainage in the soil; however, the deformation of the soil is not recovered as the soil is subject to plastic deformation.

$$\text{Liquefaction if } \sigma' = \sigma - u \leq 0 \quad \Rightarrow \underbrace{\left[\rho_r g d_{rev} + \rho_s' g(-z')\right]}_{Weight\ of\ soil\ over\ z_1'} - \underbrace{|u_r|}_{\text{Re}sidual\ pore\ pressure\ difference\ at\ z_1'} \leq 0 \tag{6.2}$$

It should be considered that the liquefaction process can also be induced by both instantaneous and residual excess pore pressures. Therefore, the liquefaction can be estimated by the superposition of both residual pore pressure u_r and the transient excess pore pressure u_{t*} as described by eq. (6.3) and Fig. 6-2.

$$\sigma' = \sigma - u \leq 0 \quad \Rightarrow \underbrace{\left[\rho_r g d_{rev} + \rho_s' g(-z')\right]}_{Weight\ of\ soil\ over\ z_1'} - \underbrace{\left|(u_{0*}) - (u_{t*} + u_r)\right|}_{\text{Pr}essure\ difference\ at\ z_1' + \text{Re}sidual\ pore\ pressure\ difference\ at\ z_1'} \leq 0 \tag{6.3}$$

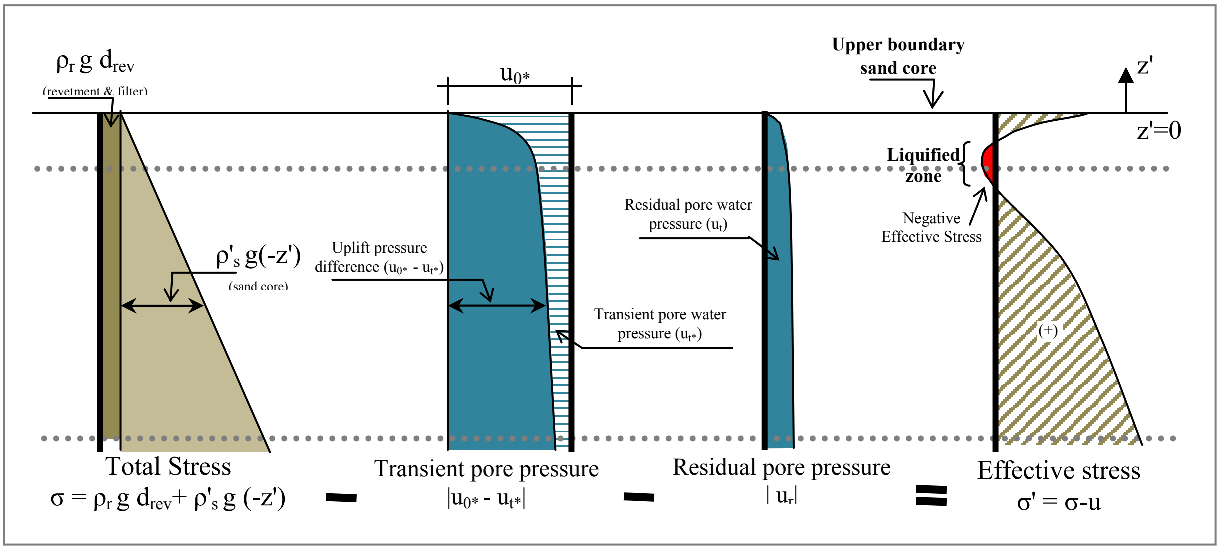

Fig. 6-2: Stability analysis basis for identification of liquefaction failures (modified from Oumeraci et al. (2010)).

Both residual and transient excess pore pressures can be obtained reliably from the numerical simulations, thus allowing the development of a methodology for the stability analysis of PBA-revetments (s. Section 6.3) according to the procedure described by Fig. 6-2 and eq. (6.3).

6.2 Uplift pressure difference

6.2.1 Preliminary analysis

In order to determine the analysis of the excess of pore pressure $\Delta u = u_{0*} - (u_{t*} + u_r)$, a preliminary analysis is performed to extract the value of u_{0*} on top of the sand core and $u_{t*} + u_r$ at different depths z' inside the sand core.

From each of the signals recorded during the numerical simulations, the value of u_{0*} was obtained (measured on top of the sand core during the wave trough). Furthermore, the values of the transient component u_{t*} and the residual component u_r of the pore pressure are obtained simultaneously in the pore pressure signal as shown in Fig. 6-3. When a filter is applied to the pore pressure time series (Oumeraci et al. (2010); Alcérreca-Huerta & Oumeraci (2012)), then it is possible to differentiate between the residual (u_r) and the transient component (u_t) (Fig. 6-3). However, the effect of both residual and transient pore pressure during the passage of the wave trough are needed to analyse the liquefaction failure (eq. (6.3)) so that no separation between both components for the purpose of the stability analysis for PBA-revetments is required. For this purpose, the value of $u_r - u_{t*}$ at each wave trough found in a pore pressure time series was extracted and the maximum $u_r - u_{t*}$ value was obtained for each pore pressure time series.

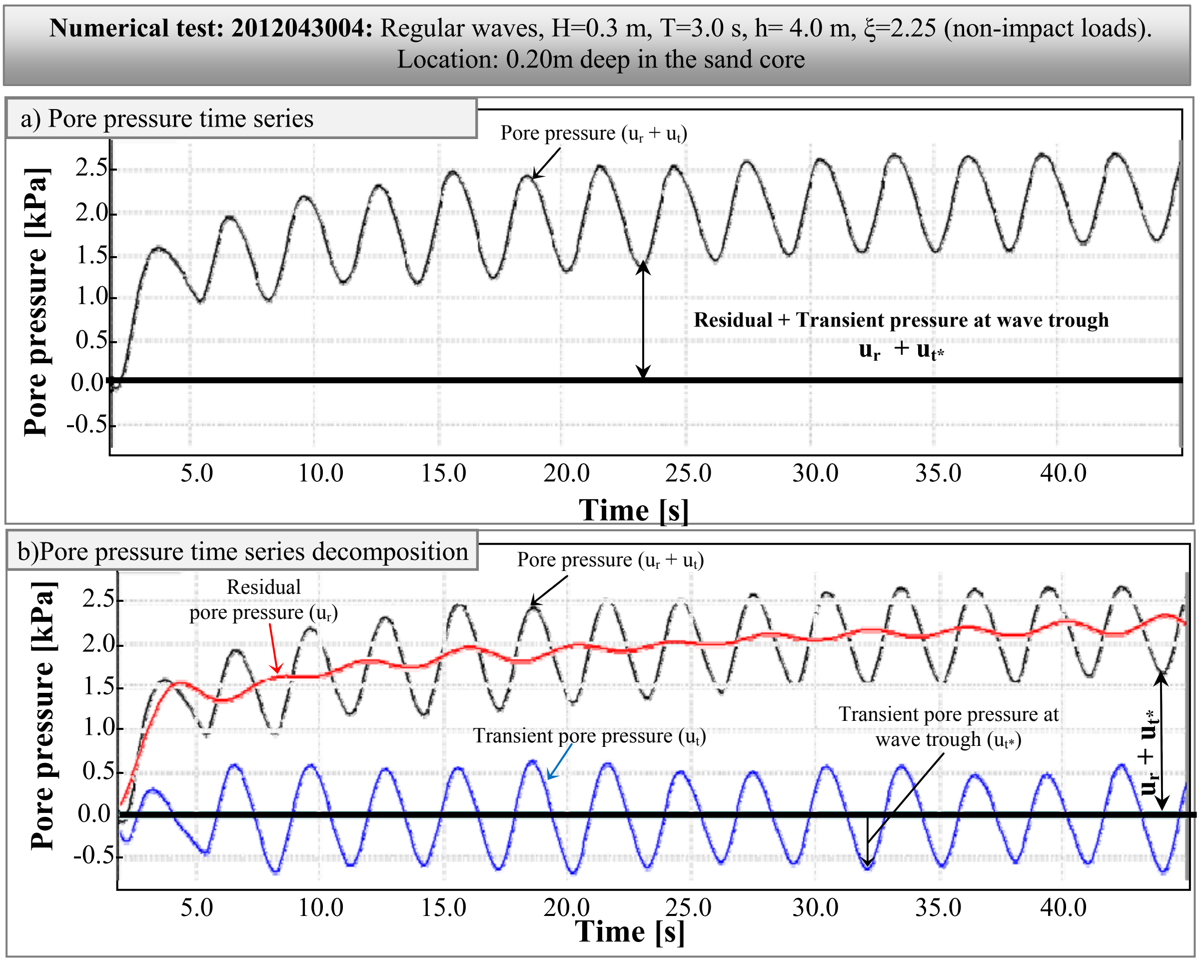

Fig. 6-3: Pore pressure time series decomposed in its residual and transient components. The excess pore pressures of interest for the stability analysis are the residual component and the transient pore pressure during the passage of the wave trough (u_{t*}).

Within the different numerical model setups of the parameter study, a considerable number of virtual pressure transducers located at the same depth inside the sand core were deployed (see Fig. 5-22). Therefore, it was decided for the stability and process analysis to review the worst case at certain depth (layer) inside the sand core where the maximum magnitude of $u_r - u_{t*}$ is achieved, so that the most critical condition (largest uplift pressure difference Δu) is obtained: $\Delta u = u_{0*} - (u_{t*} + u_r))$. The residual pore pressure extracted from the pore pressure time series also considers the effect of the variation of the internal mean water level (iMWL) inside the sand core.

6.2.2 Process analysis

The numerical results from the parameter study could not be compared systematically with large- or small-scale laboratory tests due to the limitations (technical, time and costs) of the laboratory experiments for setting several pressure transducer columns as well as different revetment geometries subject to a large range of wave conditions. However, in the stability analysis to be described in section 6.3, the measurements obtained during the failure of a PBA-revetment in large-scale tests and reported in Oumeraci et al. (2010) will be used to validate the prediction formulae developed as well as to provide more confidence on the process analysis described in this section.

For the process analysis and as a basis for the stability analysis, the excess of pore pressure Δu is described as function of the surf similarity parameter which involves both wave conditions (H_0, L_0) and the slope steepness (tan α).

The relative uplift pressure difference defined as Δu_{rel} in eq. (6.4) against the surf similarity parameter ξ_0 (s. for reference Fig. 6-4) was analysed considering different revetment-filter thickness. As a result, it was found that:

- Surprisingly, the value of Δu_{rel} is only slightly reduced when the revetment thickness d_{rev} is increased.
- The data scatter is larger when increasing d_{rev} possibly due to the increasing turbulence inside the revetment and filter layers so that fluctuations of Δu_{rel} are larger.
- The variation of Δu_{rel} with the depth for d_{rev}=0.15 m is clearly defined (particularly between z'=-0.2 m and z'=-0.4 m), while for larger d_{rev} the variation of Δu_{rel} for all depths z' becomes smaller and consequently due to the soil weight above these locations, liquefaction might occur most likely in upper depths between 0<z'<-0.2m.
- The behaviour of Δu_{rel} for d_{rev2}=0.25 m and d_{rev3}=0.35 is similar. Thus, it is expected that for d_{rev} > 0.35 m only a slight modification of Δu_{rel} would result. However, this should be verified in further studies by considering larger revetment-filter thicknesses

$$\Delta u_{rel} = \frac{|\Delta u|}{\rho g H_0} = \frac{|u_{0*} - (u_{t*} + u_r)|}{\rho g H_0} \qquad (6.4)$$

Furthermore, almost no variation is expected between the uplift pressure difference (Δu) developed at depth z'=-0.6m and depths larger than z' >-0.6 m due to the pore pressure damping induced by the sand core (see section 6.4). In Section 6.2.3, Δu_{rel} will therefore be considered equal to the value in z'=-0.6m for depths larger than z' >-0.6 m, but further studies are recommended on this issue.

6.2.3 Prediction formulae

a) *Relative excess of pore pressure in the sand core*

Regarding the prediction formula for the relative uplift pressure difference Δu_{rel} as function of the surf similarity parameter ξ_0, it is considered that for deeper soil layers (>z'=0.6 m), the value of Δu_{rel} changes only very slightly, so that the same value as for z'=0.6m is considered (s. for reference Fig. 6-4).

Furthermore, the prediction formula should fulfil the following physical limit: when $\xi_0=0$ then $\Delta u_{rel} \rightarrow 0$. Also, it is expected that when $\xi_0 \rightarrow \infty$, then $\Delta u_{rel} \rightarrow 0$ because for larger waves (resulting in large ξ_0-values) the transient and residual pore pressure difference between two layers may be released through a change of the water level inside the porous media which might be almost equal for two different locations.

Thus, this condition is obtained by fitting the numerical data to the model described in eq. (6.5) and illustrated by Fig. 6-4. The values of the coefficients A, B and C for the prediction formula described by eq. (6.5) are given in Table 6-1 for different revetment-filter thicknesses and different depths in the underlying sand core.

$$\Delta u_{rel} = \frac{A \cdot \xi_0}{1 + B \cdot \xi_0 + C \xi_0^{\,2}} \tag{6.5}$$

Table 6-1: Coefficients A, B and C for the determination of the relative difference of 'excess pore pressures' Δu_{rel} as function of the surf similarity parameter ξ_0 for eq. (6.5).

	Depth in the sand core	***Revetment-filter thickness***		
		d_{rev1}=0.15m	d_{rev2}=0.25m	d_{rev1}=0.35m
Coefficient A	z'= -0.2m	*0.224*	*0.192*	*0.217*
	z'= -0.4m	*0.226*	*0.191*	*0.217*
	z'≤ -0.6m	*0.225*	*0.166*	*0.195*
Coefficient B	z'= -0.2m	*0.083*	*0.057*	*0.013*
	z'= -0.4m	*0.010*	*0.002*	*0.017*
	z'≤ -0.6m	*-0.002*	*-0.051*	*-0.012*
Coefficient C	z'= -0.2m	*0.014*	*0.018*	*0.028*
	z'= -0.4m	*0.014*	*0.016*	*0.022*
	z'≤ -0.6m	*0.014*	*0.017*	*0.024*
Standard deviation	z'= -0.2m	*σ'=9.0%*	*σ'=7.7%*	*σ'=16.2%*
	z'= -0.4m	*σ'=12.4%*	*σ'=10.7%*	*σ'=15.6%*
	z'≤ -0.6m	*σ'=12.6%*	*σ'=10.8%*	*σ'=17.5%*

As shown in Table 6.1, the coefficients A and C are sensitive to the change in revetment-filter thickness, while the coefficient B is more sensitive to the change in soil depth where the Δu_{rel} is considered. Future analysis are required in order to define an expression of coefficients A and C as function of the revetment-thickness d_{rev} and coefficient B as function of the soil depth z'.

The prediction formula reflects very well the effects described in the process analysis and thus provides a reliable tool for the calculation of the relative uplift pressure difference Δu_{rel} which is required for the performance of the stability analysis in section 6.3

a) Revetment-filter thickness d_{rev}=0.15m

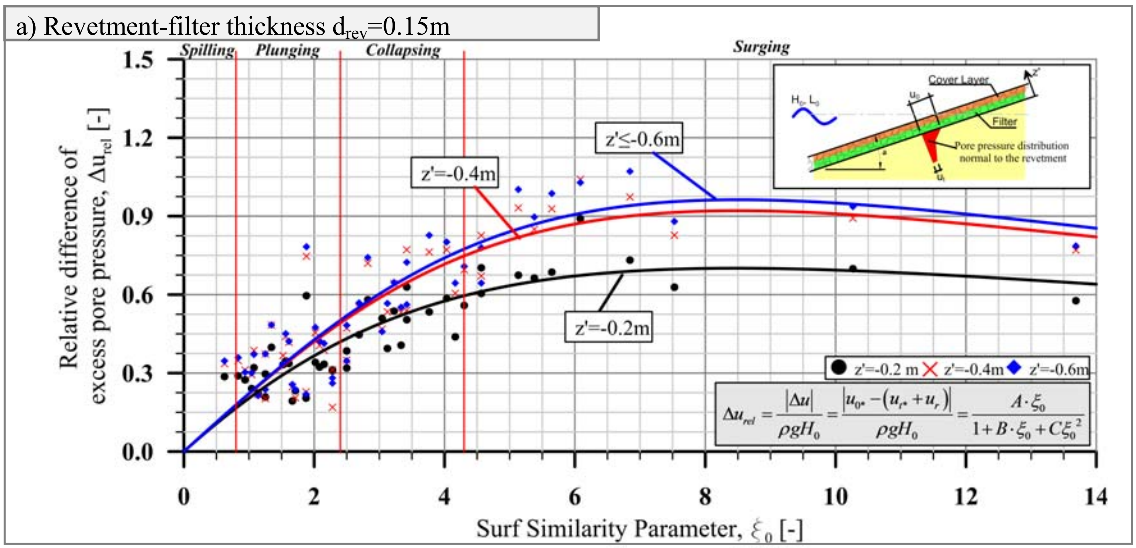

b) Revetment-filter thickness d_{rev}=0.25m

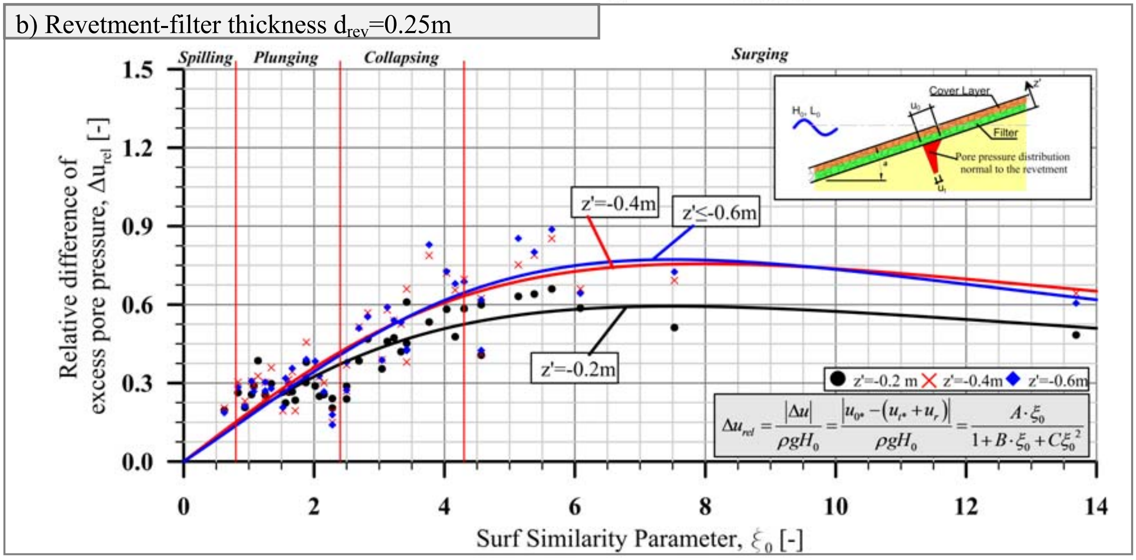

c) Revetment-filter thickness d_{rev}=0.35m

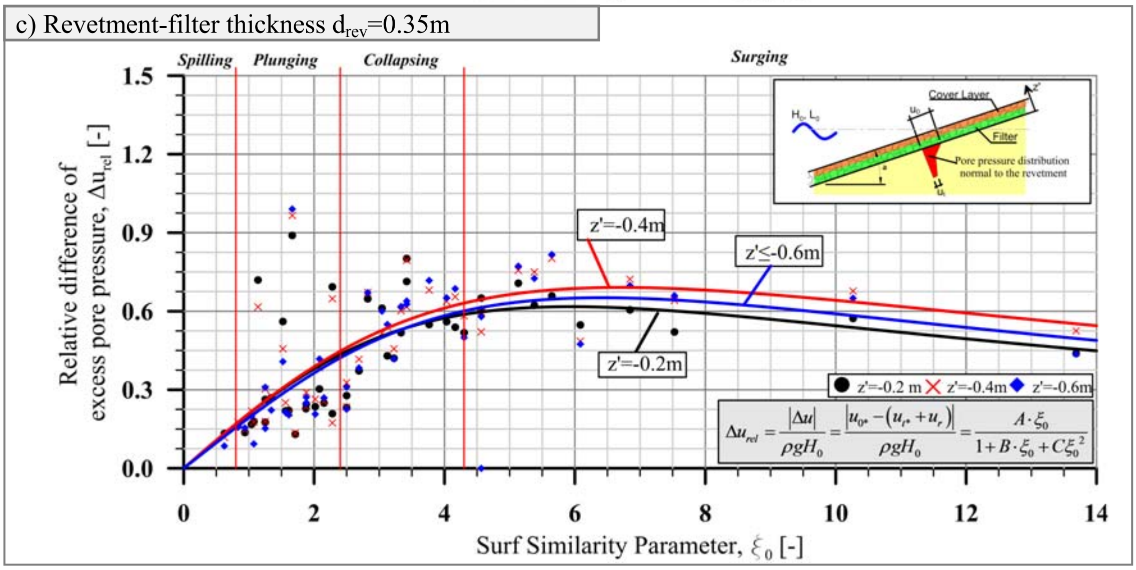

Fig. 6-4: Prediction formulae for the relative uplift pressure difference vs. surf similarity parameter at different depths inside the sand core of PBA-revetments considering different values of d_{rev}. Coefficients A, B and C for the prediction formulae are given in Table 7-1.

b) *Pressure on the revetment and on top of the sand core induced under the wave trough*

Additional to the evaluation of the uplift pressure difference Δu_{rel} between the top of the sand core and a specific depth inside, an approximate relation between the pore pressure on top of the sand core u_{0*} and the pressure on the revetment u_{TR*} induced under the wave trough is provided.

A description of u_{TR*} in terms of the surf similarity parameter ξ_0 is the most appropriate approach, as both wave conditions and the slope steepness are included in ξ_0. As result, the prediction formula shown in eq. (6.6) is obtained with a standard deviation of σ'=22.1%.

$$\frac{u_{TR*}}{\rho g H_0} = -\frac{\xi_0^{\,2} + 2.12 \cdot \xi_0}{\xi_0^{\,2} + 7.79} \tag{6.6}$$

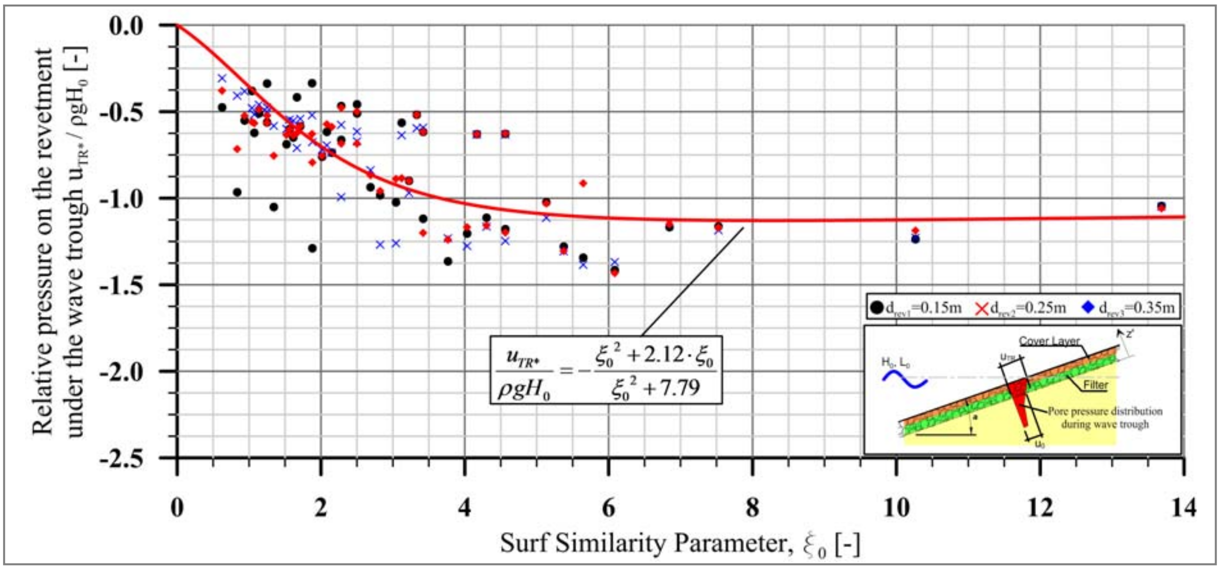

Fig. 6-5: Prediction formulae for the relative pressure on top of the revetment ($u_{TR*}/\rho g H_0$) during wave trough vs. surf similarity parameter in PBA-revetments for all tested revetment-filter thicknesses.

By comparing the relative pore pressure $u_{0*}/\rho g H_0$ on top of the sand core and the relative pressure $u_{TR*}/\rho g H_0$ on the revetment induced under the wave trough for different revetment-filter thicknesses, the results in Fig. 6-6 are obtained, showing that an increase of d_{rev} reduces $u_{0*}/\rho g H_0$. Thus, the following equations are derived for different revetment-filter thicknesses:

For d_{rev1}=0.15m
$$\frac{u_{TR*}}{\rho g H_0} = \frac{u_{0*} - 0.342}{\rho g H_0} \tag{6.7}$$

For d_{rev2}=0.25m
$$\frac{u_{TR*}}{\rho g H_0} = \frac{u_{0*} - 0.521}{\rho g H_0} \tag{6.8}$$

For d_{rev3}=0.35m
$$\frac{u_{TR*}}{\rho g H_0} = \frac{u_{0*} - 0.676}{\rho g H_0} \tag{6.9}$$

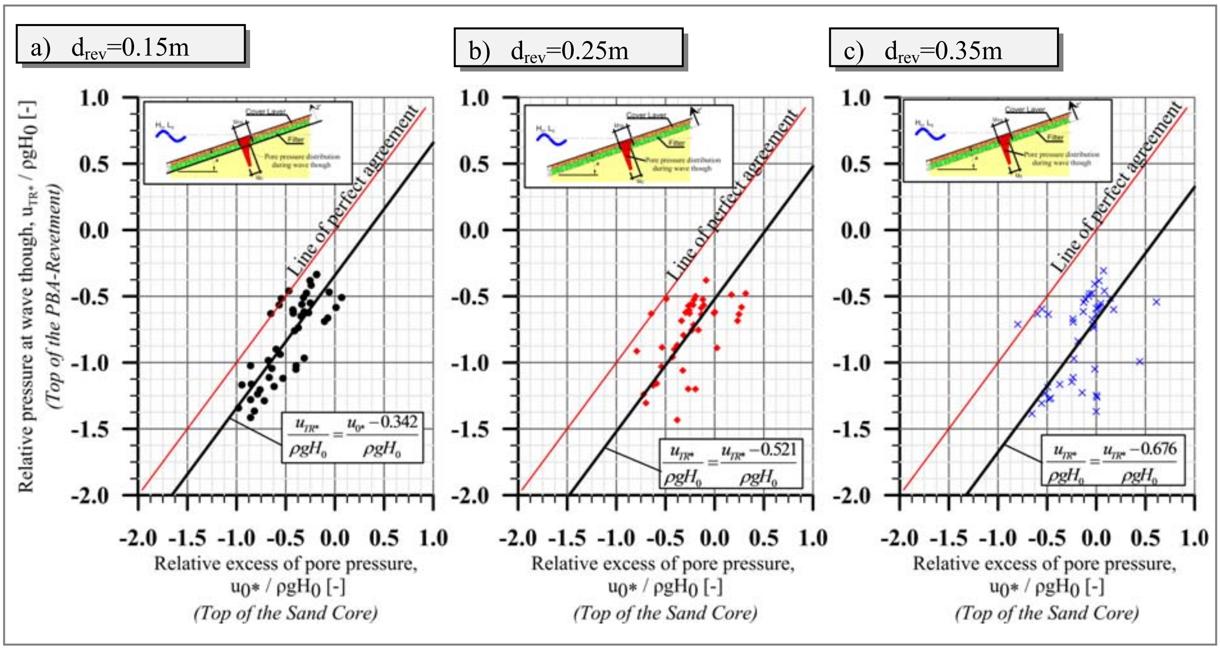

Fig. 6-6: Comparison of the relative excess of pore pressure on top of the sand core ($u_{0*}/\rho g H_0$) and the relative pressure on top of the revetment ($u_{TR*}/\rho g H_0$) induced under the wave trough, for different revetment-filter thicknesses: a) d_{rev}=0.15m, b) d_{rev}=0.25m, c) d_{rev}=0.35m

The assessment of the relative uplift pressure difference Δu_{rel} through the prediction formula in eq. (6.5) is crucial for the implementation of the stability analysis of the sand foundation of PBA-revetments as proposed in Section 6.1 and Fig. 6-2. This formula considers simultaneously the effect of wave conditions (i.e., H_0 and L_0) and the revetment slope (both included in the surf similarity parameter ξ_0). Moreover, the effect of the three revetment-filter thicknesses (d_{rev}=0.15m, 0.25m & 0.35m) is considered, but further research is required to analyse this effect for a wider range of d_{rev}-values. Also, the prediction formulae in eqs. (6.7), (6.8) and (6.9) may be useful for the stability analysis of the filter layer and the revetment against uplifting since the difference (u_{TR*}-u_{0*}) may induce the uplift pressure gradient in these layers.

6.3 Stability analysis

The proposed methodology for the stability analysis against soil liquefaction in the sand core beneath PBA-revetments induced by waves and its implementation constitute the primary focus of this section. For this purpose, a limit state equation will be first formulated. Furthermore, the results from the proposed methodology for stability analysis are compared with the comprehensive studies and the results of the analysis reported by Oumeraci et al. (2010) and Foyer (2013) on the failure of a PBA-revetment in a large-scale laboratory test.

6.3.1 Limit state equation for soil liquefaction in the sand core beneath PBA-revetments

The stability of the PBA-revetments against liquefaction of the sand core is analysed according to eq. (6.3) which is re-written below as reference for the proposed methodology:

$$\text{Liquefaction if} \qquad \sigma' = \sigma - u \le 0 \quad \Rightarrow \underbrace{\left[\rho_r g d_{rev} + \rho_s' g(-z')\right]}_{\textit{Weight of soil over } z'} - \underbrace{\left|u_{0*} - (u_{t*} + u_r)\right|}_{\textit{Uplift pressure difference, } \Delta u} \le 0$$

In eq. (6.3), the difference of transient and residual pore-pressure at z' are integrated in one term which is the called the uplift pressure difference Δu between the top of the sand core and a location at depth z'.

The first term on the left side of eq. (6.3) depends on the submerged weight of the soil material over the location of interest. The term $\rho_r g d_{rev}$ is described by the submerged density of the revetment-filter material (ρ_r), gravity acceleration (g) and the revetment-filter thickness (d_{rev}). Also, the term $\rho_s'g(-z')$ is described by the submerged density of the embankment material (ρ_r'), gravity acceleration (g) and the distance (z') from the top of the sand core to the location of interest, measured normal to the revetment slope (see Fig. 6-7 for reference). The last term on the left side of the equation, given by $|u_{0*}-(u_{t*}+u_r)|$, can be estimated by applying the prediction formulae shown in eq. (6.5), which is re-written below with coefficients A, B & C given in Table 6-1.

$$\Delta u_{rel} = \frac{|\Delta u|}{\rho g H_0} = \frac{\left|u_{0*} - (u_{t*} + u_r)\right|}{\rho g H_0} = \frac{A \cdot \xi_0}{1 + B \cdot \xi_0 + C \xi_0^{\,2}}$$

All the variables needed to define the potential of liquefaction in the sand core can now be determined. However, the limit state equation (6.3) is re-formulated in its final form (eq. (6.10)) which is intended to represent the ratio of the driving force and resistance forces at any depth z' within the sand core:

$$\text{Liquefaction if} \qquad \frac{\left|u_{0*} - (u_{t*} + u_r)\right|}{\rho_r g d_{rev} + \rho_s' g(-z')} \ge 1 \tag{6.10}$$

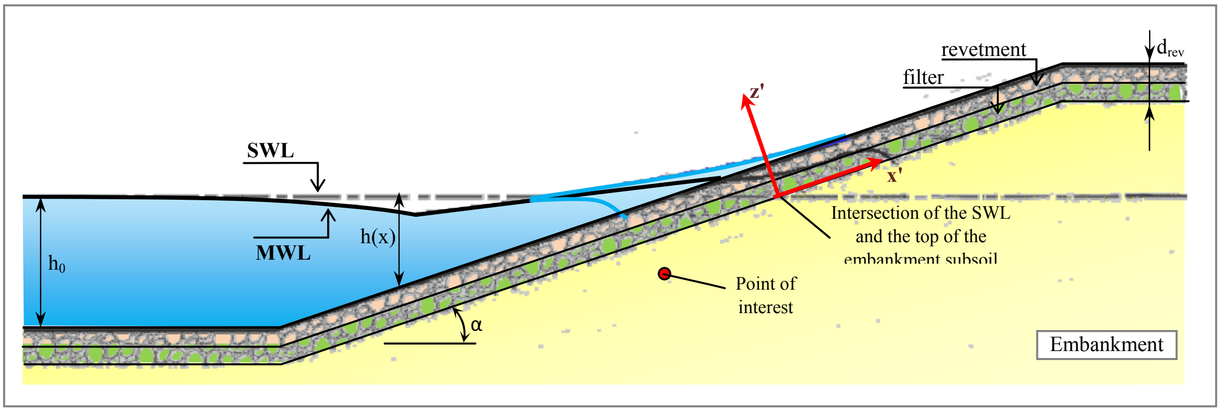

Fig. 6-7: Definition of the coordinate system z' - x'.

With eq. (6.10), it is possible to estimate the minimum revetment-filter thickness d_{rev} needed to avoid liquefaction in the sand core beneath a PBA-revetment.

Thus, the proposed methodology for the stability analysis may be summarized as follows:

i. Estimation of the relative uplift pressure difference Δu_{rel} at any location between the surface of the sand core and a depth (z') that can induce the uplifting of the soil particles. For this purpose, eq. (6.5) with coefficients described in Table 6-1 should be applied.
ii. Calculation of $|\Delta u| = |u_{0*}-(u_{t*}+u_r)|$ by using eq. (6.4) (Δu_{rel} must be multiplied by $\rho g H_0$).
iii. Calculation of the weight of the material above the point of interest (z'). This will result in the determination of the resistance pressures $[\rho_r g d_{rev} + \rho_s' g(-z')]$.
iv. Application of the limit state equation (6.10) to check if soil liquefaction occurs in the sand core beneath the PBA-revetment.

6.3.2 Implementation and validation of the proposed stability analysis

In Oumeraci et al. (2010) & (2012), a failure of a PBA-revetments is described. This failure occurred during one of the large-scale tests performed in the GWK for both regular and irregular waves. Therefore, a brief description of the failure is addressed in this section. Moreover, the implementation of the proposed methodology for the stability analysis (Section 6.3.1) is validated by considering the failure reported in the GWK test. Finally, a physical interpretation of the results is provided based on the GWK test where the failure occurred.

a) Description of the failure of the PBA-revetment in GWK tests

Three model alternatives A, B and C of PBA-revetments (Fig. 6-8) with the same slope 1:3, the same thickness 0.15 m and the same characteristics of the embankment soil (sand with d_{50}=0.35mm and U=2.46) and geotextile (Terrafix 609), but with different gravel filter thicknesses were tested in the Large Wave Flume GWK, Hannover:

- *Model Alternative A*: No gravel filter layer was included and the PBA-revetment made of crushed limestone (20/40 mm) was directly placed on the geotextile filter, thus resulting in an overall revetment-filter thickness of d_{rev}=0.15m
- *Model Alternative B*: A gravel filter layer with a thickness of 0.10 m made of limestone (20/40 mm) was added directly beneath the PBA-revetment of Model Alternative B , thus resulting in an overall revetment-filter thickness of d_{rev}=0.25m
- *Model Alternative C*. This alternative was built after the failure of Model Alternative A. The 0.15m thick PBA-revetment and the 0.20 m thick gravel filter were both made of crushed granite (16/36 mm), thus resulting in an overall revetment-filter thickness of d_{rev}=0.35m

The failure occurred on 18th May, 2009 for model alternative A under regular waves with wave height H_0=1.3 m, wave period T=5.0s and a water depth h=3.90m. These wave conditions together with a slope 1:3 induce wave-impact loads (ξ_0=1.745).

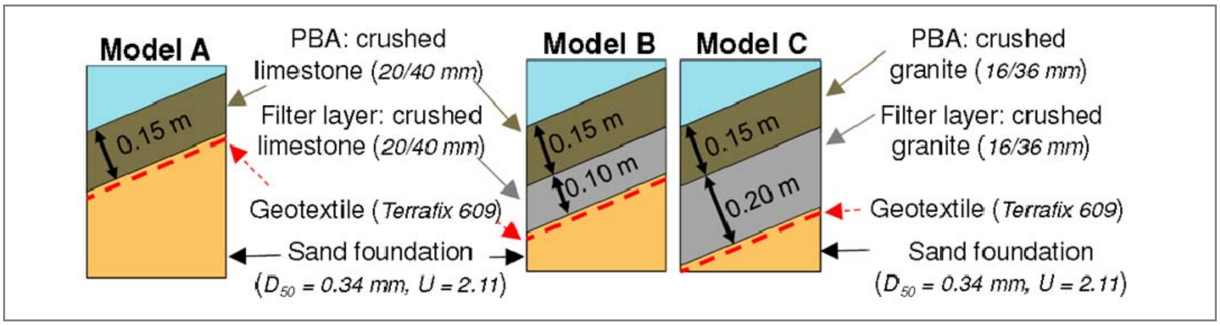

Fig. 6-8: Model alternatives in large-scale tests in the GWK (Oumeraci et al. (2010)).

b) *Application of the criteria for the assessment of the soil liquefaction potential*

The critical depth inside the sand core at which the soil liquefaction is likely to occur has first to be defined. Therefore, the analysis is performed below for three different depths. The procedure will be demonstrated exemplarily for a depth of z'= -0.20m, but the results of the analysis for all three depths are summarized in Table 6-2. It should be reminded that the failure occurred on a 0.15m thick PBA-revetment without gravel filter on a slope 1:3 subject to regular waves (H_0=1.3 m, T=5.0s, h=3.90m and ξ_0=1.745).

The proposed methodology for the assessment of soil liquefaction is systematically applied in four steps as follows for Model Alternative A (d_{rev1}=0.15m), B (d_{rev2}=0.25m), and C(d_{rev3}=0.35m) and exemplarily for a soil depth of z'= -0.20m in the sand core:

i. The relative uplift pressure difference Δu_{rel} is calculated by eq. (6.5) for a soil depth z'=-0.20m, using coefficients A, B, and C from Table 6-1:

Model Alternative A.

$$\Delta u_{rel} = \frac{u_{0*} - \left(u_{t*} + u_r\right)}{\rho g H_0} = \frac{A \cdot \xi_0}{1 + B \cdot \xi_0 + C\xi_0^2} = \frac{0.224 \cdot 1.745}{1 + 0.083 \cdot 1.745 + 0.014 \cdot 1.745^2} = 0.329\,[-]$$

Model Alternative B.

$$\Delta u_{rel} = \frac{u_{0*} - \left(u_{t*} + u_r\right)}{\rho g H_0} = \frac{A \cdot \xi_0}{1 + B \cdot \xi_0 + C\xi_0^2} = \frac{0.192 \cdot 1.745}{1 + 0.057 \cdot 1.745 + 0.018 \cdot 1.745^2} = 0.290\,[-]$$

Model Alternative C.

$$\Delta u_{rel} = \frac{u_{0*} - \left(u_{t*} + u_r\right)}{\rho g H_0} = \frac{A \cdot \xi_0}{1 + B \cdot \xi_0 + C\xi_0^2} = \frac{0.217 \cdot 1.745}{1 + 0.013 \cdot 1.745 + 0.028 \cdot 1.745^2} = 0.342\,[-]$$

ii. According to eq. (6.4), Δu_{rel} must be multiplied by $\rho g H_0$ in order to obtain $|\Delta u| = |u_{0*} - (u_{t*} + u_r)|$:

Model Alternative A.

$$\left|u_{0*} - \left(u_{t*} + u_r\right)\right| = 0.329 \cdot \rho g H_0 = 0.329 \cdot 9810 \cdot 1.3 = 4197.9\,[Pa]$$

Model Alternative B.

$$\left|u_{0*} - \left(u_{t*} + u_r\right)\right| = 0.290 \cdot \rho g H_0 = 0.290 \cdot 9810 \cdot 1.3 = 3701.7\,[Pa]$$

Model Alternative C.

$$\left|u_{0*} - \left(u_{t*} + u_r\right)\right| = 0.342 \cdot \rho g H_0 = 0.342 \cdot 9810 \cdot 1.3 = 4358.6\,[Pa]$$

iii. Calculation of the submerged weights [$\rho_r g d_{rev} + \rho_s' g(-z')$] of the material above depth z'=-0.20m in the sand core beneath PBA-revetment alternative A, B and C. The weight ρ_r and the submerged weight ρ_s' were considered in Oumeraci et al. (2010) as ρ_r=1560 [kg/m^3] and ρ_s'= 870 [kg/m^3]:

Model Alternative A. (z'=0.20m, d_{rev}=0.15m)

$$\rho_r g d_{rev} + \rho_s' g(-z') = 1560(9.81)(0.15) + 870(9.81)(0.20) = 4002.5[Pa]$$

Model Alternative B. (z'=0.20m, d_{rev}=0.25m)

$$\rho_r g d_{rev} + \rho_s' g(-z') = 1560(9.81)(0.25) + 870(9.81)(0.20) = 5532.8[Pa]$$

Model Alternative C. (z'=0.20m, d_{rev}=0.35m)

$$\rho_r g d_{rev} + \rho_s' g(-z') = 1560(9.81)(0.35) + 870(9.81)(0.20) = 7063.2[Pa]$$

iv. Application of limit state equation (6.10) to check if soil liquefaction occurs at depth z'=0.20m in the sand core beneath PBA-revetment alternative A, B and C.

Model Alternative A.

$$\frac{|u_{0*} - (u_{t*} + u_r)|}{\rho_r g d_{rev} + \rho_s' g(-z')} = \frac{|4197.9[Pa]|}{4002.5[Pa]} = 1.05 \qquad \Rightarrow 1.05 \geq 1 \qquad (liquefaction!!!)$$

Model Alternative B.

$$\frac{|u_{0*} - (u_{t*} + u_r)|}{\rho_r g d_{rev} + \rho_s' g(-z')} = \frac{|3701.7[Pa]|}{5532.8[Pa]} = 0.67 \qquad \Rightarrow 0.67 \leq 1 \qquad (no\ liquefaction)$$

Model Alternative C.

$$\frac{|u_{0*} - (u_{t*} + u_r)|}{\rho_r g d_{rev} + \rho_s' g(-z')} = \frac{|4358.6[Pa]|}{7063.2[Pa]} = 0.62 \qquad \Rightarrow 0.62 \leq 1 \qquad (no\ liquefaction)$$

The results of the stability analysis in the final step (iv) show that soil liquefaction indeed occurred only for Model Alternative A with d_{rev}=0.15m (just beyond the threshold 1 in eq. (6.10)), while Model Alternatives B and C with larger revetment-filter thicknesses (d_{rev}=0.25m and d_{rev}=0.35m, respectively) proved to be safe against soil liquefaction at the same soil depth z'=-0.20m and under the same wave conditions which caused the failure of Model Alternative A.

Finally, the analysis of this test for the different revetment alternatives and depths inside the sand core is summarized in Table 6-2 where the results of each of the four steps of the proposed methodology are described.

As shown in Table 6-2, soil liquefaction occurred only at soil depth z'=-0.20m and just for Model Alternative A, thus confirming the results of the analysis using the same stability approach reported by Oumeraci et al. (2010).

Additionally, a similar stability analysis was performed in Alcérreca-Huerta & Oumeraci (2014) for all other GWK tests with regular waves reported in Oumeraci et al. (2010). The results showed, as expected, no presence of soil liquefactions in other tests and therefore the no occurrence of failure.

Table 6-2: Stability analysis at different depths inside the sand core beneath revetment alternatives A, B and C with different revetment-filter thicknesses tested in GWK on a slope 1:3 (regular wave test with H_0=1.3m, T=5.0s, h=3.90m, ξ_0=1.745).

	Revetment filter thickness for Model Alternatives A, B, and C		
	d_{rev1}=0.15m	d_{rev2}=0.25m	d_{rev1}=0.35m
Step 1. *Relative uplift pressure difference* Δu_{rel} *[-]*			
z'= -0.2m	0.329	0.290	0.342
z'= -0.4m	0.372	0.317	0.345
z'≤ -0.6m	0.378	-0.301	0.323
Step2. *Driving force term* $\lvert u_{0*}-(u_{t*}+u_r)\rvert$ *in limit state equation* (6.10) Δu_{rel} *multiplied by* $\rho g H_0$ *[Pa]*			
z'= -0.2m	4197.9	3701.7	4358.6
z'= -0.4m	4744.4	4039.6	4403.5
z'≤ -0.6m	4818.5	3837.0	4124.5
Step3. *Resistance force term in limit state equation* (6.10)**:** $[\rho_r g d_{rev} + \rho_s' g(-z')]$ *[Pa]*			
z'= -0.2m	4002.5	5532.8	7063.2
z'= -0.4m	5709.4	7239.8	8770.1
z'≤ -0.6m	7416.4	8946.7	10477.1
Step 4. *Ratio of driving and resistance force terms:* $\lvert u_{0*}-(u_{t*}+u_r)\rvert / [\rho_r g d_{rev} + \rho_s' g(-z')]$ *[-]*			
z'= -0.2m	1.05	0.67	0.62
z'= -0.4m	0.83	0.56	0.50
z'≤ -0.6m	0.65	0.43	0.39
Soil liquefaction *(results of step 4 >1)*			
z'= -0.2m	Yes	No	No
z'= -0.4m	No	No	No
z'≤ -0.6m	No	No	No

A similar methodology to the one here proposed was also suggested by Foyer & Oumeraci (2013a) concluding in more cases with soil liquefaction for model A in GWK tests rather than just for the case where the failure occurred and exemplarily shown in this section. These results may be explained due to: i) the neglected residual pore pressure for the calculation of Δu and ii) a relocation of the sand at each wave cycle where liquefaction occurs but without leading to the total collapse of the revetment. The neglected residual pore pressure in Foyer & Oumeraci (2013a) methodology may lead to inaccuracies on the calculation of the driving force, while the relocation of the sand at each wave cycle might occur but cannot neither be confirmed nor excluded. The physical interpretation of the failure in the GWK test is therefore provided in Section 6.3.2c.

The proposed methodology for the assessment of soil liquefaction is possible by using (i) the new formulae for the prediction of the driving forces induced by a wide range of wave conditions and (ii) the improved understanding of the underlying processes of soil liquefaction beneath a porous bonded revetment which have been obtained through the results of the new model. The new formulae (eqs. (6.3)- (6.5)) are applicable for revetment-filter thicknesses d_{rev} 0.15m - 0.35m, and thus future research should be conducted for larger d_{rev}-values. Moreover, the effect of the revetment stiffness to avoid total collapse of the revetment as well as on the soil liquefaction should be also investigated.

c) *Physical interpretation of the failure presented during GWK tests with PBA-revetments (reported in Oumeraci et al. (2010))*

The physical interpretation of the failure of the PBA-revetment in GWK tests is made based on information regarding previous studies (i.e., Oumeraci et al. (2010), Oumeraci et al. (2012); Foyer & Oumeraci (2013a)) as well as the results obtained in this report. According to this study and the previous aforementioned studies, the failure of the PBA-revetment occurred due to the transient excess pore pressures inside the sand core beneath which resulted in instantaneous soil liquefaction. This failure was not present in other model alternatives since the revetment-filter thickness was sufficient to support the excess of pore pressures. It should be mentioned that the transient excess pore pressures (driving force term) vary around ±10% between Model Alternatives A, B and C subject to the same wave conditions and thus, it is assumed that the mean reason why no failure occurred for Alternative B and C may consist in the difference of the submerged weights (resistance force term) of the revetment-filter system which is ~22% and ~55% higher for Model Alternatives B and C, respectively, than Model Alternative A (a similar result is also found in Oumeraci et al. (2009)).

For Model Alternative A, the ratio of the driving and resistance force terms in the limit state equation (6.10) provided a value of 1.05, which is close to the threshold value 1.00 for incipient soil liquefaction. Furthermore, the failure was reported to occur between waves 74 and 75 after the beginning of the test, but the residual displacement of the revetment upwards normal to the slope started several wave cycles before (see Fig. 6-10 and Fig. 6-9). The time series of pressure transducer PT17 (0.20 m deep in the sand core) shows a gradual increase of the negative pore pressure several waves before the failure occurs, while the displacement signals indicate that the revetment starts to move upwards nearly at the same time and in the same direction as the negative pore pressure gradient.

Foyer & Oumeraci (2013a), reported that soil liquefaction occurred several times during the passage of the wave troughs. Thus, considering the results of the present study with a 5% exceedance of the resistance forces by the driving forces, soil liquefaction would have occurred for all waves in the regular wave test, but in practice the waves generated in the flume actually differs. Moreover, since the test was close to the limit threshold for the beginning of soil liquefaction, two scenarios might be possible:

i. The failure proceeds gradually (providing small local failures) until a limit at which the motion of particles makes unstable the sand core thus resulting in the sliding of the embankment subsoil and the revetment which may induce an increment of the displacements just a short time before the failure occurs (Fig. 6-10 and Fig. 6-9). The pore-pressure increase may occur at the beginning of the test increasing wave by wave simultaneous to the accumulation of small local failures.

ii. The succession of several liquefaction events results in the accumulation of the soil particles due to sliding down the slope. This accumulation increases up to a certain threshold which cannot be supported by the stiffness and flexural strength of the revetment leading to the cumulative residual displacement upwards of the revetment and later to the total collapse.

On one hand, a displacement downwards (Fig. 6-9a) of the revetments occurs until wave 65 for both Model Alternatives A and B. The downward revetment displacement may be explained by a primary compaction of the top of the sand since it occurs in both models. On the other hand, the negative pore-pressures slightly increase wave by wave during the test. However, after wave 65, both negative pressure and upward displacement become larger which makes scenario i) most likely to occur since the cumulative local liquefaction of the soil might not be observed in the displacement time series up to the time the liquefied soil volume is large enough to induce residual deformations. For scenario ii), the upward displacement of the revetment should be observed since the beginning of the test, which is not observed in Fig. 6-9a (rather compaction of the revetment layers of the revetment takes place) and thus this scenario might be excluded.

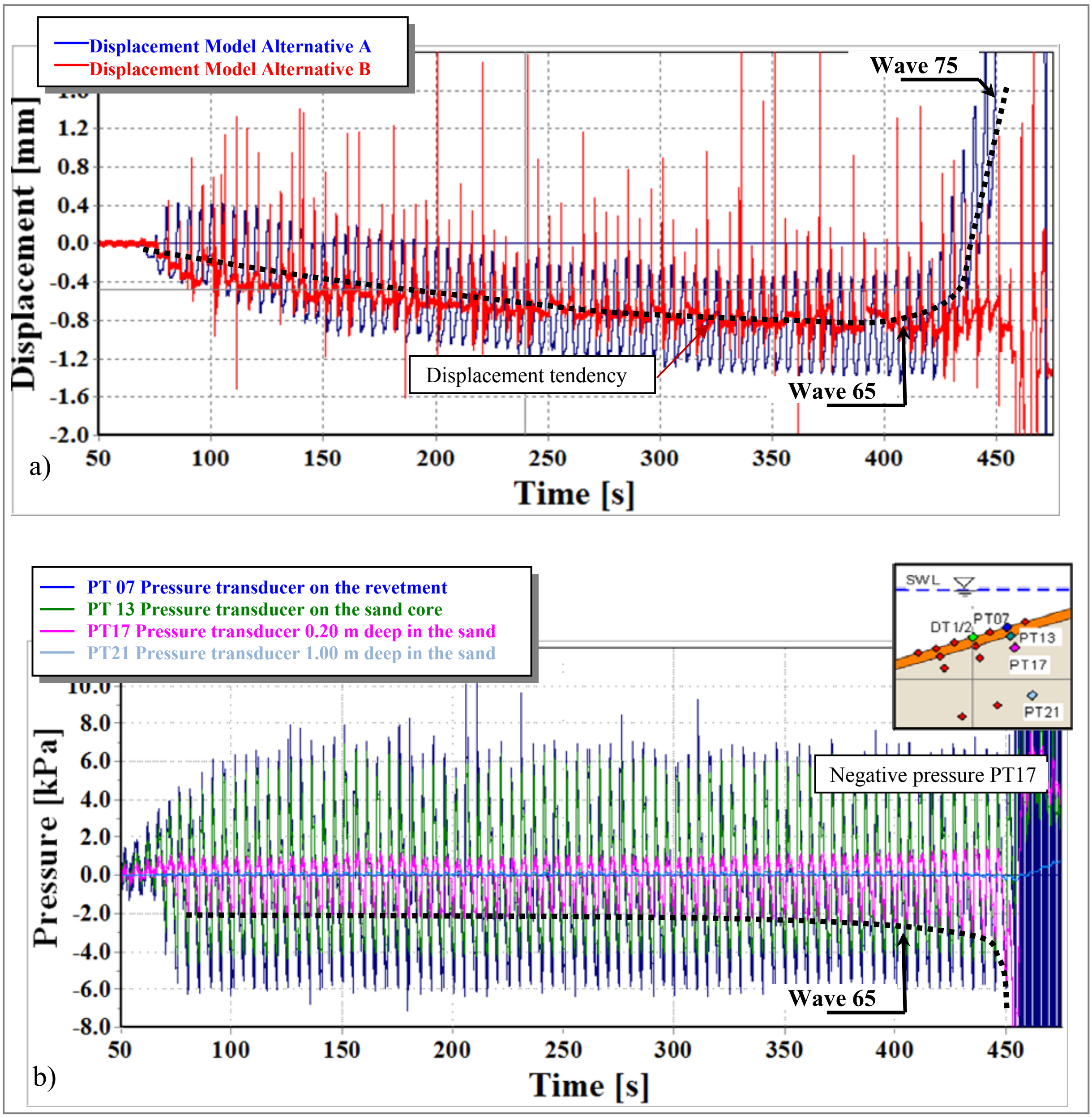

Fig. 6-9: Time series for a) revetment displacement in Model A and B and b) pressure development in Model A for the failure test in GWK.

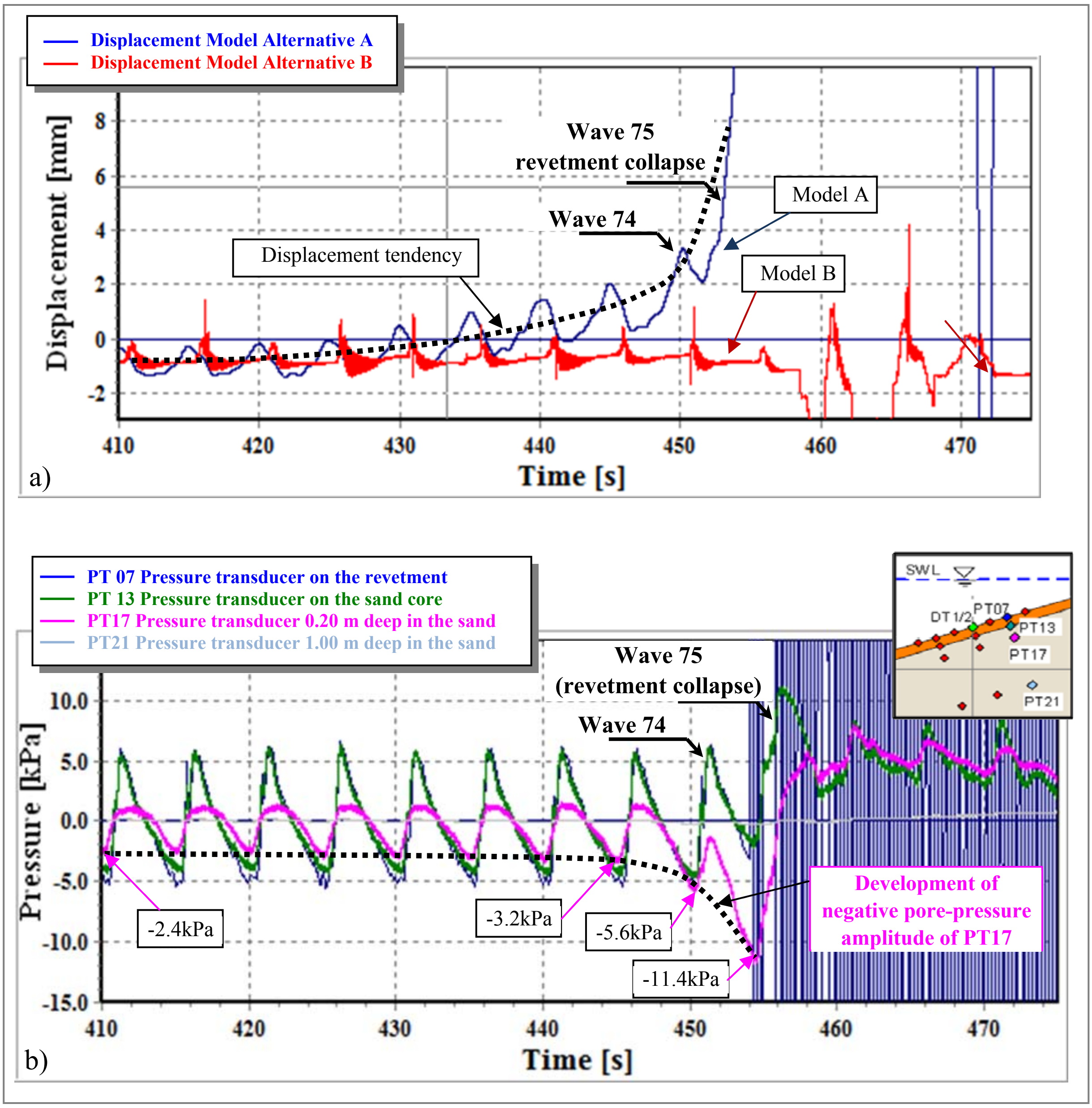

Fig. 6-10: Detail of time series (waves 65-75) for: a) revetment displacement in Model A and B and b) pressure development in Model A for the failure test in GWK (modified from Oumeraci et al. (2009)).

In summary, the observed failure may be explained as follows:

- The failure occurred as a consequence of the excess pore pressures inside the sand core (upward driving force) which exceeded the downward resisting force (submerged weights of revetment considered -filter and sand layer above location considered), The revetment-filter thickness was too small to avoid the lifting of the soil particles.
- It is possible that liquefaction started to occur since the beginning of the wave train of the test as consequence of the high excess of pore pressure. However, the liquefaction most likely produced small local failures in the sand core that were not critical at all for the stability of the whole revetment and that were probably overtaken by the particles in the vicinity of the small local failure. This is supported by:

  - the presence of liquefaction in almost all waves in Model A as concluded by Foyer & Oumeraci (2013a), but with displacements similar to model B until wave 65 (s. Fig. 6-9a and Fig. 6-10a).
  - The ratio of the driving and resistance force terms in the limit state equation (6.10) provided a value of 1.05, which is close to the threshold value 1.00 for incipient soil liquefaction.
- With the increasing number of small liquefied zones induced by each new incoming wave (Fig. 6-11a), the sand in the vicinity cannot overtake the displacements. The liquefied zone increases (Fig. 6-11b) and the upward displacements of the revetment started to increase simultaneously (waves 65-74 in Fig. 6-10a).
- The liquefied zone is large enough to induce the sliding and the collapse of the revetment.

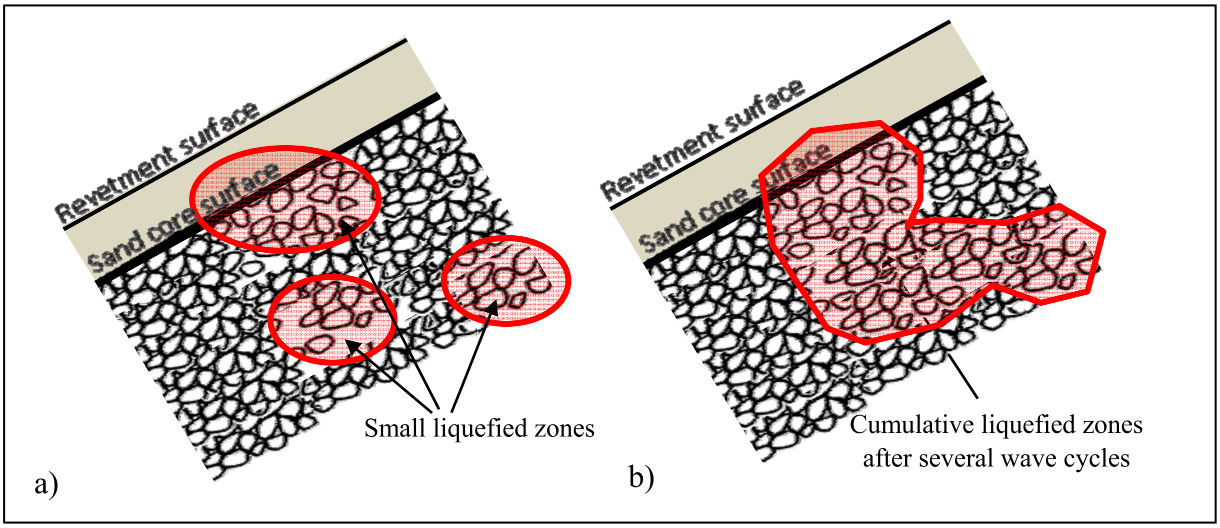

Fig. 6-11: Generation of large liquefied zone after several wave cycles (b) as consequence of the accumulation of small liquefied zones at each wave (a).

The proposed methodology for the assessment of soil liquefaction in the sand core beneath PBA-revetments together with new formulae for the driving forces presented in this section were validated with GWK tests where the failure reported was properly predicted. Based on previous studies of the failure, two possible scenarios for the failure in the GWK test were analysed. It is tentatively concluded that the failure most likely occurred due to the presence of small liquefied zones that accumulated during the test resulted in a larger liquefied zone which induced the sliding of the embankment subsoil and, consequently, the collapse of the revetment.

6.4 Summary of key results

In this chapter, the methodology for the assessment of soil liquefaction beneath PBA-revetments as initially proposed by Oumeraci et al. (2010) is adopted and prediction formulae are developed for its implementation

The prediction formulae and the methodology were validated by the results of large-scale tests with PBA-revetments in GWK (Oumeraci et al. (2010)), including one test where soil liquefaction occurred. The observed failure could be well detected by the proposed methodology and prediction formulae. Further results are reported in Alcérreca-Huerta & Oumeraci (2014) which also confirmed the GWK tests where no failure occurred.

Moreover, the prediction formulae used within the methodology can be applied for different revetment configurations, wave conditions and revetment slopes due to the use of the surf similarity parameter. The later overcomes limitations in previous studies such as Oumeraci et al. (2010) where the assessment of liquefaction was only provided for the failure test case and Foyer (2013), where the probable overestimation of the driving forces (excess of pore pressures) and presence of liquefaction were detected even for GWK tests without failure.

Additionally, the analysis of the failure developed in Model Alternative A of the GWK tests show that soil liquefaction may not only be able to induce instantaneous failure and revetment collapse but also might induce small liquefied zones which after a possible accumulation may develop to a larger liquefied zone resulting in the collapse of the entire revetment.

Therefore, it is stressed that the possibility of soil liquefaction must be avoided in the design of PBA-revetments, i.e. values far less than the threshold 1.00 for incipient soil liquefaction provided by limit state equation (6.10) are to be ensured.

The new prediction formulae for the relative uplift pressure difference Δu_{rel} as function of the surf similarity parameter may be considered as a valuable tool for liquefaction assessment in the sand core beneath PBA-revetments. However, future work is needed in order to explicitly account for the revetment-filter thickness considering thicker revetment-filter thicknesses than those tested in the numerical parameter study. The effect of different porosities, grain sizes and permeability of the revetment and filter layers on the relative uplift pressure difference Δu_{rel} might also be investigated. By considering a two-way coupling in the CFD-CSD model system "`wavePoreGeoFoam`", it might be possible to detect in real time areas that are subject to wave-induced liquefaction due to transient or residual pore pressure development. Thus, it is highly recommended to enhance the new CFD-CSD model system "`wavePoreGeoFoam`" for further research related to wave-porous structures interaction.

7 Summary, discussion and outlook

A new CFD-CSD model called `wavePoreGeoFoam` was developed and validated by laboratory tests. A systematic parameter study was applied with the validated model in order to extend the conditions tested in the laboratory and to improve the understanding of the processes associated with the interaction between waves, PBA-revetments and their soil foundation, thus allowing the development of new generic formulae.

In this concluding chapter, the calibration and performance of the new CFD-CSD model and its validation are briefly summarized. The major part of the chapter is focused on the summary and discussion of the key findings of the parameter study by applying the new validated model. This also includes an overview of the analysis of the numerical data and improved understanding gained from the parameter study.

7.1 The new CFD-CSD model system

A CFD and a CSD model (based on the OpenFOAM framework) were weakly coupled (one-way coupling) for the generation of a new CFD-CSD model system named `wavePoreGeoFoam`. The VARANS equations based on the Hsu et al. (2002) approach were implemented in the CFD solver `wavePorousFoam` in this study for the simulation of the hydrodynamic processes in porous and non-porous regions. On the other hand, the fully dynamic Biot's equations implemented in the CSD solver `geotechFoam` in another ongoing PhD study by El-Safti, H. allows us to differentiate between the soil effective stresses taken by the solid skeleton and the pore pressures developed in the water. The weakly coupling of both solvers in this study thus overcomes the limitation of the VARANS equations in the CFD model where only the effects of the porous structure on the fluid motion are considered.

The new weakly coupled CFD-CSD model system `wavePoreGeoFoam` was systematically validated considering large and small-scale laboratory tests with PBA-revetments. A relatively good agreement was obtained in terms of the shape and magnitude of the pressure time series for all layers on and beneath the revetment. Furthermore, calibration of the numerical model was conducted resulting in a sensitivity analysis. The key results may be summarized as follows: i) the porosity, and the α_f and β_f coefficients needed in the Darcy-Forchheimer equation (all related to the permeability of the porous media) have been identified as the most crucial parameters for the numerical modelling of the wave-structure-subsoil interaction; ii) for the modelling of turbulence, LES models provide better results for wave impact loading and large duration tests, while the volume-averaged k-ε turbulence model performs better for non-impact waves and short duration simulations.

With the new CFD-CSD numerical model system, a parameter study was conducted in order to better understand the hydro-geotechnical processes which may affect the stability of PBA-revetments and their foundation. A test programme was developed for the parameter study based on previous laboratory and numerical studies. This parameter study consisted of 135 numerical simulations and the model set-up was defined considering 100 to 165 locations for data extraction (depending on the revetment configuration) with a special focus on those related to the pressure and pore-pressure. The large number of locations for data extraction, together with the possibility of considering different configurations of PBA-revetments, is recognized as the key advantage of numerical modelling over laboratory tests. The numerical modelling was used together with the laboratory tests results for a systematic parameter study in order to analyse the hydro-geotechnical processes involved in the wave-structure-foundation interaction beyond the tested conditions in the laboratory.

7.2 Processes associated with wave-structure-soil interaction

The key findings of the processes involved in the interaction of the waves, the revetment and its soil foundation are summarised. As the run-up, the swash, the wave set-up and the development of the impact component of the pressure are strongly related to the revetment thickness d_{rev}, the effect of this parameter on the processes on and beneath the revetment are discussed.

a) *Wave breaking process (s. also Section 4.1.1)*

- Wave-wave interaction influences the limits between the wave breaker types in terms of surf similarity ξ_0, which were found to differ in previous studies. Based on the average ξ_0-values from this study and the studies by Oumeraci et al. (2010) and Foyer & Oumeraci (2013b) for PBA revetments, the following breaker type classification is proposed:

		Spilling	*Plunging*	*Collapsing*	*Surging*
GWK-tests (Oumeraci et al. (2010))	ξ_0	-	< 2.2	2.2 - 4.5	> 4.5
Foyer & Oumeraci (2013b)	ξ_0	< 1.0	~ 1.0 - 2.4	~ 2.4 - 5.2	> 5.2
Parameter study	ξ_0	-	0.6 - 2.4	2.4 - 3.4	> 3.4
Average		**-**	**0.8 - 2.4**	**2.4 - 4.3**	**> 4.3**

- The finding from the previous parameter study that the breaker types is also affected by the revetment thickness (Foyer (2013)) is confirmed by this study, but as in the previous study the correlation with the ξ_0 –threshold could not clearly be defined.

b) *Wave reflection (s. also Section 4.1.2)*

- As expected, wave reflection from PBA-revetments is less than that of smooth impermeable revetments. However, the revetment-filter thickness has only a slight effect on wave reflection.
- No enhancement of the results could be achieved by using the approach proposed by Foyer (2013) based on the modified surf similarity parameter (ξ_{mod}) with inclusion of the revetment-filter thickness instead of the commonly used surf similarity parameter (ξ_0).
- Therefore, in this study the revetment-filter thickness was not considered in the development of the prediction formulae for wave reflection

c) *Mean water level (MWL), wave set-up/set-down (s. also Section 4.2)*

- The length of the incident waves and the slope steepness are the key parameters governing the relative external wave set-up.
- With increasing slope steepness, the wave set-up also increases for plunging breakers while it decreases for collapsing and surging breakers.
- The effect of the revetment-filter thickness, though not very clear, is less than that of the slope steepness and almost no variation in the set-up is observed due to a change of the revetment-filter thickness.
- A lower envelope is clearly defined for the minimum value of $\eta_{S,RuG}/H_0$.
- The internal wave set-up at the revetment-filter interface is larger (about ~20%) than the external wave set-up on the revetment. However, the internal wave set-up on the sand core and the external wave set-up on the revetment are similar. This is in agreement with the results of Foyer (2013).

d) *Wave run-up/run-down (s. also Section 4.3)*

- As already found in the previous study by (Foyer (2013)), the wave run-up/run-down process can be much better understood if it is described as a swash component oscillating around the Mean Water Level (MWL) induced by the wave set-up. This provides the key for a better understanding of all processes on and beneath the revetment as they are all affected by the wave set-up. Also the wave run-up and run-down related to MWL exhibit similar values, being almost symmetrical to the MWL (Foyer (2013)).
- An increase of the revetment-filter thickness was found to: i) reduce the wave run-up and run-down on the revetment except for $2.0<\xi_0<4.0$ where both run-up and run-down increase, ii) reduce the thickness of the water layer from the previous wave on the revetment, iii) increase the swash amplitude and iv) decrease the internal wave run-up and run-down beneath the revetment.
- The wave run-up and run-down on the revetment consists of an impact- and a quasi-static component, which result from the impact load and the quasi-static load, respectively. The impact component is essentially induced by plunging breakers and partly by collapsing breakers. The quasi-static component is present for all types of breakers while it is the only component in surging breakers.
- For PBA-revetments, the maximum run-up and run-down on the revetment might occur for ξ_0-values $2.0<\xi_0<4.0$ (plunging and collapsing breakers) and not necessarily for surging breakers.
- The swash induced on the revetment is considerably damped beneath the revetment by 63% at the revetment-filter interface and 85% on top of the sand core.

e) *Wave-induced pressures (s. also Chapter 5)*

- A larger revetment-filter thickness d_{rev} decreases the relative peak pressure on the revetment $P_{1max}/\rho g H_0$ for $0.8<\xi_0<2.4$ (plunging breaker) but increases $P_{1max}/\rho g H_0$ for $2.4<\xi_0<4.3$ (collapsing breaker).

- The effect of the revetment-filter thickness is mainly observed for plunging and collapsing breakers (impact load) while surging breakers are almost un-affected (non-impact load).
- For impact loads, the thickness of a water layer on the revetment (dependent on the revetment slope, porosity and thickness of the revetment) affects the magnitude of the peak pressure. However, this effect could not be quantified and thus further research is required.
- The impact component of the peak pressure on the revetment for $1.0<\xi_0<4.3$ (plunging and collapsing breakers) significantly decreases its magnitude through the revetment and filter layers: up to 72% for a $d_{rev}=0.15$m and 76% for $d_{rev}>0.25$m.
- The quasi-static component of the pressure on the revetment for the entire range of ξ_0-values is slightly affected by the revetment-filter thickness d_{rev} (damping up to 15% through the revetment and filter layers).
- The presence of two peaks in the spatial pressure distributions on and beneath the revetment were found for both impact and non-impact loads: i) the first peak pressure on and beneath the revetments (P_{max1} and P_{max3}) is found generally below the maximum wave run-down, ii) the second peak is closer to the maximum wave run-up.
- The pore pressure distribution normal to the revetment slope inside the sand core was shown to be accurately described by De Groot's approach. Therefore, the results obtained from a porous seabed without any revetment can be also applied for a porous bed protected by a porous revetment for locations below the MWL.

7.3 Overview of prediction formulae developed for PBA-revetments

In Table 7-1, an overview of the prediction formulae developed for PBA-revetments in this study is given.

Table 7-1: Overview of the prediction formulae for PBA-revetments developed from the results of the numerical parameter study using the new CFD-CSD model `wavePoreGeoFoam`.

WAVE REFLECTION		
	$C_r = \tanh\left(0.114 \cdot \xi_0^{1.17}\right)$	eq. (4.6)

WAVE SET-UP		
- On the revetment		
	Wave set-up: $\left(\frac{\eta_{S,RuG}}{H_0}\right)_{total} = 2.03\left(\cot\alpha\right)^{-0.245} \xi_0^{B+2}$, with $B = 0.168\cot\alpha - 2.867$	eq. (4.12)
	▪ Minimum expected value: $\left(\frac{\eta_{S,RuG}}{H_0}\right)_{\min} = \left(\frac{1.35 \cdot \xi_0}{1 + 0.864 \cdot \xi_0 + 0.454 \cdot \xi_0^2}\right)$	eq. (4.10)
	▪ Maximum expected value: $\left(\frac{\eta_{S,RuG}}{H_0}\right)_{\max} = \left(\frac{1.58 \cdot \xi_0}{1 - 0.442 \cdot \xi_0 + 0.359 \cdot \xi_0^2}\right)$	eq. (4.11)
- At revetment-filter interface		
	Internal wave set-up: $\eta_{S2,RuG} = 1.218 \cdot \eta_{S,RuG}$	eq.(4.13)
- On top of the sand layer		
	Internal wave set-up: $\eta_{S3,RuG} = 0.993 \cdot \eta_{S2,RuG} \rightarrow \eta_{S3,RuG} = 1.210 \cdot \eta_{S,RuG}$	eq.(4.14)

	WAVE RUN-UP/DOWN & SWASH	
- On the revetment		
	Maximum run-up on MWL: $\left(\frac{Ru-\eta_{S,RuG}}{H_0}\right)_{UE}=\left(\frac{Ru-\eta_{S,RuG}}{H_0}\right)_{impact}+\left(\frac{Ru-\eta_{S,RuG}}{H_0}\right)_{Quasi-static}$	eq. (4.19)
	▪ Quasi-static component: *(minimum run-up on MWL)* $\left(\frac{Ru-\eta_{S,RuG}}{H_0}\right)_{Quasi-static}=\frac{\xi_0^{\ 2}+19.23\cdot\xi_0}{\xi_0^{\ 2}+130.87}$	eq.(4.17)
	▪ Impact component: $\left(\frac{Ru-\eta_{S,RuG}}{H_0}\right)_{impact}=0.5B\left(\xi_0-A\right)\cdot\exp\left[-\frac{\left(\xi_0-A\right)^2}{2B}\right]$ with A=0.5B (for d_{rev1}=0.15m, A=0.55; for d_{rev2}=0.25m, A=0.77; for d_{rev3}=0.35m, A=1.2)	eq.(4.18)
	Maximum run-down on MWL: $\frac{Rd-\eta_{S,RuG}}{H_0}=-\frac{Rd-\eta_{S,RuG}}{H_0}$ →Swash: $2\left\lvert\frac{Ru-\eta_{S,RuG}}{H_0}\right\rvert$	eq.(4.20)
- At revetment-filter interface		
	Maximum run-up/down on MWL: $\frac{Ru-\eta_{S2,RuG}}{H_0}=-\frac{Rd-\eta_{S2,RuG}}{H_0}=0.372\frac{\xi_0^{\ 2}+19.23\cdot\xi_0}{\xi_0^{\ 2}+130.87}$	eq.(4.21)
- On top of the sand core		
	Maximum run-up/down on MWL: $\frac{Ru-\eta_{S2,RuG}}{H_0}=-\frac{Rd-\eta_{S2,RuG}}{H_0}=0.159\frac{\xi_0^{\ 2}+19.23\cdot\xi_0}{\xi_0^{\ 2}+130.87}$	eq.(4.22)

	PEAK PRESSURE ON THE REVETMENT	
- Peak pressure on the revetment		
	Peak pressure: $\frac{P_{\max 1}}{\rho g H_0}=\frac{P_{diff}}{\rho g H_0}+\left(\frac{P_{stat}}{\rho g H_0}\right)_{quasi-static}$	eq.(5.4)
	▪ Quasi-static component: $\left(\frac{P_{stat}}{\rho g H_0}\right)_{quasi-static}=2\frac{\xi_0^{\ 2}+6.7\cdot\xi_0}{\xi_0^{\ 2}+38.5}$	eq.(5.5)

	▪ Pressure difference: *(Impact) - (quasi-static)* $\frac{P_{diff}}{\rho g H_0}=A\cdot\xi_0\cdot\exp\left(-\frac{\xi_0^{\ 2}}{B}\right)$
	for d_{rev}=0.15m, A=4.60, B=2.0;
	for d_{rev}=0.25m, A=2.30, B=3.4;
	for d_{rev}=0.35m, A=1.25, B=5.8
		eq. (5.6)

- Location of the peak pressure on the revetment		
	Average location: $\frac{z_{\max 1}}{H_0}=-1.62\cdot\tanh\left(0.46\cdot\xi_0^{\ 0.47}\right)$	eq.(5.9)
	▪ Minimum location: $\frac{z_{\max 1}}{H_0}=-1.64\tanh\left(1.04\cdot\xi_0^{\ 1.59}\right)$	eq.(5.10)
	▪ Maximum location: $\frac{z_{\max 1}}{H_0}=-1.34\tanh\left(0.07\cdot\xi_0^{\ 1.58}\right)$	eq.(5.11)
- Pressure distribution parallel to the revetment		
	▪ Non-impact loads: $\frac{P}{P_{\max 1}}=\frac{0.705-5.172\left(x'_{rel}\right)}{1-4.581\left(x'_{rel}\right)+0.295\left(x'_{rel}\right)^2}$, valid for $x'\leq x'_{Rd}$	eq.(5.16)
	Linear interpolation until the point $\frac{P}{P_{\max 1}}\approx 0.761$ *at* $x'_{rel}=\left[x'_{Rd}+0.83\left(x'_{Ru}-x'_{Rd}\right)\right]/\lvert x'_{\max 1}\rvert$	eq.(5.17)
	Linear interpolation until the point $\frac{P}{P_{\max 1}}=0\ at\ \frac{x'}{\lvert x'_{\max 1}\rvert}=\frac{Ru}{\lvert x'_{\max 1}\rvert}$	

- Impact loads: $\dfrac{P}{P_{\max 1}}=\dfrac{0.789-3.330\left(x'_{rel}\right)}{1-2.908\left(x'_{rel}\right)+0.211\left(x'_{rel}\right)^2}$, valid for $x'\leq x'_{Rd}$ eq.(5.18)

Linear interpolation until the point $\dfrac{P}{P_{\max 1}}\approx 0.715 \quad at \quad x'_{rel}=\left[x'_{Rd}+0.723\left(x'_{Ru}-x'_{Rd}\right)\right]/\left|x'_{\max 1}\right|$

Linear interpolation until the point $\dfrac{P}{P_{\max 1}}=0\ at\ \dfrac{x'}{\left|x'_{\max 1}\right|}=\dfrac{Ru}{\left|x'_{\max 1}\right|}$ eq.(5.19)

- General approach: $\dfrac{P}{P_{\max 1}}=\dfrac{0.747-4.251\left(x'_{rel}\right)}{1-3.745\left(x'_{rel}\right)+0.253\left(x'_{rel}\right)^2}$, valid for $x'\leq x'_{Rd}$ eq. (5.20)

Linear interpolation until the point $\dfrac{P}{P_{\max 1}}\approx 0.710 \quad at \quad x'_{rel}=\left[x'_{Rd}+0.775\left(x'_{Ru}-x'_{Rd}\right)\right]/\left|x'_{\max 1}\right|$

Linear interpolation until the point $\dfrac{P}{P_{\max 1}}=0\ at\ \dfrac{x'}{\left|x'_{\max 1}\right|}=\dfrac{Ru}{\left|x'_{\max 1}\right|}$ eq. (5.21)

(with x'_{Rd} and x'_{Ru} calculated with eq. (5.13) with z=Rd and z=Ru, respectively)

PEAK PORE PRESSURE ON TOP OF THE SAND CORE

- Peak pore pressure on top of the sand core

Peak pore pressure: $\dfrac{P_{\max 3}}{\rho g H_0}=\gamma_{RF}A\cdot\xi_0\cdot\exp\left(-\dfrac{\xi_0^{\,2}}{B'}\right)+\left(\dfrac{P_{\max 3}}{\rho g H_0}\right)_{Quasi-static}$ eq.(5.23)

$$\frac{P_{\max 3}}{\rho g H_0}=A'\cdot\xi_0\cdot\exp\left(-\frac{\xi_0^{\,2}}{B'}\right)+1.75\frac{\xi_0^{\,2}+6.7\cdot\xi_0}{\xi_0^{\,2}+38.5}$$ eq.(5.24)

for d_{rev}=0.15m, A'=1.840,B=2.0;
for d_{rev}=0.25m, A'=0.759,B=3.4;
for d_{rev}=0.35m, A'=0.375, B=5.8

- Location of the peak pore pressure on top of the sand core

Average location: $\dfrac{z_{\max 3}}{H_0}=1.19\left[-1.62\tanh\left(0.46\cdot\xi_0^{\,0.47}\right)\right]$ eq.(5.25)

- Minimum location: $\dfrac{z_{\max 3}}{H_0}=-1.77\tanh\left(0.18\cdot\xi_0^{\,0.78}\right)$ eq.(5.26)
- Maximum location: $\dfrac{z_{\max 3}}{H_0}=-1.77\tanh\left(2.07\cdot\xi_0^{\,2.09}\right)$ eq.(5.27)

- Pore pressure distribution parallel to the revetment

Similar to that described for the pressure distribution on top of the revetment parallel to the revetment slope.

- Non-impact loads: $\dfrac{P}{P_{\max 3}}=\dfrac{0.705-5.172\left(x'_{rel}\right)}{1-4.581\left(x'_{rel}\right)+0.295\left(x'_{rel}\right)^2}$, valid for $x'\leq x'_{RdLay3}$ eq.(5.29)
- Impact loads: $\dfrac{P}{P_{\max 3}}=\dfrac{0.789-3.330\left(x'_{rel}\right)}{1-2.908\left(x'_{rel}\right)+0.211\left(x'_{rel}\right)^2}$, valid for $x'\leq x'_{RdLay3}$ eq.(5.31)
- General approach: $\dfrac{P}{P_{\max 3}}=\dfrac{0.747-4.251\left(x'_{rel}\right)}{1-3.745\left(x'_{rel}\right)+0.253\left(x'_{rel}\right)^2}$, valid for $x'\leq x'_{RdLay3}$ eq. (5.32)

PORE PRESSURE INSIDE THE SAND CORE

- Pore pressure distribution in the sand core normal to the revetment slope

$\left(\dfrac{P}{P_{TopSC}}\right)=\exp\left(\dfrac{z'}{z_2}\right)$ where $z_2=\sqrt{c_{ve}\dfrac{T}{\pi}}$ with $c_{ve}=\dfrac{K}{\gamma_w\left(\beta_S+n\beta_w\right)}$ eq.(5.36)

STABILITY ANALYSIS

- Methodology

I.	Estimation of the relative uplift pressure difference Δu_{rel} between the sand core and a certain depth (z') that can produce the uplifting of the soil particles: $\frac{u_{0*}-\left(u_{t*}+u_r\right)}{\rho g H_0}=\frac{A\cdot\xi_0}{1+B\cdot\xi_0+C\xi_0^2}$ with A and B described in Table 6-1	eq.(6.5)
II.	The relative uplift pressure difference must be multiplied by $\rho g H_0$ in order to obtain $[u_{0*}-(u_{t*}+u_r)]$.	
III.	Calculation of the submerged weights of the material above the point of interest (z'). This will result in the determination of the resistance pressures: $[\rho_r' g d_{rev}+\rho_s' g(-z')]$.	
IV	Application of the following criterion to determine soil liquefaction beneath the revetment: Liquefaction if $\frac{\left\|u_{0*}-\left(u_{t*}+u_r\right)\right\|}{\rho_r' g d_{rev}+\rho_s' g\left(-z'\right)}\geq 1$	eq.(6.10)

LIST OF VARIABLES AND COMPLEMENTARY MODEL SKETCHES

Cr	-	Reflection coefficient	z_{max1}	m	Location of P_{max1}, vertically measured with origin on the shoreline and positive in upwards direction (sketch2)
c_{ve}	m^2/s	Elastic component of consolidation coefficient.			
d_{rev}	m	Revetment-filter thickness			
g	m/s^2	Gravity acceleration	z_{max3}	m	Location of P_{max3}, vertically measured with origin on the shoreline and positive in upwards direction (sketch2)
H_0	m	Wave height in deep waters			
K	m/s	Hydraulic permeability			
L_0	m	Wave length in deep waters			
n	-	Porosity	α	°	Slope angle
P	Pa	Dynamic pressure or pore pressure	β_s , B_w	m^2/N	Elastic compressibility of the sand and of the pore water
P_{max1}	Pa	Peak pressure on the revetment	γ_w	N/m^3	Unit weight of water
P_{max2}	Pa	Peak pore pressure at the revetment-filter interface	$\eta_{S,RuG}$	m	Wave set-up on the revetment
P_{max3}	Pa	Peak pressure at the filter-sand interface	$\eta_{S2,RuG}$	m	Wave set-up at the revetment-filter interface
			$\eta_{S3,RuG}$	m	Wave set-up on top of the sand core.
Ru	m	Wave run-up	ξ_0	-	Surf similarity parameter
Rd	m	Wave run-down	ρ	kg/m^3	Density of the water
T	s	Wave period	ρ_s'	kg/m^3	Submerged density of the sand core
u_{0*}	Pa	Transient excess of pore pressure induced under the wave trough on top of the sand core	ρ_r'	kg/m^3	Submerged density of the revetment-filter
u_{t*}	Pa	Transient excess of pore pressure induced under the wave trough at a depth z' in the sand core	*Definition Sketch 1* 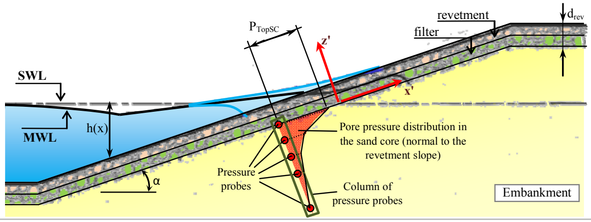 		
u_r	Pa	Residual pore pressure at a depth z' in the sand core			
x'	m	$x'=\sqrt{(z)^2+(z\cdot\cot\alpha)^2}$			
x'_{max1}	m	$x'_{max1}=\sqrt{(z_{max1})^2+(z_{max1}\cdot\cot\alpha)^2}$			
z'	m	Depth in the sand core normal to the revetment slope, zero on top of the sand core and positive in upward direction (see sketch 1)	*Definition Sketch 2* 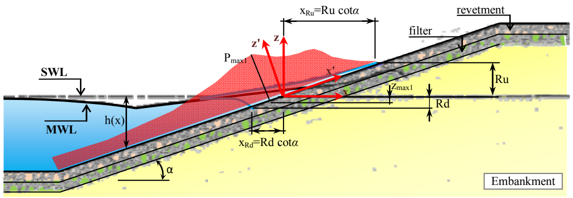 		
z_2	m	Characteristic length for pore pressure amplitude damping due to elastic storage			

7.4 Discussion

The numerical simulations performed for the parameter study based on the new weakly coupled CFD-CSD model developed within the OpenFOAM® framework are in very good agreement with those obtained for similar tests performed in the Large Wave Flume GKW (Oumeraci et al. (2010)). Both hydrodynamic and hydro-geotechnical processes involved in the interaction of the waves with the PBA-revetments and their soil foundation were successfully reproduced.

The CFD-CSD model was reliably used in a comprehensive and systematic parameter study to extend the data from the large-scale tests in GWK for a much wider range of wave and structure parameters.

Among the findings and results described in this thesis, the most valuable and relevant are: i) the effect of the revetment-filter thickness on the hydrodynamic processes, ii) the description of the wave run-up/run-down and the wave-induced pressures considering the effects of both impact and quasi-static components of the wave loading, iii) the implementation of a methodology for the stability analysis of PBA-revetments against soil liquefaction at different depths which considers the effect of the revetment-filter thickness and explicitly accounts for the revetment slope and wave conditions (wave height and wave length)

The prediction formulae for PBA-revetments (summarized in Table 7-1) were developed considering the extreme boundary conditions ($\xi_0 \rightarrow 0$ and $\xi_0 \rightarrow \infty$). Moreover, the methodology proposed for the stability analysis of PBA-revetments and the new formulae developed for its implementation are physically based. Therefore, the prediction formulae and the methodology are applicable to different configurations of PBA-revetments and a wide range of wave conditions. However, caution is recommended for its application outside the limits of conditions tested within this study.

7.5 Outlook

The numerical simulations using the new CFD-CSD model have proved to be a very valuable tool for the study of the wave-structure-subsoil interaction in PBA-revetments. Thus, further studies should be conducted in order to study the effect of other parameters on the hydraulic performance and loading response of PBA-revetments subject to a change of porosity in time due to clogging of the porous revetment (see e.g., Roca Barceló (2014)). Furthermore, the effects of porosity and permeability should be explicitly accounted in the formulae describing the PBA-performance as recently suggested by Liebisch & Oumeraci (2012). Moreover, the relationship of porosity and permeability with other features such as the revetment-filter thickness should be examined.

However, limitations of the parameter study with numerical simulations were identified especially when the focus is on: i) long term processes, such as the definition of the MWL, ii) the simulation of wave spectra that requires tests of long-duration and iii) large spatial domains where detailed wave-structure interaction is desired. The previous conditions generally result in high computational costs and could be better performed by laboratory tests or by the enhancement of the numerical model used in this PhD study.

It is recommended that a two-way CFD-CSD coupling should be developed in order to enhance the results provided by numerical simulations for the wave-structure-subsoil interaction. Moreover, a proper consideration of air compressibility would be required for those conditions where the air-water interactions are crucial, such as in wave-induced impact loads.

Even in its current version, the CFD-CSD model "`wavePoreGeoFoam`" was shown to represent a proper research tool for: i) the optimisation of laboratory tests programmes and model setups by considering preliminary results from the numerical model, ii) the visualisation of and insight into hydrodynamic and hydro-geotechnical processes hardly accessible to measurements and observations in the laboratory and iii) the synergy between the results provided by numerical simulations and experimental results to enhance the understanding of the process to be investigated. Therefore, the CFD-CSD model is recommended as a research tool complementary to laboratory tests which might extend the understanding of the processes under study.

8 References

Ahrens, J.P. (1981): Irregular wave run-up on smooth slopes. Coastal Engineering Research Center, USA.

Ahrens, J.P.; Heisnbaugh, M.S. (1988): Approximate upper limit of irregular wave run-up on riprap. Coastal Engineering Research Center, USA, 1- 32.

Alcérreca-Huerta, J.C.; Oumeraci, H. (2012): Wave loading and response of impermeable block revetments and highly porous PBA revetment: Comparative analysis of large-scale model datasets. Leichtweiß-Institut für Wasserbau, Braunschweig, Germany.

Alcérreca-Huerta, J.C.; Oumeraci, H. (2013): Model equations and validations tests of the numerical modelling of porous structures: focus on solvers developed within the OpenFOAM framework. Leichtweiß-Institut for Hydraulic Engineering and Water Resources, Germany, 120.

Alcérreca-Huerta, J.C.; Oumeraci, H. (2014): Process analysis on PBA-revetments -A parametric study with a CFD-CSD numerical model within the OpenFOAM framewoek-. Leichtweiß-Institut für Wasserbau- Technische Universität Braunschweig, Braunschweig.

Anderson, J.; Degrez, G.; Degroote, J.; Dick, E.; Grundaman, F.; Vierendeels, J. (2009): Computational fluid dynamics: An introduction. Berlin: Springer-Verlag.

ANSYS, I. (2014): ANSYS.

Barree, R.D.; Conway, M.W. (2004): Beyond Beta Factors: A complete Model for Darcy, Forchheimer, and Trans- Forchheimer Flow in Porous media. SPE Annual Techinical Conference and Exhibition, Society of Petroleum Engineers, Houston, Texas.

BASF (2008): Elastocoast - An innovative Technology in Coastal Protection... today and tomorrow. GmbH, B.P., ed., 112.

Battjes, J.A. (1972): Set-up due to irregular waves. Delft University of Technology, Netherlands.

Battjes, J.A. (1974): Surf Similarity. *14th International Conference on Coastal Engineering*, American Society of Civil Engineers, 1, Copenhague, Denmark, 466-480.

Battjes, J.A.; Roos, A. (1974): Characteristics of flow in run-up of periodic waves. Delft Unitversity of Technology, Netherlands.

Battjes, J.A.J., J P (1978): Energy loss and set-up due to breaking of irregular waves. *Proceedings 16th Coastal Engineering Conference*, ASCE, 569-587.

Baumert, H.Z.; Simpson, J.; Sündermann, J. (2011): Marine Turbulence -Theories, Observations and Models -. United Kingdom, 654.

Bear, J. (1972): Dynamics of Fluids in Porous Media. New York: Elsevier.

Bennethum, L.S.; Giorgi, T. (1997): Generalized Forchheimer equation for two-phase flow based on hybrid mixture theory. *Transport in porous media*, 26, 3, 261-275.

Bezuijen, A.; Klein Breteler, M.; Bakker, K.J. (1987): Design criteria for placed block revetment and granular filters. *2nd International Conference on Coastal and Port Engineering in Developing Countries*, COPEDEC, Beijing, China.

Bezuijen, A.; Kruse, G.A.M. (1998): Advanced assessing of the stability of existing placed block revetments. *Proceedings of the 26th International Conference on Coastal Engineering*, Copenhagen, Denmark, 1567-1575.

Biot, M.A. (1956): The theory of propagation of elastic waves in a fluid-saturated porous solid. I. Low-frequency range, II. Higher frequency range. *J. Acoust. Soc. Am.*, 28, 168-191.

Bjarne, J.; Jacobsen, N.G.; Christensen, E.D. (2014): Investigations on the porous media equations and resistance coefficients for coastal structures. *Coastal Engineering*, 84, 56-72.

Bowen, A.J.; Inman, D.L.; Simmons, V.P. (1968): Wave set-down and set-up. *Journal of Geophysical Research*, 73, 8, 2569-2577.

Bruun, P.; Günbak, A.R. (1977): Stability of sloping structures in relation to surf similarity parameter. Risk criteria in design. *Coastal Engineering*, 1, 287-322.

Bruun, P.J.P. (1974): A critical review of the hydraulics of rubble mound structures. The University of Trodheim- The Norwegian Institute of Technology, Trondheim, Norway, 67.

Bullock, G.N.; Obhrai, C.; Peregrine, D.H.; Bredmose, H. (2007): Violent breaking wave impacts. Part I: results from large-scale regular wave tests on vertical and sloping walls. *Coastal Engineering*, 54, 602-617.

Burcharth, H.F. (1978): The effect of wave grouping on on-shore structures. *Coastal Engineering*, 2, 0, 189-199.

Burcharth, H.F. (1998): Influence of Core Permeability on Accropode Armour Layer Stability. *Proceedings of the International Conference: coastlines, structures and breakwater*, Thomas Telford, London, U.K., 34-35.

Burcharth, H.F.; Christensen, C. (1991): On stationary and non-stationary porous flow in coarse granular materials. Inst. for Vand, Jord og Miljøteknik, Aalborg.

Camenen, B.; Larson, M. (2007): Predictive formulas for breaker depth index and breaker type. *Journal of Coastal Research*, 23, 4, 1028-1041.

Collins, J.I.W., W (1969): Probabilities of wave characteristics in the surf zone. Tetra Tech Inc., Pasadena, California.

Davidse, M.P. (2009): Wave impact on asphlatic concrete revetments. Ph.D. thesis, *Faculty of Civil Engineering*, Delft University of Technology, The Netherlands, 108.

Davidson, M.A.; Bird, P.A.D.; Bullock, G.N.; Huntley, D.A. (1996): A new non-dimensional number for the analysis of wave reflection from rubble mound breakwaters. *Coastal Engineering*, 28, 1-4, 93-120.

De Groot, M.B.; Bolton, M.D.; Foray, P.; Meijers, P.; Palmer, A.C.; Sandven, R.; Sawicki, A.; Teh, T.C. (2006): Physics of liquefaction phenomena around marine structures. *Journal of Waterway, Ports, Coastal and Ocean Engineering, ASCE*, 132, 4, 227-243.

de Lemos, M.J.S.; Pedras, M.H.J. (2001): Recent mathematical models for turbulent flow in saturated rigid porous media. *ASME Journal of Fluids Engineering*, 123, 4, 935-940.

de Waal, J.P.; van der Meer, J. (1992): Wave run-up and overtopping on coastal structures. *Proceedings of the 23rd Conference on Coastal Engineering*, Venice, Italy, 1758-1771.

Dean, R.G.; Dalrymple, R.A. (1991): Water wave mechanics for engineers and scientists. New Jersey: World Scientific Press.

Dean, R.G.; Walton, T.L. (2008): Wave setup- A State of the art review. Beaches and Shores Resources Center- Institute of Science and Public Affairs- Florida State University, 26.

Dean, R.G.; Walton, T.L. (2010): Wave Setup. *In: Kim, Y.C. (ed.): Handbook of coastal and ocean engineering*, Los Angeles, USA: World Scientific Press, 1190.

del Jesús Peñil, M. (2011): Análisis tridimensional de la interacción del oleaje con obras marítimas. Ph.D. thesis, *Departamento de Ciencias y Técnicas del Agua y del Medio Ambiente*, Universidad de Cantabria, Santander, Spain.

den Adel, H. (1987): Cyclic permeability of granular material. Delft Soil Mechanics.

Dobry, R. (2014): Simplified methods in Soil Dynamics. *Soil Dynamics and Earthquake Engineering*, 61-62, June-July, 246-268.

Dorrestein, R. (1962): Wave set-up on a beach. *Proceedings of the 2nd Technical Conference on Hurricanes*, Miami Beach, Washington, D.C, 230-241.

El Safti, H.; Kudella, M.; Oumeraci, H. (2012): Modelling wave-induced residual pore pressure and deformation of sand foundations underneath caisson breakwaters. *Proceedings of the 33rd. International Conference on Coastal Engineering*, Santander, Spain.

El Safti, H.; Oumeraci, H. (2012): Wave-structure-foundation interaction for gravity marine structures: the structural model. Leichtweiß-Institut, TU Braunschweig, Braunschweig, Germany.

El Safti, H.; Oumeraci, H. (2013): Modelling sand foundation behaviour underneath caisson breakwaters subject to breaking wave impact. *Proceedings of the 32nd International Conference on Ocean, Offshore and Arctic Engineering*, Nantes, France.

Engelund, F. (1953): On the laminar and turbulent flow of ground water through homogeneous sand. *Trans. Danish academy of Technical sciences*, 3.

Ergun, S. (1952): Fluid flow through packed columns. *Chemical Engineering Progress*, 48, 2, 89-94.

EurOtop (2007): European Overtopping of Sea Defences and Related Structures: Assessment Manual. Kuratotium für Forschung im Küsteningenieurwesen: Die Küste. Heft 73.

Eymard, R.; Gallouët, T.; Herbin, R. (2003): Finite Volume methods. France, Centre de Mathèmatiques et Informatique (CMI), Unitè Mixte de Recherche.

Favre, A. (1965): Equations de gaz turbulents compressibles. *Journal de mecanique*, Vol 3 & 4.

Foyer, G. (2013): Prediction formulae for processes on and in Porous Bonded Revetments. Ph.D. thesis, *Fakültat Architektur, Bauingenieurwesen und Umweltwissenschaften*, Technische Universität Braunschweig, Braunschweig, Germany, 164.

Foyer, G.; Oumeraci, H. (2012): External and internal wave set-up at porous PBA revetments on a sand foundation. *Proceedings of the 33rd International Conference on Coastal Engineering*, Santander, Spain.

Foyer, G.; Oumeraci, H. (2013a): Experimental Analysis -Process analysis and model development of wave loads on open-pored and elastically bonded revetments. Leichtweiß-Institut for Hydraulic Engineering and Water Resources, Braunswhweig, Germany.

Foyer, G.; Oumeraci, H. (2013b): Numerical Analysis -Process analysis and model development of wave loads on open-pored and elastically bonded revetments. Leichtweiß-Institut for Hydraulic Engineering and Water Resources, Braunschweig, Germany.

Führböter, A.; Dette, H.H.; Grüne, J. (1976): Response of seadykes due to wave impacts. *Proceedings of the International Conference on Coastal Engineering*, ASCE, Hawaii.

Galvin, C.J. (1968): Breaker type classifications of three laboratory beaches. *Journal of Geophysical Research*, 73, 12.

Galvin, C.J. (1969): Breaker travel and choice of design wave height. *Journal of Waterway, Harbors, Coastal Engineering Div.*, ASCE, WW2, 175-200.

García, N.; Lara, J.L.; Losada, I.J. (2004): 2-D numerical analysis of near-field flow at low-crested permeable breakwaters. *Coastal Engineering*, 51, 10, 991-1020.

Gezuine, C.; Remacle, J.F. (2009): Gmsh: a three-dimensional finite element mesh generatr with built-in pre- and post-processing facilities. *International Journal for Numerical Methods in Engineering*, 79, 11, 1309-1331.

Ghosh, S.; Reins, G.; Koo, B.; Wang, Z.; Yang, J.; Stern, F. (2007): Plunging wave breaking: EFD and CFD. *International Conference on Violent Flows*, Fukuoka, Japan.

Gier, F.; Schüttrumpf, H. (2011): Wissenschaftliche Untersuchung der Stabilität von Verkalit®-Deckwerksteinen. Lehrstuhl und Institut für Wasserbau und Wasserwirtschaft - RWTH Aachen University, 114.

Goda, Y. (1970): A synthesis of breaker indices. *Trans. of the Japan society of Civil Engineering*, 2, 39-49.

Goda, Y. (1974): A new method of wave pressure calculation for the design of composite breakwater. *Proceedings of the 14th International Conference on Coastal Engineering*, Copenhagen, Denmark.

Goda, Y. (2010a): Random wave breaking and nonlinearity evolution across the surf zone. *In: Kim, Y.C. (ed.): Handbook of Coastal and Ocean Engineering*, Singapore: World Scientific Publishing Co., 87-113.

Goda, Y. (2010b): Reanalysis of regular and random breaking wave statistics. *Coastal Engineering*, 52, 1, 71-106.

Gourlay, M.R. (1978): Wave generated currents. Ph.D. thesis, *Department of Civil Engineering*, University of Queensland.

Gourlay, M.R. (1992): Wave set-up, wave run-up and beach water table: Interaction between surf zone hydraulics and groundwater hydraulics. *Coastal Engineering*, 17, 93-144.

Griffiths, J. (1993): The effects of aeration on wave impacts. Ph.D. thesis, *School of Civil and Structural Engineering*, University of Plymouth, United Kingdom, 291.

Harlow, F.; Welch, J.E. (1965): Numerical calculation of time-dependent viscous incompressible flow of fluid with a free interface. *Phys Fluids*, 8, 2182-2189.

Hedges, T.S.; Mase, H. (2004): Modified Hunt's Equation Incorporating Wave Set-up. *Journal of Waterway, Ports, Coastal and Ocean Engineering, ASCE*, 130, 3, 109-113.

Herbers, T.H.C.; Elgar, S.; Guza, R.T. (1995): Generation and propagation of infragravity waves. *Journal of Geophysical Research*, 100, C12, 24863-24872.

Higuera, P.; del Jesús Peñil, M.; Lara, J.L.; Losada, I.J.; Guanche, Y.; Barajas, G. (2013a): Numerical simulation of three-dimensional breaking waves on a gravel slope using a two-phase flow Navier-Stokes model. *Journal of Computational and Applied Mathematics*, 246, 144-152.

Higuera, P.; Lara, J.L.; Losada, I.J. (2013b): Realistic wave generation and active wave absoprtion for Navier-Stokes models. Application to OpenFoam. *Coastal Engineering*, 71, 102-118.

Higuera, P.; Lara, J.L.; Losada, I.J. (2014): Three-dimensional interaction of waves and porous coastal structures using OpenFOAM. Part I: Formulation and validation *Coastal Engineering*, 83, 243-258.

Hirt, C.W. (2012): CFD-101: The Basics of Computational Fluid Dynamics ModelingFLOW3D.

Horikawa, K. (1988): Nearshore dynamics and coastal processes. Tokyo, Japan: University of Tokyo Press, 522.

Hsu, T.-J.; Sakakiyama, T.; Liu, P.L.F. (2002): A numerical model for wave motions and turbulence flows in front of a composite breakwater. *Coastal Engineering*, 46, 1, 25-50.

Hsu, T.-W.; Hsu, J.R.C.; Weng, W.-K.; Wang, S.-K.; Ou, S.-H. (2006): Wave setup and setdown generated by obliquely incident waves. *Coastal Engineering*, 53, 10, 865-877.

Hughes, S.A. (2004): Estimation of wave run-up on smooth, impermeable slopes using the wave momentum flux parameter. *Coastal Engineering*, 51, 11-12, 1085-1104.

Hunt, I.A. (1959): Design of seawalls and breakwaters. *Journal of Waterways and Harbors Division, ASCE*, 85, WW3.

IH-Cantabria (2012): IH-FOAM. IH-FOAM es un modelo numérico tridimensional de reciente creación, y por lo tanto en continuo desarrollo. Está basado en OpenFOAM, un modelo multifísica muy avanzado y robusto que actualmente tiene gran impantación en la industria. El modelo desarrollado se encuentra en el estado del arte de la ingeniería de costas, permitiendo la simulación de flujo bifase en el interior medios porosos y por lo tanto dotándolo de la capacidad de simular todo tipo de estructuras costeras.

Iribarren, R. (1965): Fórmulas para el cálculo de los diques de escolleras naturales o artificiales. *Revista de Obras Públicas*, 113, Spain, 829-849.

Iversen, H. (1952): Laboratory study of breakers. National Bureau Standards Circular Techinical Report 52., Washington, D.C.

Jacobsen, N.G.; Fuhrman, D.R.; Fredsoe, J. (2012): A wave generation toolbox for the open-source CFD library: OpenFOAM. *Int. J. Numerl. Meth. Fluids*, 70, 9, 1073-1088.

Jakobsen, H.A. (2008): Chemical reactor modelling: Multiphase reactive flows. Berlin Heidelberg: Springer-Verlag, 1296.

Jeng, D.-S. (2008): Effects of Wave non-Linearity on residual pore pressures in Marine Sediments. *The Open Civil Engineering Journal*, 2, 63-74.

Kajima, R.; Shimizu, T.; Maruyama, K.; Saito, S. (1983): On-offshore sediment transport experiment by using large scale wave flume. Collected data No. 1-8, Central Research Insitutte of Electric Power Industry, Japan.

Kamphuis, J.W. (1991): Incipient wave breaking. *Coastal Engineering*, 15, 3, 185-203.

Kemp, P.H.; Plinston, D.T. (1974): Internal velocities in the uprush and backwash zone. *Proceedings of 14th Conference on Coastal Engineering*, 14, Copenhagen, Denmark, 575-585.

Kishi, T.; Saeki, H. (1966): The shoaling, breaking and run-up of the solitary wave on impermeable rough slopes. *Proceedings of the 10th International Conference on Coastal Engineering*, ASCE, Tokyo, Japan, 322-348.

Klein Breteler, M. (2007): Validatie van GOLFKLAP. WL | TU DELFT, The Netherlands.

Kobayashi, T.; Cox, D.T.; Wurjanto, A. (1992): Irregular wave reflection and run-up on rough impermeable slopes. *Journal of Waterway, Ports, Coastal and Ocean Engineering, ASCE*, 116, 6, 708-726.

Koenders, M.A. (1985): Hydraulic criteria for filters. Estuary Physics, Kew.

Kudella, M.; Oumeraci, H. (2006): Development of residual pore pressure in the sand bed beneath a caisson breakwater. *Proceedings of the 30th International Conference in Coastal Engineering*, World Scientific Publishing Co., San Diego, California, USA, 4554-4566.

Lai, C.G. (2013): Advanced numerical modelling of soil-structure interaction: peculiarities, examples and case studies. *24th Alert Workshop and School*, The Alliance of Laboratories in Europe for Research and Technology, Aussois, France.

Lambe, W.T.; Whitman, R.V. (1969): Soil Mechanics. New York: John Wiley & Sons, 548.

Lara, J.L.; Losada, I.J. (2006): RANS modelling applied to random wave interaction with sumerged permeable structures. *Coastal Engineering*, 53, 395-417.

Lara, J.L.; Losada, I.J.; Liu, P.L.F. (2006): Breaking waves over a mild slope gravel slope: experimental and numerical analysis. *Journal of Geophysical Research- Oceans*, 111, C11.

Larson, M.K., N C (1989): SBEACH: Numerical model for simulating storm-induced beach change. US Army Corps of Engineers, USA.

Li, T.; Troch, P.; De Rouck, J. (2004): Wave overtopping over a sea dike. *Journal of Computational Physics*, 198, 686-726.

Liebisch, S.; Alcérreca H, J.C.; Foyer, G.; Oumeraci, H. (2014): Physikalische und numerische Untersuchungen offenporiger, gebundener Deckwerke. 100 Jahre HTG, Hafentechnische Gesellschaft e.V. (HTG), Berlin, Germany.

Liebisch, S.; Alcérreca H, J.C.; Kortenhaus, A.; Oumeraci, H. (2012): Bonded porous revetments -effect of porosity on wave-induced loads and hydraulic performance-. *Proceedings of the 33rd International Conference on Coastal Engineering*, Santander, Spain.

Liebisch, S.; Oumeraci, H. (2012): BoPoRe- Bonded Porous Revetments: Preliminary model tests to investigate the effect of porosity on wave induced loads and hydraulic performance. Leichtweiß-Institute for Hydraulic Engineering and Water Resources, Germany, 90.

Liebisch, S.; Oumeraci, H. (2014): BoPoRe - Bonded porous revetments- Experimental analyses of the main model tests and model development. Leichtweiß-Institute for Hydraulic Engineering and Water Resources, Braunschweig, Germany.

Lin, P. (1998): Numerical modeling of breaking waves. Ph.D. thesis, Cornell University, USA.

Lin, P.; Liu, P.L.F. (1998): A numerical study of breaking waves in the surf zone. *Journal of Fluid Mechanics*, 359, 239-264.

Lin, P.; Liu, P.L.F. (1999): Internal wave maker for Navier-Stokes equations models. *Journal of Waterway, Ports, Coastal and Ocean Engineering, ASCE*, 125, 4.

Liu, P.L.F.; Lin, P.; Chang, K.; Sakakiyama, T. (1999): Numerical modelling of wave interaction with porous structures. *Journal of Waterway, Ports, Coastal and Ocean Engineering, ASCE*, 125, 6, 322-330.

Liu, P.L.F.; Losada, I.J. (2002): Wave propagation modelling in coastal engineering. *Journal of Hydraulic Research*, 40, 3.

Liu, X.; Cheng, X.H.; Scarpas, A.; Blaauwendraad, J. (2005): Numerical modelling of nonlinear response of soil. Part 1: Constitutive model. *International Journal of Solids and Structures*, 42, 7, 1849-1881.

Lo, M.J. (1988): Dynamic Wave Set-up. *Proceedings of the 21st of the International Coastal Engineering Conference*, Costa del Sol-Malaga, Spain, 999-1010.

Longuet-Higguins, M.S.; Stewart, R.W. (1963): A note on Wave Setup. *Journal of Marine Research*, 21, 1, 4-10.

Losada, I.J.; Lara, J.L.; Guanche, Y.; González-Ondina, J.M. (2008): Numerical analysis of wave overtopping of rubble mound breakwaters. *Coastal Engineering*, 55, 1, 47-62.

Losada, I.J.; Silva, R.; Losada, M.A. (1996): Interaction of non-breaking directional random waves with submerged breakwaters. *Coastal Engineering*, 28, 249-266.

Losada, M.A.; Giménez-Curto, L.A. (1981): Flow characteristics on rough, permeable slopes under water action. *Coastal Engineering*, 4, 187-206.

Lundgren, H. (1963): Wave thrust and energy level *Proceedings of the International Association for Hydro-Environment Engineering*, London, 147-151.

Madsen, P.A.; Fuhrman, D.R. (2008): Run-up of tsunamis and long waves in terms of surf similarity *Coastal Engineering*, 55, 3, 209-223.

MARIN (2013): ComFlow 3D.

Mase, H. (1989): Random wave runup height on gentle slope. *Journal of Waterway, Ports, Coastal and Ocean Engineering, ASCE*, 115, 5, 649-661.

McCowan, J. (1894): On the highest wave of permanent type. *Philosophical Magazine*, 38, 351-358.

Mei, C.C.; Foda, M.A. (1980): Wave induced responses in a fluid-filled poro-elastic solid with a free surface -a boundary layer theory. *Geophysical Journal of the Royal Astronomical Society*, 66, 3, 597-631.

Miche, M. (1951): Le pouvoir reflêchissant des ouvrages maritimes exposés à l'action de la houle. *Annales des Ponts et Chaussées, Vol. 121 (1951), pp. 285-319. Key: citeulike:5675022*, 121, 285-319.

Miche, R. (1944): Mouvements ondulatoires des mers en profondeur constante on decroissante., Paris: Ann. des Ponts et Chaussees, 131-164.

Morris, D.A.; Johnson, I.A. (1967): Summary of hydrologic and physical properties of rock and soil materials as analyzed by the Hydrologic Laboratory of the US Geological Survey. U.S. Geological Survey, Water-Supply, U.S. Geolocical Survey, U.S.A.

Muttray, M.; Oumeraci, H.; ten Oever, E. (2006): Wave reflection and wave run-up at rubble mound breakwaters. *Proceedings of the 30th International Conference on Coastal Engineering*, San Diego, U.S.A., 12.

Na, S.J.; Do, K.D.; Suh, K.-D. (2011): Forecast of wave run-up on coastal structure using offshore wave forecast data. *Coastal Engineering*, 58, 8, 739-748.

NAFEMS (2014): The importance of mesh convergence -1. Knowledge Base.

Nakayama, A.; Kuwahara, F. (1999): A Macroscopic Turbulence Model for Flow in Porous Media. *Journal of Fluids Engineering*, 121, 427-433.

Neelamani, S. (2005): Subareal wave pressures, layer thickness, run-up and run-down velocity on sea walls. *Indian Journal of Marine Sciences*, 34, 3, 299-309.

Neelamani, S.; Sandhya, N. (2005): Surface roughness effect of vertical and slope seawalls in incident random wave fields. *Ocean Engineering*, 32, 395-416.

Okazaki, S.i.; Sunamura, T. (1991): Re-examination of breaker-type classification on uniformly inclined laboratory beaches. *Journal of Coastal Research*, 7, 2, 559-564.

OpenFOAM (2013): OpenFOAM- The open source CFD toolbox.

OriginLab (2014): OriginLab - Programming Guide.

Ostendorf, D.W.; Madsen, O.S. (1979): An analysis of longshore current and associated sediment transport in the surf zone. MIT, USA.

Oumeraci, H.; Kudella, M. (2004): Wave-induced pore pressure in the sandy seabed underneath a caisson breakwater. Leichtweiß-Insittut für Wasserbau, Technische Universität Braunschweig, Braunschweig, Germany, 119.

Oumeraci, H.; Kudella, M.; Staal, T. (2009): Failure of the Elastocoast revetment during the large-scale model tests in GWK. Leichtweiß-Institut für Wasserbau, Technische Universität Braunschweig, Braunschweig, Germany.

Oumeraci, H.; Staal, T.; Pförtner, S.; Ludwigs, G. (2012): Hydraulic performance, wave loading and response of PBA revetments and their foundations. *European Journal of Environmental and Civil Engineering*, 16, 8.

Oumeraci, H.; Staal, T.; Pförtner, S.; Ludwigs, G.; Kudella, M. (2010): Hydraulic Performance, Wave Loading and Response of Elastocoast Revetments and their Foundation - A Large Scale Model Study-. Leichtweiß Institut für Wasserbau, Braunschweig.

Pedrozo-Acuña, A.; Ruiz de Alegría-Arzaburu, A.; Torres-Freyermuth, A.; Mendoza, E.; Silva, R. (2011): Laboratory investigation of pressure gradients induced by plunging breakers. *Coastal Engineering*, 58, 722-738.

Pilarczyk, K.W. (1987): Sea defences- dutch guidelines on dike protection-. Dutch Ministry of Transport and Public Works, Netherlands.

Pilarczyk, K.W. (1998): Dikes and revetments: design, maintenance and safety. The Netherlands: A.A. Balkema Publishers.

Piontkowitz, T.; Verhagen, H.J.; Verheig, H.; Mai Cao, T.; Dassanayake, D.; Roelvink, D.; Utili, S.; Zielinski, M.; Kont, A.; Ploompuu, T. (2009): EroGRASS- Failure of grass cover layers at seward and shoreward dike slopes. Design, construction and performance. EroGRASS User Group, Lemvig, Denmark.

Polubarinova-Kochina, P.Y. (1962): Theory of ground water movement. Princeton, N.J.: Princeton Univrsity Press.

Postma, G.M. (1989): Wave reflection from rock slopes under random wave attack. Ph.D. thesis, *Department of Civil Engineering*, Delft University of Technology, The Netherlands, 112.

Prosperetti, A.; Tryggvason, G. (2009): Computational methods for multiphase flow. United Kingdom: Cambridge University Press.

Rattanapitikon, W.; Shibayama, T. (2000): Verification and modification of breaker height formulas. *Coastal Engineering Journal, JSCE*, 2, 389-406.

Rattanapitikon, W.; Shibayama, T. (2002): Comparison of breaker height formulas using large-scale wave tanks. *Journal of Science and Technology*, 24, 4, 663-674.

Reedijk, B.; Muttray, M.; van den Berge, A.; de Rover, R. (2008): Effect of core permeability on armour layer stability. *Proceedings of the 31st International Conference on Coastal Engineering*, World Scientific Publishing, 3358-3367.

Roca Barceló, F. (2014): Effect of porosity on hydrodynamic perfomance of Porous Bonded Revetments- numerical modelling and application for shore protection at Valencia, Spain-. Ph.D. thesis, *Escuela Técnica Superior de Ingenieros de Caminos, Canales y Puertos*, Universidad Politécnica de Valencia, Valencia, Spain, In progress.

Sangrey, D.A. (2011): Marine geotechnology - state of the art-. *Marine Geotechnology*, 2, 1-4, 45-80.

Schüttrumpf, H. (2001): Wellenüberlaufströmung bei Seedeichen -Experimentelle und theoretiches Untersuchungen-. Dissertation, Technische Universität Carolo-Wilhemina zu Braunschweig, Germany.

Schüttrumpf, H.; van der Meer, J.; Kortenhaus, A.; Bruce, T.; Franco, L. (2010): Wave run-up and wave overtopping at armored rubble slopes and mounds. *In: Kim, Y.C. (ed.): Handbook of Coastal and Ocean Engineering*, Singapore: World Scientific Publishing Co., 383-409.

Seelig, W.N.; Ahrens, J.P. (1981): Estimation of wave reflection and energy dissipation coefficients for beaches, revetments and breakwaters. U.S. Army, Corps of Engineers, USA.

Sethian, J.A. (1999): Level set methods and fast marching methods: Evolving interfaces in computational geometry, fluid mechanics, computer vision and materials science. Berkeley, California, USA: Cambridge University Press.

Shah, C. (2002): Mesh discretization error and criteria for accuracy of finite element solutions. International ANSYS Conference, ANSYS, 12.

Shih, R.W.K. (1990): Permeability characteristics of rubble material, new formulae. *Proceedings of the International Conference in Coastal Engineering*, 2, Delft, 1499-1512.

Silva, R.; Govaere, G.; Martín, F. (1998): A statistical tool for breakwater design. *Proceedings of 26th Conference on Coastal Engineering*, ASCE, Copenhagen, Denmark, 1920-1933.

Sridharan, A.; Prakash, K. (2002): Permeability of two layer soils. *Geotechnical Testing Journal*, 25, 4.

Stanczak, G. (2008): Breaching of sea dikes initiated from the seaside by breaking wave impacts. Ph.D. thesis, *Faculty of Engineering*, University of Florence, Florence, Italy, 144.

Svendsen, A. (2006): Introduction to nearshore hydrodynamics. Singapore: World Scientific Printers, 744.

Tannehill, J.C.; Anderson, D.A.; Pletcher, R.H. (1997): Computational fluid mechanics and heat transfer. USA: Taylor & Francis.

Terzaghi, K.; Peck, R.B.; Mesri, G. (1996): Soil Mechanichs in Engineering Practice. U.S.A.: John Wiley & Sons, 3rd Edition, 664.

Troch, P. (1997): VOFbreak(2), a numerical model for simulation of wave interaction with rubble mound breakwaters. *Environmental and coastal hydraulics: protecting the aquatic habitat, Proceedings of theme B*, Vols. 1 &2, 1366-1371.

Troch, P.; De Rouck, J.; Burcharth, H.F. (2002): Experimental study and numerical modeling of wave induced pore pressure attenuation inside a rubble mound breakwater. *Proceedings of the 28th International Conference on Coastal Engineering*, World Scientific, United Kingdom, 1607-1619.

USACE (2002): Coastal Engineering Manual. Washington, D.C. : Engineer Manual 1110-2-1100, U.S. Army Corps of Engineers.

van der Meer, J. (1988): Rock slopes anda gravel beaches under wave attack. Ph.D. thesis, *Civil Engineering and Geosciences Faculty*, TU Delft, Netherlands, 214.

van der Meer, J.; Janssen, J.P.F.M. (1995): Wave run-up and wave overtopping at dikes. *In: Structures, T.C.o.F.o.I.a.V.W. (ed.): Wave Forces on inclined and vertical wall structures*, USA: ASCE, 1-27.

van der Meer, J.; Stam, C.J.M. (1992): Wave run-up on smooth and rock slopes of coastal structures. *Journal of Waterway, Ports, Coastal and Ocean Engineering, ASCE*, 118, WW4.

van Gent, M.R. (1993): Stationary and oscillatory flow through coarse porous media. Ph.D. thesis, *Communications on Hydraulic and Geotechnical Engineering*, Delft University of Technology, The Netherlands.

van Gent, M.R. (1994): The modelling of wave action on and in coastal structures. *Coastal Engineering*, 22, 3-4, 311-339.

van Gent, M.R.; Smale, A.J.; Kuiper, C. (2004): Stability of rock slopes with shallow foreshore. *Proceedings of the 4th Interantional Coastal Structures Conference*, ASCE, Portland.

van Vledder, G.P. (1990): Literature survey to wave impacts on dike slopes. DELFT Hydraulics, DELFT, 180.

Venkatramaiah, C. (2006): Geotechnical Engineering. India: New Age International, 3th Edition, 947.

Ward, J.C. (1964): Turbulent flow in porous media. *Journal of Hydraulics Div, ASCE*, 90, HY5, 1-11.

Whitaker, S. (1986): Flow in Porous Media I: A theoretical Derivation of Darcy's Law. *Transport in porous media*, 1, 3-25.

Whitman, R.V. (2000): Fifty years of soil dynamics. Fifteenth Nabor Carrillo Lecture, 20th National meeting of soil mechanics, Oaxaca, Mexico.

Wilcox, D.C. (2006): Turbulence modeling for CFD. USA: D C W Industries, Third Edition.

Witte, H.H. (1988): Wave-induced impact loading in deterministic and stochastic reflection. Leichtweiss Institut für Wasserbau, Technische Universität Braunschweig, Braunschweig, Germany, 1-227.

Yamada, H.; Kimura, G.; Okabe, J. (1968): Precise determination of the solitary waves extreme height on water of a uniform depth. *Rep. Res. Inst. Appl. Mech.*, XVI, 52, 15-32.

Zanuttigh, B.; van der Meer, J. (2006): Wave reflection from coastal structures. *Proceedings of the 30th International Conference on Coastal Engineering*, San Diego, California, USA.

Zanuttigh, B.; van der Meer, J.W. (2008): Wave reflection from coastal structures in design conditions. *Coastal Engineering*, 55, 10, 771-779.

Zen, K.; Yamazaki, H. (1990): Oscillatory pore pressures and liquefaction in seabed induced by ocean waves. *Soils Foundations*, 30, 4, 147-161.

Zen, K.; Yamazaki, H. (1991): Field observations and analysis of wave-induced liquefaction in seabed. *Soils Foundations*, 31, 4, 161-179.

Zhang, J.S.; Jeng, D.S.; Liu, P.L.F. (2011): Numerical study for waves propagating over a porous seabed around a submerged permeable breakwater: PORO-WSSI II model. *Ocean Engineering*, 38, 7, 954-966.

Zienkiewicz, O.C.; Chan, A.H.C. (1988): Computational approach to soil dynmics. *Developments in Geotechnical Engineering*, 42, 3-17.

Zienkiewicz, O.C.; Chan, A.H.C.; Pastor, M.; Schrefler, B.A.; Shiomi, T. (1999): Computational geomechanics with special reference to earthquake engineering. England: John Wiley & Sons Ltd.